ELECTRICAL PERFORMANCE ANALYSIS OF HIGH-SPEED INTERCONNECTS AND CIRCUITS BY NUMERICAL MODELING METHODS

LIU ENXIAO

(B. Eng., M. Eng., Xi'an Jiaotong University, P. R. China)

A THESIS SUBMITTED

FOR THE DEGREE OF DOCTOR OF PHILOSOPHY

DEPARTMENT OF ELECTRICAL & COMPUTER ENGINEERING

NATIONAL UNIVERSITY OF SINGAPORE

2005

Summary

Accurate electromagnetic modeling of high-speed interconnects and multilayer circuits together with efficient simulation of mixed electromagnetic and circuit problems play an important role in modern circuit design and analysis. This thesis focuses on developing accurate and efficient modeling and simulation methods to analyze high-speed interconnects and circuits and perform mixed electromagnetic and circuit simulation.

Specifically, in this thesis an accurate and systematic FDTD-macromodeling approach is implemented for signal integrity analysis of high-speed interconnects, which couples the full-wave FDTD method with the SPICE circuit simulator by using the macromodeling approach. Firstly, the full-wave FDTD method is applied to extract network parameters of the subnetwork consisting of complex interconnects. Then the rational function approximation is performed on these frequency-dependent network parameters to build a macromodel of the interconnect subnetwork by employing the robust and accurate vector fitting method. Finally, the signal integrity analysis of the overall circuit is fulfilled by macromodel synthesis and the SPICE circuit simulator. Numerical results demonstrate that the proposed approach is accurate and efficient to address mixed electromagnetic and circuit problems, in which the electromagnetic effects are fully considered and the strength of the SPICE circuit simulator is also exploited.

Furthermore, a hybrid FDTD and MPIE method is proposed to efficiently analyze multilayer circuits with locally inhomogeneous penetrable objects. The Green's functions for the multilayer planar media are extended to account for general electric and magnetic sources. The numerical integration method with large argument extractions as well as the DCIM (discrete complex image method) is employed to evaluate the Sommerfeld integrals and

compute the spatial-domain Green's functions. Both the direct and iterative approaches are presented to solve the hybrid FDTD-MPIE model. Numerical experiments reveal that the iterative approach is more efficient than the direct one, and the proposed hybrid method can take advantage of the FDTD method for the treatment of inhomogeneous objects and the MPIE method for the solution of multilayered structures. Numerical experiments also demonstrate that the proposed hybrid method is accurate, fairly fast and memory efficient.

Acknowledgements

First and foremost, I would like to express my deepest gratitude to my supervisor Dr. Li Er-Ping for giving me the opportunity to explore the area of electromagnetics (EM), and offering me his invaluable guidance, good research ideas and suggestions, great patience and encouragement throughout my Ph.D. study.

I am also sincerely grateful to my supervisor Prof. Li Le-wei for equipping me with the advanced knowledge both in EM theory and CEM techniques and providing me with invaluable guidance and great support.

I also feel gratitude to Prof. Leong Mook-Seng and Prof. Ooi Ban-Leong for being on my thesis advising committee and giving me their support. Special thanks go to Prof. Ooi Ban-Leong and all the reviewers for their valuable comments and suggestions to improve this thesis.

This thesis benefits from the discussion and support of many people, which include Dr. Yuan Wei-Liang, Dr. Wei Xing-Chang, Mr. Pan Shu-Jun, Dr. Ewe Wei-Bin, Ms Jin Hong-Fang, and other fellow colleagues and staff both from the MRL and RSPL Labs at National University of Singapore (NUS) and the CEE division at the Institute of High Performance Computing (IHPC).

The scholarship awarded by IHPC of A*STAR and NUS is greatly appreciated.

My master degree mentor Prof. Wu Hou-Yu, who guided me into the realm of numerical computation for engineering applications, deserves my appreciation. I also feel gratitude to Madam Zhang Guan-Rong for her care for me. My sincere gratitude also goes to Dr. Wu Qian who is always willing to offer his help to me.

I am indebted to my beloved wife Ms Li Peng-Jun, who shares my pains and joys throughout all these years. It would not be possible for me to finish my study without her patience and encouragement, her confidence in me, and her devotion to the family. Last but not least, my deepest gratitude goes to my beloved parents and younger sister for their selfless love and support.

Table of Contents

List of Symbols

English Alphabets:

A	coefficient matrix
a_k	incident wave
B	column vector in linear system of equations or matrix in state-space equations
b_k	reflected wave
C , D	matrices in state-space equations
C^{Φ}, C^{Ψ}	correction terms for Green's functions
c	direct coupling constant
c_0	speed of light in free space
d_i	coefficients for the denominator polynomial in a rational function or layer thickness
$\mathbf{E}$	electric field (vector)
e	TM mode
f	frequency
G	diagonal matrix containing the starting poles
$\tilde{G}_{\infty}$	large argument approximation of spectral domain Green's function
G_0	spatial domain counterpart of $\tilde{G}_{\infty}$

$\bar{\mathbf{G}}^A$	dyadic Green's function for the magnetic vector potential
$\bar{\mathbf{G}}^F$	dyadic Green's function for the electric vector potentials
$\bar{\mathbf{G}}^{PQ}(\mathbf{r}\,\|\,\mathbf{r}')$	dyadic Green's functions for a P-type field at $\mathbf{r}$ due to a Q-type unit current source at $\mathbf{r}'$
g_i	coefficients for the numerator polynomial in a rational function
$g(t)$	Gaussian pulse in time-domain
$\mathbf{H}$	magnetic field (vector)
$H(\omega)$	transfer function of a network
H	conjugate transpose
$H_0^{(2)}(x)$	zero-order Hankel function of the second type
h	TE mode
I	current
i	current source for a transmission line
$\mathbf{J}$	electric current
$J_n(x)$	cylindrical Bessel function
k	wavenumber
K^{Φ}, K^{ψ}	Green's functions for scalar potentials
k_ρ	wavenumber in ρ direction

$k_x,\ k_y,\ k_z$	wavenumbers in x, y and z directions
$\mathbf{M}$	magnetic current
p_k	poles
Q	number of poles
R^T	row vector comprising the residues
$\mathbf{r}$	spherical coordinate
r_k	residues
$S(\omega)$	scattering matrix of a network
$S_0[\cdot],\ S_1[\cdot]$	Sommerfeld integral of zero or first order
s	Laplace variable
T	pulse width or similarity transform matrix
$T_x(r),\ T_y(r)$	rooftop basis functions along x, y directions
t	time variable or running variables in DCIM
t_r	rising time of a signal
U	left-hand singular vector in SVD
$\hat{\mathbf{u}}$	unit vector
V	voltage or right-hand singular vector in SVD
v	voltage source for a transmission line
X	unknown column vector

x, y, z	Cartesian coordinate
$x(t)$	state variables
$Y(\omega)$	admittance matrix of a network
$y(t)$	system output
Z	impedance
z_k	zeros

Greek Alphabets:

$\Delta x, \Delta y, \Delta z$	space steps in x, y and z directions
Δt	time step
δ	Dirac delta
ε	electric permittivity
$\mathcal{F}$	Fourier transform
Γ	voltage reflection coefficient of a transmission line
Φ	electric scalar potential
ϕ	azimuthal angle
Ψ	magnetic scalar potential
ξ	spectral domain coordinate rotation angle
Λ	column vector of ones

λ	wavelength
$\lambda(s)$	scaling function in the vector fitting method
μ	magnetic permeability
$v_{\max}$	maximum signal phase velocity
ω	angular frequency
$\Pi_x(r),\ \Pi_y(r)$	surface charge density related to rooftop bases
$\boldsymbol{\rho}$	cylindrical coordinate
σ	conductivity
σ_i	singular values of a matrix
$\overline{\Sigma}$	diagonal matrix containing singular values
$\sim$	variables in Spectral-domain
'	variables related to a source
†	Moore-Penrose pseudo-inverse

List of Tables

List of Figures

List of Acronyms

ABC	Absorbing Boundary Condition
CG	Conjugate Gradient
DCIM	Discrete Complex Image
DGF	Dyadic Green's Function
DRA	Dielectric Resonator Antenna
EMI	Electromagnetic Interference
FDTD	Finite-Difference Time-Domain
FEM	Finite Element Method
FFT	Fast Fourier Transform
GPOF	General Pencil of Function
MoM	Method of Moments
MPIE	Mixed Potential Integral Equation
PCB	Printed Circuit Board
SIP	Sommerfeld Integral Path
SPICE	Simulation Program with Integrated Circuits Emphasis
SVD	Singular Value Decomposition
TLGF	Transmission Line Green's Function
TF/SF	Total Field/Scattered Field
ULSI	Ultra Large Scale Integration
VFM	Vector Fitting Method
VLSI	Very Large Scale Integration

Chapter 1. Introduction

Computer aided modeling and simulation, which penetrate nearly every discipline of science and engineering, play an important role in helping human beings explore the nature of science and engineering fields, and expedite the advancements of modern science and technology. In the field of electrical engineering, modeling and simulation are also regarded as indispensable tools in addition to physical experiments. In this thesis modeling and simulation efforts are devoted to developing numerical methods for the electrical analysis of high-speed interconnects and multilayer circuits.

1.1 Background

1.1.1 High-Speed Interconnects and Circuits

In the past decades engineers in the electrical field have seen the rapid evolution of electronic circuits, which advanced from a very simple form with only discrete components capable of manipulation by hands to integrated circuits of VLSI and ULSI with millions of transistors per chip. Examples of modern advanced integrated circuits include microprocessor unit (MPU), dynamic random-access memory (DRAM), application-specific integrated circuit (ASIC),

system-on-chip (SOC) and analog/mixed-signal circuits [1].

The rapid progress in the VLSI technology can be attributed to the proliferation of computers, electronic communication including wireless applications, and consumer electronics. In particular, it is owing to the semiconductor industry's ability to exponentially decrease the minimum feature sizes used to fabricate integrated circuits following Moore's law [1].

Over the past three decades the performance of integrated circuits has been dominated by device properties. To enhance the circuit and system performance, the major effort has been focused on improving the device speed through scaling of device dimensions. Nowadays the trend in VLSI industry has been directed toward more complex designs, higher operating frequencies (increasing to multiple GHz range), sharper rise times, shrinking device sizes and low power consumption [2].

Due to the steady increase in device speed and clock frequencies in the GHz regime, interconnects play an increasingly important role in modern deep submicron VLSI circuits. The electrical performance of interconnects becomes more and more significant, sometimes even dominant in determining the overall electrical performance of state-of-art VLSI circuits and systems [2, 3].

1.1.1.1 Classification of Interconnects

Interconnects can be at various levels of the design hierarchy [2, 4]. Roughly speaking they can be classified into two levels, i.e., on-chip interconnects and package/board level interconnects.

On-chip interconnects mainly comprise the on-chip metallization, which are also called the first-level interconnections. The on-chip metallization is fabricated on top of the semiconductor devices and substrates by photolithographic processes.

Package/board level interconnects are used for chip-to-chip interconnections or module-to-module interconnections. Chip-to-chip interconnects provide connections between pins or pads of IC chips and/or other components, which are also called the second-level interconnections. Examples for this kind of interconnects include printed circuit boards (PCB), and multichip modules (MCM). Module-to-module interconnections are the highest level interconnections inside a circuit system. They provide connections between subsystem modules such as PCBs or MCMs.

The function of interconnects is to distribute clock and other signals and provide power/ground to various circuits and systems functions on a chip. The fundamental development requirement for interconnect is to meet the high-speed transmission needs of chips despite further scaling of feature sizes [1].

1.1.1.2 High-Speed Interconnect Effects

The term, high-speed, is usually defined in terms of the frequency content of a signal on interconnects. In most digital applications the desired highest operating frequency of interest $f_{\max}$ depends on the rise/fall time t_r of the propagating signal. The commonly used relationship between $f_{\max}$ and t_r is given by [2] [5, 6]

$$f_{\max} \approx 0.35/t_r \,. \tag{1.1}$$

It implies that the energy of a signal is mainly distributed in the frequency range $[0,\ f_{\max}]$, and the overall shape of the signal is affected little by those components in the spectrum beyond $f_{\max}$.

The ever-increasing demands for high-speed applications have exhibited the importance of interconnect effects on overall electrical performance of the VLSI circuits and systems.

The previously negligible effects of interconnects become prominent at high frequencies. These effects include signal delay, ringing, distortion and reflections on single interconnect line as well as crosstalk between adjacent lines (see Fig. 1.1) [2]. At the same time, shorter rise time and small feature size increase the electromagnetic interference (EMI) problem including both susceptibility of a device to fields from outside world that couple in and radiation emissions from a device that result in the failure of passing compliance tests. If these interconnects effects are not addressed during early design stages, they may cause malfunction of a fabricated digital circuit, or distort an analogue signal such that it fails to meet the required specifications [7]. To avoid the high cost for extra iterations in a design cycle, accurate and efficient modeling and simulation of interconnects become imperative in the high-speed regime.

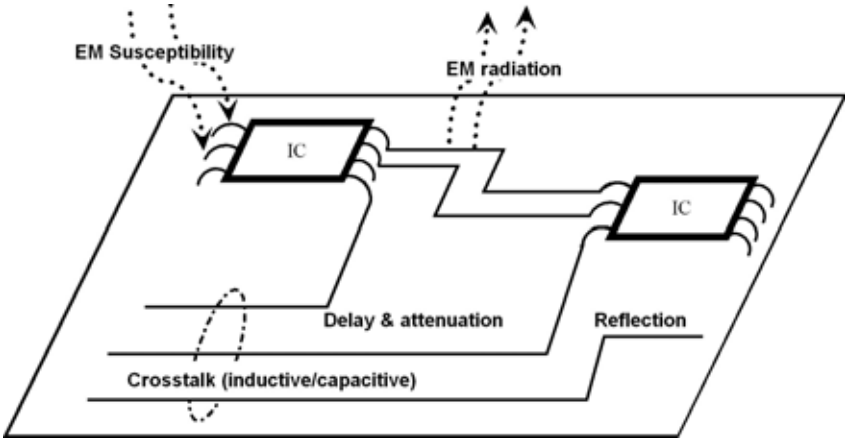

Fig. 1.1 Schematic diagram showing high-speed interconnects effects.

1.1.2 Modeling and Simulation of Interconnects and Circuits

1.1.2.1 EM-oriented Approach and Circuit-oriented Approach

A variety of approaches have been proposed for system-level modeling and simulation of interconnect systems. Basically they can be grouped into electromagnetic (EM) -oriented

approaches and circuit-oriented approaches (see Fig. 1.2).

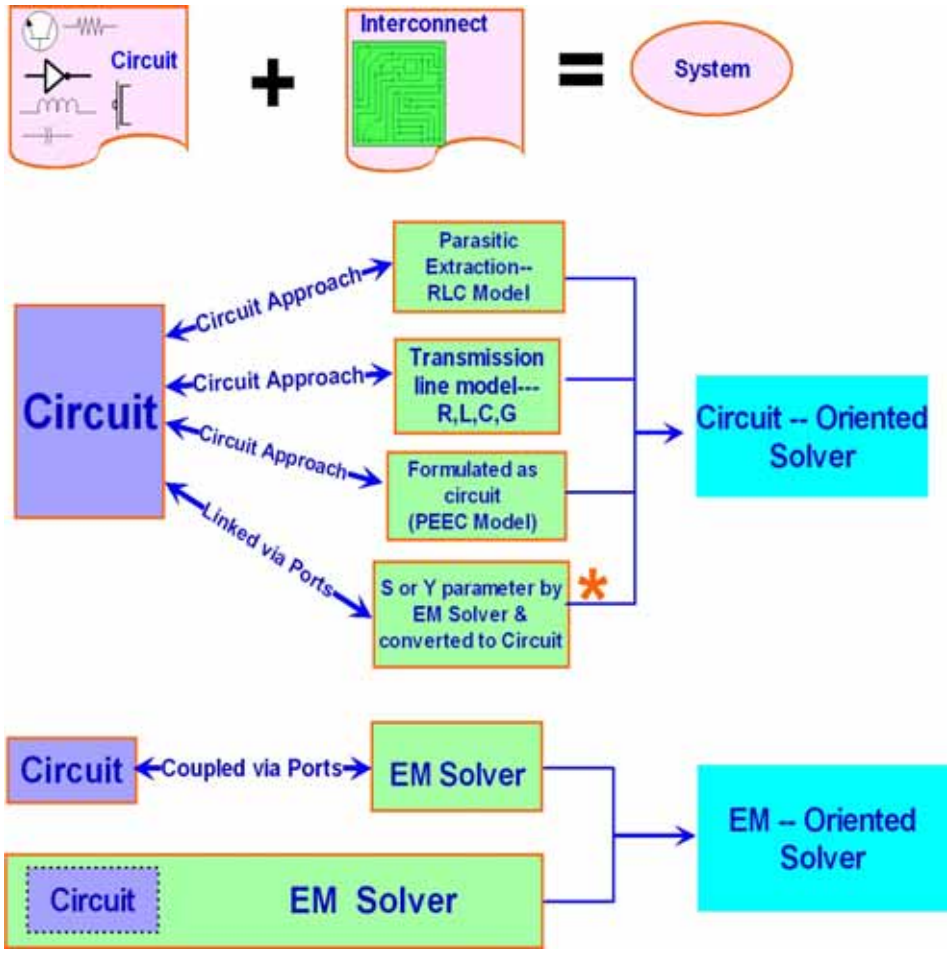

Fig. 1.2 Approaches used for modeling and simulation of interconnect systems.

EM-oriented approaches can be classified into two categories. One category is the hybridized EM-SPICE approach. Perhaps the hybrid FDTD (finite-difference time-domain) and SPICE method [8, 9] is the most widely used method in this category. Another category is that the EM solver directly incorporates the lumped circuit elements. Among all the full-wave electromagnetic methods (e.g., the FDTD method, the integral method and the finite element method), the FDTD method is probably the first EM solver that was extended to handle lumped circuit elements and perform the mixed electromagnetic and circuit analysis [9, 10]. In addition to the extended FDTD method, the time-domain integral equation method was

also developed in [11] to perform the analysis of coupled electromagnetic and circuit problems. Although adding lumped passive circuits to a full-wave EM simulator is straightforward, it is not a routine procedure to coupling a full-wave EM solver with a non-linear circuit solver.

In circuit-oriented approaches interconnects are usually converted into circuits by using parasitic extraction methods, transmission line methods, or macromodel identification method. Therefore, the resultant circuits together with other linear or nonlinear circuit components can be simulated by the powerful SPICE-like circuit simulator for system-level electrical performance analysis.

Parasitic extraction has long been reported in the literature for modeling of interconnects [12, 13]. Early efforts on parasitic extraction have been focused on the resistance extraction [14, 15] and capacitance extraction [16-18]. In recent years electromagnetic modeling of interconnects has become a critical issue for integrated circuit analysis [19], which demands extraction of the inductance of interconnects to account for magnetic coupling [20, 21]. Inductance extraction is in general more complicated than resistance or capacitance extraction due to the difficulty in determining an appropriate current return path.

The partial element equivalent circuits (PEEC) method proposed by Ruehli [22] has been extensively used in electromagnetic analysis of interconnects. This method can perform capacitance extraction [23], inductance extraction, or RLC extraction [24, 25].

For certain applications where lumped models based on parasitic extraction are not adequate, the transmission line model governed by the Telegrapher's equations can be used to characterize the interconnects by distributed RLCG (Resistance, inductance, capacitance and conductance) per unit length (p.u.l.) parameters or by transmission line stamps [2].

An attractive method in the circuit-oriented category is called the macromodeling method, which is based on the network parameters obtained by full-wave analysis of interconnects. The macromodeling method based on EM simulation results is an implementation of the idea of "divide-and-conquer" to tackle complex circuit systems. This method can provide a trade-off between accuracy and speed for modeling and simulation of mixed electromagnetic and circuit problems.

1.1.2.2 Overview of Computational Electromagnetic Methods

Generally speaking, numerical methods for electromagnetic modeling of high-speed interconnects and multilayer circuits can be grouped into two categories, i.e., differential equation methods, such as finite-difference time-domain method (FDTD) [9, 26] and finite element method (FEM) [27, 28]; and integral equation methods, such as the surface integral method and the volume integral method [29, 30].

Each computational electromagnetic method has its own advantages as well as drawbacks. Therefore, the efficiency of a numerical technique is very often problem dependent. In general, the differential equation method is a volume method which requires discretization of the entire solution domain. In contrast, usually only the surface of a solution domain needs to be discretized when using the surface integral equation method, which reduces the unknowns in the problem. Therefore, the linear system of equations yielded by the integral equation method is smaller than that resulted from the differential equation method. Nevertheless, compared to the sparse matrix produced by the differential equation method, the solution of the dense matrix equations obtained by the integral equation method consumes more CPU time. In addition, the differential equation method is more suitable for inhomogeneous and closed-boundary problems. Conversely, the integral equation method is good at handling

homogeneous and open boundary problems.

Among all the computational electromagnetic techniques, the FDTD method is one of the most widely used time-domain methods. The feature of the FDTD method is that one single running of the FDTD solver can generate wide band information of interconnects. Such a prominent feature together with its simplicity in algorithm implementation makes the FDTD method a good candidate for modeling and simulation of interconnects.

Recently, with the development of macromodeling technique [31, 32], high-speed interconnects characterized by network parameters can be integrated into the SPICE circuit simulator to fulfill the mixed electromagnetic and circuit simulation. Using the macromodeling approach, we can solve the mixed electromagnetic and circuit problems by using two steps. In the first step the conventional FDTD method can still be employed to characterize high-speed interconnects by network parameters. In the second step, the macromodeling technique can be used to integrate the network parameters with the SPICE circuit simulator for the solution of the mixed electromagnetic and circuit problems.

As discussed in the previous sections, the constant quest for high-speed applications is always pushing the operating speed and integration density of ICs and circuit boards towards higher levels. To meet the demand of high integration density, multilayer substrates have been widely used. Furthermore, the revolutionary growth of wireless communications has also spurred new designs using three-dimensional heterogeneous integration. In this thesis we will focus on a special kind of multilayer structures, i.e., a multilayer structure with locally inhomogeneous objects. When it comes to modeling such a complex problem, one single method may not be efficient to perform the task [33] and a hybrid method may be a good choice.

1.2 Motivation

The near-term difficult challenges in high-speed interconnects and circuits modeling for DRAM half-pitch greater than 45 nm through year 2010 have been highlighted in the ITRS (International Technology Roadmap for Semiconductor) publications (see Table 1.1). These challenges include accurate and yet efficient 3D interconnect models, especially for transmission lines and S parameters; efficient simulation techniques handling multilayer dielectrics; high-frequency circuit models including non-quasi-static, substrate noise and parasitic coupling; and parameter extraction assisted by numerical electrical simulation instead of RF measurements.

Table 1.1 Near-term capability requirements for modeling and simulation technology adapted from ITRS publications [1].

Year of production	**2003**	**2004**	**2005**	**2006**	**2007**	**2008**	**2009**
DRAM Half-pitch (nm)	**100**	**90**	**80**	**70**	**65**	**57**	**50**
Circuit Component Modeling							
Interconnects and integrated passives	On-chip inductance effects + frequency dependent resistance		Hierarchical full chip RLC		Include reliability		
Package Modeling							
Electrical modeling	Unified RLC extraction for package/chips			Reduced order models		Full-wave analysis	
Numerical Analysis							
Algorithms	Robust, reliable 3D grid generation		Faster algorithms including linear solvers		Exploit parallel computation		

Interconnects play an increasingly important role for staying in pace with Moore' law to double the maximum clock frequency every 1.5 years. As the operation speed of devices is increasing to the multiple GHz range and the complexity of interconnect systems continuously increases, software tools with higher accuracy and better efficiency become necessary. Accurate modeling of high-frequency electromagnetic properties and the ability to

predict the electrical and parasitic properties of complex interconnect structures continues to be a challenge. In particular for some special interconnect structures, such as corners and bends, two-dimensional approximations based on transmission-line theory are unable to predict their performance and a full wave analysis is required. An increasing need is also directed to characterize integrated passives in the high-frequency regime. Full wave description of interconnect devices like transmission lines and antennas will be common for high speed or high frequencies.

Therefore, the research in this thesis will focus on developing numerical methods for the electrical analysis of high-speed interconnects requiring full-wave modeling and multilayer circuits.

In order to handle interconnects requiring full-wave modeling, the full-wave FDTD method and the macromodeling technique will be employed to perform their electrical performance analysis. The integration of these two techniques takes advantage of the accuracy of the full-wave FDTD modeling and the speed of the macromodeling technique in dealing with mixed time and frequency domain problems, which will finally provide a trade-off between accuracy and speed for modeling and simulation of mixed electromagnetic and circuit problems.

Literature review shows that little work has been done on the topic of integrating FDTD results with the SPICE circuit simulator. Watanabe and Asai [34] presented an approach based on the admittance parameter representation of passive devices by using the FDTD method. However, in contrast to the calculation of scattering parameters, direct calculation of admittance parameters corresponded to solving an unloaded oscillator circuit, which caused slow convergence of the transient waveforms due to the mismatch of the terminations [35].

Scattering parameters are the better choice to represent the network parameters of the passive devices because they are stable parameters and can readily be obtained from the full-wave FDTD modeling. Furthermore, the rational function approximation techniques used in [34] introduced many redundant poles and increased the burden of subsequent SPICE simulation of the whole system. Therefore, a robust technique to generate macromodels will be employed in this thesis to facilitate the subsequent SPICE simulation.

A hybrid method may provide an efficient solution for modeling and simulation of multilayer circuits with locally inhomogeneous objects. Although many studies have been done on the hybridization of conventional electromagnetic modeling methods, such as hybrid surface-volume integral method and hybrid FEM-integral equation method [36], little work has been done in hybridizing the FDTD and MPIE method for the analysis of multilayer passive devices with locally inhomogeneous objects. On one hand, the FDTD method can easily handle inhomogeneous media and has the advantage of obtaining wide-band information in a single simulation. On the other hand, the MPIE method is more suitable for modeling multilayer structures [33, 37, 38]. Therefore, hybridizing these two methods may provide an efficient solution for modeling of complex multilayer devices with locally inhomogeneous objects.

1.3 Objectives

The overall objective of the research in this thesis is to develop accurate and efficient numerical methods for the electrical analysis of high-speed interconnects and multilayer circuits. The detailed objectives are given as follows:

- **To implement a macromodeling method using scattering or admittance parameters**

obtained from a full-wave FDTD modeling of high-speed interconnects for mixed electromagnetic and circuit simulation.

The FDTD method is chosen to extract the scattering or admittance parameters of interconnect subnetworks because it can provide wide-band information in a single simulation. The integration of scattering or admittance parameters from the FDTD simulation with the SPICE circuit simulator will be addressed in the thesis for the successful analysis of mixed electromagnetic and circuit problems.

- **To derive and evaluate Green's functions for multilayer planar media due to general electric and magnetic sources.**

In order to model locally inhomogeneous objects embedded in a multilayer structure, Green's functions due to general electric and magnetic sources need to be derived. Furthermore, efficient evaluation of the Sommerfeld integrals arising from computing the spatial-domain Green's functions will be addressed to enhance the MPIE-MOM solution of multilayer circuits.

- **To develop a new hybrid method for modeling and simulation of complex multilayer circuits with locally inhomogeneous objects.**

A new hybrid FDTD-MPIE method will be developed for analysis of the above-mentioned multilayer circuits. By using the equivalence principle, the multilayer structure excluding the inhomogeneous objects can be analyzed by the MPIE method and the inhomogeneous objects by the FDTD method. Continuity of tangential electromagnetic fields links together the MPIE model and the FDTD model to yield the final solutions to the original problem.

1.4 Thesis Organization

This thesis is organized as follows:

The FDTD-macromodeling method is presented in Chapters 2 and 3. Chapter 2 describes the FDTD method used for the extraction of network parameters of high-speed interconnects.

In Chapter 3 a robust vector fitting method is employed to build the macromodel of interconnect subnetworks. The macromodel synthesis is implemented to facilitate the SPICE simulation of the mixed electromagnetic and circuit problem.

Chapter 4 is devoted to the derivation and evaluation of Green's functions for planar multilayered media due to general electric and magnetic sources. Both the numerical integration method with large argument extraction and the DCIM method are implemented to efficiently evaluate spatial-domain Green's functions.

Chapter 5 presents the solution of the MPIE for multilayer structures with PECs using the methods of moments (MoM).

A new hybrid FDTD-MPIE method is proposed and implemented in chapter 6 to efficiently analyze multilayer structures with locally inhomogeneous objects. Numerical examples are presented to validate the proposed hybrid method.

The conclusions and future work of this thesis are presented in Chapter 7.

1.5 Original Contributions

The original contributions of this thesis are presented as follows:

- **An FDTD-macromodeling method is proposed and implemented in this thesis for accurate and efficient electrical analysis of high-speed interconnects systems.**

The full-wave FDTD method coupled with a macromodeling technique via rational

function approximation is proposed and implemented in Chapters 2 and 3 of this thesis. The three-dimensional FDTD method is implemented to extract the frequency-dependent scattering or admittance parameters of high-speed interconnects. The vector fitting method is employed to perform robust and accurate rational function approximation and generate macromodels for high-speed interconnects.

Equivalent circuits obtained through macromodel synthesis are embedded into the SPICE circuit simulator to perform the mixed electromagnetic and circuit simulation. The mixed frequency/time domain problem is thus overcome, which facilitates the signal integrity analysis of a circuit system containing both distributed and nonlinear components.

Numerical results show that the FDTD-macromodeling method is an accurate and efficient approach to address mixed electromagnetic and circuit problems where the electromagnetic field effects are fully considered and the strength of SPICE circuit simulator is also exploited.

- **Green's functions for multilayer planar media are extended to account for general electric and magnetic sources.**

The Green's functions for planar multilayered media are extended in Chapter 4 to account for general electric and magnetic sources. The Green's functions due to general electric and magnetic sources are derived. Both the numerical integration and the DCIM (discrete complex image) methods have been implemented for the evaluation of the Sommerfeld integrals associated with the spatial-domain Green's functions. Large argument extraction is performed to accelerate the evaluation of Green's functions by the numerical integration method. A two-level DCIM using GPOF method has been applied to creating closed-form spatial-domain Green's functions. The efficient and accurate evaluation of spatial-domain

Green's functions facilitates the MoM matrix filling process.

- **A new hybrid FDTD-MPIE method is developed for analysis of multilayer planar circuits with locally inhomogeneous objects.**

A new hybrid FDTD-MPIE method is developed in Chapter 6 to efficiently analyze multilayer structures with locally inhomogeneous objects. Its solution by using both the direct approach and the iterative approach is implemented. The new hybrid method can combine the advantages of the FDTD method for the treatment of inhomogeneous objects and the MPIE method for the solution of multilayer structures. Numerical experiments reveal that the hybrid method is accurate, fairly fast and more memory efficient for analysis of multilayer structures with locally inhomogeneous objects.

Chapter 2. Finite-Difference Time-Domain Method for Network Parameter Extraction

This chapter will focus on the three-dimensional finite-difference time-domain (3D-FDTD) method, which is employed to characterize high-speed interconnects and extract their network parameters. These network parameters will be used to build macromodels for signal integrity analysis.

2.1 Introduction

2.1.1 Overview of Interconnects Simulation Approach

In this thesis an accurate and systematic approach for signal integrity analysis of high-speed interconnects is presented (see Fig. 2.1). The approach employs the full-wave FDTD method to modeling the interconnect subnetwork and extracting its scattering parameters or admittance parameters. Rational function approximation by the vector fitting method is then applied to creating the macromodel of the interconnect subnetwork. Finally, the signal integrity analysis of the mixed electromagnetic and circuit system is fulfilled by using the macromodel synthesis and the SPICE circuit simulator.

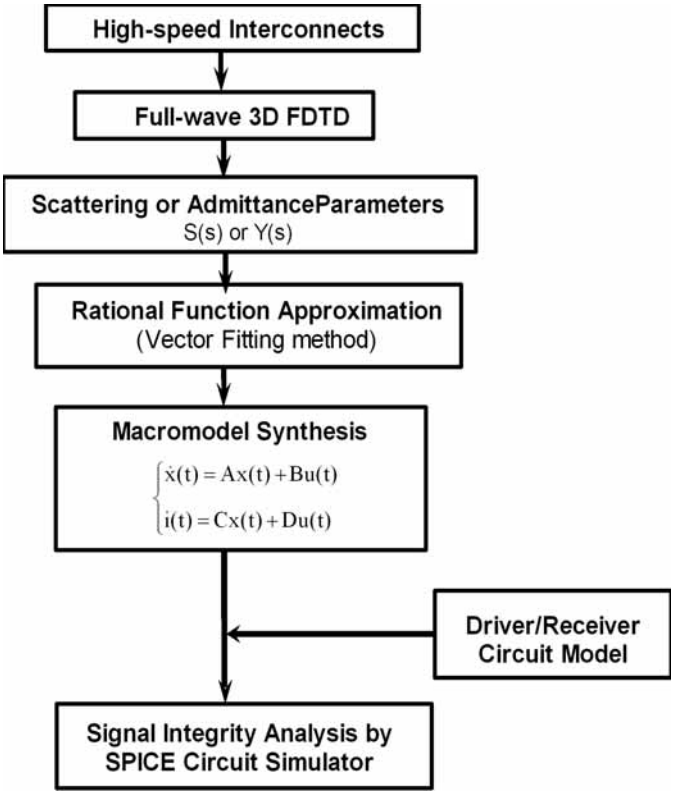

Fig. 2.1 Overall procedures for the mixed electromagnetic and circuit simulation.

2.1.2 Review of FDTD Method

The finite-difference time-domain (FDTD) method, which was originally introduced by K. S. Yee in 1966 [26], is a full-wave, dynamic, and powerful tool for solving the Maxwell's equations. It is one of the most popular numerical techniques for electromagnetic modeling and simulation [9]. And it has been applied to a variety of electromagnetic problems including antennas, biomedical application, microwave circuit, interconnects, electronic packaging, and electromagnetic scattering and penetration. The popularity of the method is partially attributed to its simplicity in algorithm implementation, its ability to handle complex geometries and complex media. Most of all, its prominent feature as a time domain method implies that one single computation can produce a wide-band full-wave electromagnetic solution. Such an

advantage enables the FDTD method to be well suited for high-speed interconnect simulation where a wide-band information is often concerned.

Early research efforts have been mainly focused on applying the FDTD method to studying the properties of passive interconnects. Zhang *et al.* applied the FDTD method to analyzing microstrip transmission lines with discontinuity [39]. The three-dimensional FDTD method was subsequently employed to perform the full-wave simulation of a few typical microstrip circuits [40]. Later on, the FDTD method was also used to generate equivalent circuits for interconnects [41, 42]. Nevertheless, these equivalent circuits can only be derived after several iterations before they finally match the scattering parameters of the interconnects.

Extension of the conventional FDTD method to include lumped circuit elements [10] has paved a new way for the simulation of mixed electromagnetic and circuit systems. In [43] the method was further extended to handle three-dimensional (3D) problems. However, the extended FDTD method is not efficient in dealing with nonlinear circuit elements, because the FDTD time step has to be reduced to a value even far below the upper limit imposed by the Courant stability criterion in order to ensure the convergence of the simulation [44]. In order to efficiently handle general lumped elements, the hybrid FDTD-SPICE method [8] was implemented by deriving an equivalent circuit for the entire FDTD lattice as observed at each FDTD-circuit interface. However, this approach also suffers from the CPU-efficiency and convergence problem.

An attractive alternative to address this kind of interconnect problem is to use the FDTD-macromodeling method. Such an approach was first implemented in [34] using admittance parameters. However, the method used for rational approximation was not robust.

Furthermore, in contrast to compute scattering parameters, direct computation of admittance parameters for an interconnect subnetwork corresponds to simulate an unloaded oscillator circuit, which causes slow convergence of the resultant transient waveforms due to the mismatch of the terminations [35]. In practice, scattering parameters are stable parameters readily available from full-wave FDTD analysis. In this thesis we employ both the admittance parameter and the scattering parameter approaches. Furthermore, a new and robust rational function approximation method is exploited to build the macromodel of the interconnect subnetwork, which will be the topic of the next chapter. Now we will discuss the extraction of admittance (Y) and scattering (S) parameters using the FDTD method.

2.2 Three Dimensional FDTD Method

2.2.1 Maxwell's Equations

In a source-free, linear, isotropic and nondispersive medium (i.e., the electric and magnetic properties of the media is independent of field, direction and frequency), the time-dependent Maxwell's curl equations take the following form:

$$\nabla \times \mathbf{E} = -\frac{\partial \mathbf{B}}{\partial t} \qquad \text{(Faraday's law)} \qquad (2.1)$$

$$\nabla \times \mathbf{H} = \frac{\partial \mathbf{D}}{\partial t} + \mathbf{J} \qquad \text{(Maxwell-Ampere's law)} \qquad (2.2)$$

where $\mathbf{E}$ and $\mathbf{H}$ are the electric field intensity (volts/meter) and magnetic field intensity (amperes/meter), respectively. t is the time variable.

Upon using constitutive relations we can obtain

$$\frac{\partial \mathbf{H}}{\partial t} = -\frac{1}{\mu}\nabla \times \mathbf{E} \tag{2.3}$$

$$\frac{\partial \mathbf{E}}{\partial t} = \frac{1}{\varepsilon}\left(\nabla \times \mathbf{H} - \sigma \mathbf{E}\right) \tag{2.4}$$

where the constants ε, μ, and σ denote the electric permittivity (farads/meter), magnetic permeability (henrys/meter) and electric conductivity (siemens/meter), respectively.

In a three-dimensional Cartesian coordinate system, (2.3) and (2.4) can be expanded into the following six coupled partial differential equations:

$$\frac{\partial H_x}{\partial t} = \frac{1}{\mu}\left(\frac{\partial E_y}{\partial z} - \frac{\partial E_z}{\partial y}\right) \tag{2.5a}$$

$$\frac{\partial H_y}{\partial t} = \frac{1}{\mu}\left(\frac{\partial E_z}{\partial x} - \frac{\partial E_x}{\partial z}\right) \tag{2.5b}$$

$$\frac{\partial H_z}{\partial t} = \frac{1}{\mu}\left(\frac{\partial E_x}{\partial y} - \frac{\partial E_y}{\partial x}\right) \tag{2.5c}$$

$$\frac{\partial E_x}{\partial t} = \frac{1}{\varepsilon}\left(\frac{\partial H_z}{\partial y} - \frac{\partial H_y}{\partial z} - \sigma E_x\right) \tag{2.6a}$$

$$\frac{\partial E_y}{\partial t} = \frac{1}{\varepsilon}\left(\frac{\partial H_x}{\partial z} - \frac{\partial H_z}{\partial x} - \sigma E_y\right) \tag{2.6b}$$

$$\frac{\partial E_z}{\partial t} = \frac{1}{\varepsilon}\left(\frac{\partial H_y}{\partial x} - \frac{\partial H_x}{\partial y} - \sigma E_z\right). \tag{2.6c}$$

2.2.2 Implementation of FDTD Algorithm

The fundamental ingredient of the FDTD algorithm involves direct discretization of the time dependent Maxwell's equations by writing the spatial and time derivatives in a central finite

difference form. This approximation is second-order accurate in both space and time, and it requires the electric and magnetic fields to be offset from one another in space. Furthermore, this two-step "leap-frog" algorithm requires the electric and magnetic fields to be updated at staggered half-time steps. The updating algorithm is explicit, so new values of electromagnetic field components depend only on those at previous time and half-time steps.

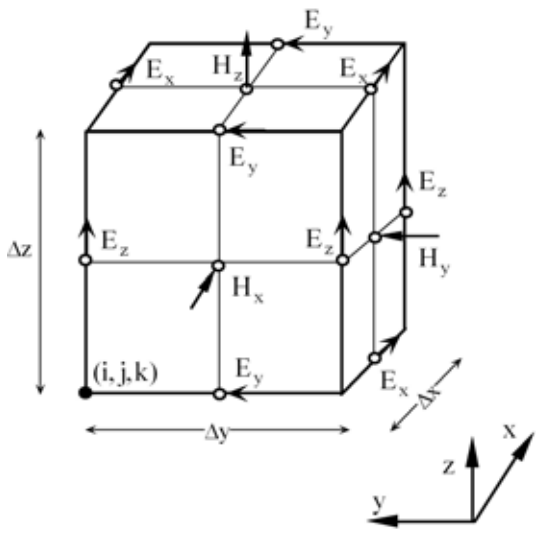

Fig. 2.2 Yee cell and the arrangement of the **E** and **H** field components.

For an arbitrary function $F(x, y, z, t)$, we can use the following compact notation to represent its discretization in space and time:

$$F|_{i,j,k}^{n} = F(i\Delta x, j\Delta y, k\Delta z, n\Delta t) \tag{2.7}$$

where $\Delta x,\ \Delta y,\ \Delta z,$ and Δt are the increments along $x,\ y,\ z,$ and t, respectively.

Yee applied the central difference scheme with second order accuracy to derive the FDTD algorithm [26]:

$$\frac{\partial F|_{i,j,k}^{n}}{\partial x} = \frac{F|_{i+1/2,j,k}^{n} - F|_{i-1/2,j,k}^{n}}{\Delta x} + \mathcal{O}\left[(\Delta x)^2\right] \tag{2.8}$$

$$\frac{\partial F|_{i,j,k}^{n}}{\partial t}=\frac{F|_{i,j,k}^{n+1/2}-F|_{i,j,k}^{n-1/2}}{\Delta t}+\mathcal{O}\left[(\Delta t)^2\right]. \tag{2.9}$$

Referring to the allocation of the field components on the Yee cell shown in Fig. 2.2 and using the above central difference expressions, we can finally derive the following Yee's leap-frog algorithm for updating the six electromagnetic field components:

$$H_x|_{i,j,k}^{n+1/2}=H_x|_{i,j,k}^{n-1/2}-C_h\left(\frac{E_z|_{i,j,k}^{n}-E_z|_{i,j-1,k}^{n}}{\Delta y}-\frac{E_y|_{i,j,k}^{n}-E_y|_{i,j,k-1}^{n}}{\Delta z}\right) \tag{2.10a}$$

$$H_y|_{i,j,k}^{n+1/2}=H_y|_{i,j,k}^{n-1/2}-C_h\left(\frac{E_x|_{i,j,k}^{n}-E_x|_{i,j,k-1}^{n}}{\Delta z}-\frac{E_z|_{i,j,k}^{n}-E_z|_{i-1,j,k}^{n}}{\Delta x}\right) \tag{2.10b}$$

$$H_z|_{i,j,k}^{n+1/2}=H_z|_{i,j,k}^{n-1/2}-C_h\left(\frac{E_y|_{i,j,k}^{n}-E_y|_{i-1,j,k}^{n}}{\Delta x}-\frac{E_x|_{i,j,k}^{n}-E_x|_{i,j-1,k}^{n}}{\Delta y}\right) \tag{2.10c}$$

$$E_x|_{i,j,k}^{n+1}=C_{ea}E_x|_{i,j,k}^{n}+C_{eb}\left(\frac{H_z|_{i,j+1,k}^{n+1/2}-H_z|_{i,j,k}^{n+1/2}}{\Delta y}-\frac{H_y|_{i,j,k+1}^{n+1/2}-H_y|_{i,j,k}^{n+1/2}}{\Delta z}\right) \tag{2.11a}$$

$$E_y|_{i,j,k}^{n+1}=C_{ea}E_y|_{i,j,k}^{n}+C_{eb}\left(\frac{H_x|_{i,j,k+1}^{n+1/2}-H_x|_{i,j,k}^{n+1/2}}{\Delta z}-\frac{H_z|_{i+1,j,k}^{n+1/2}-H_z|_{i,j,k}^{n+1/2}}{\Delta x}\right) \tag{2.11b}$$

$$E_z|_{i,j,k}^{n+1}=C_{ea}E_z|_{i,j,k}^{n}+C_{eb}\left(\frac{H_y|_{i+1,j,k}^{n+1/2}-H_y|_{i,j,k}^{n+1/2}}{\Delta x}-\frac{H_x|_{i,j+1,k}^{n+1/2}-H_x|_{i,j,k}^{n+1/2}}{\Delta y}\right) \tag{2.11c}$$

where the coefficients are defined as

$$C_h=\Delta t/\mu \tag{2.12}$$

$$C_{ea} = \frac{1-\sigma \Delta t/2\varepsilon}{1+\sigma \Delta t/2\varepsilon} \tag{2.13}$$

$$C_{eb} = \frac{\Delta t/\varepsilon}{1+\sigma \Delta t/2\varepsilon}. \tag{2.14}$$

And the semi-implicit expressions such as

$$H_x|_{i,j,k}^{n} = \frac{H_x|_{i,j,k}^{n+1/2} + H_x|_{i,j,k}^{n-1/2}}{2} \tag{2.15}$$

have been used to derive the field updating equations. The semi-implicit expressions result in numerically stable and accurate results [9].

In the above six FDTD field updating equations, the permittivity and permeability are set to appropriate values depending on the location of the field components. For the electric field components located on the dielectric interface, the average permittivity of the two media, i.e. $(\varepsilon_i + \varepsilon_{i+1})/2$, should be used [45]. For the perfect electric conductors, all the tangential electric field and normal magnetic field on their surface must be zero, which is implemented by setting all the tangential electric field components to zero at any time step.

2.3 Numerical Dispersion and Stability

For any finite difference scheme a stability condition must be found to guarantee that the numerical error generated in one step of the calculation does not accumulate and grow to cause stability problems. In order to reduce the truncation and grid dispersion errors, a rule-of-thumb choice of spatial cell size Δx, Δy, and Δz is to restrict them to be at least less than $1/10$ of the minimum wavelength within the frequency range of interest. It is to be noted that in the analysis

of high-speed interconnects and passive circuits by the FDTD method, it is usually the minimum dimension of physical circuits which dominates the choice of the FDTD cell size.

In addition to the restrictions on the cell size in the FDTD implementation to control the numerical error, the time step Δt must comply with the Courant condition [46] to ensure the stability of the FDTD simulation:

$$\Delta t \le \frac{1}{v_{\max}} \left[\frac{1}{(\Delta x)^2} + \frac{1}{(\Delta y)^2} + \frac{1}{(\Delta z)^2} \right]^{-\frac{1}{2}} \tag{2.16}$$

where $v_{\max}$ is the maximum signal phase velocity in the computational volume. Typically, $v_{\max}$ will be the velocity of light in free space unless the entire volume is filled with dielectric.

2.4 Source Excitations

In order to produce the time domain response by the FDTD algorithms, we must apply source excitations to the physical structures. A proper excitation to a particular structure will excite a field distribution that is expected to be very close to that of eigenmode of the configuration. On the other hand, an improper excitation could lead to spurious solutions that may not physically exist. In addition, the frequency bandwidth of interest for the system is controlled by the width of the time domain excitation pulse. In general, the width of a time domain pulse is inversely proportional to its counterpart in the frequency domain.

The choice of the source excitations for the FDTD simulation is actually problem dependent. A variety of excitation sources have been devised [9], which can be categorized as point-wise **E** and **H** hard sources, current sources, plane-wave sources, plane-wave sources realized by the TF/SF (total-field and scattered-field) techniques, and waveguide sources. In

this section we will review some source excitations used in this thesis.

2.4.1 Gaussian Pulse Source and Its Implementation

A Gaussian pulse, either base-band or modulated, is often used because it has a smooth and well-defined waveform and Fourier spectrum. The mathematical expressions of a Gaussian pulse and a Gaussian pulse modulated by a sine function are given by

$$g(t) = e^{-(t-t_0)^2/T^2} \tag{2.17}$$

$$g(t) = e^{-(t-t_0)^2/T^2} \sin(2\pi f_0 t) \tag{2.18}$$

where the center of the Gaussian pulse is t_0; the pulse width at the $1/e$ points is denoted by T; and f_0 is the modulation frequency.

The spectral domain counterparts of (2.17) and (2.18) can be obtained by Fourier transform. It can be proved that both pulses have the same normalized Gaussian profile in spectral domain:

$$\tilde{g}(f) \propto e^{-(\pi T f)^2}. \tag{2.19}$$

The only difference is that the Gaussian pulse has DC components while the modulated Gaussian pulse does not have.

Based on (2.19) the following relations can be derived to estimate the useful frequency bandwidth for an FDTD simulation from the pulse width T [47]:

$$f_{\max}(\text{GHz}) \approx 500/T(\text{ps}) \qquad \text{for Gaussian Pulse} \tag{2.20}$$

$$\Delta T \approx 1000/T(\text{ps}) \qquad \text{for modulated Gaussian pulse} \tag{2.21}$$

where $f_{\max}$ can be considered as the desired frequency for the FDTD simulation to get accurate results, and ΔT denotes the effective bandwidth in the spectrum of the modulated Gaussian pulse.

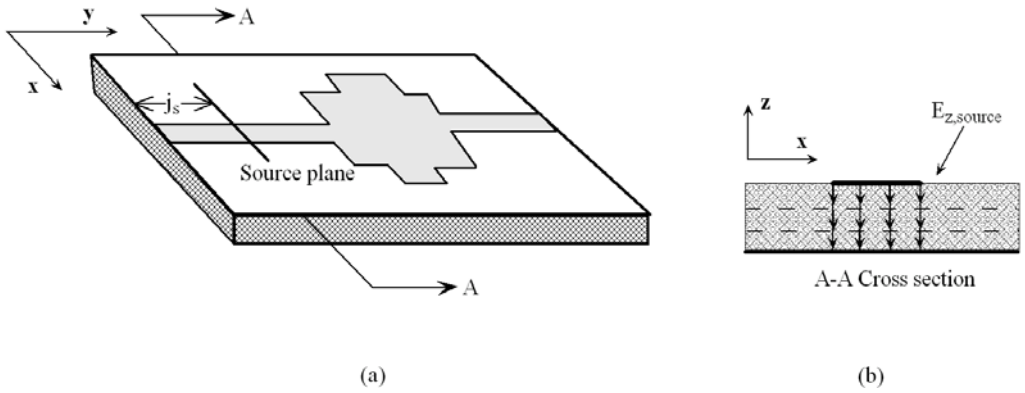

Fig. 2.3 Soft source excitation scheme applied to a microstrip circuit: (a) Location of the source plane; (b) Assumed field distribution on the source plane underneath the microstrip line.

A simple yet efficient source excitation scheme proposed in [48] is employed in this chapter to analyze the high-speed interconnects, which is illustrated in Fig. 2.3, where the source plane is slightly shifted inside the FDTD grid and the soft source scheme is used to effectively separate the wave interactions between the source excitation and reflection from discontinuities of the structure. The excitation source denoted by $E_{z,source}$ is simply imposed onto the FDTD updating equations:

$$E_z\big|_{i,j_s,k}^{n+1} = C_{ea}E_z\big|_{i,j_s,k}^{n} + C_{eb}\left(\frac{H_y\big|_{i+1,j_s,k}^{n+1/2} - H_y\big|_{i,j_s,k}^{n+1/2}}{\Delta x} - \frac{H_x\big|_{i,j_s+1,k}^{n+1/2} - H_x\big|_{i,j_s,k}^{n+1/2}}{\Delta y}\right) + E_{z,source}\big|_{i,j_s,k}^{n} \quad (2.22)$$

2.4.2 Total-field/Scattered-field Technique

The objective of the total-field/scattered-field (TF/SF) technique is to efficiently realize plane

wave source conditions [46]. The underlying principle of the technique is the linearity of the Maxwell's curl equations, which can be described as

$$\mathbf{E}_{\text{total}} = \mathbf{E}_{\text{inc}} + \mathbf{E}_{\text{scat}}, \qquad \mathbf{H}_{\text{total}} = \mathbf{H}_{\text{inc}} + \mathbf{H}_{\text{scat}} \tag{2.23}$$

where $\mathbf{E}_{\text{inc}}$ and $\mathbf{H}_{\text{inc}}$ are incident fields known at all lattice points and all time steps. $\mathbf{E}_{\text{scat}}$ and $\mathbf{H}_{\text{scat}}$ represent unknown scattered fields to be determined.

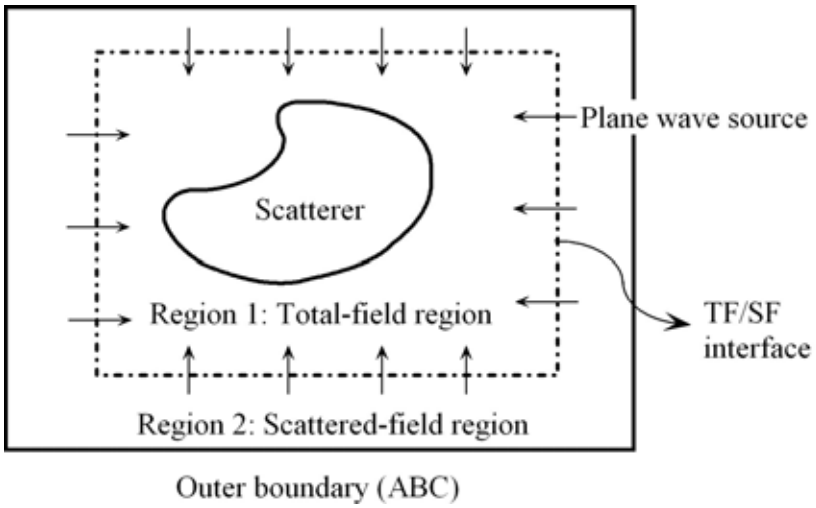

Fig. 2.4 Total-field/scattered-field zoning of the FDTD space lattice.

The FDTD algorithm can be applied with equal validity to the incident-field components, scattered-field components and total-field components. This property enables us to zone the FDTD space lattice into two distinct regions as shown in Fig. 2.4, separated by a nonphysical virtual surface that serves to connect the fields in each region and generate an incident wave. The inner region (Region 1) is denoted as the total-field region, within which both the incident wave and the scattered wave propagate in the presence of the scatterer of interest. The outer region (Region 2) is designated as the scattered-field region because only the scattered wave appears in this region. The outer lattice planes bounding Region 2 are used to

truncate the computational domain and serve to implement ABCs (absorbing boundary conditions).

The TF/SF technique will be applied to the iterative solution for the hybrid FDTD-MPIE method proposed in Chapter 6 of this thesis. Details of the TF/SF technique will then be discussed.

2.5 Mur's ABC and UPML

Many practical electromagnetic problems involve geometries defined in open regions where the computational domain in space is unbounded in one or more coordinate directions. Due to the limitation of computer resources, an absorbing boundary condition (ABC) must be introduced at the outer lattice boundary to simulate the extension of the computational domain to infinity. A variety of ABCs based on either mathematical or physical principles are available for truncating the computational domain. A detailed discussion and comparison of different ABCs can be found in [9].

Both the Mur's 2nd-order ABC [49] and UPML (uniaxial perfectly matched layer) [50] are employed in this thesis. The Mur's ABC is used for interconnect analysis because it is simple and fast for interconnect analysis. Whereas the UPML is used in the hybrid FDTD-MPIE method to reduce the reflection error from the ABC and achieve higher numerical accuracy. The detailed implementation of the Mur's 2nd-order ABC and UPML can be found in [9].

2.6 Extraction of Network Parameters

The transient results for high-speed interconnects can be easily obtained from the three-dimensional FDTD simulation. However, very often the frequency-dependent property of these interconnects is concerned. The Fourier transform is used for this purpose.

High-speed interconnects can be treated as n-port networks. Both the admittance (Y) and scattering (S) parameters of the interconnects can be extracted by the FDTD method. The frequency-dependent admittance parameters $Y_{ij}(\omega)$ can be obtained by

$$Y_{ij}(\omega) = \left.\frac{I_i(\omega)}{V_j(\omega)}\right|_{Vm=0, if\ m\neq j; m=1,2\cdots n} \tag{2.24}$$

where $I_i(\omega)$ and $V_j(\omega)$ are the current and voltage at Port i and j, respectively. For a non-symmetrical n-port network, the FDTD simulation should be performed n times to obtain the admittance matrix. Similarly, the frequency-dependent scattering parameters S_{ij} can be derived by [9]:

$$S_{ij}(\omega) = \frac{V_i(\omega)}{V_j(\omega)}\sqrt{\frac{Z_{0,j}(\omega)}{Z_{0,i}(\omega)}} \tag{2.25}$$

where V_i and V_j are the voltages at port i and j, respectively. $Z_{0,i}$ and $Z_{0,j}$ are the characteristic impedance of the feeding line connected to these ports.

These admittance or scattering parameters will be used to derive macromodels of the interconnects for analysis of the mixed electromagnetic and circuit problems, which is the topic of the next chapter.

2.7 Numerical Examples

2.7.1 Error Analysis of Mur's ABC and UPML

A uniform microstrip line (Fig. 2.5) is used as an example to study the performance of the Mur's 2nd-order ABC and UPML. The dielectric substrate is alumina with $\varepsilon_r = 9.6$ and its thickness is $d = 0.1$ mm. The width of the microstrip line is also $d = 0.1$ mm and its length is 5 mm. The FDTD cell size is $\Delta x = \Delta y = 0.02$ mm and $\Delta z = 0.05$ mm and the total FDTD grid size including ABCs is $25\Delta x \times 45\Delta y \times 100\Delta z$. A 10-cell polynomial-graded UPML is used for this problem. A Gaussian pulse with a 50-GHz bandwidth is placed at $z = 20\Delta z$. The observation point is located at $z = 82\Delta z$ and underneath the microstrip line, which means that the observation point is 8-cell way from the end UPML normal to z.

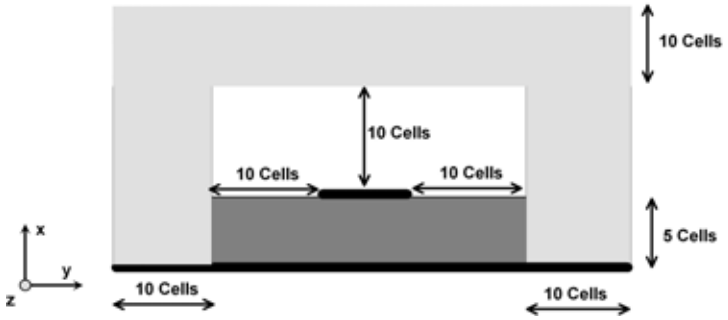

Fig. 2.5 FDTD model for a uniform microstrip line enclosed by ABCs.

By applying the Fourier transform to the ratio of the small reflection caused by ABCs to the incident signal, we can obtain the reflection error due to a specific ABC. Fig. 2.6 shows that the Mur's 2nd-order ABC can achieve the same accuracy of the 10-cell UPML with $\sigma_{\max} = 30$, and the reflection error is around -40 dB. Thus the Mur's ABC can still give accurate results for many practical problems. In addition, compared to the UPML the Mur's ABC obviates the needs of parameter tuning. Therefore, we still employ the Mur's 2nd-order

ABC in the FDTD analysis of interconnects.

From Fig. 2.6 we can also observe that the reflection error is reduced with the increase in the PML conductivity. By carefully tuning the thickness, the maximum conductivity and the order of the polynomial used for the UPML, we can reduce the reflection error caused by the UMPL to less than -100 dB [9], which outperforms the Mur's ABC. Therefore, the UMPL is used in Chapter 6 for the hybrid FDTD-MPIE method to achieve high accuracy of the simulation results.

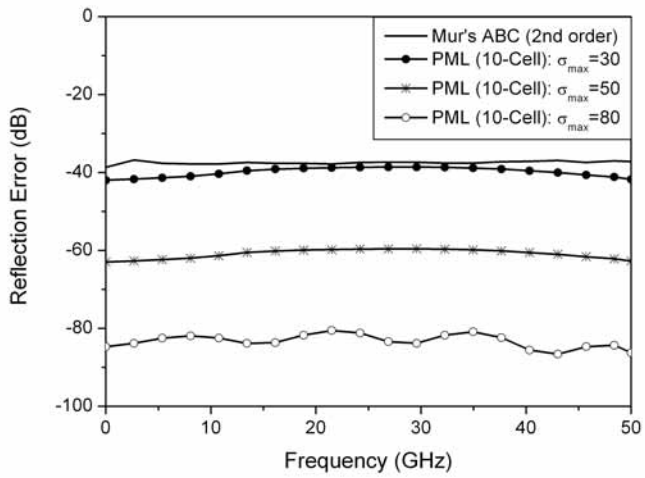

Fig. 2.6 Reflection errors caused by Mur's 2nd-order ABC and UPML. The conductivity of the 10-cell UPML has a profile of a fourth-order polynomial and three different values are studied.

2.7.2 Simulation of a Filter

A microstrip low-pass filter previously studied in [40] is simulated by using the FDTD code developed in this chapter. The geometry and dimensions of the filter are shown in Fig. 2.7. The detailed parameters for the FDTD simulation are as follows: the unit cell size (mm) is $\Delta x = 0.4233, \Delta y = 0.4064, \Delta z = 0.265$; the time step is $\Delta t = 0.441$ ps ; total grid size is $80\Delta x \times 110\Delta y \times 16\Delta z$ and total simulation time steps are 5000. Gaussian pulse source is used in the FDTD simulation.

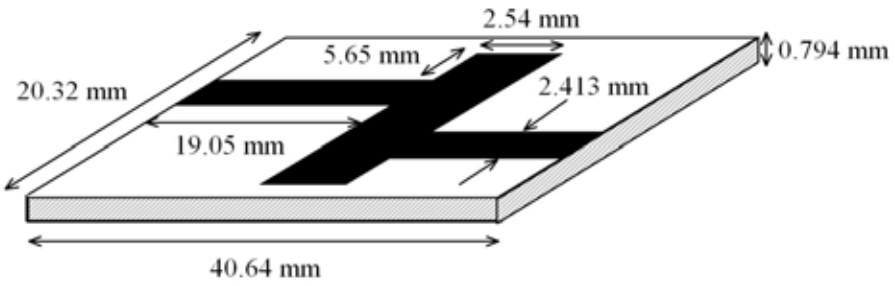

Fig. 2.7 Geometry of a microstrip low pass filter.

It can be observed from Fig. 2.8 that the FDTD simulation results for the scattering parameters are in substantial agreement with the experimental data in [40], which confirms the validity of the FDTD code developed in this chapter.

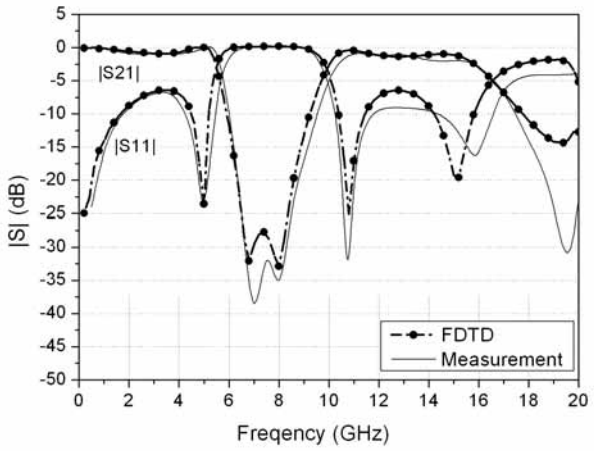

Fig. 2.8 Comparison of scattering parameters for the microstrip low-pass filter.

However, some small discrepancies do exist between the FDTD simulation results and the experimental data. These discrepancies are due to the following modeling errors: the modeling error caused by the inability of the three-dimensional FDTD cubic cell to accurately model the circuit geometry; the modeling error arising from exclusion of conductor loss and dielectric loss in the FDTD simulation; the modeling error introduced by the dispersive absorbing boundary condition. In addition, the discrepancies are also attributed to the

experimental errors [40].

2.8 Summary

This chapter reviews the theoretical foundations of the FDTD method and issues related to the implementation of the FDTD method for analysis of high-speed interconnects. The FDTD code derived from this chapter is validated by numerical examples. The resultant admittance or scattering parameters from the FDTD simulation of the high-speed interconnects will be used to create macromodels, which will be the topic of the next chapter.

Chapter 3. Rational Function Approximation and Macromodel Synthesis

In the previous chapter the frequency-dependent scattering or admittance parameters of interconnects have been obtained by the FDTD method. The next stage for the simulation of mixed electromagnetic and circuit problems is to incorporate the frequency dependent network parameters into the final time domain circuit analysis, which is the topic of this chapter.

3.1 Introduction

The frequency-dependent scattering or admittance parameters extracted by the three-dimensional FDTD method can not be readily linked with nonlinear circuit elements to efficiently perform the time-domain signal integrity analysis at the system-level due to the mixed frequency/time domain problem.

Many approaches have been proposed to address the mixed domain problem. A straightforward approach for this problem was to employ the inverse fast Fourier transform (IFFT) and convolution method [51]. However, this approach suffers from excessive computational cost in the convolution process. Another approach to solve this mixed domain problem was based on the complex frequency hopping (CFH) method by moment matching [7, 52]. The difficulty of the approach is that for every moment a corresponding derivative of

each parameter must be computed using numerical integration across the entire time domain. This process has to be repeated on multiple frequency expansion points, which is cumbersome for a high-order approximation or networks with many ports.

An efficient macromodeling approach based on sampled frequency data has been discussed in [31, 32, 34, 35, 53-55], which employs the rational function approximation to tackle the mixed frequency/time domain problem. The macromodel obtained by the rational function approximation can be used in conjunction with recursive convolution [56] to efficiently simulate the interconnects along with nonlinear devices. Alternatively, the resultant macromodel can be converted to an equivalent circuit for the SPICE simulation [2].

Many researchers have applied different methods to performing the rational function approximation. The section-by section approximation approach was proposed in [53], which partitioned the frequency rang of the data set into small sections to avoid ill-conditioning problems. The approximation of a section took into account the local rational approximation from a previous section. The drawback of this approach is that the overall model has an artificially large number of poles accumulated from the approximation of each section. Therefore, the order of the resultant model has to be reduced by additional computational efforts.

The matrix equations in [31] introduced unnecessary ill-conditioning to the approximation by using the terms ω^2 in the numerator and denominator polynomials. An improved approach was proposed to recursively compute pole–zero pairs [54]. But this approach is only valid for real poles, which restricts its application to RL and RC circuits.

The vector fitting (VF) method developed by Gustavsen and Semlyen [57] is a robust method for rational function approximation. The vector fitting method has some advantages

over other fitting methodologies [58]. Most fitting methods rely on nonlinear optimization algorithms that are complex and may converge to a local minimum. Conversely, the vector fitting method relies on the solution of two linear least-squares problems to obtain the optimal solution. At the same time, the vector fitting method does not suffer much from the numerical stability problem even when the bandwidth of interest is wide. Furthermore, one single run of the vector fitting method can achieve the rational function approximation of all the elements in a transfer function matrix with the same set of poles. Therefore, in this chapter we will employ the vector fitting method to perform the rational function approximation of the scattering or admittance network parameters for interconnects. Subsequently, the macromodel generated by the vector fitting method is synthesized as an equivalent circuit, which is compatible with the SPICE circuit simulator and can be combined with other external linear or nonlinear circuits to perform signal integrity analysis.

3.1.1 Rational Function Approximation

The general form of an N-port network parameters for interconnects is given by

$$H(\omega_i)=\begin{bmatrix} H_{11}(\omega_i) & H_{12}(\omega_i) & \cdots & H_{1N}(\omega_i) \\ H_{21}(\omega_i) & H_{22}(\omega_i) & \cdots & H_{2N}(\omega_i) \\ \vdots & \vdots & \ddots & \vdots \\ H_{N1}(\omega_i) & H_{N2}(\omega_i) & \cdots & H_{NN}(\omega_i) \end{bmatrix}, \qquad i=1,\cdots,M \qquad (3.1)$$

where $H(\omega_i)$ can be the discrete scattering parameter $S(\omega_i)$ or admittance parameter $Y(\omega_i)$. And ω_i is the angular frequency.

To facilitate the analysis of signal integrity of a circuit system involving interconnect components, the frequency-dependent data in (3.1) can be approximated by rational functions to obtain its macromodel. The idea of the rational function approximation is to fit the

frequency response of a network by a ratio of two polynomials with real coefficients in Laplace domain:

$$H_{ij}(s) = \frac{g_0 + g_1 s + g_2 s^2 + \cdots + g_n s^n}{1 + d_1 s + d_2 s^2 + \cdots + d_m s^m} = \frac{\sum_{i=0}^{n} g_n s^n}{1 + \sum_{i=1}^{m} d_m s^m} \tag{3.2}$$

where g_i's denote the real coefficients for the numerator polynomial of degree n and d_i's represent the real coefficients for the denominator polynomial of degree m. d_0 in the denominator is normalized to one. Apparently $H_{ij}(s)$ can either be $Y_{ij}(s)$ or $S_{ij}(s)$.

Asymptotically equation (3.2) can be written as

$$H_{ij}(s) \approx \left(\frac{g_n}{d_m} \right) s^{n-m}, \tag{3.3}$$

and the following expressions hold

$$H_{ij}(\infty) = \begin{cases} 0, & \text{if } n < m, \\ \dfrac{g_n}{d_m}, & \text{if } n = m, \\ \pm\infty, & \text{if } n > m. \end{cases} \tag{3.4}$$

If $n \le m$, then the rational function in (3.2) is called proper; otherwise, it is called improper. The case of $n > m$ usually does not occur in the circuit analysis [59].

A common way of performing rational function approximation is to multiply both sides of (3.2) by its denominator. For M discrete frequency data, the resultant linear equations with respect to the unknowns g_i's and d_i's are given by

$$\begin{bmatrix} 1 & j\omega_0 & (j\omega_0)^2 & \cdots & (j\omega_0)^n & -j\omega_0 H(\omega_0) & (-j\omega_0)^2 H(\omega_0) \\ 1 & j\omega_1 & (j\omega_1)^2 & \cdots & (j\omega_1)^n & -j\omega_1 H(\omega_1) & (-j\omega_1)^2 H(\omega_1) \\ \vdots & \vdots & \vdots & \vdots & \vdots & \vdots & \vdots \\ 1 & j\omega_M & (j\omega_M)^2 & \cdots & (j\omega_M)^n & -j\omega_M H(\omega_M) & (-j\omega_M)^2 H(\omega_M) \end{bmatrix}$$

$$\begin{bmatrix} \cdots & (-j\omega_0)^m H(\omega_0) \\ \cdots & (-j\omega_1)^m H(\omega_1) \\ & \vdots \\ \cdots & (-j\omega_M)^m H(\omega_M) \end{bmatrix} \begin{bmatrix} g_0 \\ g_1 \\ \vdots \\ g_n \\ d_1 \\ d_2 \\ \vdots \\ d_m \end{bmatrix} = \begin{bmatrix} H(\omega_0) \\ H(\omega_1) \\ \vdots \\ H(\omega_M) \end{bmatrix} \tag{3.5}$$

where the subscripts i and j for $H(s)$ are dropped for brevity. This convention is used throughout this chapter unless otherwise stated.

It is obvious that when a higher degree of the polynomial is needed for rational function approximation over a wide frequency range, (3.5) may suffer from the numerical stability problem, which is attributed to the large discrepancy among the entries of the matrix in the left-hand side of (3.5). The numerical stability problem can be overcome by the robust vector fitting method, which will be detailed in the following section.

3.2 Vector Fitting Method for Rational Function Approximation

Equation (3.2) can be expanded into the following pole-residue form to facilitate the subsequent macromodel synthesis:

$$H(s) = c + \sum_{k=1}^{Q} \frac{r_k}{s - p_k} \tag{3.6}$$

where the real constant c is the direct coupling term. r_k's and p_k's are the residues and poles of $H(s)$, respectively, which are either real or complex conjugate pairs. And Q is the number of poles.

Equation (3.6) is a nonlinear problem since the unknowns p_k are included in the denominator. However, the vector fitting method proposed by Gustavsen and Semlyen in [57] solves this equation as a linear problem in two steps.

3.2.1 Two-Step Vector Fitting Method

The vector fitting method [57] consists of two steps: the first step is to compute the poles by scaling and iterative procedures; and the second step is to identify the residues.

3.2.1.1 First Step: Pole Identification

Instead of directly computing the poles p_k in (3.6), the vector fitting method computes them via a scaling process and converts the problem of calculating the poles into a problem of computing zeros.

Firstly, a set of starting poles $\tilde{p}_k$ is selected as an initial guess of the actual poles in (3.6). And an unknown scaling function $\lambda(s)$ is expanded using the starting pole set:

$$\lambda(s) = 1 + \sum_{k=1}^{Q} \frac{\tilde{r}_k}{s - \tilde{p}_k} \tag{3.7}$$

where $\tilde{r}_k$'s are the corresponding residues of the scaling function; and the direct coupling term is normalized to one.

Secondly, the original function $H(s)$ in (3.6) is multiplied by the scaling function $\lambda(s)$. The product of the two functions is denoted as $\theta(s)$, which is also approximated by the same starting pole set $\tilde{p}_k$:

$$\theta(s) = \lambda(s)H(s) = \hat{c} + \sum_{k=1}^{Q} \frac{\hat{r}_k}{s - \tilde{p}_k}. \tag{3.8}$$

Substituting $\lambda(s)$ in (3.8) with (3.7), we can obtain

$$\left(1+\sum_{k=1}^{Q}\frac{\tilde{r}_k}{s-\tilde{p}_k}\right)H(s)=\hat{c}+\sum_{k=1}^{Q}\frac{\hat{r}_k}{s-\tilde{p}_k}. \tag{3.9}$$

Since the starting pole set $\tilde{p}_k$ is known, equation (3.9) is linear with respect to the unknowns $\tilde{r}_k$, $\hat{r}_k$ and $\hat{c}$. We can re-arranged it as

$$\left(\hat{c}+\sum_{k=1}^{Q}\frac{\hat{r}_k}{s-\tilde{p}_k}\right)-\left(\sum_{k=1}^{Q}\frac{\tilde{r}_k}{s-\tilde{p}_k}\right)H(s)=H(s). \tag{3.10}$$

For a given frequency point s_l, equation (3.10) becomes

$$A_l X_l = H(s_l) \tag{3.11}$$

where

$$A_l=\left\{1 \quad (s_l-\tilde{p}_1)^{-1} \quad \cdots \quad (s_l-\tilde{p}_Q)^{-1} \quad \frac{-H(s_l)}{(s_l-\tilde{p}_1)} \quad \cdots \quad \frac{-H(s_l)}{(s_l-\tilde{p}_Q)}\right\}, \tag{3.12}$$

$$X_l=\left\{\hat{c} \quad \hat{r}_1 \quad \hat{r}_2 \quad \cdots \quad \hat{r}_Q \quad \tilde{r}_1 \quad \tilde{r}_2 \quad \cdots \quad \tilde{r}_Q\right\}^T. \tag{3.13}$$

Because the coefficients for the numerator and denominator in (3.2) are real, any complex poles and residues will appear in conjugate pairs. Equation (3.12) is modified to preserve the conjugate property of the complex residues [57]. Assuming that the kth and $(k+1)$-th terms for the partial fraction expansions in (3.10) contain complex conjugate pole and residue pairs, i.e.,

$$\tilde{p}_{k+1}=\tilde{p}_k^*=\mathrm{Re}(\tilde{p}_k)+j\,\mathrm{Im}(\tilde{p}_k), \qquad \hat{r}_{k+1}=\hat{r}_k^*=\mathrm{Re}(\hat{r}_k)+j\,\mathrm{Im}(\hat{r}_k). \tag{3.14}$$

Thus we can use $\mathrm{Re}(\hat{r}_k)$ and $\mathrm{Im}(\hat{r}_k)$ as the new unknowns to replace the original complex variables $\hat{r}_k$ and $\hat{r}_{k+1}$ in (3.13). This can be easily done by re-arranging the two corresponding elements in the row vector A_l into the following form:

$$A_{l,k} = \frac{1}{s-\tilde{p}_k} + \frac{1}{s-\tilde{p}_k^*}, \quad A_{l,k+1} = \frac{j}{s-\tilde{p}_k} - \frac{j}{s-\tilde{p}_k^*}. \tag{3.15}$$

For all the M discrete frequencies, (3.11) becomes an overdetermined linear matrix equation if $M > 2Q+1$:

$$\begin{bmatrix} A_1 \\ A_2 \\ \vdots \\ A_l \\ \vdots \\ A_{M-1} \\ A_M \end{bmatrix}_{M\times(2Q+1)} \begin{bmatrix} \hat{c} \\ \hat{r}_1 \\ \vdots \\ \hat{r}_Q \\ \tilde{r}_1 \\ \vdots \\ \tilde{r}_Q \end{bmatrix}_{(2Q+1)\times 1} = \begin{bmatrix} H(s_1) \\ H(s_2) \\ \vdots \\ H(s_l) \\ \vdots \\ H(s_{M-1}) \\ H(s_M) \end{bmatrix}_{M\times 1}, \tag{3.16}$$

which can be written in a compact form:

$$AX = B. \tag{3.17}$$

The problem of finding a vector X which minimize L_2 norm of the residue, i.e., $\|B - AX\|_2$, is called a least-squares problem. Since only positive frequencies are used in the fitting process, once again the entries of A and B in (3.17) are formulated using real quantities to retain the conjugate property of the solutions:

$$\begin{bmatrix} \mathrm{Re}(A) \\ \mathrm{Im}(A) \end{bmatrix} \{X\} = \begin{bmatrix} \mathrm{Re}(B) \\ \mathrm{Im}(B) \end{bmatrix}. \tag{3.18}$$

The least-squares solution X with the smallest norm $\|X\|$ is unique and given by [60]

$$A^T AX = A^T B \tag{3.19}$$

or equivalently

$$X = \left(A^T A\right)^{-1} A^T B = A^{\dagger} B \tag{3.20}$$

where the superscript T denotes the transpose operation. And the Moore-Penrose pseudoinverse $A^{\dagger}$, which can be regarded as a generalization of matrix inversion to non-square matrices, is computed from the singular value decomposition (SVD) [60, 61].

Upon solving (3.18) we can proceed to compute the poles of the original problem. Notice that $\lambda(s)$ and $\theta(s)$ can be expanded into the following pole-zero forms:

$$\lambda(s) = \frac{\prod_{k=1}^{Q}(s - \tilde{z}_k)}{\prod_{k=1}^{Q}(s - \tilde{p}_k)}, \tag{3.21}$$

and

$$\theta(s) = \kappa \frac{\prod_{k=1}^{Q}(s - \hat{z}_k)}{\prod_{k=1}^{Q}(s - \tilde{p}_k)} \tag{3.22}$$

where $\tilde{z}_i$ and $\hat{z}_i$ are the zeros of $\lambda(s)$ and $\theta(s)$, respectively. κ is a real constant. Therefore,

$$H(s) = \frac{\theta(s)}{\lambda(s)} = \kappa \frac{\prod_{k=1}^{Q}(s - \hat{z}_k)}{\prod_{k=1}^{Q}(s - \tilde{z}_k)} \quad . \tag{3.23}$$

Equation (3.23) reveals that the poles of the original function $H(s)$ are equal to the zeros of $\lambda(s)$ because of the same set of starting poles used for their expansions.

Following the solution of the linear equation (3.18), the zeros of $\lambda(s)$ can be calculated as the eigenvalues of the following matrix [57]:

$$\Upsilon = G - \Lambda R^T . \tag{3.24}$$

If only real poles are involved, G is a diagonal matrix containing the starting poles $\tilde{p}_k$; Λ is a column vector of ones; and R^T is a row vector comprising the residues of $\lambda(s)$. They are given by

$$G = \begin{bmatrix} \tilde{p}_1 & 0 & \cdots & 0 \\ 0 & \tilde{p}_2 & \vdots & 0 \\ \vdots & \vdots & \ddots & \vdots \\ 0 & 0 & \cdots & \tilde{p}_Q \end{bmatrix} \tag{3.25}$$

$$\Lambda = \begin{bmatrix} 1 & 1 & \cdots & 1 \end{bmatrix}^T_{1\times Q} \tag{3.26}$$

$$R^T = \begin{bmatrix} \tilde{r}_1 & \tilde{r}_2 & \cdots & \tilde{r}_Q \end{bmatrix}. \tag{3.27}$$

Therefore, in the case of real poles equation (3.24) can be written explicitly as

$$\Upsilon = \begin{bmatrix} \tilde{p}_1 & 0 & 0 & 0 \\ 0 & \tilde{p}_2 & 0 & 0 \\ \vdots & \vdots & \ddots & \vdots \\ 0 & 0 & 0 & \tilde{p}_Q \end{bmatrix} - \begin{bmatrix} \tilde{r}_1 & \tilde{r}_2 & \cdots & \tilde{r}_Q \\ \tilde{r}_1 & \tilde{r} & \cdots & \vdots \\ \vdots & \vdots & \cdots & \vdots \\ \tilde{r}_1 & \tilde{r} & \cdots & \tilde{r}_Q \end{bmatrix}. \tag{3.28}$$

It is obvious that the product ΛR^T is a $Q\times Q$ matrix, but its rank has only one. Equations (3.24) or (3.28) can be considered as a special case of a generalized companion matrix used for the root finding of a polynomial by the eigenvalue method [62].

If a complex pair of poles, e.g., $\tilde{p}_k$ and $\tilde{p}_{k+1}$ ($\tilde{p}_{k+1} = \tilde{p}^*_{k+1}$), is present, the submatrices in (3.24) corresponding to the complex conjugate poles are modified through a similarity transformation (cf. (3.44)). The submatrices corresponding to the complex pole pair have the

following final form:

$$G'_{2\times 2}=\begin{bmatrix} \mathrm{Re}(\tilde{p}_k) & \mathrm{Im}(\tilde{p}_k) \\ -\mathrm{Im}(\tilde{p}_k) & \mathrm{Re}(\tilde{p}_k) \end{bmatrix},\ \Lambda'_{2\times 2}=\begin{bmatrix} 2 & 0 \end{bmatrix}^T,\ \text{and } R'^{T}_{2\times 1}=\begin{bmatrix} \mathrm{Re}(\tilde{r}_k) & \mathrm{Im}(\tilde{r}_k) \end{bmatrix}. \quad (3.29)$$

Again the modification keeps Υ in (3.24) as a real matrix even in the presence of complex poles, which ensure that its complex eigenvalues will be computed as conjugate pairs. If both real poles and complex conjugate poles appear, the matrix G in (3.24) is a tri-diagonal matrix. The eigenvalues of Υ in (3.24) can be computed using the QR-decomposition algorithm [61]. These eigenvalues are the new poles for (3.10).

3.2.1.2 Second Step: Residue Identification

Substituting the new poles obtained in the first step into (3.6) and writing it at a series of discrete frequencies, we can obtain an overdetermined linear problem similar to (3.17), which is formulated with respect to the unknowns c and r_k. Solving the linear least-squares problem can produce the new residues corresponding to the new poles.

The above two steps may have to be repeated several times with the new poles obtained in the first step as starting poles until the approximation converges. It can be observed from (3.7) and (3.8) that if the convergence is achieved and the actual poles and residues of $H(s)$ are obtained, $\theta(s)$ will degenerate into unity, or equivalently all $\tilde{r}_k$'s become zeros. Usually less than five iterations are needed for an approximation [57]. The procedures of the vector fitting method are summarized and shown in Fig. 3.1.

So far, the vector fitting algorithm is applied to a scalar function. As suggested by its name, the vector fitting method is also applicable to a vector to produce a common set of poles for all the elements in the vector. The property of all the elements in the vector sharing a common

set of poles will in general reduce the order of the macromodel for the multiport network and facilitate the macromodel synthesis.

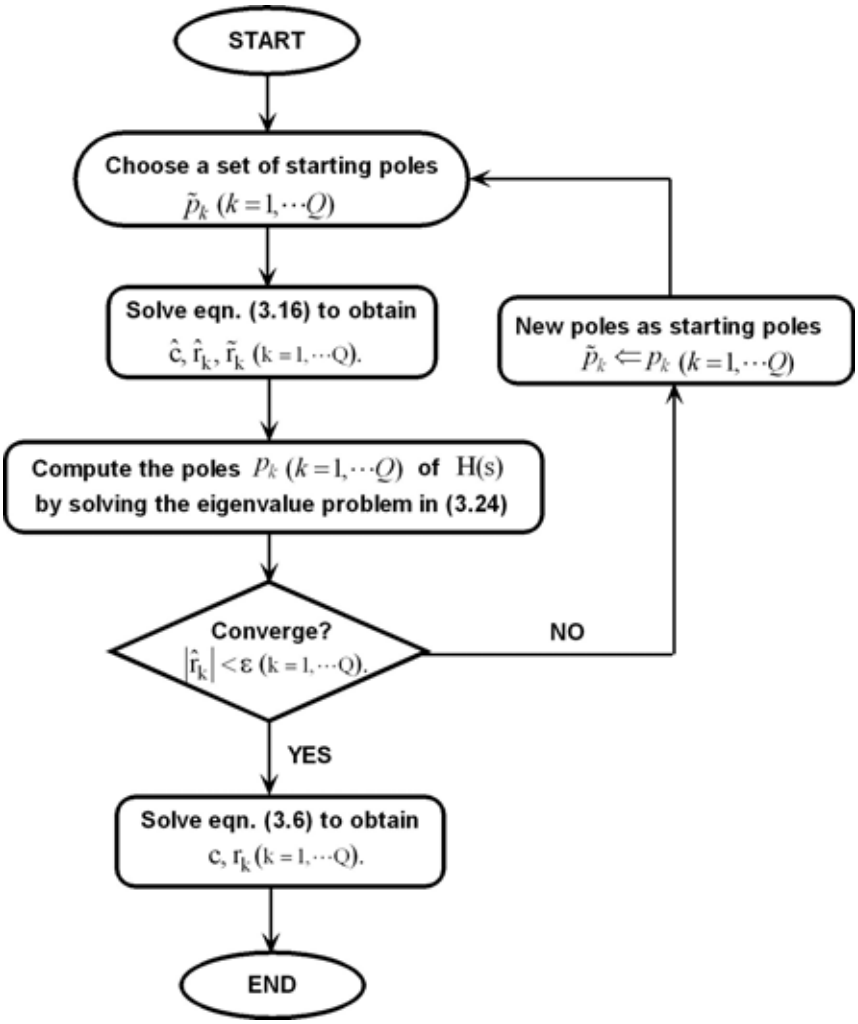

Fig. 3.1 Procedures for rational function approximation via the vector fitting method.

It is straightforward to generalize the vector fitting method to fit a vector. Consider a vector with N elements:

$$\mathbf{H}=\begin{bmatrix} H_1(s) \\ H_2(s) \\ \vdots \\ H_N(s) \end{bmatrix}. \tag{3.30}$$

Since all the elements have the same set of poles, the starting poles and the scaling function remain the same as those in (3.7) for the scalar case. But equation (3.10) is modified as

$$\begin{bmatrix} \left(\hat{c}^1 + \sum_{k=1}^{Q} \frac{\hat{r}_k^1}{s-\tilde{p}_k}\right) \\ \left(\hat{c}^2 + \sum_{k=1}^{Q} \frac{\hat{r}_k^2}{s-\tilde{p}_k}\right) \\ \vdots \\ \left(\hat{c}^N + \sum_{k=1}^{Q} \frac{\hat{r}_k^N}{s-\tilde{p}_k}\right) \end{bmatrix} - \begin{bmatrix} \left(\sum_{k=1}^{Q} \frac{\tilde{r}_k}{s-\tilde{p}_k}\right) H_1(s) \\ \left(\sum_{k=1}^{Q} \frac{\tilde{r}_k}{s-\tilde{p}_k}\right) H_2(s) \\ \vdots \\ \left(\sum_{k=1}^{Q} \frac{\tilde{r}_k}{s-\tilde{p}_k}\right) H_N(s) \end{bmatrix} = \begin{bmatrix} H_1(s) \\ H_2(s) \\ \vdots \\ H_N(s) \end{bmatrix}. \tag{3.31}$$

The linear matrix equation can be written as

$$AX = B \tag{3.32}$$

where

$$A = \begin{bmatrix} A_a & 0 & \cdots & 0 & A_b^1 \\ 0 & A_a & 0 & \vdots & A_b^2 \\ \vdots & 0 & \ddots & 0 & \vdots \\ 0 & \cdots & 0 & A_a & A_b^N \end{bmatrix}, \tag{3.33}$$

$$X = \begin{bmatrix} \hat{c}^1 & \hat{r}_1^1 & \cdots & \hat{r}_Q^1 & \cdots & \hat{c}^M & \hat{r}_1^M & \cdots & \hat{r}_Q^M & \tilde{c}^M & \tilde{r}_1^M & \cdots & \tilde{r}_Q^M \end{bmatrix}^T, \tag{3.34}$$

$$B = \begin{bmatrix} H_1(s) & H_2(s) & \cdots & H_N(s) \end{bmatrix}. \tag{3.35}$$

The submatrices A_a and A_b^i in (3.33) are given by

$$A_a = \begin{Bmatrix} 1 & (s_1 - \tilde{p}_1)^{-1} & \cdots & (s_1 - \tilde{p}_Q)^{-1} \\ \vdots & \vdots & \vdots & \vdots \\ 1 & (s_M - \tilde{p}_1)^{-1} & \cdots & (s_M - \tilde{p}_Q)^{-1} \end{Bmatrix}, \tag{3.36}$$

$$A_b^i = \begin{Bmatrix} \dfrac{-H_i(s_1)}{(s_1-\tilde{p}_1)} & \cdots & \dfrac{-H_i(s_1)}{(s_1-\tilde{p}_Q)} \\ \vdots & & \\ \dfrac{-H_i(s_M)}{(s_M-\tilde{p}_1)} & & \dfrac{-H_i(s_M)}{(s_M-\tilde{p}_Q)} \end{Bmatrix}, \qquad i=1,2,\cdots,N. \tag{3.37}$$

Solving the linear system of equations in (3.32) by using (3.20), we can find the residues $\tilde{r}_k$ of the scaling function $\lambda(s)$. Then the new poles can be computed as the eigenvalues of Υ in (3.24). After a few iterations the accurate poles for the vector in (3.30) can be obtained. Then the corresponding residues for each element in the vector can be computed independently by solving linear least-squares problems.

3.2.2 Selection of Starting Poles and Stability of Fitting Model

Two important problems for the implementation of the vector fitting method are discussed in this section: 1) selection of the starting poles, which is concerned with the convergence of the fitting process; and 2) stability of the fitting model, which is to ensure that the model is useful for time-domain simulation.

3.2.2.1 Selection of Starting Poles

In general, iterations are needed for the vector fitting method to identify the actual poles of a transfer function. Proper selection of starting poles $\tilde{p}_k$ in the first step of the vector fitting method is important to speed up the convergence process.

A set of real poles, which is linearly or logarithmically spaced as a function of frequency, can be used as starting poles for a smooth transfer function [57].

In contrast, for transfer functions with many resonant peaks, the starting poles should be chosen as complex conjugate pairs. Furthermore, the imaginary parts of these conjugate pairs

shall be linearly distributed over the frequency range of interest and at least one hundred times larger than their real parts [57], i.e., $\left|\mathrm{Im}\{\tilde{p}_k\}\right| \geq 100 \times \left|\mathrm{Re}\{\tilde{p}_k\}\right|$. Choosing complex pole pairs with weak attenuation as the starting poles will reduce the number of iterations of the vector fitting method.

3.2.2.2 Stability of Fitting Model

From the linear system theory [63] we have the following conclusions on the stability of a linear system: When all the real parts of the exponents representing a system in time domain are strictly negative, exponential stability occurs and the signals decay within an exponential envelope. When the real parts of the exponents are zero, the corresponding response of the system never decays or grows in amplitude, which is called marginal stability. When at least one real part of the exponents is positive, then the response grows without bound, which causes the system unstable.

Therefore, in order to make the fitting model useful for time-domain simulations, all the poles obtained by the rational function approximation must be stable. The condition to ensure the stability of the fitting model is that all the poles of the fitting model must reside in the left half of the complex plane, i.e. $\mathrm{Re}\{p_k\} \leq 0$.

However, some unstable poles may emerge during the vector fitting process. The constraint on the fitting model is often enforced by some simple treatments, e.g., directly deleting the unstable poles or flipping them around the imaginary axis to the left half-plane before computing their corresponding residues [57]. Flipping an unstable pole p_k with $\mathrm{Re}(p_k) > 0$ from the right half to the left half of the complex plane is equivalent to multiplying the approximant by an all-pass function:

$$P(s) = \frac{s - p_k}{s - \left[-\mathrm{Re}(p_k) + j\,\mathrm{Im}(p_k) \right]}, \tag{3.38}$$

and

$$\left| P(j\omega) \right| = \frac{\sqrt{\left| -\mathrm{Re}(p_k) \right|^2 + \left| \omega - \mathrm{Im}(p_k) \right|^2}}{\sqrt{\left| \mathrm{Re}(p_k) \right|^2 + \left| \omega - \mathrm{Im}(p_k) \right|^2}} = 1, \tag{3.39}$$

which reveals that the pole flipping does not change the amplitude of the original system.

3.3 Macromodel Synthesis

From the previous section we can finally obtain the following macromodel in the pole-residue form for the transfer function $H(s)$ in (3.1):

$$H(s) = \begin{bmatrix} c^{1,1} + \sum_{k=1}^{Q} \frac{r_k^{1,1}}{s - p_k} & c^{1,2} + \sum_{k=1}^{Q} \frac{r_k^{1,2}}{s - p_k} & \cdots & c^{1,N} + \sum_{k=1}^{Q} \frac{r_k^{1,N}}{s - p_k} \\ c^{2,1} + \sum_{k=1}^{Q} \frac{r_k^{2,1}}{s - p_k} & c^{2,2} + \sum_{k=1}^{Q} \frac{r_k^{2,2}}{s - p_k} & \cdots & c^{2,N} + \sum_{k=1}^{Q} \frac{r_k^{2,N}}{s - p_k} \\ \vdots & \vdots & \ddots & \vdots \\ c^{N,1} + \sum_{k=1}^{Q} \frac{r_k^{N,1}}{s - p_k} & c^{N,2} + \sum_{k=1}^{Q} \frac{r_k^{N,2}}{s - p_k} & \cdots & c^{N,N} + \sum_{k=1}^{Q} \frac{r_k^{N,N}}{s - p_k} \end{bmatrix} \tag{3.40}$$

where p_k's are the common poles of the interconnect network, which are identical for all the entries in the transfer function. $c^{i,j}$'s and $r_k^{i,j}$'s are the direct coupling constants and residues for the entries in the transfer function matrix, respectively.

Derivation of partial differential equations from the macromodel in (3.40) is referred to as macromodel synthesis [2]. In general, a set of first-order differential equations, which is also called state-space equations, can be formulated as

$$\begin{cases} \dfrac{d}{dt}x(t) = Ax(t) + Bu(t) \\ \quad y(t) = Cx(t) + Du(t) \end{cases} \tag{3.41}$$

where $A \in R^{L\times L}, B \in R^{L\times N}, C \in R^{N\times L}, D \in R^{N\times N}$. L is the total number of state variables, which is equal to the product of the total number of poles and the total number of ports, i.e., $L = Q \times N$. If the transfer function $H(s)$ is an admittance matrix, the k-th element of the input vector $u(t)$ and the output vector $y(t)$ corresponds to the voltage $v_k(t)$ and current $i_k(t)$ at port k, respectively. Whereas, if $H(s)$ denotes a scattering matrix, they represent the incident wave $a_k(t)$ and the reflected wave $b_k(t)$ at port k, respectively. The incident and reflected waves are defined in terms of the port voltage $v_k(t)$ and current $i_k(t)$ with respect to a reference impedance Z_0 at port k:

$$\begin{cases} a_k(t) = [v_k(t) + z_0\, i_k(t)] \big/ (2\sqrt{z_0}) \\ b_k(t) = [v_k(t) - z_0\, i_k(t)] \big/ (2\sqrt{z_0}) \end{cases}. \tag{3.42}$$

3.3.1 Jordan Canonical Method for Macromodel Synthesis

Because two equivalent state-space systems have the same transfer function, the transfer function in (3.40) can be realized by different state-space forms [64]. In this chapter the Jordan-canonical form of realization [2, 63] is used for macromodel synthesis.

For a general N-port subnetwork, assuming that the submatrices A_r, B_r and C_r contain only real poles and their corresponding residues; whereas the submatrices A_c, B_c and C_c comprise only complex poles and their corresponding residues, we can write the Jordan-canonical realization of (3.40) as

$$\begin{Bmatrix} \dot{x}_1 \\ \dot{x}_2 \\ \dot{x}_3 \end{Bmatrix} = \begin{bmatrix} A_r & 0 & 0 \\ 0 & A_c & 0 \\ 0 & 0 & A_c^* \end{bmatrix} \begin{Bmatrix} x_1 \\ x_2 \\ x_3 \end{Bmatrix} + \begin{bmatrix} B_r \\ B_c \\ B_c^* \end{bmatrix} u \tag{3.43a}$$

$$i = \begin{bmatrix} C_r & C_c & C_c^* \end{bmatrix} \begin{Bmatrix} x_1 \\ x_2 \\ x_3 \end{Bmatrix} + Du \tag{3.43b}$$

where the asterisk denotes complex conjugate. Since complex poles do not have a direct meaning in time domain [2], the similarity transform is introduced by

$$\tilde{x} = Tx \tag{3.44}$$

where $\tilde{x} = \{\tilde{x}_1 \quad \tilde{x}_2 \quad \tilde{x}_3\}^T$ and $x = \{x_1 \quad x_2 \quad x_3\}^T$ are the vectors containing state variables. The transformation matrix is defined as

$$T = \begin{bmatrix} I & 0 & 0 \\ 0 & I & I \\ 0 & jI & -jI \end{bmatrix}, \tag{3.45}$$

where I is the identity matrix and j equals $\sqrt{-1}$. It can be proved that similarity transformation does not change the transfer function of the original system [63].

Finally, equations (3.43a) and (3.43b) can be expressed as

$$\begin{bmatrix} \dot{\tilde{x}}_1 \\ \dot{\tilde{x}}_2 \\ \dot{\tilde{x}}_3 \end{bmatrix} = \begin{bmatrix} A_r & 0 & 0 \\ 0 & \mathrm{Re}(A_c) & \mathrm{Im}(A_c) \\ 0 & -\mathrm{Im}(A_c) & \mathrm{Re}(A_c) \end{bmatrix} \begin{bmatrix} \tilde{x}_1 \\ \tilde{x}_2 \\ \tilde{x}_3 \end{bmatrix} + \begin{bmatrix} B_r \\ 2\,\mathrm{Re}(B_c) \\ -2\,\mathrm{Im}(B_c) \end{bmatrix} u \tag{3.46a}$$

$$y = \begin{bmatrix} C_r & \mathrm{Re}(C_c) & \mathrm{Im}(C_c) \end{bmatrix} \begin{bmatrix} \tilde{x}_1 \\ \tilde{x}_2 \\ \tilde{x}_3 \end{bmatrix} + Du\,. \tag{3.46b}$$

For a general N-port subnetwork characterized by q_1 real poles and q_2 complex conjugate pole pairs, the dimension of the matrix A is $(q_1 + 2 \times q_2) \times N$.

An example of a two-port network with two common poles is used to illustrate the

macromodel synthesis of an admittance matrix:

$$\begin{bmatrix} c^{1,1}+\sum_{k=1}^{2}\frac{r_k^{1,1}}{s-p_k} & c^{1,2}+\sum_{k=1}^{2}\frac{r_k^{1,2}}{s-p_k} \\ c^{2,1}+\sum_{k=1}^{2}\frac{r_k^{2,1}}{s-p_k} & c^{2,2}+\sum_{k=1}^{2}\frac{r_k^{2,2}}{s-p_k} \end{bmatrix}\begin{bmatrix} V_1 \\ V_2 \end{bmatrix}=\begin{bmatrix} I_1 \\ I_2 \end{bmatrix} \tag{3.47}$$

If all the poles are real, then only four state variables are needed and the final state-space equations are given by

$$\begin{aligned} \begin{Bmatrix} \dot{x}_1 \\ \dot{x}_2 \\ \dot{x}_3 \\ \dot{x}_4 \end{Bmatrix} &= \begin{bmatrix} p_1 & 0 & 0 & 0 \\ 0 & p_1 & 0 & 0 \\ 0 & 0 & p_2 & 0 \\ 0 & 0 & 0 & p_2 \end{bmatrix}\begin{Bmatrix} x_1 \\ x_2 \\ x_3 \\ x_4 \end{Bmatrix}+\begin{bmatrix} 1 & 0 \\ 0 & 1 \\ 1 & 0 \\ 0 & 1 \end{bmatrix}\begin{bmatrix} v_1 \\ v_2 \end{bmatrix} \\ y=\begin{bmatrix} i_1 \\ i_2 \end{bmatrix} &= \begin{bmatrix} r_1^{1,1} & r_1^{1,2} & r_2^{1,1} & r_2^{1,2} \\ r_1^{2,1} & r_1^{2,2} & r_2^{2,1} & r_2^{2,2} \end{bmatrix}\begin{Bmatrix} x_1 \\ x_2 \\ x_3 \\ x_4 \end{Bmatrix}+\begin{bmatrix} c^{1,1} & c^{1,2} \\ c^{2,1} & c^{2,2} \end{bmatrix}\begin{bmatrix} v_1 \\ v_2 \end{bmatrix} \end{aligned} \tag{3.48}$$

If one pair of complex conjugate poles $w' \pm jw''$ presents in (3.47) and the corresponding residues are $r'_{k,l} \pm jr''_{k,l}$ $(k,l=1,2)$, the final state-space realization is given by

$$\begin{aligned} \begin{Bmatrix} \dot{\tilde{x}}_1 \\ \dot{\tilde{x}}_2 \\ \dot{\tilde{x}}_3 \\ \dot{\tilde{x}}_4 \end{Bmatrix} &= \begin{bmatrix} w' & 0 & w'' & 0 \\ 0 & w' & 0 & w'' \\ -w'' & 0 & w' & 0 \\ 0 & -w'' & 0 & w' \end{bmatrix}\begin{Bmatrix} \tilde{x}_1 \\ \tilde{x}_2 \\ \tilde{x}_3 \\ \tilde{x}_4 \end{Bmatrix}+\begin{bmatrix} 2 & 0 \\ 0 & 2 \\ 0 & 0 \\ 0 & 0 \end{bmatrix}\begin{bmatrix} v_1 \\ v_2 \end{bmatrix} \\ y=\begin{bmatrix} i_1 \\ i_2 \end{bmatrix} &= \begin{bmatrix} r'_{1,1} & r'_{1,2} & r''_{1,1} & r''_{1,2} \\ r'_{2,1} & r'_{2,2} & r''_{2,1} & r''_{2,2} \end{bmatrix}\begin{Bmatrix} \tilde{x}_1 \\ \tilde{x}_2 \\ \tilde{x}_3 \\ \tilde{x}_4 \end{Bmatrix} \end{aligned} \tag{3.49}$$

3.3.2 Equivalent Circuits

The SPICE (Simulation Program with Integrated Circuits Emphasis), which is used to verify circuit designs and to predict circuit behaviors, is a powerful general-purpose circuit simulation program for nonlinear DC, nonlinear transient and linear AC analyses. It was originally

developed at the Electronics Research Laboratory of the University of California, Berkeley in 1975. Many commercial versions of the SPICE such as PSpice and HSpice are widely used [65]. However, some of the SPICE simulators may not directly accept the differential equations (3.41) as input. Then the macromodel represented by (3.41) can be converted to an equivalent circuit network to facilitate the signal integrity analysis using SPICE simulator [2, 55].

3.3.2.1 Admittance Matrix Based Equivalent Circuits

A two-port network with two states variables characterized by the admittance parameters is used for the purpose of illustration:

$$\begin{Bmatrix} \dot{x}_1 \\ \dot{x}_2 \end{Bmatrix} = \begin{bmatrix} a_{11} & a_{12} \\ a_{21} & a_{22} \end{bmatrix} \begin{Bmatrix} x_1 \\ x_2 \end{Bmatrix} + \begin{bmatrix} b_{11} & b_{12} \\ b_{21} & b_{22} \end{bmatrix} \begin{Bmatrix} v_1 \\ v_2 \end{Bmatrix}$$
$$\begin{Bmatrix} i_1 \\ i_2 \end{Bmatrix} = \begin{bmatrix} c_{11} & c_{12} \\ c_{21} & c_{22} \end{bmatrix} \begin{Bmatrix} x_1 \\ x_2 \end{Bmatrix} + \begin{bmatrix} d_{11} & d_{12} \\ d_{21} & d_{22} \end{bmatrix} \begin{Bmatrix} v_1 \\ v_2 \end{Bmatrix} \quad . \tag{3.50}$$

An equivalent circuit network representing (3.50) is shown in Fig. 3.2. (v_1, v_2) and (i_1, i_2) are the port voltages and currents, respectively. State variables x_1 and x_2 are the voltages across the capacitors, whereas voltage controlled current sources (VCCS) are used to replace the terms such as $c_{11}x_1$. Equivalent circuit realization can be easily generalized to the case of more state variables and more ports.

3.3.2.2 Scattering Matrix Based Equivalent Circuits

Similarly, a simple two-port network with two state variables characterized by scattering parameters is considered:

$$\begin{Bmatrix} \dot{x}_1 \\ \dot{x}_2 \end{Bmatrix} = \begin{bmatrix} a_{11} & a_{12} \\ a_{21} & a_{22} \end{bmatrix} \begin{Bmatrix} x_1 \\ x_2 \end{Bmatrix} + \begin{bmatrix} b_{11} & b_{12} \\ b_{21} & b_{22} \end{bmatrix} \begin{Bmatrix} a_1 \\ a_2 \end{Bmatrix}$$
$$\begin{Bmatrix} b_1 \\ b_2 \end{Bmatrix} = \begin{bmatrix} c_{11} & c_{12} \\ c_{21} & c_{22} \end{bmatrix} \begin{Bmatrix} x_1 \\ x_2 \end{Bmatrix} + \begin{bmatrix} d_{11} & d_{12} \\ d_{21} & d_{22} \end{bmatrix} \begin{Bmatrix} a_1 \\ a_2 \end{Bmatrix} \tag{3.51}$$

where a_k and b_k are the incident wave and the reflected wave at port k, respectively. Additional equations relating the wave variables to the port voltages and currents need to be supplemented:

$$\begin{cases} i_k(t) = \dfrac{1}{\sqrt{Z_0}}[a_k(t) - b_k(t)] \\ v_k(t) = \sqrt{Z_0}[a_k(t) + b_k(t)] \end{cases} \tag{3.52}$$

where Z_0 is the reference impedance at Port k.

An equivalent circuit network representing (3.51) and (3.52) is shown in Fig. 3.3. Its generalization to the case of more state variables or ports is straightforward.

It is to be noted that besides accuracy and stability, a macromodel should possess the passivity property. The passivity property is important because stable but non-passive macromodels may lead to unstable systems when connected to other passive components [2]. Recently several approaches for passivity checking and compensation have been proposed, which include the quadratic and convex optimization [66, 67], trace parameterization [68], perturbation of residues [69, 70], and perturbation of Hamiltonian eigenvalues [71]. The FDTD-macromodel approach proposed in this chapter can be easily extended to account for the passivity issues by using the algorithms proposed in [69] (admittance parameters) and [71] (scattering parameters), which could be the future work of this thesis.

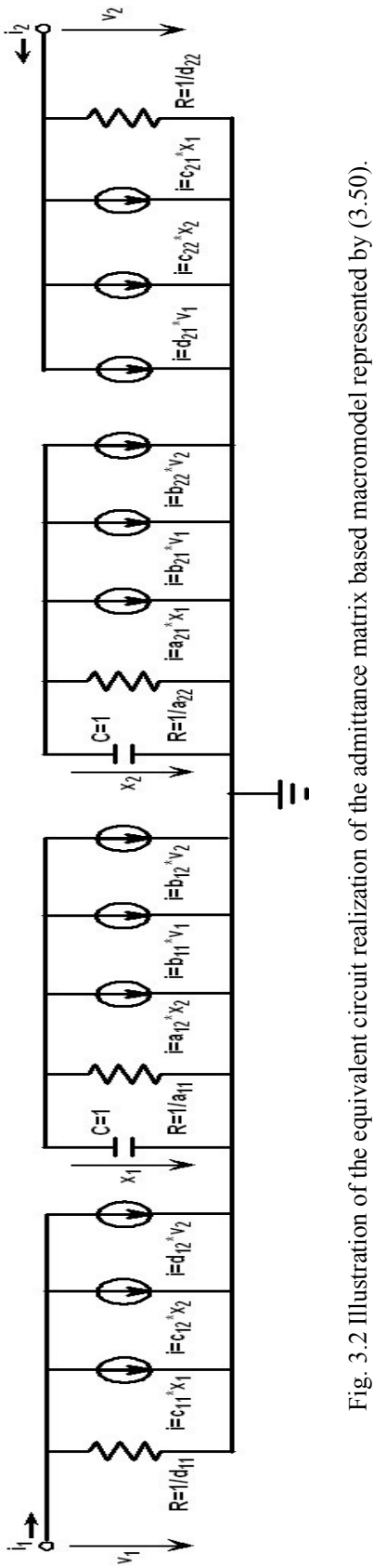

Fig. 3.2 Illustration of the equivalent circuit realization of the admittance matrix based macromodel represented by (3.50).

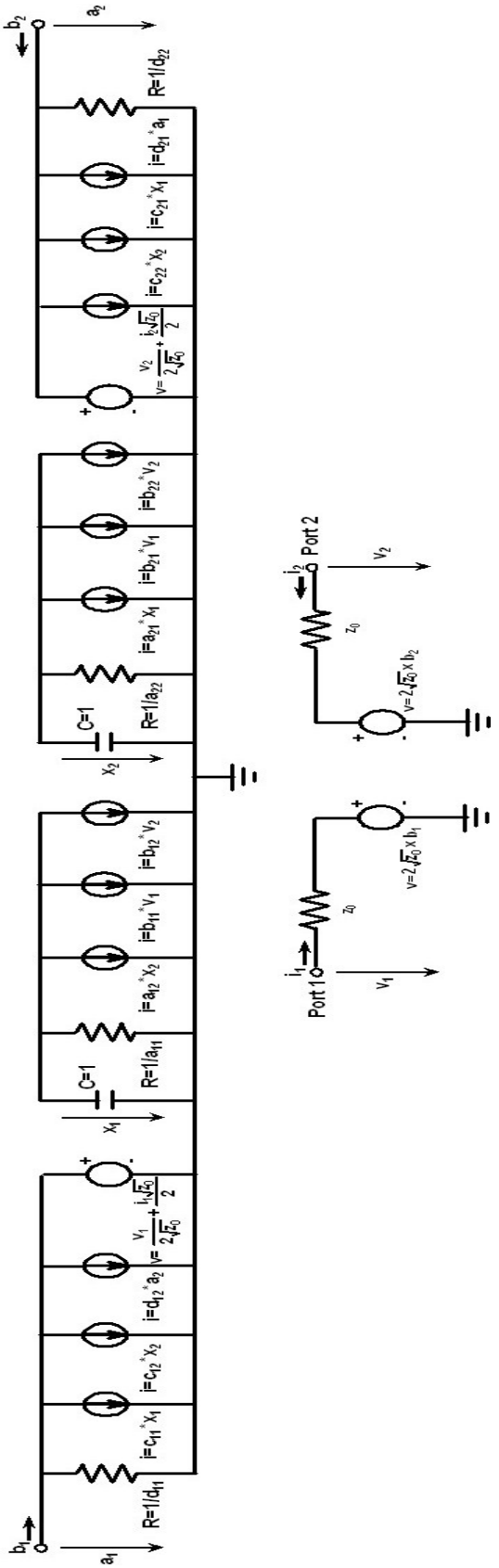

Fig. 3.3 Illustration of the equivalent circuit realization of the scattering matrix based macromodel represented by (3.51) and (3.52)

3.4 Numerical Examples

In this section several numerical examples are presented to demonstrate the validity and accuracy of the FDTD-macromodeling method developed in this thesis. Both the scattering matrix based method and the admittance matrix based method are validated.

In order to verify the accuracy of the proposed scattering matrix based rational function approximation and macromodel synthesis approach, a lumped element example is simulated and the results are compared with those from SPICE circuit simulator [72]. The second example is presented to verify the validity and accuracy of the proposed systematic approach of FDTD macromodeling. The signal integrity analysis of another two circuit examples with two and three ports is performed to further demonstrate the validity of the proposed method.

In addition, four circuit examples, which include a mixer circuit, two microstrip discontinuity circuits and a via coupling circuit, are presented to validate the FDTD macromodeling approach based on the admittance matrix.

3.4.1 FDTD Macromodeling Based on Scattering Matrix

3.4.1.1 A Lumped Circuit with Nonlinear Components

A lumped circuit with nonlinear components is shown in Fig. 3.4a and the CMOS inverter is realized by two MOSFET transistors (see Fig. 3.4b). The scattering parameters of the two-port subnetwork enclosed in the dashed rectangle in Fig. 3.4a are obtained analytically with a reference port impedance of $30\ \Omega$.

Rational function approximation is performed on the scattering matrix by using the vector fitting method. A macromodel with six poles, i.e., two real poles and four complex poles (see

Fig. 3.5) is created to replace the original transfer function of the circuit. Very good agreement can be observed between the analytical results and the results based on the macromodel obtained by the vector fitting method (VFM) (see Fig. 3.6).

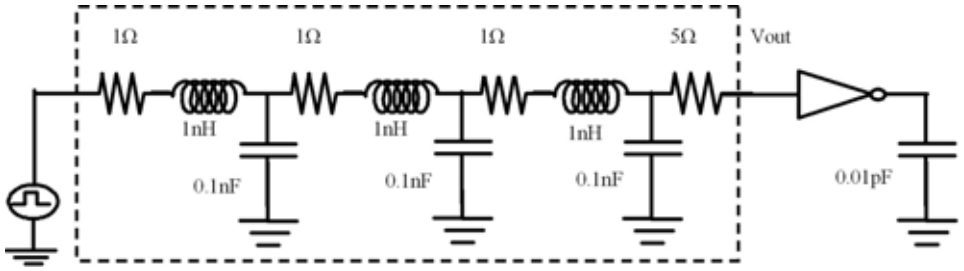

(a)

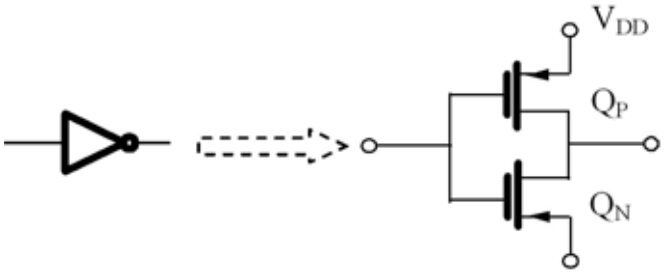

(b)

Fig. 3.4 Schematic diagram of the circuit: a) a lumped circuit with nonlinear components; b) The inverter realized by two MOSFET.

Table 3.1 Two real poles, two pairs of complex conjugate poles, and the corresponding residues identified by vector fitting method. All the values are normalized by 1.0e9.

Poles	**Residues (S11)**	**Residues (S12 & S21)**	**Residues (S22)**
-0.2029	0.21	0.1853	0.1636
-30.6775	-60.6235	-6.57e-06	2.43e-07
-0.6520+3.1517j	0.1561-0.0504j	-0.1388+0.0302j	0.1222-0.0142j
-0.6520-3.1517j	0.1561+0.0504j	-0.1388-0.0302j	0.1222+0.0142j
-0.5506+5.4617j	0.0507-0.0189j	0.0462-0.0088j	0.0409-0.0007j
-0.5506-5.4617j	0.0507+0.0189j	0.0462+0.0088j	0.0409+0.0007j

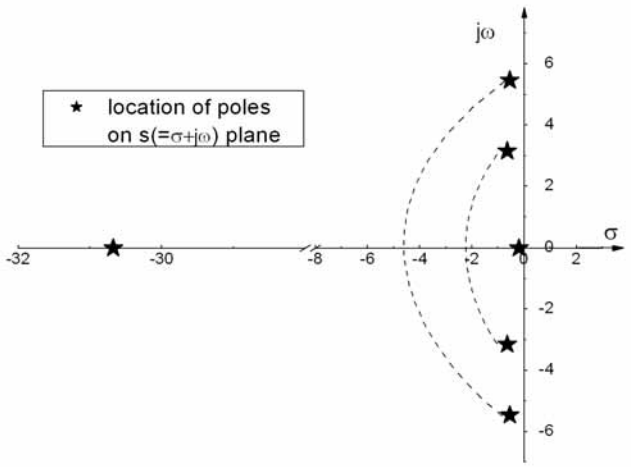

Fig. 3.5 Distribution of the poles in the s-plane obtained by the vector fitting method.

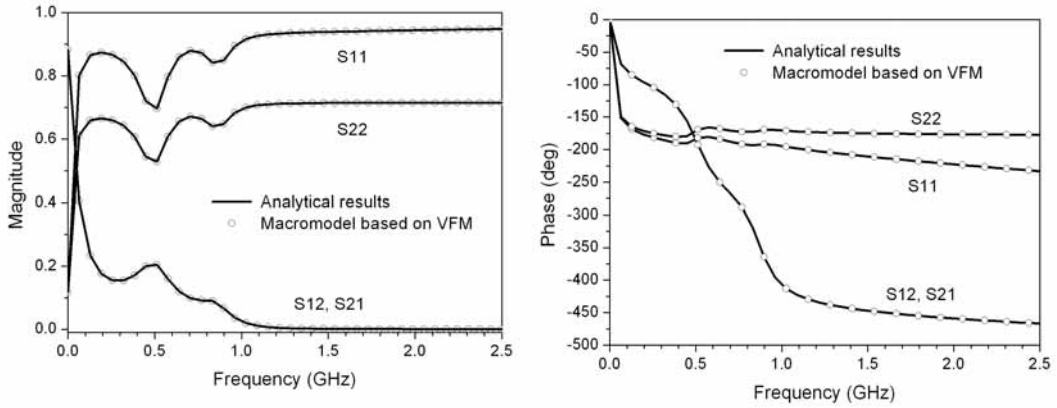

(a) (b)

Fig. 3.6 Comparison of scattering parameters for the circuit enclosed in the dashed rectangle in Fig. 3.4a: analytical results vs. macromodel based on the vector fitting method.

The transient simulation results for the circuit system are shown in Fig. 3.7. The results obtained by the method presented in the thesis are compared with those produced by the direct SPICE simulation. Very good agreements can be observed. The excitation source used for the transient simulation is a pulse with a rise/fall time of 0.5 ns and a pulse width of 5 ns.

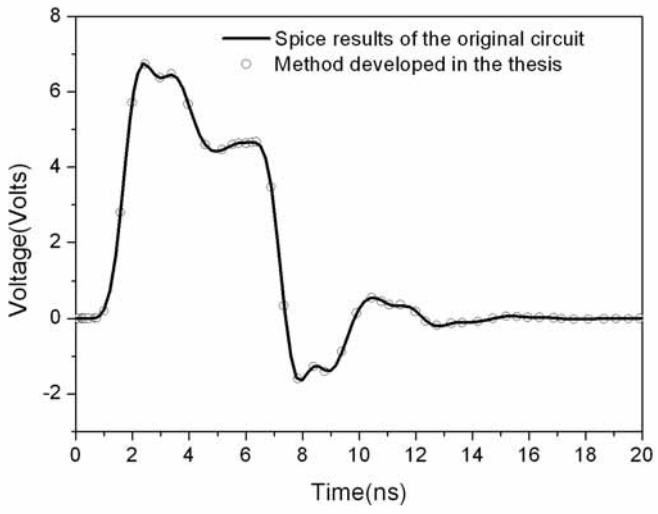

Fig. 3.7 Transient voltage waveform V_{out} at the output port of the circuit in Fig. 3.4a.

3.4.1.2 A Circuit with a Uniform Microstrip Line

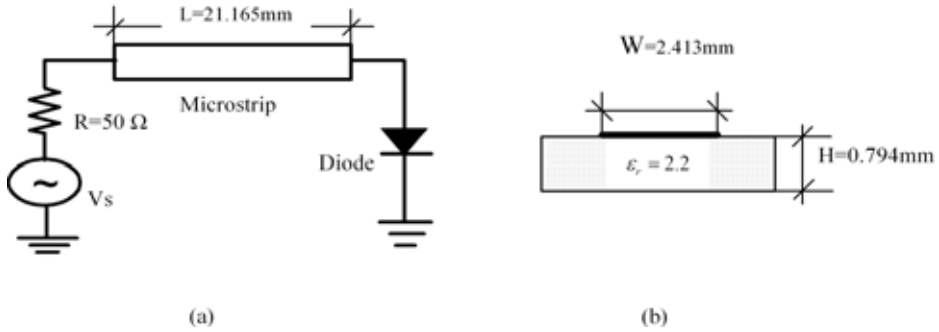

Fig. 3.8 Configuration of a transmission line circuit: a) schematic diagram of the circuit; b) cross-section of the microstrip line.

A circuit with a uniform microstrip line [73] as shown in Fig. 3.8 is simulated to verify the accuracy of the proposed method in the thesis. The circuit comprises a uniform microstrip and a diode.

The scattering parameters for the microstrip line are extracted by the full-wave FDTD method. The vector fitting method is used to construct the macromodel of the microstrip line. The approximated scattering parameters are compared with those from the FDTD simulation (Fig. 3.9) and good accuracy is achieved.

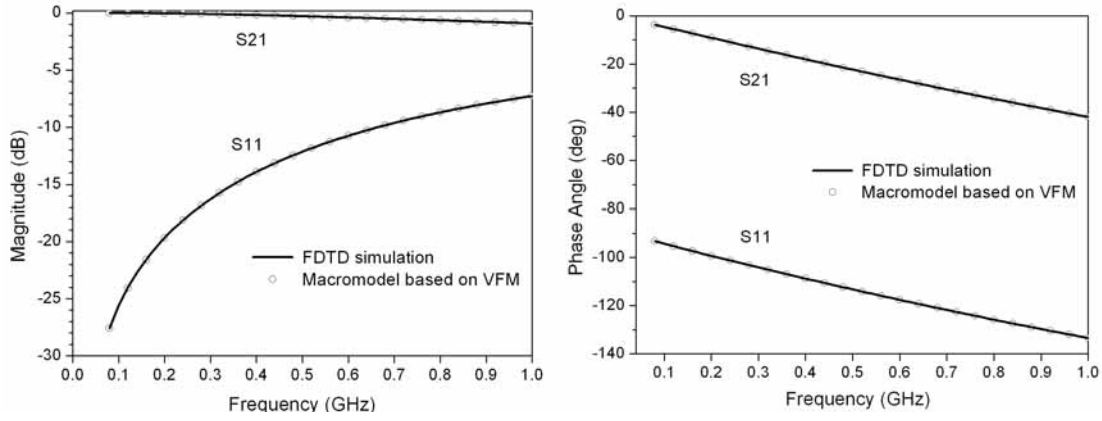

(a) (b)

Fig. 3.9 Comparison of the scattering parameters for the microstrip line.

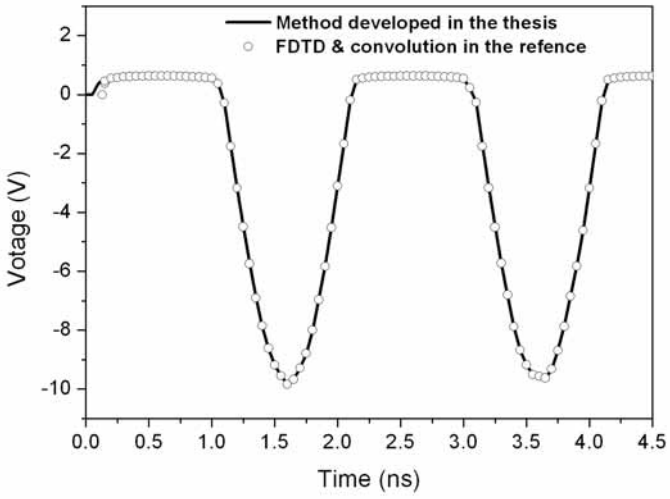

Fig. 3.10 Waveform of the transient voltage across the diode.

Finally, the macromodel synthesis technique converts the macromodel of the microstrip line into equivalent circuits, which are used in the SPICE circuit simulator to perform the signal integrity analysis of the whole circuit system. The transient voltage across the diode is shown in Fig. 3.10, where a voltage source v_s is applied ($v_s = 10\sin(2\pi f_0 t)$ and $f_0 = 500$ MHz). The good agreements between the results by the method proposed in this thesis and those by the convolution method [73] verify the accuracy of the proposed FDTD macromodeling method.

3.4.1.3 A Microstrip Low- Pass Filter Circuit

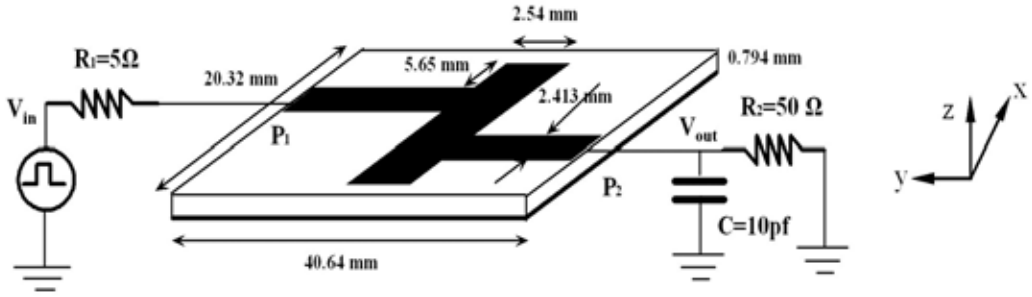

Fig. 3.11 Schematic of a microstrip low-pass filter circuit.

A circuit with a microstrip low-pass filter is analyzed in this example. The configuration of the microstrip filter is taken from [40] and repeated here in Fig. 3.11.

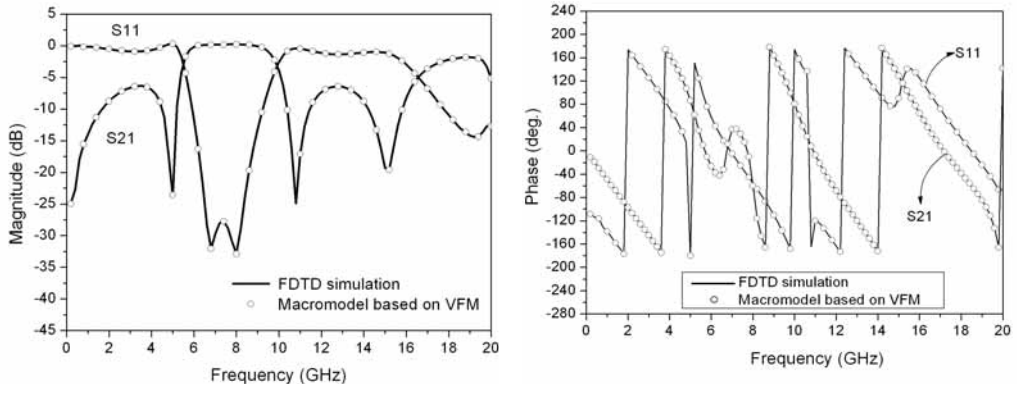

(a) (b)

Fig. 3.12 Comparison of the scattering parameters for the microstrip low pass filter.

The scattering parameters for the microstrip filter have been obtained in the previous chapter. Twenty poles (2 real poles and 9 complex conjugate pole pairs) are extracted by the vector fitting method to match the scattering parameters of the two-port low-pass filter up to 20 GHz (see Fig. 3.12). The signal integrity analysis by the SPICE circuit simulator is performed and the results are shown in Fig. 3.13.

The total CPU time used by this example on a PC is about 15 minutes which include less than 3 minutes consumed by the rational function approximation and transient simulation.

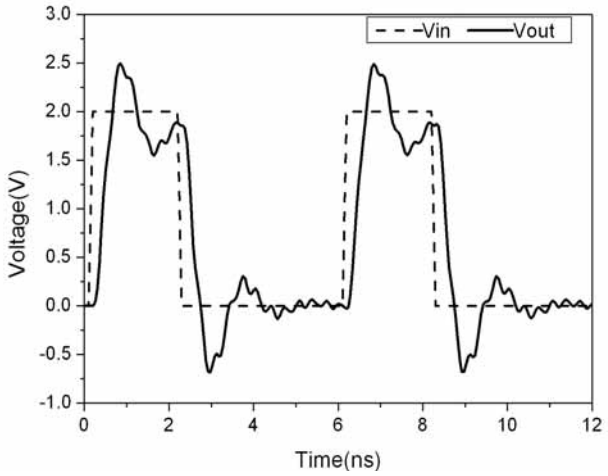

Fig. 3.13 Transient waveform V_{out}. The rise/fall time of the input pulse is 0.1 ns and the width 2 ns.

3.4.1.4 A Three-Port Microstrip Circuit

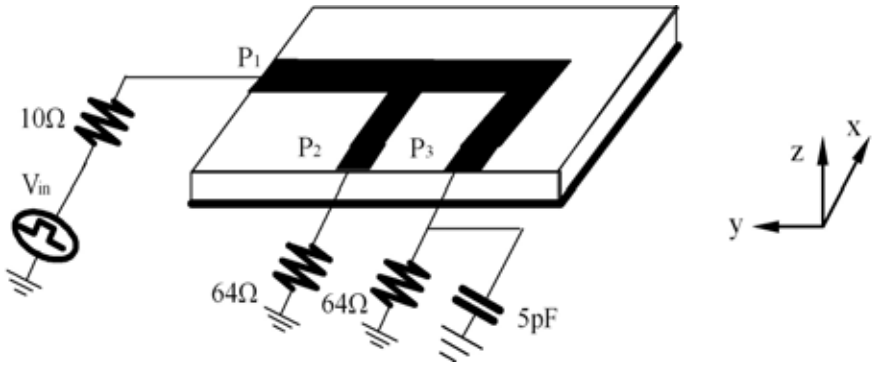

Fig. 3.14 Schematic diagram for a three-port microstrip circuit.

A fairly complex three-port circuit is shown in Fig. 3.14. The dimensions of the microstrip circuit are $20\ \text{mm} \times 20\ \text{mm} \times 0.5\ \text{mm}$ in x, y and z directions. The width of the microstrip conductor is $0.8\ \text{mm}$.

The 3D FDTD method is used to extract the scattering parameters of the microstrip line. The unit cell size in the FDTD simulation is $\Delta x = \Delta y = 0.4\ \text{mm}$, and $\Delta z = 0.25\ \text{mm}$; the time step is $\Delta t = 0.421\ \text{ps}$; the total grid size is $90\Delta x \times 90\Delta y \times 20\Delta z$ and the total simulation time steps are 3000.

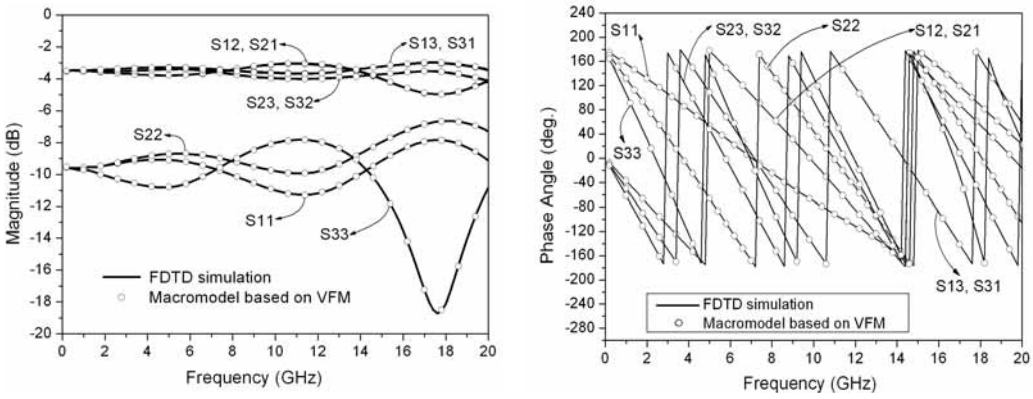

(a) (b)

Fig. 3.15 Comparison of the scattering parameters for the microstrip line.

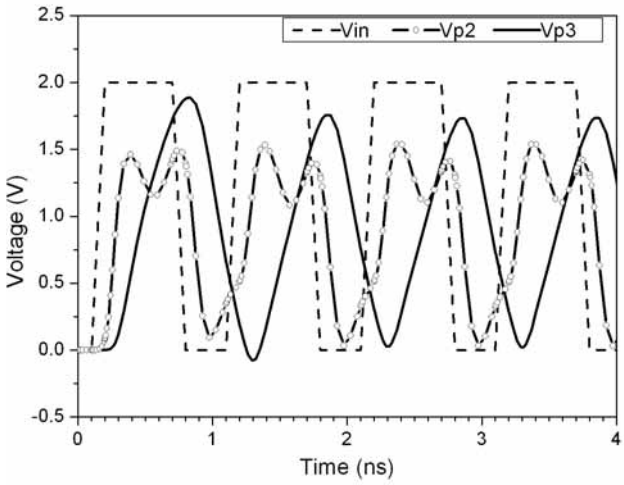

Fig. 3.16 Input voltage (V_{in}), and transient output voltages (V_{p2} and V_{p3}) at ports 2 and 3, respectively.

Fig. 3.15 shows the scattering parameters of the macromodel based on the vector fitting method (VFM) in the frequency range up to 20 GHz. Again the vector fitting method can achieve good accuracy. The transient simulation results for the whole circuit in Fig. 3.14 are shown in Fig. 3.16, where a pulse excitation with 0.1 ns rise/fall time and a width of 2ns is used. The total CPU time for this example is about 12 minutes.

3.4.2 FDTD Macromodeling Based on Admittance Matrix

3.4.2.1 A Mixer

The mixer [74] is shown in Fig. 3.17, which consists of two interconnect components, i.e., a uniform microstrip and a microstrip stub. The two voltage sources are 2.23 GHz and 2 GHz sinusoidal signals.

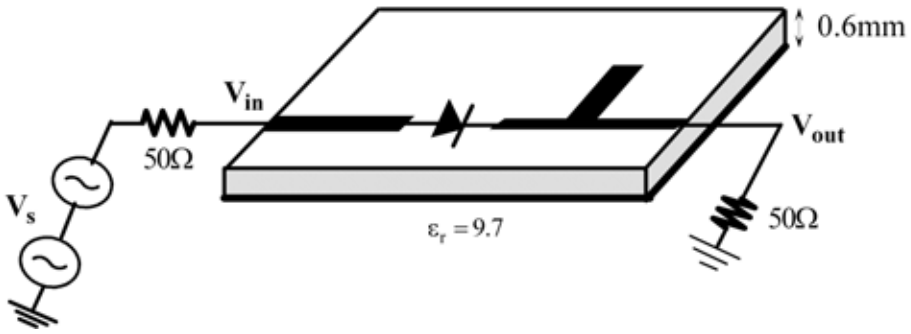

Fig. 3.17 Schematic diagram of a mixer.

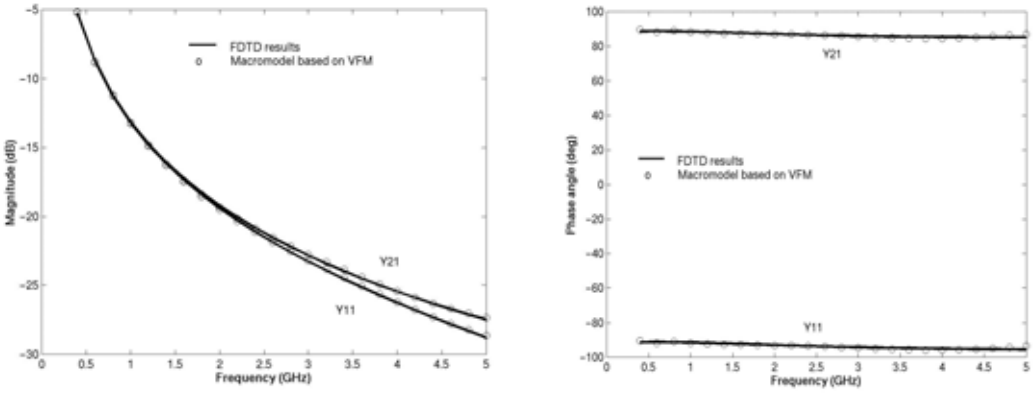

(a) (b)

Fig. 3.18 Comparison of the admittance parameters for the uniform microstrip line.

The admittance parameters of the uniform microstrip line and microstrip stub are obtained by the 3D FDTD simulation. The unit cell sizes used for both circuits are $\Delta x = \Delta y = 0.1$ mm, $\Delta z = 0.2$ mm, and the time step is $\Delta t = 0.2$ ps. The total grid size is $46\Delta x \times 36\Delta y \times 15\Delta z$ for the uniform microstrip and $110\Delta x \times 115\Delta y \times 15\Delta z$ for the stub.

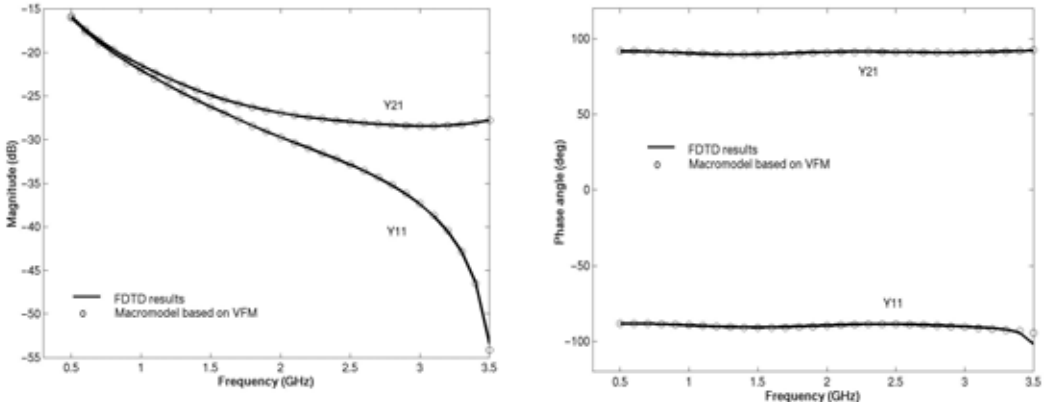

(a) (b)

Fig. 3.19 Comparison of the admittance parameters for the microstrip stub.

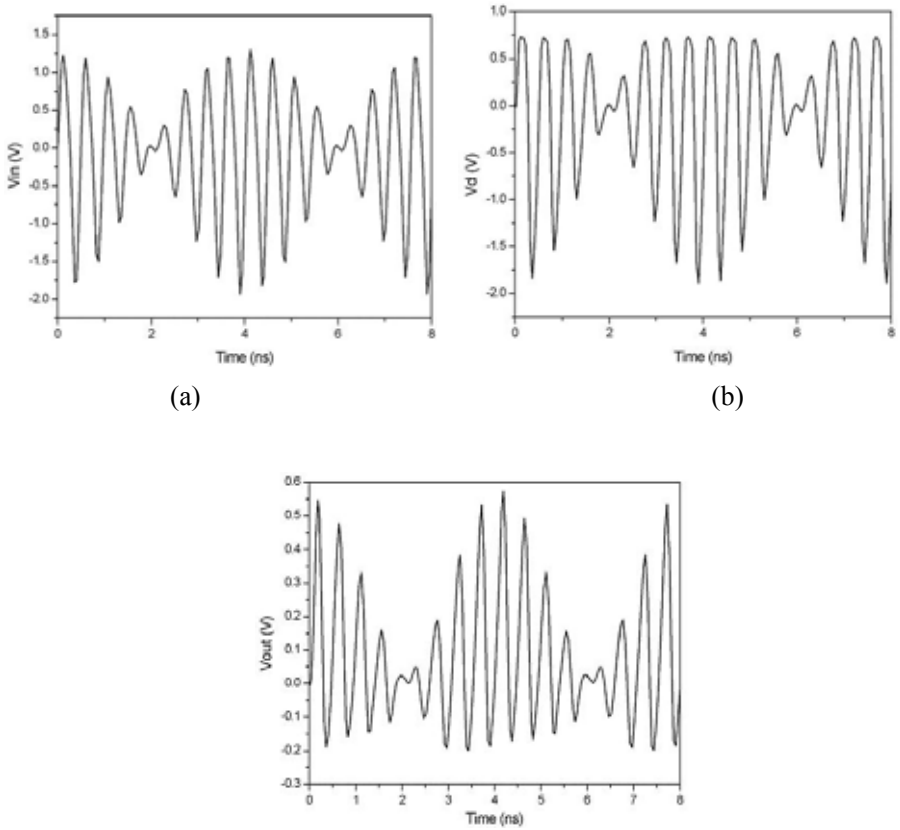

(a) (b)

(c)

Fig. 3.20 Transient simulation results: a) the input voltage; b) the diode voltage; c) the output voltage.

The admittance parameters extracted by the FDTD method for both microstrip lines are compared with those from the macromodels built by the vector fitting method (VFM), which are shown in Fig. 3.18 and Fig. 3.19, respectively. The transient simulation results for the

whole mixer circuit are shown in Fig. 3.20. These results are in good agreement with those reported in [74] and the small discrepancy is mainly due to the difference in the diode model.

3.4.2.2 A Two-port Microstrip Circuit

The configuration of a two-port microstrip loaded by lumped circuit elements is shown in Fig. 3.21.

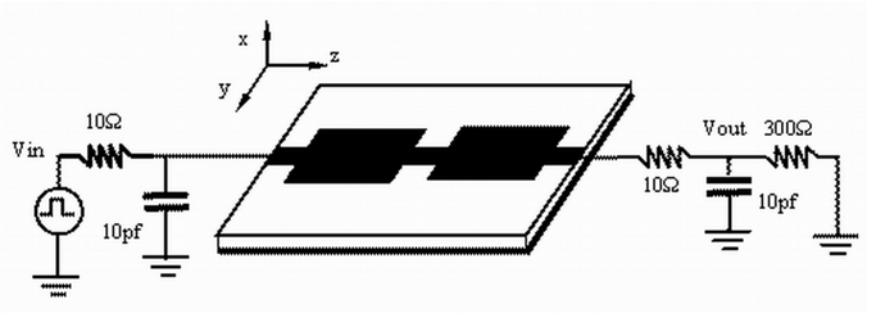

Fig. 3.21 Schematic diagram of a microstrip circuit.

The three-dimensional FDTD method is employed to obtain the admittance parameters of the distributed part of the circuit in Fig. 3.21. The unit cell size in millimeter for the FDTD simulation is $\Delta x = 0.16,\ \Delta y = 0.125,\ \Delta z = 0.1$ and the total grid size is $20\Delta x \times 58\Delta y \times 135\Delta z$.

The admittance parameters of the two-port interconnect are approximated by the vector fitting method to create its macromodel. Twelve poles including two real poles and ten complex conjugate poles are identified to match the admittance parameters of the two-port interconnect subnetwork up to 5 GHz. Good agreements can be observed between the FDTD simulated admittance parameters and those of the macromodel based on the vector fitting method (Fig. 3.22).

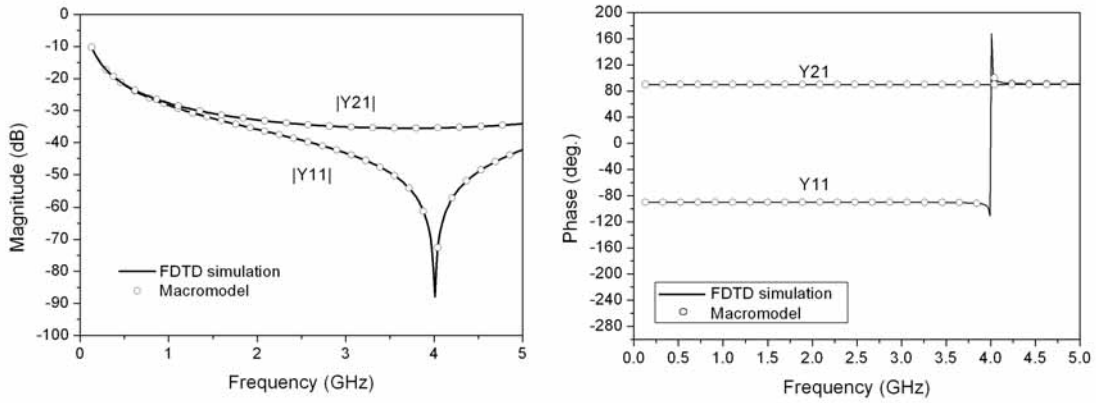

(a) (b)

Fig. 3.22 Comparison of the admittance parameters for the microstrip line.

The equivalent circuit is synthesized and inserted into the SPICE circuit simulator to perform the transient analysis of the circuit system in Fig. 3.21. The results are shown in Fig. 3.23, where an input pulse with a 0.5 ns rise/fall time is used.

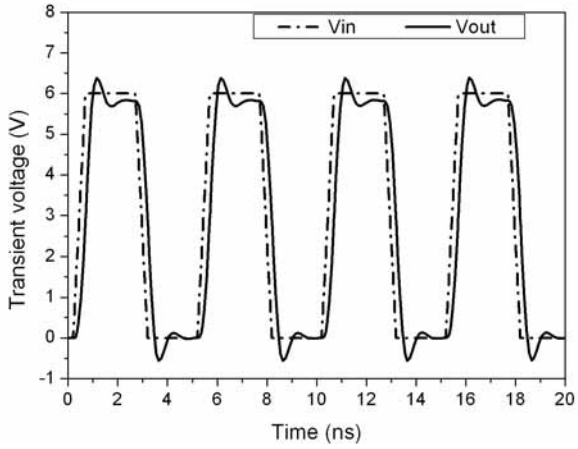

Fig. 3.23 Transient results of the two-port microstrip circuit.

3.4.2.3 A Corner Discontinuity with Nonlinear Loads

A corner discontinuity loaded with a nonlinear circuit element is shown in Fig. 3.24. The unit cell size used in the FDTD simulation is $\Delta x = 0.265$ mm, $\Delta y = \Delta z = 0.4064$ mm and the total grid size is $20\Delta x \times 72\Delta y \times 72\Delta z$. Sixteen poles comprising two real poles and fourteen complex

conjugate poles are extracted by the vector fitting method to match the admittance parameters of the two-port corner discontinuity up to 10 GHz.

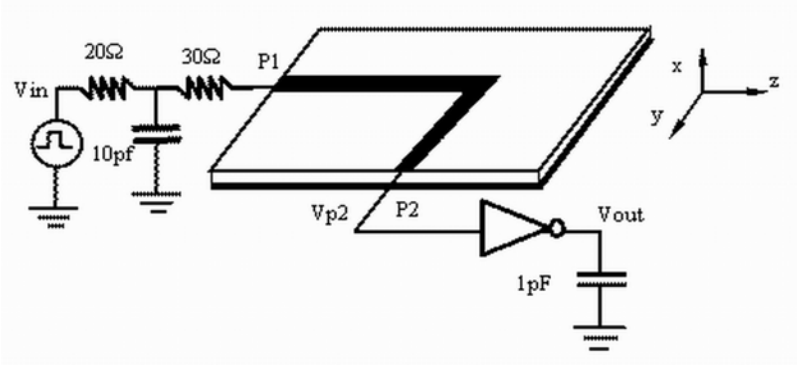

Fig. 3.24 Schematic diagram of a circuit composed of corner discontinuity and nonlinear loads.

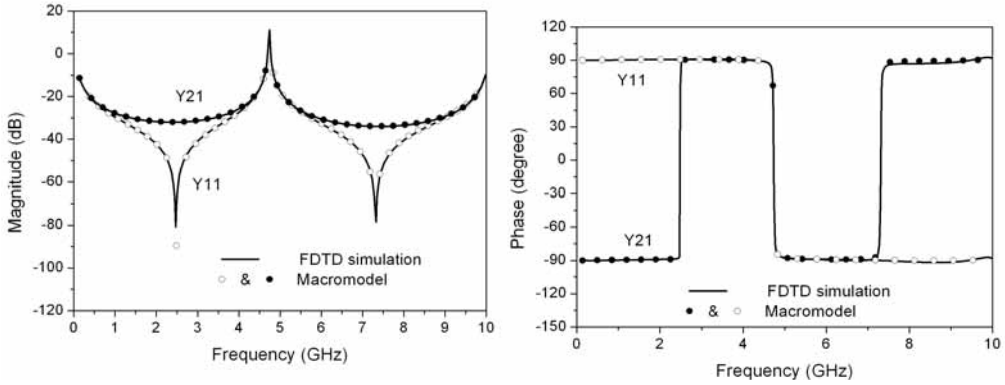

(a) (b)

Fig. 3.25 Comparison of the admittance parameters for the corner discontinuity.

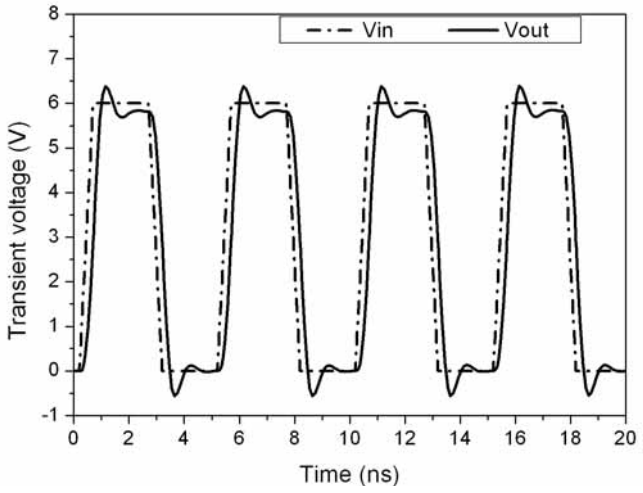

Fig. 3.26 Transient response of the whole circuit system.

The approximated admittance parameters of the macromodel are compared with those from the FDTD simulation (see Fig. 3.25). Again it can be observed that the results obtained by the two methods are in good agreement. Fig. 3.26 shows the transient simulation results of the overall circuit, where the circuit is excited by a 6 V pulse with 0.1 ns rise/fall time.

3.4.2.4 A Four-port Microstrip Network With Vias

A four-port microstrip network with vias similar to that in [42] is analyzed. The configurations and circuit layout are shown in Fig. 3.27 and Fig. 3.28, respectively.

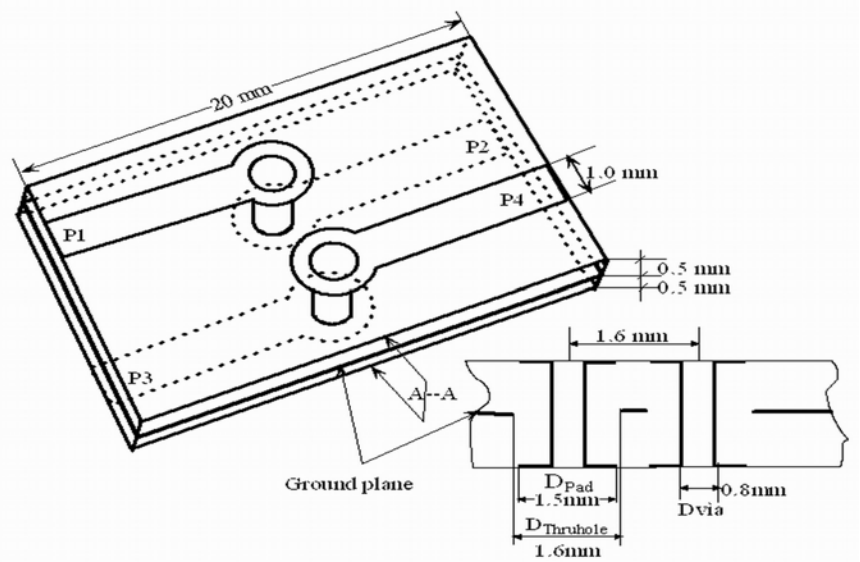

Fig. 3.27 Configuration of a four-port microstrip lines with vias.

The unit cell size used in the FDTD simulation is $\Delta x = \Delta y = \Delta z = 0.1$ mm and the total grid size is $50\Delta x \times 86\Delta y \times 270\Delta z$. Twenty-two poles are extracted by the vector fitting method to match the admittance parameters of the four-port network up to 15 GHz. The approximated admittance parameters of the macromodel agree well with those obtained from the FDTD simulation (see Fig. 3.29). Because of the symmetry of this four-port network, only four entries of the admittance matrix are plotted. The phase comparison is omitted for brevity.

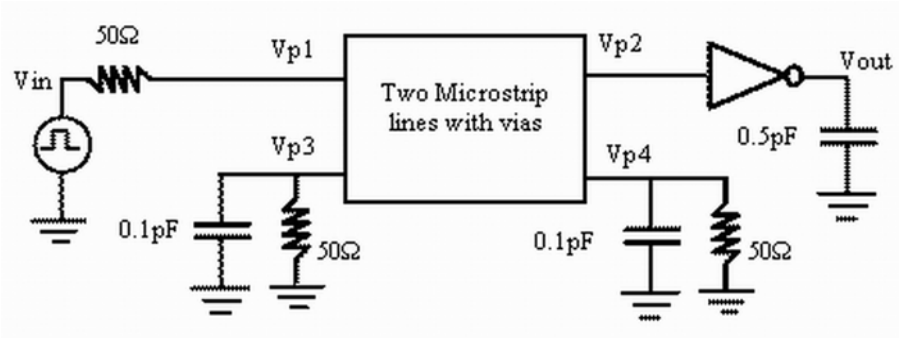

Fig. 3.28 Schematic circuit diagram of the four-port network of microstrip lines with vias loaded by lumped circuit components.

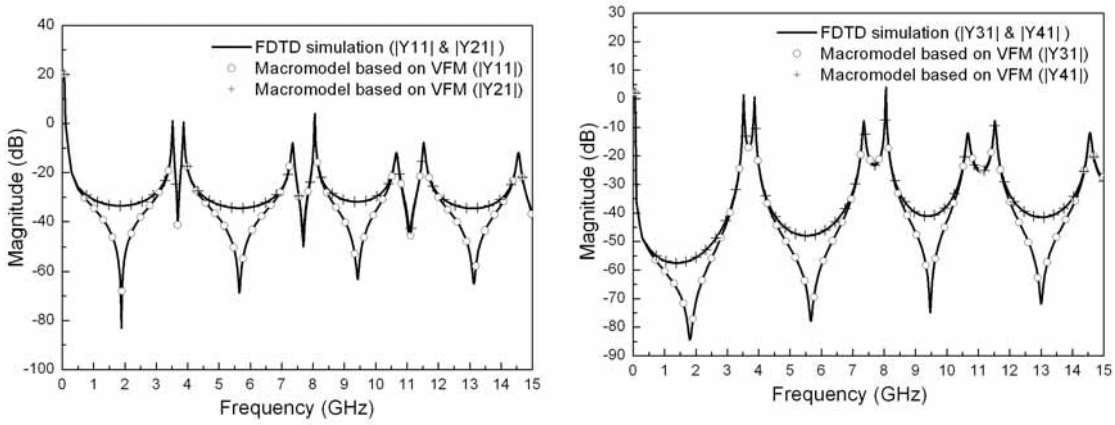

(a) (b)

Fig. 3.29 Comparison of the admittance parameters for the microstrip network with vias: (a) Y11 and Y21; (b) Y31 and Y41.

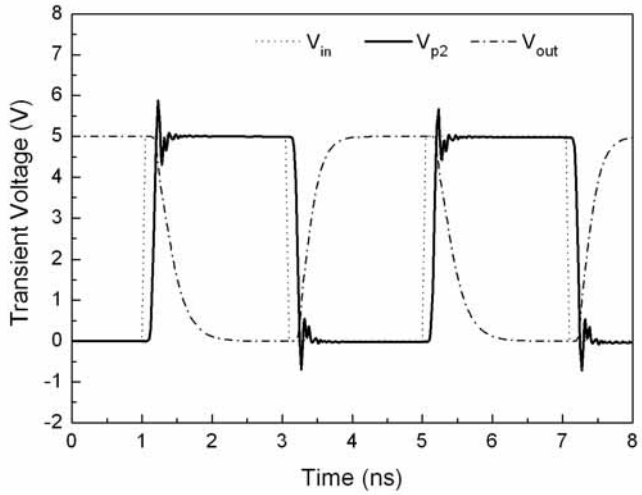

(a)

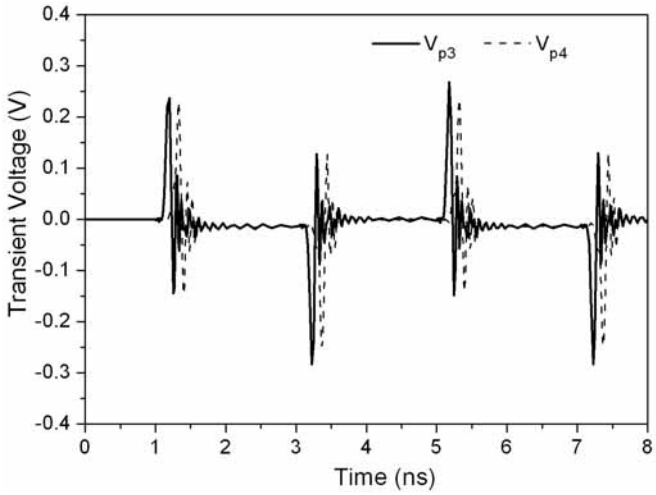

(b)

Fig. 3.30 Transient voltage waveforms: (a) at Port 2 (V_{p2}) and the observation point (V_{out}); (b) at Port 3 (V_{p3}) and Port 4 (V_{p4}).

The circuit is excited at port 1 by a pulse with 0.05 ns rise/fall time and 4 ns pulse width. The transient simulation results are shown in Fig. 3.30.

3.5 Summary

The full-wave FDTD method coupled with macromodeling by the rational function approximation is an accurate and efficient approach to address the mixed electromagnetic (interconnect part) and circuit problem where the electromagnetic field effects are fully considered and the strength of the SPICE circuit simulator is also exploited. The frequency-dependent nature of the interconnect subnetwork is well accounted for by the scattering or admittance parameters extracted by the three-dimensional FDTD method.

It should be pointed out that the proposed approach in the thesis can be readily applied to interconnect structures characterized by tabulated scattering or admittance parameters produced by measurement or other computational electromagnetic methods.

Chapter 4. Green's Functions for General Sources in Planar Multilayered Media

This chapter will discuss the evaluation of Green's functions for planar multilayered media due to general electric and magnetic sources.

4.1 Introduction

In order to develop the hybrid FDTD-MPIE method (Chapter 6) for inhomogeneous penetrable objects embedded in multilayered media, the mixed-potential integral equations (MPIE) for multilayered media will be derived in this chapter. Prior to formulating the mixed-potential integral equations, the dyadic Green's functions need to be addressed. After reviewing the derivation of the spectral and spatial domain dyadic Green's functions for electric scalar and vector potentials, we extend them to account for general electric and magnetic sources. Their closed-form expressions in spectral domain will be explicitly presented. Since Green's functions for multilayered media have closed-form solutions only in spectral-domain, their spatial-domain counterparts have to be obtained through Sommerfeld integrals. Both the

numerical integration method with extraction of large argument approximations and the discrete complex image method (DCIM) are implemented to evaluate the Sommerfeld integrals. In addition, the DCIM method will be extended to account for general electric and magnetic sources. Numerical examples for the Green's functions in multilayered media due to general sources will be presented. Throughout this thesis the time convention of $e^{j\omega t}$ is assumed unless otherwise stated.

4.2 Field-Source Relationship for Planar Multilayer Problems

4.2.1 Problem Statement

As mentioned in Chapter 1, the topic of characterizing electromagnetic waves in planar multilayered media has been studied intensively because of its many practical applications. Examples of these applications [33] include microstrip antennas, monolithic microwave/millimeter wave integrated circuits (MIC/MMIC), wave propagation and transmission, geophysical prospecting and remote sensing.

A general N-layer planar structure, which is laterally unbounded, is illustrated in Fig. 4.1. According to the different layout of the top and bottom layers, it can be further classified into three cases: a) both the top and bottom layers are half spaces; b) both of the outmost layers are grounded; c) only one of the outmost layers is half space or perfect electric conductor (PEC). For brevity, only the first two cases are shown in Fig. 4.1. The layers are numbered as 1, 2,⋯, and N from the top to the bottom. All the interfaces of two adjacent layers are arranged to be parallel to the $x-y$ plane in Cartesian coordinates, and their corresponding z coordinates are denoted by z_i's. Moreover, the ith layer with the

thickness d_i is bounded by two interfaces z_i and z_{i+1}. The only exception of it is that if the outmost layer is half space (Fig. 4.1(a)), an fictitious interface is introduced to keep an identical representation for all the different configurations of the multilayered media and the thickness d_1 or d_N of these layers is arbitrary. The medium in the i th layer is characterized by its permittivity ε_i and permeability μ_i, which are complex numbers if the medium is lossy.

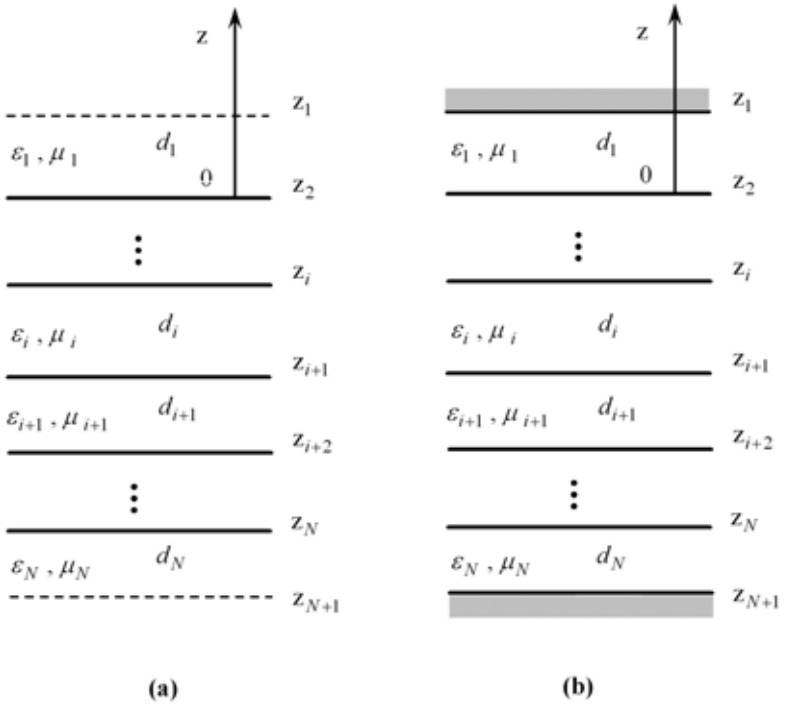

Fig. 4.1 Configuration of a general N-layer planar structure with different layout of the top and bottom layers: (a) both are half spaces; (b) both are terminated by PECs.

4.2.2 Mixed Potential Form of Field-Source Relationship

For the linear multilayered media shown in Fig. 4.1, the fields due to arbitrary current distributions $(\mathbf{J}, \mathbf{M})$ can be expressed as [33]

$$\mathbf{E}(\mathbf{r}\,|\,\mathbf{r}') = <\bar{\mathbf{G}}^{EJ}(\mathbf{r}\,|\,\mathbf{r}'); \mathbf{J}(\mathbf{r}\,|\,\mathbf{r}')> + <\bar{\mathbf{G}}^{EM}(\mathbf{r}\,|\,\mathbf{r}'); \mathbf{M}(\mathbf{r}\,|\,\mathbf{r}')> \qquad (4.1)$$

$$\mathbf{H}(\mathbf{r}\,|\,\mathbf{r}') = <\bar{\mathbf{G}}^{HJ}(\mathbf{r}\,|\,\mathbf{r}');\mathbf{J}(\mathbf{r}\,|\,\mathbf{r}')> + <\bar{\mathbf{G}}^{HM}(\mathbf{r}\,|\,\mathbf{r}');\mathbf{M}(\mathbf{r}\,|\,\mathbf{r}')> \tag{4.2}$$

where $\bar{\mathbf{G}}^{PQ}(\mathbf{r}\,|\,\mathbf{r}')$ denotes the dyadic Green's function (DGF) for a P-type field at $\mathbf{r}$ due to a Q-type unit current source at $\mathbf{r}'$. The symbol $<;>$ stands for the inner product of two functions separated by the comma and the dot over the comma indicates a dot product.

Once the dyadic Green's functions (DGF's) for the layered media are known, it is quite straightforward to formulate the integral equations governing the multilayered problem by applying appropriate boundary conditions. Similar to the free-space problems, there are several ways to express the field-source relationship [30, 75, 76]. Because of the hyper-singular behavior of $\bar{\mathbf{G}}^{EJ}$ and $\bar{\mathbf{G}}^{HM}$, it is often preferable to choose their mixed-potential form in the final integral equations.

However, compared to free-space problems, it requires more effort to develop the mixed-potential form for the multilayer problems because the scalar potential kernels associated with the horizontal and vertical currents are different for layered media [77]. Therefore, either the scalar or the vector potential kernel must be modified or corrected to address the problem. Referring to the approaches presented in [78, 79], we can express the mixed-potential forms of the field-source relationship as [33]

$$\mathbf{E} = -j\omega\left\langle\bar{\mathbf{G}}^{A};\mathbf{J}\right\rangle + \frac{1}{j\omega}\nabla\left(\left\langle K^{\Phi},\nabla'\cdot\mathbf{J}\right\rangle + \left\langle C^{\Phi}\hat{z};\mathbf{J}\right\rangle\right) + \left\langle\bar{\mathbf{G}}^{EM};\mathbf{M}\right\rangle \tag{4.3}$$

$$\mathbf{H} = -j\omega\left\langle\bar{\mathbf{G}}^{F};\mathbf{M}\right\rangle + \frac{1}{j\omega}\nabla\left(\left\langle K^{\Psi},\nabla'\cdot\mathbf{M}\right\rangle + \left\langle C^{\Psi}\hat{z};\mathbf{M}\right\rangle\right) + \left\langle\bar{\mathbf{G}}^{HJ};\mathbf{J}\right\rangle \tag{4.4}$$

where $\bar{\mathbf{G}}^{A}$ and $\bar{\mathbf{G}}^{F}$ are dyadic Green's functions for magnetic and electric vector potentials, respectively; K^{Φ} and K^{Ψ} are the corresponding scalar potential kernels. Two correction terms

C^{Φ} and C^{Ψ} are associated with the longitudinal (z) electric and magnetic currents, respectively.

Different treatments of the correction terms in (4.3) and (4.4) result in different formulations for the vector and scalar potential Green's functions [78, 80-83]. Among many authors studying this topic, Michalski and Zheng [33, 78, 84, 85] have greatly contributed to the method of moment (MoM) resolution of the planar multilayered media problems. They proposed three formulations for Green's functions associated with vector and scalar potentials for multilayered media, which are named as Formulation-A, Formulation-B and Formulation-C, respectively. Despite the undesirable effects of introducing two additional components in the dyadic kernels of the vector potential, the Formulation-C is particularly well suited for the method of moments because the continuity property of the Green's function for the scalar potential obviates the need for computing additional contour integrals in the MoM resolution [84]. Therefore, the Formulation-C Green's functions are employed in this thesis to build the integral equations for planar multilayer problems.

4.3 Spectral-Domain Green's Functions for Multilayered Media

It is well known that Green's functions for laterally unbounded multilayered planar media have closed-form expressions only in the spectral domain. This can be explained mathematically that by applying Fourier transform to the governing equations of the multilayer problems, the differential operators can be turned into algebraic operators, which finally results in closed-form expressions in spectral domain for the original multilayered media problem. To keep the thesis self-contained, we will first review the derivation of the Formulation-C Green's functions [78, 84]. Thereafter, we will extend them to account for general electric and magnetic

sources.

4.3.1 Decoupling Maxwell's Equations in Spectral Domain

The $(\mathbf{E}, \mathbf{H})$ fields at an arbitrary point $\mathbf{r}$ due to a specified current distribution $(\mathbf{J}, \mathbf{M})$ in multilayered media are still governed by the Maxwell's equations:

$$\nabla \times \mathbf{E} = -j\omega\mu\mathbf{H} - \mathbf{M} \tag{4.5}$$

$$\nabla \times \mathbf{H} = j\omega\varepsilon\mathbf{E} + \mathbf{J} \tag{4.6}$$

where ω denotes the radian frequency.

The solution of the Maxwell's equations is facilitated by introducing two dimensional Fourier transform pair with respect to (x, y) and (k_x, k_y):

$$\tilde{f}(\mathbf{k}_\rho; z) = \mathcal{F}\left[f(\boldsymbol{\rho}; z)\right] = \int_{-\infty}^{+\infty}\int_{-\infty}^{+\infty} f(\boldsymbol{\rho}; z) e^{-j\mathbf{k}_\rho \boldsymbol{\rho}} dx\, dy \tag{4.7}$$

$$f(\boldsymbol{\rho}; z) = \mathcal{F}^{-1}\left[\tilde{f}(\mathbf{k}_\rho; z)\right] = \frac{1}{(2\pi)^2}\int_{-\infty}^{+\infty}\int_{-\infty}^{+\infty} \tilde{f}(\mathbf{k}_\rho; z) e^{j\mathbf{k}_\rho \boldsymbol{\rho}} dk_x\, dk_y \tag{4.8}$$

where

$$\boldsymbol{\rho} = x\hat{\mathbf{x}} + y\hat{\mathbf{y}} \tag{4.9}$$

$$\mathbf{k}_\rho = k_x\hat{\mathbf{x}} + k_y\hat{\mathbf{y}}. \tag{4.10}$$

The elegant property of the Fourier transform is given by

$$\mathcal{F}\left[\nabla\right] = \tilde{\nabla} = jk_\rho\hat{\mathbf{u}} + \frac{d}{dz}\hat{\mathbf{z}} \tag{4.11}$$

$$\mathcal{F}\left[\nabla'\right] = \tilde{\nabla}' = -jk_\rho \hat{\mathbf{u}} + \frac{d}{dz'}\hat{\mathbf{z}}. \tag{4.12}$$

The primes on the coordinates and operations in the above equations are used to distinguish the source from the field. The symbol ~ denotes spectral-domain variables. These conventions are applied throughout this thesis unless otherwise stated.

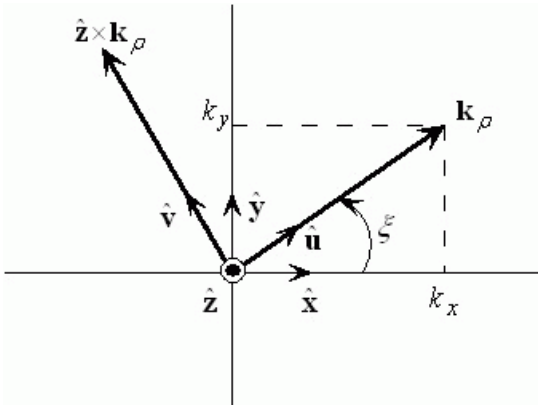

Fig. 4.2 Spatial and spectral domain coordinate systems.

The unit vectors $(\hat{\mathbf{u}}, \hat{\mathbf{v}})$ (see Fig. 4.2) are related to the rotated spectral-domain coordinate system $(\mathbf{k}_\rho, \hat{\mathbf{z}}\times\mathbf{k}_\rho)$ by

$$\hat{\mathbf{u}} = \frac{\mathbf{k}_\rho}{k_\rho} = \frac{k_x}{k_\rho}\hat{\mathbf{x}} + \frac{k_y}{k_\rho}\hat{\mathbf{y}} \tag{4.13}$$

$$\hat{\mathbf{v}} = \hat{\mathbf{z}}\times\hat{\mathbf{u}} = -\frac{k_y}{k_\rho}\hat{\mathbf{x}} + \frac{k_x}{k_\rho}\hat{\mathbf{y}} \tag{4.14}$$

where $k_\rho = \sqrt{k_x^2 + k_y^2}$.

The relationship between the two coordinate systems can be written in a matrix form:

$$\begin{bmatrix}\hat{\mathbf{u}}\\ \hat{\mathbf{v}}\\ \hat{\mathbf{z}}\end{bmatrix} = \begin{bmatrix}\cos\xi & \sin\xi & 0\\ -\sin\xi & \cos\xi & 0\\ 0 & 0 & 1\end{bmatrix}\begin{bmatrix}\hat{\mathbf{x}}\\ \hat{\mathbf{y}}\\ \hat{\mathbf{z}}\end{bmatrix}, \qquad \cos\xi = \frac{k_x}{k_\rho}, \qquad \sin\xi = \frac{k_y}{k_\rho} \tag{4.15}$$

where ξ is the coordinate rotation angle (see Fig. 4.2).

Since the multilayered structure discussed in this thesis can be regarded as a uniform cylindrical waveguide of infinite cross section, the solution of the problem can be facilitated by decomposing the field and source vectors into transverse and longitudinal parts [84, 86]. Applying the Fourier transform (4.7) and (4.11) to (4.5) and (4.6), we can obtain the following equations regarding the transverse components of the electric and magnetic fields:

$$\frac{d}{dz}\tilde{\mathbf{E}}_\rho = \frac{1}{j\omega\varepsilon}(k^2 - \mathbf{k}_\rho \mathbf{k}_\rho \cdot)(\tilde{\mathbf{H}}_\rho \times \hat{\mathbf{z}}) - \frac{\tilde{J}_z}{\omega\varepsilon}\mathbf{k}_\rho - \tilde{\mathbf{M}}_\rho \times \hat{\mathbf{z}} \tag{4.16}$$

$$\frac{d}{dz}\tilde{\mathbf{H}}_\rho = \frac{1}{j\omega\mu}(k^2 - \mathbf{k}_\rho \mathbf{k}_\rho \cdot)(\hat{\mathbf{z}} \times \tilde{\mathbf{E}}_\rho) - \frac{\tilde{M}_z}{\omega\mu}\mathbf{k}_\rho - \hat{\mathbf{z}} \times \tilde{\mathbf{J}}_\rho \tag{4.17}$$

where $k = \omega\sqrt{\mu\varepsilon}$.

The longitudinal components can be easily derived from the above transverse components:

$$\tilde{E}_z = \frac{1}{\omega\varepsilon}\mathbf{k}_\rho \cdot (\tilde{\mathbf{H}}_\rho \times \hat{\mathbf{z}}) - \frac{1}{j\omega\varepsilon}\tilde{J}_z \tag{4.18}$$

$$\tilde{H}_z = \frac{1}{\omega\mu}\mathbf{k}_\rho \cdot (\hat{\mathbf{z}} \times \tilde{\mathbf{E}}_\rho) - \frac{1}{j\omega\mu}\tilde{M}_z. \tag{4.19}$$

Upon using the rotated spectral-domain coordinate system, we can express the transverse electric and magnetic fields as

$$\begin{aligned} \tilde{\mathbf{E}}_\rho &= V^e\hat{\mathbf{u}} + V^h\hat{\mathbf{v}} \\ \tilde{\mathbf{H}}_\rho \times \hat{\mathbf{z}} &= I^e\hat{\mathbf{u}} + I^h\hat{\mathbf{v}}. \end{aligned} \tag{4.20}$$

Substituting (4.20) into (4.16) and (4.17), we can decouple and transform them into the following two sets of transmission line equations:

$$\begin{aligned} \frac{dV^p}{dz} &= -jk_z Z^p I^p + v^p \\ \frac{dI^p}{dz} &= -jk_z Y^p V^p + i^p \end{aligned} \tag{4.21}$$

where the superscript p can either be e − transverse magnetic (TM_z) or h − transverse electric (TE_z). The propagation wavenumbers and the characteristic impedances and admittances of the equivalent transmission lines are given by

$$k_z = \sqrt{k^2 - k_\rho^2} \tag{4.22}$$

$$\begin{aligned} Z^e &= \frac{1}{Y^e} = \frac{k_z}{\omega\varepsilon} \\ Z^h &= \frac{1}{Y^h} = \frac{\omega\mu}{k_z} \end{aligned} \tag{4.23}$$

where the square root branch in (4.22) is selected to ensure that the condition of $-\pi < \arg\{k_z\} \le 0$ or equivalently the radiation boundary condition is satisfied [86]. The voltage and current sources in (4.21) are given by

$$\begin{aligned} v^e &= -\frac{k_\rho}{\omega\varepsilon}\tilde{J}_z - \tilde{M}_v, \quad i^e = -\tilde{J}_u \\ i^h &= \frac{k_\rho}{\omega\mu}\tilde{M}_z - \tilde{J}_v, \qquad v^h = \tilde{M}_u . \end{aligned} \tag{4.24}$$

Now the analogy between the planar multilayered media and the transmission line networks is explicitly formulated, where the components of $\tilde{\mathbf{E}}_\rho$ and $\tilde{\mathbf{H}}_\rho$ in (4.20) may be interpreted as the voltages and currents on a transmission line network along the z axis (See Fig. 4.3). The solution of (4.21) is presented in Appendix C of this thesis.

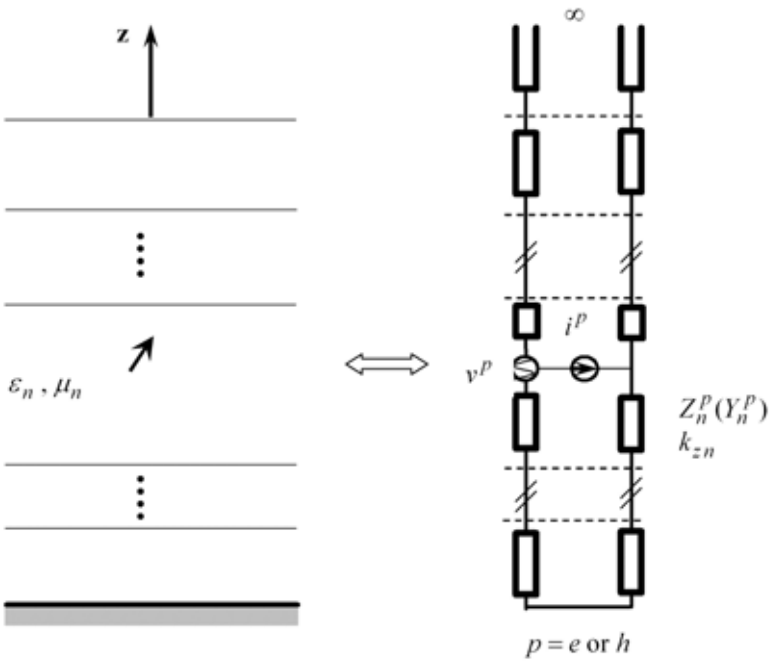

Fig. 4.3 Analogy between the planar multilayered media and the Transmission line networks.

Based on (4.18), (4.19) and (4.20), the electromagnetic fields in the spectral domain are given by

$$\begin{aligned}\tilde{\mathbf{E}} &= V^e\hat{\mathbf{u}} + V^h\hat{\mathbf{v}} + \frac{1}{j\omega\varepsilon}(jk_\rho I^e - \tilde{J}_z)\hat{\mathbf{z}} \\ \tilde{\mathbf{H}} &= -I^h\hat{\mathbf{u}} + I^e\hat{\mathbf{v}} - \frac{1}{j\omega\mu}(jk_\rho V^h + \tilde{M}_z)\hat{\mathbf{z}}.\end{aligned} \tag{4.25}$$

4.3.2 Formulation-C Spectral-Domain Green's Functions

The spectral-domain counterparts of (4.1) and (4.2) can be written as:

$$\tilde{\mathbf{E}} = <\tilde{\bar{\mathbf{G}}}^{EJ};\tilde{\mathbf{J}}> + <\tilde{\bar{\mathbf{G}}}^{EM};\tilde{\mathbf{M}}> \tag{4.26}$$

$$\tilde{\mathbf{H}} = <\tilde{\bar{\mathbf{G}}}^{HJ};\tilde{\mathbf{J}}> + <\tilde{\bar{\mathbf{G}}}^{HM};\tilde{\mathbf{M}}> \tag{4.27}$$

where $\tilde{\bar{\mathbf{G}}}^{PQ}(k_{\boldsymbol{\rho}};z,z')$ denote the spectral-domain dyadic Green's functions (DGF's). They are

given by

$$\tilde{\tilde{\mathbf{G}}}^{EJ} = -\hat{\mathbf{u}}\hat{\mathbf{u}}V_i^e - \hat{\mathbf{v}}\hat{\mathbf{v}}V_i^h - \hat{\mathbf{z}}\hat{\mathbf{u}}\frac{k_\rho}{\omega\varepsilon}I_i^e - \hat{\mathbf{u}}\hat{\mathbf{z}}\frac{k_\rho}{\omega\varepsilon'}V_v^e + \hat{\mathbf{z}}\hat{\mathbf{z}}\frac{1}{j\omega\varepsilon'}\left[\frac{k_\rho^2}{j\omega\varepsilon}I_v^e - \delta(z-z')\right], \quad (4.28)$$

$$\tilde{\tilde{\mathbf{G}}}^{HM} = -\hat{\mathbf{u}}\hat{\mathbf{u}}I_v^h - \hat{\mathbf{v}}\hat{\mathbf{v}}I_v^e - \hat{\mathbf{z}}\hat{\mathbf{u}}\frac{k_\rho}{\omega\mu}V_v^h - \hat{\mathbf{u}}\hat{\mathbf{z}}\frac{k_\rho}{\omega\mu'}I_i^h + \hat{\mathbf{z}}\hat{\mathbf{z}}\frac{1}{j\omega\mu'}\left[\frac{k_\rho^2}{j\omega\mu}V_i^h - \delta(z-z')\right], \quad (4.29)$$

$$\tilde{\tilde{\mathbf{G}}}^{EM} = -\hat{\mathbf{u}}\hat{\mathbf{v}}V_v^e + \hat{\mathbf{v}}\hat{\mathbf{u}}V_v^h - \hat{\mathbf{z}}\hat{\mathbf{v}}\frac{k_\rho}{\omega\varepsilon}I_v^e + \hat{\mathbf{v}}\hat{\mathbf{z}}\frac{k_\rho}{\omega\mu'}V_i^h, \quad (4.30)$$

$$\tilde{\tilde{\mathbf{G}}}^{HJ} = \hat{\mathbf{u}}\hat{\mathbf{v}}I_i^h - \hat{\mathbf{v}}\hat{\mathbf{u}}I_i^e + \hat{\mathbf{z}}\hat{\mathbf{v}}\frac{k_\rho}{\omega\mu}V_i^h - \hat{\mathbf{v}}\hat{\mathbf{z}}\frac{k_\rho}{\omega\varepsilon'}I_v^e. \quad (4.31)$$

Although the spectral DGF's can be directly applied to integral-equation formulations based on the spectral-domain approach [87-89], the spatial domain MPIE is preferred because the spectral-domain approach is less flexible in terms of modeling geometry and evaluating double spectral integrals, and thus less efficient than the spatial-domain MPIE [33].

Now we will focus on the derivation of the Formulation-C spectral domain Green's functions. We first consider the case of electric current sources. The magnetic and electric fields can be expressed in terms of vector and scalar potentials via the following equations:

$$\begin{aligned} \mathbf{H} &= \frac{1}{\mu}\nabla\times\mathbf{A} \\ \mathbf{E} &= -j\omega\mathbf{A} - \nabla\Phi. \end{aligned} \quad (4.32)$$

The vector potential Green's function can be easily derived from the magnetic field Green's function:

$$\bar{\mathbf{G}}^{HJ} = \frac{1}{\mu}\nabla\times\bar{\mathbf{G}}^{A}. \quad (4.33)$$

Since $\bar{\mathbf{G}}^A$ is not uniquely determined by (4.33), many different forms may be formulated [84]. The Formulation-C Green's functions in [84] is based on the traditional form of $\bar{\mathbf{G}}^A$. To simplify the derivation it is preferable to go back to the spectral domain:

$$\tilde{\bar{\mathbf{G}}}^A = \tilde{G}^A_{vv}(\hat{\mathbf{u}}\hat{\mathbf{u}} + \hat{\mathbf{v}}\hat{\mathbf{v}}) + \tilde{G}^A_{zu}\hat{\mathbf{z}}\hat{\mathbf{u}} + \tilde{G}^A_{zz}\hat{\mathbf{z}}\hat{\mathbf{z}}. \tag{4.34}$$

Based on (4.31), (4.34) and the spectral counterpart of (4.33), we can finally obtain

$$\tilde{G}^A_{vv} = \frac{1}{j\omega}V_i^h, \quad \tilde{G}^A_{zz} = \frac{\mu}{j\omega\varepsilon'}I_v^e, \tag{4.35}$$

$$\frac{d\tilde{G}^A_{vv}}{dz} = -\mu I_i^h, \quad \tilde{G}^A_{zu} = -\frac{\mu}{jk_\rho}(-I_i^e - \frac{1}{\mu}\frac{d\tilde{G}^A_{vv}}{dz}) = \frac{\mu}{jk_\rho}(I_i^e - I_i^h). \tag{4.36}$$

Thus, (4.34) becomes

$$\tilde{\bar{\mathbf{G}}}^A = \frac{1}{j\omega}V_i^h(\hat{\mathbf{u}}\hat{\mathbf{u}} + \hat{\mathbf{v}}\hat{\mathbf{v}}) + \frac{\mu}{jk_\rho}(I_i^e - I_i^h)\hat{\mathbf{z}}\hat{\mathbf{u}} + \frac{\mu}{j\omega\varepsilon'}I_v^e\hat{\mathbf{z}}\hat{\mathbf{z}}, \tag{4.37}$$

which can be transformed back to the (x, y, z) coordinate system by using (4.15):

$$\tilde{\bar{\mathbf{G}}}^A = \frac{1}{j\omega}V_i^h(\hat{\mathbf{x}}\hat{\mathbf{x}} + \hat{\mathbf{y}}\hat{\mathbf{y}}) + \frac{jk_x\mu}{k_\rho^2}(I_i^h - I_i^e)\hat{\mathbf{z}}\hat{\mathbf{x}} + \frac{jk_y\mu}{k_\rho^2}(I_i^h - I_i^e)\hat{\mathbf{z}}\hat{\mathbf{y}} + \frac{\mu}{j\omega\varepsilon'}I_v^e\hat{\mathbf{z}}\hat{\mathbf{z}}. \tag{4.38}$$

Upon finding the vector potential Green's function in the spectral domain, the subsequent task is to derive a suitable scalar potential Green's function for the multilayer problem. For free-space problems the scalar potential can be uniquely determined by the Lorentz Gauge:

$$\begin{aligned} -j\omega\mu\varepsilon\Phi &= \nabla\cdot\mathbf{A} \\ &= \left\langle \nabla\cdot\bar{\mathbf{G}}^A; \mathbf{J} \right\rangle, \end{aligned} \tag{4.39}$$

which is equivalent to the charge continuity equation:

$$-j\omega\rho_e = \nabla' \cdot \mathbf{J} \tag{4.40}$$

where ρ_e is defined as the electric charge.

However, for multilayered media it is impossible to find a unique scalar potential via the following equation [77]:

$$\Phi = \left\langle G^{\Phi}, \rho_e \right\rangle = -\frac{1}{j\omega}\left\langle G^{\Phi}, \nabla' \cdot \mathbf{J} \right\rangle. \tag{4.41}$$

A correction term C^{Φ} is needed to modify (4.41) and produce a unique scalar potential [84]:

$$\begin{aligned} -j\omega\Phi &= \left\langle K^{\Phi}, \nabla' \cdot \mathbf{J} \right\rangle + \left\langle C^{\Phi}\hat{z}; \mathbf{J} \right\rangle \\ &= \left\langle -\nabla' K^{\Phi} + C^{\Phi}\hat{z};\ \mathbf{J} \right\rangle. \end{aligned} \tag{4.42}$$

By comparing (4.42) with (4.39) we can obtain

$$-\nabla' K^{\Phi} + C^{\Phi}\hat{z} = \frac{1}{\mu\varepsilon}\nabla \cdot \bar{\mathbf{G}}^{A}. \tag{4.43}$$

Once again the solution of (4.43) is carried out in the spectral domain. Since $\tilde{\bar{\mathbf{G}}}^{A}$ has been obtained in (4.38), we finally have

$$\tilde{K}^{\Phi} = \frac{j\omega}{k_\rho^2}(V_i^e - V_i^h). \tag{4.44}$$

It is easy to observe that $\tilde{K}^{\Phi}$ is the same as the traditional form of the scalar potential Green's function for a horizontal electric dipole (HED) [84], i.e.,

$$\tilde{K}^{\Phi} = \tilde{G}_x^{\Phi} = \frac{j\omega}{k_\rho^2}(V_i^e - V_i^h). \tag{4.45}$$

Furthermore,

$$\tilde{C}^{\Phi} = \frac{\omega^2 \mu'}{k_\rho^2}(V_v^h - V_v^e). \tag{4.46}$$

Instead of leaving $\tilde{C}^{\Phi}$ as an independent term in the MPIE formulation, the Formulation-C Green's functions [84] absorb this extra term in the vector potential Green's functions. The final Formulation-C spectral-domain Green's functions in the Cartesian coordinate system are summarized as follows:

$$\begin{aligned}\tilde{\tilde{\mathbf{G}}}^{A} &= \begin{bmatrix} \tilde{G}_{xx}^{A} & 0 & \tilde{G}_{xz}^{A} \\ 0 & \tilde{G}_{yy}^{A} & \tilde{G}_{yz}^{A} \\ \tilde{G}_{zx}^{A} & \tilde{G}_{zy}^{A} & \tilde{G}_{zz}^{A} \end{bmatrix} \\ &= \begin{bmatrix} \dfrac{V_i^h}{j\omega} & 0 & \dfrac{\mu' k_x}{jk_\rho^2}(V_v^e - V_v^h) \\ 0 & \dfrac{V_i^h}{j\omega} & \dfrac{\mu' k_y}{jk_\rho^2}(V_v^e - V_v^h) \\ \dfrac{\mu k_x}{jk_\rho^2}(I_i^e - I_i^h) & \dfrac{\mu k_y}{jk_\rho^2}(I_i^e - I_i^h) & \dfrac{\mu}{j\omega\varepsilon'}\left[\dfrac{k'^2}{k_\rho^2} I_v^h + \left(1 - \dfrac{k'^2}{k^2}\dfrac{k_z^2}{k_\rho^2}\right) I_v^e\right] \end{bmatrix}, \end{aligned} \tag{4.47}$$

$$\tilde{G}^{\Phi} = \frac{j\omega}{k_\rho^2}(V_i^e - V_i^h). \tag{4.48}$$

Using (4.31) we can derive $\tilde{\tilde{\mathbf{G}}}^{HJ}$, which is given by

$$\tilde{\bar{\mathbf{G}}}^{HJ} = \begin{bmatrix} \tilde{G}_{xx}^{HJ} & \tilde{G}_{xy}^{HJ} & \tilde{G}_{xz}^{HJ} \\ \tilde{G}_{yx}^{HJ} & \tilde{G}_{yy}^{HJ} & \tilde{G}_{yz}^{HJ} \\ \tilde{G}_{zx}^{HJ} & \tilde{G}_{zy}^{HJ} & 0 \end{bmatrix}$$

$$= \begin{bmatrix} \frac{k_x k_y}{k_\rho^2}(I_i^e - I_i^h) & \frac{k_y^2}{k_\rho^2} I_i^e + \frac{k_x^2}{k_\rho^2} I_i^h & \frac{k_y}{\omega\varepsilon'} I_v^e \\ -\frac{k_x^2}{k_\rho^2} I_i^e - \frac{k_y^2}{k_\rho^2} I_i^h & -\frac{k_x k_y}{k_\rho^2}(I_i^e - I_i^h) & -\frac{k_x}{\omega\varepsilon'} I_v^e \\ -\frac{k_y}{\omega\mu} V_i^h & \frac{k_x}{\omega\mu} V_i^h & 0 \end{bmatrix}. \tag{4.49}$$

Once the Green's functions for vector and scalar potentials due to general electric sources are obtained, the Green's functions for vector and scalar potentials due to general magnetic sources can be formulated using duality principle.

$$\tilde{\bar{\mathbf{G}}}^{F} = \begin{bmatrix} \tilde{G}_{xx}^{F} & 0 & \tilde{G}_{xz}^{F} \\ 0 & \tilde{G}_{yy}^{F} & \tilde{G}_{yz}^{F} \\ \tilde{G}_{zx}^{F} & \tilde{G}_{zy}^{F} & \tilde{G}_{zz}^{F} \end{bmatrix}$$

$$= \begin{bmatrix} \frac{I_v^e}{j\omega} & 0 & \frac{\varepsilon' k_x}{j k_\rho^2}(I_i^h - I_i^e) \\ 0 & \frac{I_v^e}{j\omega} & \frac{\varepsilon' k_y}{j k_\rho^2}(I_i^h - I_i^e) \\ \frac{\varepsilon k_x}{j k_\rho^2}(V_v^h - V_v^e) & \frac{\varepsilon k_y}{j k_\rho^2}(V_v^h - V_v^e) & \frac{\varepsilon}{j\omega\mu'}\left[\frac{k'^2}{k_\rho^2} V_i^e + \left(1 - \frac{k'^2}{k^2}\frac{k_z^2}{k_\rho^2}\right) V_i^h\right] \end{bmatrix}, \tag{4.50}$$

$$\tilde{G}^{\Psi} = \frac{j\omega}{k_\rho^2}(I_v^h - I_v^e). \tag{4.51}$$

$$\tilde{\bar{\mathbf{G}}}^{EM} = \begin{bmatrix} \tilde{G}_{xx}^{EM} & \tilde{G}_{xy}^{EM} & \tilde{G}_{xz}^{EM} \\ \tilde{G}_{yx}^{EM} & \tilde{G}_{yy}^{EM} & \tilde{G}_{yz}^{EM} \\ \tilde{G}_{zx}^{EM} & \tilde{G}_{zy}^{EM} & 0 \end{bmatrix}$$
$$= \begin{bmatrix} \frac{k_x k_y}{k_\rho^2}(V_v^e - V_v^h) & -\frac{k_y^2}{k_\rho^2}V_v^h - \frac{k_x^2}{k_\rho^2}V_v^e & -\frac{k_y}{\omega\mu'}V_i^h \\ \frac{k_x^2}{k_\rho^2}V_v^h + \frac{k_y^2}{k_\rho^2}V_v^e & -\frac{k_x k_y}{k_\rho^2}(V_v^e - V_v^h) & \frac{k_x}{\omega\mu'}V_i^h \\ \frac{k_y}{\omega\varepsilon}I_v^e & -\frac{k_x}{\omega\varepsilon}I_v^e & 0 \end{bmatrix}. \quad (4.52)$$

Up to now we obtain the spectral domain Formulation-C Green's functions due to general electric and magnetic current sources. In the next section we will derive the spatial domain Green's functions due to general electric and magnetic current sources.

4.4 Spatial-Domain Green's Functions for Multilayered Media

Table 4.1 Summary of the spectral domain to spatial domain transformations: only zero-th and first-order Sommerfeld integrals are used.

Spectral	Spectral Domain
$\tilde{f}$	$S_0\left[\tilde{f}\right]$
$-jk_x\tilde{f}$	$\cos\phi\, S_1\left[\tilde{f}\right]$
$-jk_y\tilde{f}$	$\sin\phi\, S_1\left[\tilde{f}\right]$
$-k_x^2\tilde{f}$	$\frac{\cos 2\phi}{\rho} S_1\left[\tilde{f}\right] - \cos^2\phi\, S_0\left[k_\rho^2\tilde{f}\right]$
$-k_y^2\tilde{f}$	$-\frac{\cos 2\phi}{\rho} S_1\left[\tilde{f}\right] - \sin^2\phi\, S_0\left[k_\rho^2\tilde{f}\right]$
$-k_x k_y\tilde{f}$	$\frac{\sin 2\phi}{\rho} S_1\left[\tilde{f}\right] - \frac{1}{2}\sin 2\phi\, S_0\left[k_\rho^2\tilde{f}\right]$

Since the spatial-domain approach for the integral equations is employed in this thesis, we will in this section derive the spatial domain Green's functions for multilayered media. The spatial

domain Green's function can be derived from their spectral-domain counterparts by using the inverse Fourier transform in (4.8).

It can be proved that the inverse Fourier transform in (4.8) can be expressed in the form of the well-known Sommerfeld integral (See (B.6)). A general Sommerfeld integral of order n is given by [90, 91]

$$\begin{aligned} S_n[\tilde{f}(k_\rho, z)] &= \frac{1}{4\pi}\int_{-\infty}^{\infty} \tilde{f}(k_\rho, z)\, H_0^{(2)}(k_\rho \rho)\, k_\rho^{n+1}\, dk_\rho \\ &= \frac{1}{2\pi}\int_{0}^{\infty} \tilde{f}(k_\rho, z)\, J_n(k_\rho \rho)\, k_\rho^{n+1}\, dk_\rho. \end{aligned} \tag{4.53}$$

In the above equation, $H_0^{(2)}$ is the zero-order Hankel function of the second-type, and J_n is the Bessel function of order n. For arbitrary source and field locations the horizontal distance ρ and the azimuthal angle ϕ between them are defined as

$$\begin{aligned} \rho &= \sqrt{(x-x')^2 + (y-y')^2}, \\ \phi &= \arctan\left(\frac{y-y'}{x-x'}\right). \end{aligned} \tag{4.54}$$

Using the transformation relations listed in Table 4.1, we can finally derive the spatial domain Green's functions due to general electric and magnetic sources, which are summarized below:

$$\begin{cases} G_{xx}^{A} = G_{yy}^{A} = \dfrac{1}{j\omega} S_0\left[V_i^h\right] \\ \dfrac{G_{zx}^{A}}{\cos\phi} = \dfrac{G_{zy}^{A}}{\sin\phi} = \mu\, S_1\left[\dfrac{1}{k_\rho^2}(I_i^e - I_i^h)\right] \\ \dfrac{G_{xz}^{A}}{\cos\phi} = \dfrac{G_{yz}^{A}}{\sin\phi} = \mu'\, S_1\left[\dfrac{1}{k_\rho^2}(V_v^e - V_v^h)\right] \\ G_{zz}^{A} = \dfrac{\mu}{j\omega\varepsilon'} S_0\left[\dfrac{k'^2}{k_\rho^2} I_v^h + \left(1 - \dfrac{k'^2}{k^2}\dfrac{k_z^2}{k_\rho^2}\right) I_v^e\right], \end{cases} \tag{4.55}$$

$$G^{\Phi} = j\omega S_0\left[\frac{1}{k_\rho^2}(V_i^e - V_i^h)\right], \tag{4.56}$$

$$\begin{cases} G_{xx}^{HJ} = -G_{yy}^{HJ} = -\dfrac{\sin 2\phi}{\rho} S_1\left[\dfrac{1}{k_\rho^2}(I_i^e - I_i^h)\right] + \dfrac{1}{2}\sin 2\phi\, S_0\left[(I_i^e - I_i^h)\right] \\ \dfrac{G_{xz}^{HJ}}{\sin\phi} = -\dfrac{G_{yz}^{HJ}}{\cos\phi} = \dfrac{-1}{j\omega\varepsilon'} S_1\left[I_v^e\right] \\ \dfrac{G_{zx}^{HJ}}{\sin\phi} = -\dfrac{G_{zy}^{HJ}}{\cos\phi} = \dfrac{1}{j\omega\mu} S_1\left[V_i^h\right] \\ G_{xy}^{HJ} = \dfrac{\cos 2\phi}{\rho} S_1\left[\dfrac{1}{k_\rho^2}(I_i^e - I_i^h)\right] + \sin^2\phi\, S_0\left[(I_i^e - I_i^h)\right] + S_0\left[I_i^h\right] \\ G_{yx}^{HJ} = \dfrac{\cos 2\phi}{\rho} S_1\left[\dfrac{1}{k_\rho^2}(I_i^e - I_i^h)\right] - \cos^2\phi\, S_0\left[(I_i^e - I_i^h)\right] - S_0\left[I_i^h\right]. \end{cases} \tag{4.57}$$

$$\begin{cases} G_{xx}^{F} = G_{yy}^{F} = \dfrac{1}{j\omega} S_0\left[I_v^e\right] \\ \dfrac{G_{zx}^{F}}{\cos\phi} = \dfrac{G_{zy}^{F}}{\sin\phi} = \varepsilon\, S_1\left[\dfrac{1}{k_\rho^2}(V_v^h - V_v^e)\right] \\ \dfrac{G_{xz}^{F}}{\cos\phi} = \dfrac{G_{yz}^{F}}{\sin\phi} = \varepsilon'\, S_1\left[\dfrac{1}{k_\rho^2}(I_i^h - I_i^e)\right] \\ G_{zz}^{F} = \dfrac{\varepsilon}{j\omega\mu'} S_0\left[\dfrac{k'^2}{k_\rho^2} V_i^e + \left(1 - \dfrac{k'^2}{k^2}\dfrac{k_z^2}{k_\rho^2}\right) V_i^h\right], \end{cases} \tag{4.58}$$

$$G^{\Psi} = j\omega S_0\left[\frac{1}{k_\rho^2}(I_v^h - I_v^e)\right], \tag{4.59}$$

$$\begin{cases} G_{xx}^{EM} = -G_{yy}^{EM} = -\dfrac{\sin 2\phi}{\rho} S_1\left[\dfrac{1}{k_\rho^2}(V_v^e - V_v^h)\right] + \dfrac{1}{2}\sin 2\phi\, S_0\left[(V_v^e - V_v^h)\right] \\ \dfrac{G_{xz}^{EM}}{\sin\phi} = -\dfrac{G_{yz}^{EM}}{\cos\phi} = \dfrac{1}{j\omega\mu'} S_1\left[V_i^h\right] \\ \dfrac{G_{zx}^{EM}}{\sin\phi} = -\dfrac{G_{zy}^{EM}}{\cos\phi} = \dfrac{-1}{j\omega\varepsilon} S_1\left[I_v^e\right] \\ G_{xy}^{EM} = \dfrac{\cos 2\phi}{\rho} S_1\left[\dfrac{1}{k_\rho^2}(V_v^e - V_v^h)\right] + \sin^2\phi\, S_0\left[(V_v^e - V_v^h)\right] - S_0\left[V_v^e\right] \\ G_{yx}^{EM} = \dfrac{\cos 2\phi}{\rho} S_1\left[\dfrac{1}{k_\rho^2}(V_v^e - V_v^h)\right] - \cos^2\phi\, S_0\left[(V_v^e - V_v^h)\right] + S_0\left[V_v^e\right]. \end{cases} \tag{4.60}$$

Altogether there are 32 components for vector and scalar Green's functions due to general electric and magnetic sources, it can be seen from (4.55)-(4.60) that only 11 Sommerfeld integrals are needed to compute all the 32 components of Green's functions if the duality property of the TLGF's in (C.4) is used. The 11 Sommerfeld integrals are listed as follows:

$$\begin{aligned} &S_0\left[V_i^h\right],\ S_1\left[\frac{1}{k_\rho^2}(I_i^e - I_i^h)\right], S_0\left[\frac{k'^2}{k_\rho^2} I_v^h + \left(1 - \frac{k'^2}{k^2}\frac{k_z^2}{k_\rho^2}\right) I_v^e\right], S_0\left[\frac{1}{k_\rho^2}(V_i^e - V_i^h)\right], \\ &S_0\left[I_v^e\right],\ S_0\left[\frac{k'^2}{k_\rho^2} V_i^e + \left(1 - \frac{k'^2}{k^2}\frac{k_z^2}{k_\rho^2}\right) V_i^h\right], S_0\left[\frac{1}{k_\rho^2}(I_v^h - I_v^e)\right], \\ &S_0\left[(V_v^e - V_v^h)\right], S_1\left[V_i^h\right], S_1\left[I_v^e\right], S_0\left[V_v^e\right]. \end{aligned} \tag{4.61}$$

Evaluation of the 11 Sommerfeld integrals in (4.61) will be discussed in the next section.

4.5 Numerical Integration Method for Sommerfeld Integrals

4.5.1 Overview of Evaluation of Sommerfeld Integrals

To formulate the integral equations in spatial domain for the multilayered media, it is indispensable to evaluate all or some of the Sommerfeld integrals in (4.61). These integrals

have to be repeatedly computed in the MoM matrix filling process. Therefore, efficient computation of these integrals is of great importance. However, computation of the Sommerfeld integrals is quite difficult mainly for two reasons [92]: a) the integrands of the Sommerfeld integrals present singularities in the complex k_ρ plane; b) the integrands of the Sommerfeld integrals have oscillatory tails due to Bessel functions.

The integrand singularities of the Sommerfeld integrals, which occur in complex conjugate pairs in the second and fourth quadrants of the complex k_ρ plane, consist of poles and branch points [91] (See Fig. 4.4). For lossless media, the poles lie on the real axis, which causes the integrals impossible to evaluate. Therefore, the integration path in Fig. 4.4 must be indented into the first quadrant to avoid them. These poles, which correspond to the TM and TE guided waves, can be found as roots of the resonant denominator D_n^p in (C.11) for any finite thickness layer, or as roots of the denominator of the reflection coefficient in (C.13) looking into the layered medium from a half-space.

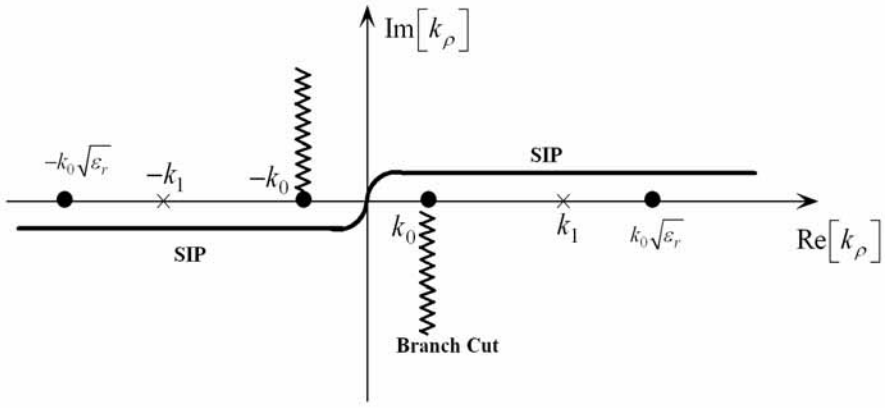

Fig. 4.4 Sommerfeld integration Path (SIP) in the complex k_ρ plane with possible branch cuts and poles. k_0 is the wavenumber for the half space.

In general the number of poles is infinite, but only a finite number of them appear on the proper sheet in the case of vertically unbounded media. As for the branch points it can be

proved [91] that they are only associated with the outermost unbounded regions in a layered medium, i.e., only when either the top or the bottom layer is a half-space. In this case the integration path must approach infinity on the proper sheet of the Riemann surface associated with the longitudinal propagation wavenumbers in (4.22) for the half-spaces [33].

Many numerical integration approaches have been developed to evaluate the Sommerfeld integral [85, 92-94]. A good summary of these numerical techniques can be found in [84]. Nevertheless, it is fair to say that a completely satisfactory solution to this problem is still lacking, especially in the case of arbitrarily shaped objects extending over more than one layer of the multilayered medium. But of all the variants of the integral paths, the real-axis path indented into the first quadrant to avoid the branch points and pole singularities [94], has been proved to be the most convenient one for multilayer problem, because it obviates the needs to locate the poles and thus greatly reduce the evaluation time [33]. The integral over the tail of the real-axis path can be computed as a sum of an alternating series of integrals between zeros of the Bessel function. Series acceleration techniques are often used to speed up the convergence of the tail integration, such as the method of averages [80] or the continued fraction expansion [95].

In this chapter the deformed real-axis integration path modified in [96] is employed to evaluate the Sommerfeld integrals, and the weighted averages method [92] is exploited to accelerate the evaluation of the Sommerfeld integral tails [97]. Details of the numerical integration approach are presented in the following sections.

4.5.2 Details of Numerical Integration Method

4.5.2.1 Integration over a Half-elliptical Path

As mentioned above, the poles of the Green's functions are associated with propagation waves. Therefore, there must exist at least one real valued k_{zn} [98], i.e.,

$$k_{zn}^2 = k_n^2 - k_\rho^2 = k_0^2 \varepsilon_{rn} \mu_{rn} - k_\rho^2 > 0 \tag{4.62}$$

which yields the following condition:

$$k_\rho < k_0 \cdot \max_n (\sqrt{\varepsilon_{rn} \mu_{rn}}) \tag{4.63}$$

where ε_{rn} and μ_{rn} denote the relative permittivity and permeability of layer n ($n = 1, \cdots, N$), respectively; k_0 is the free-space wavenumber and $k_0 = \omega\sqrt{\mu_0 \varepsilon_0}$. Equation (4.63) actually defines an upper bound for the location of the poles. Essentially the poles in the complex k_ρ plane are located in the interval $\left[k_0,\ k_0 \cdot \max_n (\sqrt{\varepsilon_{rn} \mu_{rn}})\right]$. We can divide the semi-infinite range $[0, \infty)$ into two segments: $[0, 2a]$ and $[2a, \infty)$ (see Fig. 4.5).

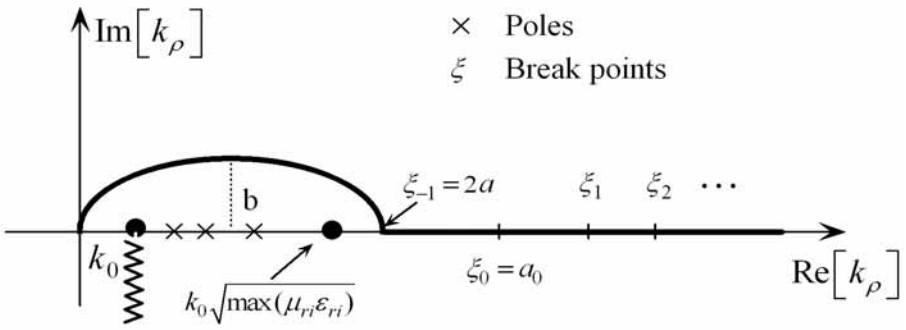

Fig. 4.5 Deformed real-axis integration Path in the complex k_ρ plane. The deformed path in the first quadrant is a half ellipse, whose semimajor axis is a and semiminor axis is b. The break points along the remaining part of the positive real axis are used for the weighted-averages method.

The first segment of the integration path is deformed into the first quadrant to avoid the

guided-wave poles and branch points of the integrand [97]. The half-elliptical integration path proposed in [96] is employed to evaluate the Sommerfeld integrals. Similar to the choice made in [93] we choose the semiminor axis as

$$b = \begin{cases} \dfrac{1.0}{\chi}, & \text{if } \rho < \chi \\ \dfrac{1.0}{\rho}, & \text{if } \rho > \chi \end{cases} \tag{4.64}$$

where $\chi = |z| + |z'|$. The choice of b restricts the contour to small $\rho \mathrm{Im}(k_\rho)$. Therefore, this path accelerates the convergence of the exponential function and contains the divergence of the Bessel function. The choice of the semimajor axis is quite arbitrary if only it complies with the constraint of $a > \frac{1}{2} k_0 \cdot \max_n(\sqrt{\varepsilon_{rn}\mu_{rn}})$. For example, the semimajor axis can be chosen as $a = \frac{1}{2}\left(1.0 + k_0 \cdot \max_n(\sqrt{\varepsilon_{rn}\mu_{rn}})\right)$. Finally, the line integral in the complex plane can be easily done by parameterizing the ellipse and performing either the Gauss quadrature or adaptive Romberg integration approaches [99].

4.5.2.2 Integration of Sommerfeld Tails

Following the successful treatment of the Sommerfeld integral over the first segment of the integration path, its integration over the second segment, which is referred to as Sommerfeld integral tails, is discussed in this section. The convergence of the integral tails can be very slow due to the oscillatory behavior of the integral kernel. Therefore, the extrapolation method is often used to accelerate the computation of the integral tails. The most efficient approach to evaluate the Sommerfeld integral tails is the integration-then-summation procedure, in which the integral is evaluated as a sum of a series of partial integrals over subintervals given by [97]

$$S_\infty = \int_{2a}^{\infty} \tilde{G}(z,z';k_\rho) J_n(k_\rho\rho) k_\rho dk_\rho \triangleq \int_{2a}^{\infty} f(k_\rho) dk_\rho$$
$$= \sum_{i=0}^{\infty} \int_{\xi_{i-1}}^{\xi_i} f(k_\rho) dk_\rho \tag{4.65}$$

where ξ_i's are the break points (see Fig. 4.5) with $\xi_{-1} = 2a$ and $\xi_0 = a_0$.

The break points can be chosen according to the asymptotic behavior of the integrands. The spectral domain Green's functions have the following general asymptotic form:

$$\tilde{G}(z,z';k_\rho) \sim \frac{e^{-\beta k_\rho}}{k_\rho^\alpha}\left[C + O(k_\rho^{-1})\right] \tag{4.66}$$

where C is a constant. β and α can be determined from the expressions of spectral-domain Green's functions (4.47)-(4.52). In addition, for large arguments the Bessel function behaves as

$$J_n(k_\rho\rho) \sim \sqrt{\frac{2}{\pi k_\rho \rho}} \cos(k_\rho\rho - n\frac{\pi}{2} - \frac{\pi}{4}). \tag{4.67}$$

However, for simplicity the break points can be made evenly distributed along the integral interval [97]:

$$\xi_n = a_0 + nq, \qquad n \geq 0 \tag{4.68}$$

and q can either be equivalent to the asymptotic half-period of the Bessel function or to be related to the exponential behavior of Green's functions, i.e.,

$$q = \begin{cases} \dfrac{\pi}{\rho}, & \rho \neq 0 \\ \dfrac{\pi}{\beta}, & \rho = 0 \end{cases}. \tag{4.69}$$

The computation of the tail integral in (4.65) has thus been reduced to find the limit of a sequence of partial sums:

$$S_n = \sum_{i=0}^{n} \int_{\xi_{i-1}}^{\xi_i} f(k_\rho) dk_\rho \tag{4.70}$$

as $n \to \infty$. However, this sequence usually converges very slowly. Therefore, a sequence transformation is needed to accelerate the convergence of $\{S_n\}$. The underlying principle of the transformation is to obtain an improved estimated sequence recursively from the previous estimated sequence, which is called the partition-extrapolation method. The recursive process is illustrated in Fig. 4.6.

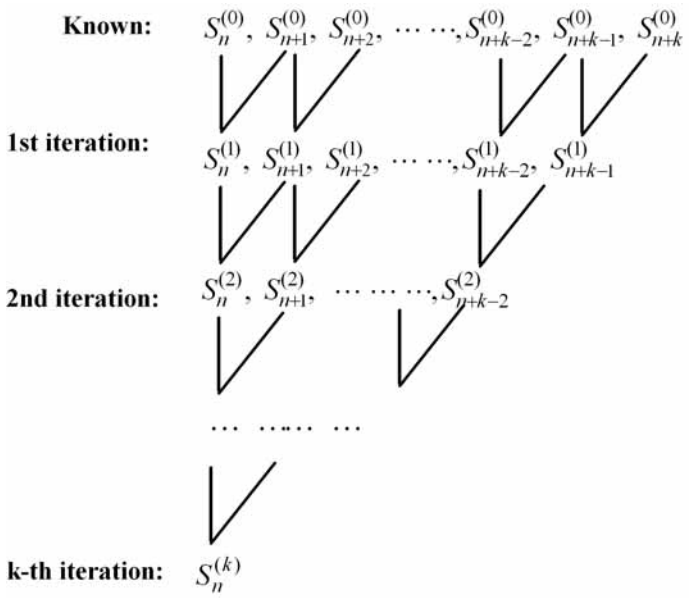

Fig. 4.6 Recursive process of the sequence transformation to accelerate the convergence of the original sequence.

For the generalized weighted-averages algorithm, the recursive formula is given by [97]

$$S_n^{(\mathrm{k}+1)} = \frac{S_n^{(\mathrm{k})} + \eta_n^{(\mathrm{k})} S_{n+1}^{(\mathrm{k})}}{1 + \eta_n^{(\mathrm{k})}}, \qquad \mathrm{n}, \mathrm{k} \geq 0 . \tag{4.71}$$

And the ratio of the weights $\eta_n^{(k)}$ can be obtained by

$$\eta_n^{(k)} = \pm e^{\beta \mathrm{q}} \left(\frac{\xi_{n+1}}{\xi_n} \right)^{\alpha+2\mathrm{k}} \tag{4.72}$$

where the plus and minus signs apply to the alternating convergence ($\rho > 0$) and linear monotone convergence ($\rho = 0$), respectively. The condition to judge the convergence of the tail integral may be defined as

$$\frac{\left| S_n^k - S_n^{k-1} \right|}{\left| (S_n^k + S_n^{k-1})/2.0 \right|} < error \tag{4.73}$$

The *error* can be assigned a value, say, 10^{-8}.

Now the approach for evaluating the Sommerfeld integral has been realized. However, in order to further facilitate the evaluation of the improper Sommerfeld integrals, it is better to extract the large argument ($k_\rho \to \infty$) approximation of the Sommerfeld integrands [92] before performing numerical integration.

4.5.3 Large Argument Approximation and Singularity Extraction

For all the 11 Sommerfeld integrals in (4.61) some may converge faster than others, e.g., the convergence for large source-field distance $\left| z - z' \right|$ is better than those for small $\left| z - z' \right|$; and when the field point approaches the source point, i.e., $\rho \to \rho', z \to z'$, some of the integrals may present logarithmic singularity and converge slowly [100]. On top of using weighted-averages method to speed up the computation of the integral tails, a remedy to further accelerate the evaluation of these integrals is to extract from the integrands their large argument approximations $\tilde{G}_\infty$, i.e.,

$$\tilde{G} = \tilde{G}_{\infty} + (\tilde{G} - \tilde{G}_{\infty}) \tag{4.74}$$

and integrate these extraction terms analytically. Then the remaining integrands can be efficiently evaluated by the deformed real-axis integration approach discussed in the preceding section.

The large argument approximation is based on the relation that when k_ρ approaches ∞, k_{zn} will degenerate to $-jk_\rho$. The condition of $k_\rho \to \infty$ also corresponds to the case of $k_n = 0$, which is the static case. Based on the previous work in [100, 101], large argument approximation is extended in this chapter to the Green's functions due to electric and magnetic sources.

4.5.3.1 Large Argument Approximation of the Spectral-domain TLGF's

Since all the spectral-domain Green's functions in (4.47)-(4.52) are expressed in terms of TLGF's, it is straightforward to first find all the large argument approximations related to TLGF's. They are summarized below:

$$k_\rho \to \infty \Rightarrow k_{zn} = \sqrt{k_n^2 - k_\rho^2} \to -jk_\rho \tag{4.75}$$

$$k_\rho \to \infty \Rightarrow \begin{cases} \Gamma_{ij,\infty}^{e} = \lim\limits_{k_\rho \to \infty} \Gamma_{ij}^{e} = \dfrac{\varepsilon_j - \varepsilon_i}{\varepsilon_j + \varepsilon_i} \\ \Gamma_{ij,\infty}^{h} = \lim\limits_{k_\rho \to \infty} \Gamma_{ij}^{h} = \dfrac{\mu_i - \mu_j}{\mu_j + \mu_i} \end{cases} \tag{4.76}$$

$$k_\rho \to \infty \Rightarrow \begin{cases} \vec{\Gamma}^p_{n,\infty} = \Gamma^p_{n-1,n,\infty} = \begin{cases} \dfrac{\varepsilon_n - \varepsilon_{n-1}}{\varepsilon_n + \varepsilon_{n-1}}, & \text{for } p = e \\ \dfrac{\mu_{n-1} - \mu_n}{\mu_{n-1} + \mu_n}, & \text{for } p = h \end{cases} \\ \overleftarrow{\Gamma}^p_{n,\infty} = \Gamma^p_{n+1,n,\infty} = \begin{cases} \dfrac{\varepsilon_n - \varepsilon_{n+1}}{\varepsilon_n + \varepsilon_{n+1}}, & \text{for } p = e \\ \dfrac{\mu_{n+1} - \mu_n}{\mu_{n+1} + \mu_n}, & \text{for } p = h \end{cases} \end{cases} \tag{4.77}$$

$$k_\rho \to \infty \Rightarrow \begin{cases} t_n = e^{-2jk_{zn}d_n} \to 0 \\ D^p_{n,\infty} = \lim\limits_{k_\rho \to \infty} D^p_\infty = \lim\limits_{k_\rho \to \infty} (1 - \vec{\Gamma}^p_n \overleftarrow{\Gamma}^p_n t_n) = 1 \end{cases} \tag{4.78}$$

$$k_\rho \to \infty \Rightarrow \begin{cases} \vec{T}^{vp}_{k,\infty} = \begin{cases} 0, & \text{if } m < n\text{-}1 \\ 1, & \text{if } m = n\text{-}1 \end{cases} \\ \overleftarrow{T}^{vp}_{k,\infty} = \begin{cases} 0, & \text{if } m > n+1 \\ 1, & \text{if } m = n+1 \end{cases} \end{cases} \tag{4.79}$$

$$m = n \Rightarrow \begin{cases} |z - z'| \to 0, & \text{if } z \to z' \\ \gamma_{n1} = 2z_n - (z + z') \to 0, & \text{if } z' = z_n \text{ and } z \to z' \\ \gamma_{n2} = (z + z') - 2z_{n+1} \to 0, & \text{if } z' = z_{n+1} \text{ and } z \to z' \\ \gamma_{n3} = 2d_n + (z - z') \neq 0, & \text{for all cases} \\ \gamma_{n4} = 2d_n - (z - z') \neq 0, & \text{for all cases} \end{cases} \tag{4.80}$$

$$m \neq n \Rightarrow \begin{cases} m < n \Rightarrow \left\{ \begin{matrix} z - z_{m+1} \to 0 \\ d_m + z_m - z \neq 0 \end{matrix} \right\}, & \text{if } m = n-1 \text{ and } z \to z_n \\ m > n \Rightarrow \left\{ \begin{matrix} z_m - z \to 0 \\ d_m + z - z_{m+1} \neq 0 \end{matrix} \right\}, & \text{if } m = n+1 \text{ and } z \to z_{n+1} \end{cases} \tag{4.81}$$

Extraction of singularity for all the components of $\bar{\mathbf{G}}^A$ has been presented thoroughly in [101]. Here we will briefly summarize the results for $\bar{\mathbf{G}}^A$ and then extend the procedure to

other vector and scalar Green's functions due to general electric and magnetic sources.

4.5.3.2 Extraction from $\bar{\mathbf{G}}^A$

Now we take $\tilde{G}_{xx}^A(m,z\,|\,n,z') = \dfrac{V_i^h}{j\omega}$ for an example to perform the large argument approximation. The term corresponding to the large argument approximation is denoted by $\tilde{G}_{xx,\infty}^A$. Its spatial domain counterpart is represented by $G_{xx,0}^A$, which is equivalent to the singular term in spatial domain and obtained through Sommerfeld identity (B.8). Only when the source and field points are located in the same or adjacent layers can the singularity present.

Table 4.2 summarizes the extracted terms in spectral domain and their counterparts in spatial domain due to different source and field locations. The spatial-domain singularity in all the five cases shown in Table 4.2 can be further represented by the following unified expression:

$$G_{xx,0}^A(m,z\,|\,n,z';\rho) = S_{xx,mn}^A \frac{e^{-jk_m r}}{4\pi r} \tag{4.82}$$

where

$$r = \sqrt{\rho^2 + (z-z')^2}\,, \tag{4.83}$$

$$S_{xx,mn}^A = \begin{cases} \mu_l, & \text{for } m=n=l,\ z_l > z' > z_{l+1} \\ \dfrac{2\mu_l\mu_{l-1}}{\mu_l+\mu_{l-1}}, & \text{for } z'=z_l,\ m=l \text{ or } l-1, n=l \text{ or } l-1 \\ 0, & \text{Others} \end{cases}. \tag{4.84}$$

and m, n and l are the layer numbers.

It can be observed that the four components of $\bar{\mathbf{G}}^A$, i.e., $G_{zx}^A, G_{zy}^A, G_{xz}^A$ and G_{yz}^A have no

singular terms to be extracted.

The singular term of G_{zz}^{A} is

$$G_{zz,0}^{A}(m,z\mid n,z';\rho)=S_{zz,mn}^{A}\frac{e^{-jk_m r}}{4\pi r} \tag{4.85}$$

where

$$S_{zz,mn}^{A}=\begin{cases}\mu_l, & \text{for } m=n=l,\ z_l>z'>z_{l+1}\\ \mu_l(1+\vec{\Gamma}_{l,\infty}^{h}-2\vec{\Gamma}_{l,\infty}^{e}), & \text{for } z'=z_{l,}\ m=l,n=l\\ \mu_l\left[-(1-\vec{\Gamma}_{l,\infty}^{h})+(1+\frac{k_{l-1}^2}{k_l^2})(1-\vec{\Gamma}_{l,\infty}^{e})\right], & \text{for } z'=z_{l,}\ m=l-1,n=l\\ \mu_l\left[1+\overleftarrow{\Gamma}_{l,\infty}^{h}-2\overleftarrow{\Gamma}_{l,\infty}^{e}\right], & \text{for } z'=z_{l,}\ m=l-1,n=l-1\\ \mu_{l-1}\left[-(1-\overleftarrow{\Gamma}_{l-1,\infty}^{h})+(1+\frac{k_l^2}{k_{l-1}^2})(1-\overleftarrow{\Gamma}_{l-1,\infty}^{e})\right], & \text{for } z'=z_{l,}\ m=l,n=l\\ 0, & \text{others}\end{cases} \tag{4.86}$$

4.5.3.3 Extraction from G^{Φ}

The singular term of G^{Φ} is

$$G_{0}^{\Phi}(m,z\mid n,z';\rho)=S_{mn}^{\Phi}\frac{e^{-jk_m r}}{4\pi r} \tag{4.87}$$

where

$$S_{mn}^{\Phi}=\begin{cases}\dfrac{1}{\varepsilon_l}, & \text{for } m=n=l,\ z_l>z'>z_{l+1}\\ \dfrac{2}{\varepsilon_l+\varepsilon_{l-1}}, & \text{for } z'=z_{l,}\ m=l \text{ or } l-1,n=l \text{ or } l-1\\ 0, & \text{Otherwise}\end{cases}. \tag{4.88}$$

Table 4.2 Large argument approximation ($\tilde{G}^A_{xx,\infty}$) of $\tilde{G}^A_{xx}$ and their spatial-domain counterparts ($G^A_{xx,0}$) extracted according to different source and field locations.

Conditions	$\tilde{G}^A_{xx,\infty}$	$G^A_{xx,0}$
$m = n$ & $z_{n+1} < z' < z_n$ n, $z_\bullet$, z_{n+1}, z'^*, z_n	$\frac{\mu_n}{2jk_{zn}} e^{-jk_{zn}\lvert z-z'\rvert}$	$\mu_n \frac{e^{-jk_n r}}{4\pi r}$
$m = n$; $z' = z_n$ n, $z_\bullet$, z_{n+1}, z'^*, z_n	$\frac{\mu_n}{2jk_{zn}} \left(e^{-jk_{zn}\lvert z-z'\rvert} + \frac{\mu_{n-1}-\mu_n}{\mu_{n-1}+\mu_n} e^{-jk_{zn}[2z_n-(z+z')]} \right)$	$\frac{2\mu_{n-1}\mu_n}{\mu_{n-1}+\mu_n} \frac{e^{-jk_n r}}{4\pi r}$
$m = n$; $z' = z_{n+1}$ z'^*, z_{n+1}, n, $z_\bullet$, z_n	$\frac{\mu_n}{2jk_{zn}} \left(e^{-jk_{zn}\lvert z-z'\rvert} + \frac{\mu_{n+1}-\mu_n}{\mu_{n+1}+\mu_n} e^{-jk_{zn}[2z_n-(z+z')]} \right)$	$\frac{2\mu_{n+1}\mu_n}{\mu_{n+1}+\mu_n} \frac{e^{-jk_n r}}{4\pi r}$
$m = n-1$; $z' = z_n$ n, z', z_{n+1}, z'^*, n-1, $z_\bullet$, z_n	$\frac{\mu_n}{2jk_{zn}} \frac{2\mu_{n-1}}{\mu_{n-1}+\mu_n} e^{-jk_{zm}\lvert z-z'\rvert}$	$\frac{2\mu_{n-1}\mu_n}{\mu_{n-1}+\mu_n} \frac{e^{-jk_m r}}{4\pi r}$
$m = n+1$; $z' = z_{n+1}$ n+1, $z_\bullet$, z'^*, n	$\frac{\mu_n}{2jk_{zn}} \frac{2\mu_{n+1}}{\mu_{n+1}+\mu_n} e^{-jk_{zm}\lvert z-z'\rvert}$	$\frac{2\mu_{n+1}\mu_n}{\mu_{n+1}+\mu_n} \frac{e^{-jk_m r}}{4\pi r}$

Now we will perform the large argument approximation and singularity extraction of other vector and scalar potential Green's functions.

4.5.3.4 Extraction from $\bar{\mathbf{G}}^F$

The singular terms for all the components of $\bar{\mathbf{G}}^F$ can be obtained by duality principle. The singular term of G_{xx}^F is

$$G_{xx,0}^F(m,z\,|\,n,z';\rho)=S_{xx,mn}^F\frac{e^{-jk_m r}}{4\pi r} \tag{4.89}$$

where

$$S_{xx,mn}^F=\begin{cases}\varepsilon_l, & \text{for } m=n=l,\ z_l>z'>z_{l+1}\\ \dfrac{2\varepsilon_l\varepsilon_{l-1}}{\varepsilon_l+\varepsilon_{l-1}}, & \text{for } z'=z_l,\ m=l \text{ or } l-1, n=l \text{ or } l-1\\ 0, & \text{Others}\end{cases}. \tag{4.90}$$

Similarly, $\mathrm{G}_{zx}^F, \mathrm{G}_{zy}^F, \mathrm{G}_{xz}^F$ and G_{yz}^F have no singular terms to be extracted.

The singular term of G_{zz}^F is

$$G_{zz,0}^F(m,z\,|\,n,z';\rho)=S_{zz,mn}^F\frac{e^{-jk_m r}}{4\pi r} \tag{4.91}$$

where

$$S_{zz,mn}^F=\begin{cases}\varepsilon_l, & \text{for } m=n=l,\ z_l>z'>z_{l+1}\\ \varepsilon_l(1-\vec{\Gamma}_{l,\infty}^e+2\vec{\Gamma}_l^h), & \text{for } z'=z_l,\ m=l, n=l\\ \varepsilon_l\left[-(1+\vec{\Gamma}_{l,\infty}^e)+(1+\dfrac{k_{l-1}^2}{k_l^2})(1+\vec{\Gamma}_{l,\infty}^h)\right], & \text{for } z'=z_l,\ m=l-1, n=l\\ \varepsilon_l\left[1-\vec{\Gamma}_{l,\infty}^e+2\vec{\Gamma}_{l,\infty}^h\right], & \text{for } z'=z_l,\ m=l-1, n=l-1\\ \varepsilon_{l-1}\left[-(1-\vec{\Gamma}_{l-1,\infty}^h)+(1+\dfrac{k_l^2}{k_{l-1}^2})(1-\vec{\Gamma}_{l-1,\infty}^h)\right], & \text{for } z'=z_l,\ m=l, n=l\\ 0, & \text{others}\end{cases}. \tag{4.92}$$

4.5.3.5 Extraction from G^{ψ}

The singular term of G^{ψ} takes the following form:

$$G_0^{\psi}(m,z\,|\,n,z';\rho) = S_{mn}^{\psi}\frac{e^{-jk_m r}}{4\pi r} \tag{4.93}$$

where

$$S_{mn}^{\psi} = \begin{cases} \dfrac{1}{\mu_l}, & \text{for } m=n=l,\ z_k > z' > z_{l+1} \\ \dfrac{2}{\mu_l+\mu_{l-1}}, & \text{for } z'=z_l,\ m=l \text{ or } l-1, n=l \text{ or } l-1 \\ 0, & \text{Others} \end{cases} . \tag{4.94}$$

4.5.3.6 Extraction from $\bar{\bar{\mathbf{G}}}^{HJ}$

Extraction of the terms relevant to the integrand of $S_0\left[I_i^e - I_i^h\right]$: The spectral kernel $\tilde{U}_a = I_i^e - I_i^h$ is related to $\tilde{G}_{xx}^{HJ}$ and $\tilde{G}_{yy}^{HJ}$. The large argument approximation of $\tilde{U}_a$ is found to be

$$\tilde{U}_{a,\infty}(m,z\,|\,n,z';k_\rho) = S_{a,mn}\,e^{-jk_\rho h_z^a} \tag{4.95}$$

where

$$S_{a,mn} = \begin{cases} \dfrac{1}{2}(-\vec{\Gamma}_{n,\infty}^{e}+\vec{\Gamma}_{n,\infty}^{h}), & \text{for } m=n \text{ or } n\text{-}1,\ z'=z_n \\ \dfrac{1}{2}(\overleftarrow{\Gamma}_{n,\infty}^{e}-\overleftarrow{\Gamma}_{n,\infty}^{h}), & \text{for } m=n \text{ or } n+1,\ z'=z_{n+1} \\ 0, & \text{Others} \end{cases} , \tag{4.96}$$

$$h_z^a = \begin{cases} z'-z, & \text{for } m=n,\ z'=z_n \text{ or } m=n+1, z'=z_{n+1} \\ z-z', & \text{for } m=n,\ z'=z_{n+1} \text{ or } m=n-1, z'=z_n \end{cases}. \tag{4.97}$$

The singular term of U_a can be derived by the identity (B.11):

$$U_{a,\infty}(m,z \mid n,z';k_\rho) = S_{a,mn} \frac{h_z^a}{2\pi\sqrt{\left[(h_z^a)^2+\rho^2\right]^3}}. \tag{4.98}$$

Extraction of the terms relevant to the integrand of $\frac{1}{j\omega\varepsilon'} S_1\left[I_v^e\right]$: The spectral kernel $\tilde{U}_b = \frac{1}{j\omega\varepsilon'} I_v^e$ is relevant to $\tilde{G}_{xz}^{HJ}$ and $\tilde{G}_{yz}^{HJ}$. The large argument approximation of $\tilde{U}_b$ can be expressed as

$$\tilde{U}_{b,\infty}(m,z \mid n,z';k_\rho) = S_{b,mn} \frac{e^{-jk_{zm}h_z^b}}{2jk_{zm}} \tag{4.99}$$

where

$$S_{b,mn} = \begin{cases} 1, & \text{for } m=n, z_n > z' > z_{n+1} \\ \dfrac{2\varepsilon_{n-1}}{\varepsilon_n+\varepsilon_{n-1}}, & \text{for } m=n \text{ or } n-1,\ z'=z_n \\ \dfrac{2\varepsilon_{n+1}}{\varepsilon_n+\varepsilon_{n+1}}, & \text{for } m=n \text{ or } n+1,\ z'=z_{n+1} \\ 0, & \text{Others} \end{cases}, \tag{4.100}$$

$$h_z^b = \begin{cases} \left|z'-z\right|, & \text{for } m=n, z_n > z' > z_{n+1} \\ z'-z, & \text{for } m=n,\ z'=z_n \text{ or } m=n+1, z'=z_{n+1} \\ z-z', & \text{for } m=n,\ z'=z_{n+1} \text{ or } m=n-1, z'=z_n \end{cases}. \tag{4.101}$$

The singular term of U_b can be derived by the identity (B.10):

$$U_{b,\infty}(m,z \mid n,z';k_\rho) = S_{b,mn} \frac{e^{-jk_m r}}{4\pi r^3}(1+jk_m r)\rho. \tag{4.102}$$

Extraction of the terms relevant to the integrand of $\frac{1}{j\omega\mu}S_1\left[V_i^h\right]$: The spectral kernel $\tilde{U}_c = \frac{1}{j\omega\mu}V_i^h$ composes $\tilde{G}_{zx}^{HJ}$ and $\tilde{G}_{zy}^{HJ}$. The large argument approximation of $\tilde{U}_c$ can be formulated by

$$\tilde{U}_{c,\infty}(m,z\,|\,n,z';k_\rho) = S_{c,mn}\frac{e^{-jk_{zm}h_z^c}}{2jk_{zm}} \tag{4.103}$$

where

$$S_{c,mn} = \begin{cases} 1, & \text{for } m = n,\ z_n > z' > z_{n+1} \\ \dfrac{2\mu_{n-1}}{\mu_n + \mu_{n-1}}, & \text{for } m = n \text{ or } n-1,\ z' = z_n \\ \dfrac{2\mu_{n+1}}{\mu_n + \mu_{n+1}}, & \text{for } m = n \text{ or } n+1,\ z' = z_{n+1} \\ 0, & \text{Others} \end{cases} . \tag{4.104}$$

and h_z^c is the same as h_z^b in (4.101).

The singular term of U_c can be derived by the identity (B.10):

$$U_{c,\infty}(m,z\,|\,n,z';k_\rho) = S_{c,mn}\frac{e^{-jk_m r}}{4\pi r^3}(1+jk_m r)\rho\,. \tag{4.105}$$

Extraction of the terms relevant to the integrand of $S_0\left[I_i^h\right]$: The spectral kernel $\tilde{U}_d = I_i^h$ is related to $\tilde{G}_{xy}^{HJ}$ and $\tilde{G}_{yx}^{HJ}$. The large argument approximation of $\tilde{U}_d$ is found to be

$$\tilde{U}_{d,\infty}(m,z\,|\,n,z';k_\rho) = S_{d,mn}e^{-jk_\rho h_z^d} \tag{4.106}$$

where

$$S_{d,mn}=\begin{cases}\dfrac{1}{2}\mathrm{Sign}(z-z'), & \text{for } m=n, z_n>z'>z_{n+1}\\ \dfrac{1}{2}\left[\mathrm{Sign}(z-z')-\vec{\Gamma}^h_{n,\infty}\right], & \text{for } m=n \text{ or } n-1,\ z'=z_n\\ \dfrac{1}{2}\left[\mathrm{Sign}(z-z')+\overleftarrow{\Gamma}^h_{n,\infty}\right], & \text{for } m=n \text{ or } n+1,\ z'=z_{n+1}\\ 0, & \text{Others}\end{cases} . \quad (4.107)$$

and h_z^d is the same as h_z^b in (4.101).

The singular term of U_d can be derived by the identity (B.11):

$$U_{d,\infty}(m,z\,|\,n,z';k_\rho)=S_{d,mn}\frac{h_z^d}{2\pi\sqrt{\left[(h_z^d)^2+\rho^2\right]^3}} . \quad (4.108)$$

4.5.3.7 Extraction from $\bar{\mathbf{G}}^{EM}$

Extraction of the terms relevant to $\tilde{G}_{xx}^{EM}$ and $\tilde{G}_{yy}^{Em}$: They involve two Sommerfeld integrals- one is $S_1\left[\frac{1}{k_\rho^2}(V_v^e-V_v^h)\right]$ which has no singular terms; the other is $S_0\left[V_v^e-V_v^h\right]$ whose singular terms are dual to those of $S_0\left[I_i^e-I_i^h\right]$. The large argument approximation of $\tilde{U}_e=V_v^e-V_v^h$ is given by

$$\tilde{U}_{e,\infty}(m,z\,|\,n,z';k_\rho)=S_{e,mn}\,e^{-jk_\rho h_z^e} \quad (4.109)$$

where

$$S_{e,mn}=\begin{cases}\dfrac{1}{2}(\vec{\Gamma}^e_{n,\infty}-\vec{\Gamma}^h_{n,\infty}), & \text{for } m=n \text{ or } n\text{-}1,\ z'=z_n\\ \dfrac{1}{2}(-\overleftarrow{\Gamma}^e_{n,\infty}+\overleftarrow{\Gamma}^h_{n,\infty}), & \text{for } m=n \text{ or } n+1,\ z'=z_{n+1}\\ 0, & \text{Others}\end{cases} . \quad (4.110)$$

and h_z^e is the same as h_z^a in (4.97).

The singular term of U_a is

$$U_{e,\infty}(m,z\,|\,n,z';k_\rho) = S_{e,mn}\frac{h_z^e}{2\pi\sqrt{\left[(h_z^e)^2+\rho^2\right]^3}}. \tag{4.111}$$

The large argument approximation and singular term extraction relevant to $\tilde{G}_{xz}^{EM}$, $\tilde{G}_{yz}^{EM}$, $\tilde{G}_{zx}^{EM}$, and $\tilde{G}_{zy}^{EM}$ are the same as the corresponding components in the previous section which are not repeated here.

Extraction of the terms relevant to $\tilde{G}_{xy}^{EM}$ and $\tilde{G}_{yx}^{Em}$: They are composed of two Sommerfeld integrals. One is $S_0\left[V_v^e - V_v^h\right]$, which has just been examined; the other is $S_0\left[V_v^e\right]$, whose spectral kernel $\tilde{U}_f = V_v^e$ is dual to $\tilde{U}_d$ in the previous section. Therefore, the large argument approximation of $\tilde{U}_f$ is found to be

$$\tilde{U}_{f,\infty}(m,z\,|\,n,z';k_\rho) = S_{f,mn}\,e^{-jk_\rho h_z^f} \tag{4.112}$$

where

$$S_{f,mn} = \begin{cases} \dfrac{1}{2}\mathrm{Sign}(z-z'), & \text{for } m=n,\ z_n > z' > z_{n+1} \\ \dfrac{1}{2}\left[\mathrm{Sign}(z-z') + \vec{\Gamma}_{n,\infty}^h\right], & \text{for } m=n \text{ or } n-1,\ z'=z_n \\ \dfrac{1}{2}\left[\mathrm{Sign}(z-z') - \overleftarrow{\Gamma}_{n,\infty}^h\right], & \text{for } m=n \text{ or } n+1,\ z'=z_{n+1} \\ 0, & \text{Others} \end{cases}. \tag{4.113}$$

and h_z^f is the same as h_z^b in (4.101).

The singular term of U_f is

$$U_{f,\infty}(m,z\,|\,n,z';k_\rho) = S_{f,mn}\frac{h_z^f}{2\pi\sqrt{\left[(h_z^f)^2+\rho^2\right]^3}}. \qquad (4.114)$$

Up to now the Sommerfeld integrals for those Green's functions can be efficiently evaluated by first extracting the large argument approximations and then applying the deformed real-axis integration approach combined with the weighted-averages method. Numerical examples are presented in the following section.

4.5.4 Numerical Examples

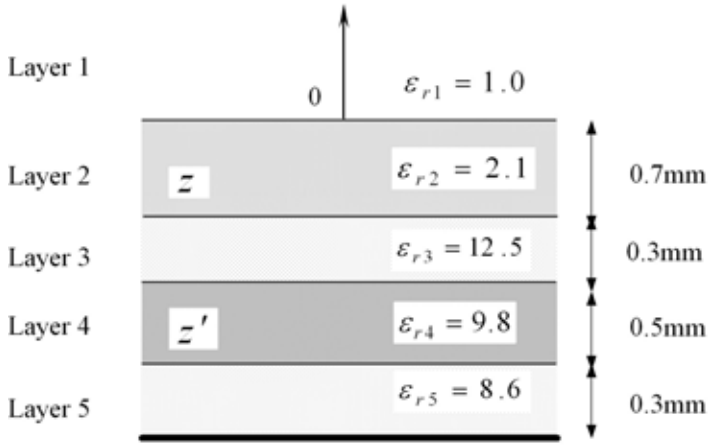

Fig. 4.7 Schematic diagram of a PEC (Perfect Electric Conductor) backed five-layer structure.

A PEC backed five-layer structure [102] (Fig. 4.7) is used as an example to demonstrate and verify the numerical integration approach. Two cases are considered: 1) the observation point is in the second layer with $z = -0.4$ mm and the source point in the fourth layer with $z' = -1.4$ mm ; 2) both the observation and the source points are located in the fourth layer with $z = z' = -1.4$ mm

The numerical integration results of Green's functions due to general electric and magnetic sources in both cases are shown in Fig. 4.8 and Fig. 4.9, respectively. The results of

$\overline{\mathrm{G}}^{\mathrm{A}}$ in both cases agree well with those reported in [102].

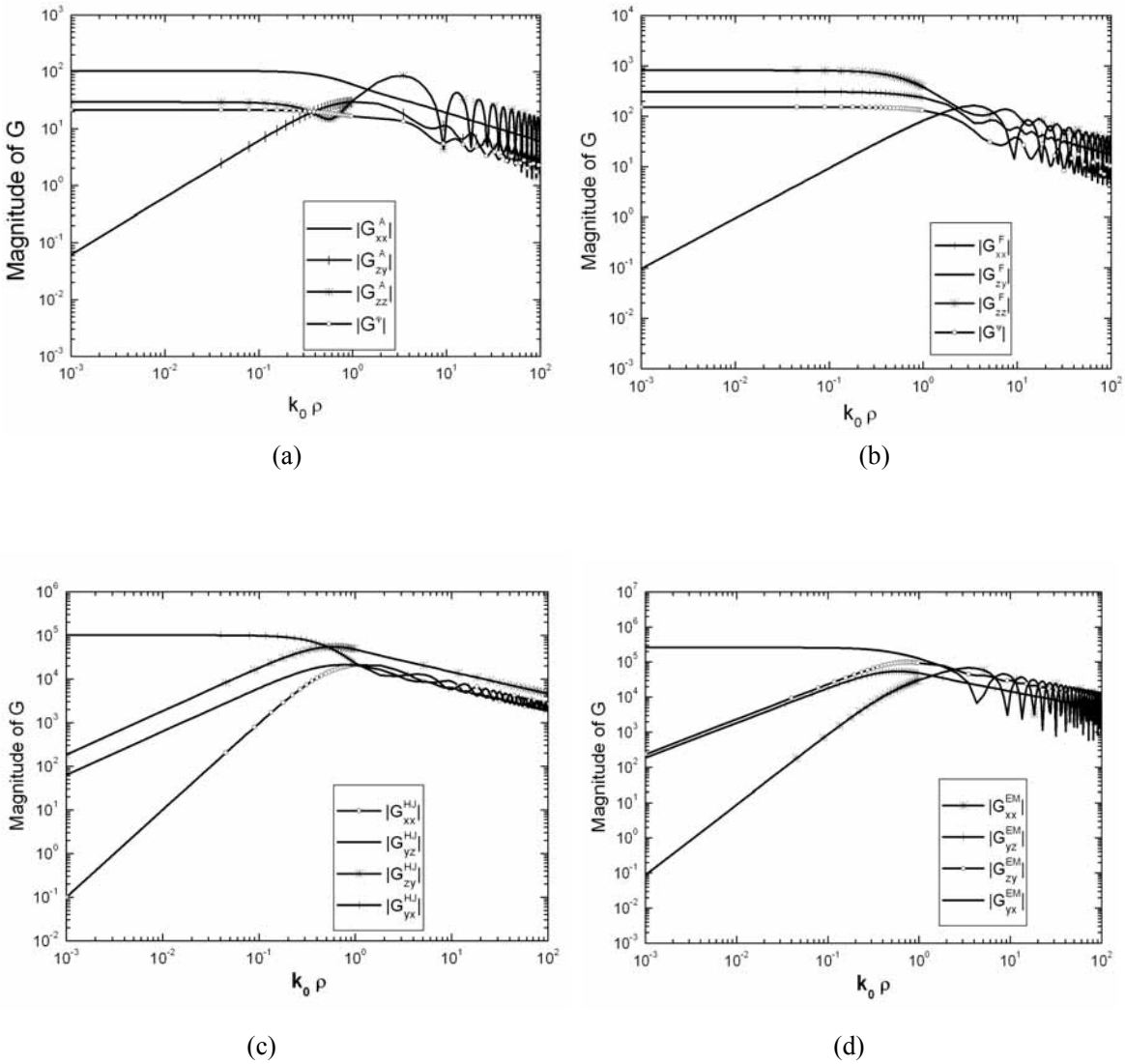

Fig. 4.8 Numerical integration results---Magnitude of Green's functions for the PEC backed five-layer media with $z=-0.4$ mm, $z'=-1.4$ mm and $f=30$ GHz: (a) $G_{xx}^{A}, G_{zy}^{A}, G_{zz}^{A}$ normalized by μ_0 and G^{Φ} normalized by $1/\varepsilon_0$; (b) $G_{xx}^{F}, G_{zy}^{F}, G_{zz}^{F}$ normalized by ε_0 and G^{Ψ} normalized by $1/\mu_0$; (c) G_{xx}^{HJ}, G_{yz}^{HJ}, G_{zy}^{HJ}, and G_{yx}^{HJ}; (d) G_{xx}^{EM}, G_{yz}^{EM}, G_{zy}^{EM}, and G_{yx}^{EM}.

Although the evaluation of the Green's functions is accelerated by the techniques presented in the previous section, it may still consume much computation time in the MPIE-MoM solution. A look-up table, which is pre-computed and stored, can be used for

MoM matrix filling by an interpolation method. One [92], two [38], and even three-dimensional interpolation with respect to ρ, z, and z' [103] may be needed depending on whether the PEC is strictly planar, confined to a single layer or multiple layers [33]. In addition to the interpolation technique, another attractive approach to tackle this problem is called the discrete complex image method (DCIM), which will be discussed in the following section.

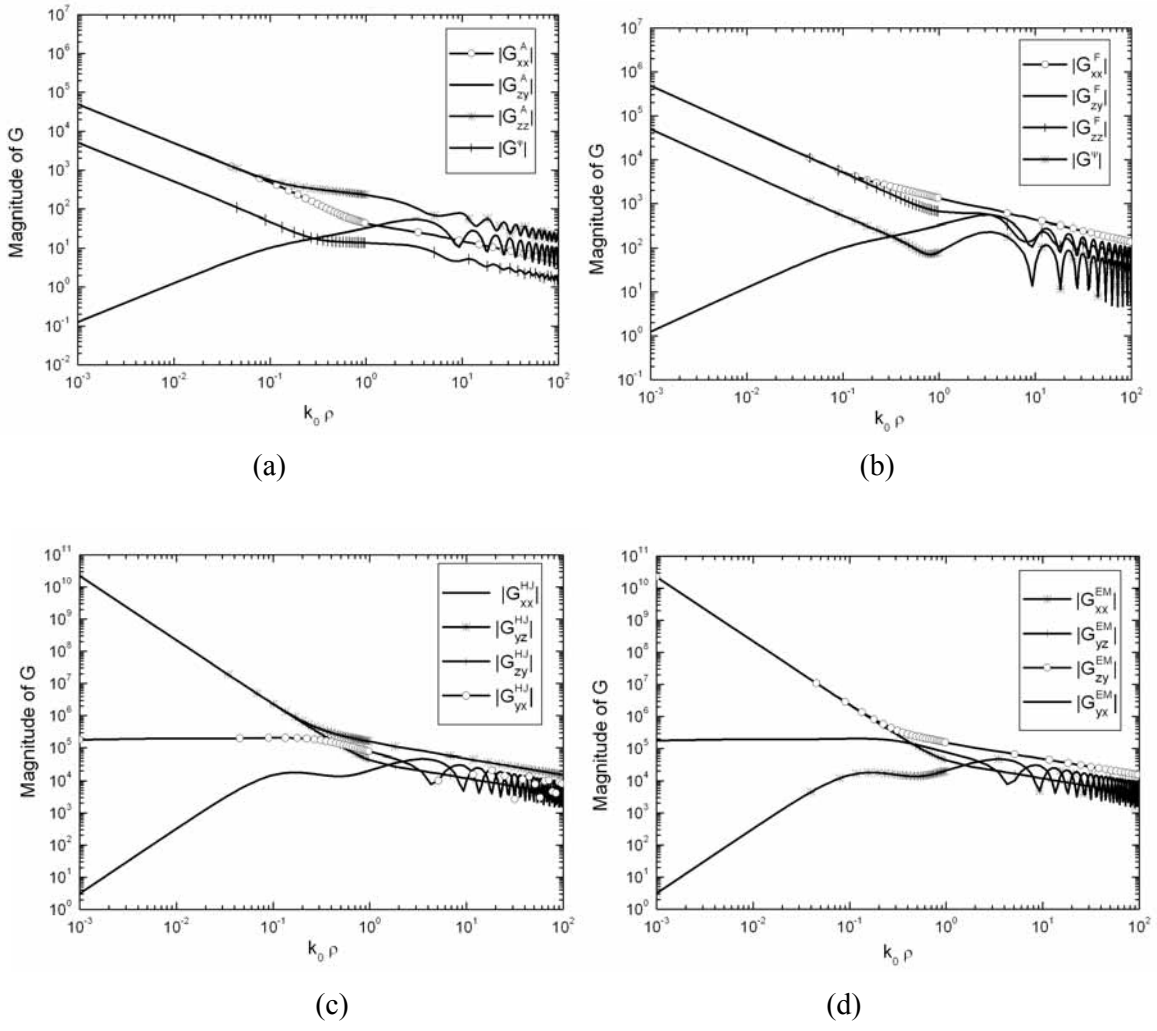

Fig. 4.9 Numerical integration results---Magnitude of Green's functions for the PEC backed five-layer media with $z = z' = -1.4$ mm and $f = 30$ GHz : (a) $G^A_{xx}, G^A_{zy}, G^A_{zz}$ normalized by μ_0 and G^{Φ} normalized by $1/\varepsilon_0$; (b) $G^F_{xx}, G^F_{zy}, G^F_{zz}$ normalized by ε_0 and G^{Ψ} normalized by $1/\mu_0$; (c) G^{HJ}_{xx} , G^{HJ}_{yz} , G^{HJ}_{zy} , and G^{HJ}_{yx} ;(d) G^{EM}_{xx} , G^{EM}_{yz} , G^{EM}_{zy} , and G^{EM}_{yx} .

4.6 DCIM Method for Closed-form Green's Functions

4.6.1 Overview of DCIM

The discrete complex image method (DCIM) was first proposed by Fang in [104]. The purpose of developing the DCIM method is to find closed-form spatial-domain Green's functions and to obviate the time-consuming process of evaluation of Sommerfeld integrals by numerical integration. Chew *et al.* proposed a standard procedure to implement the DCIM method for the thick microstrip substrate [105]. First, the quasi-static and the surface-wave terms are extracted from the spectral-domain Green's function kernels. Then the remaining part of the kernels is approximated by a sum of complex exponentials using Prony's method. Subsequently the Sommerfeld identity (B.8) is used to convert the improper Sommerfeld integrals into closed-form expression. The DCIM method can greatly expedite the MoM matrix filling process.

Another contribution to the advancement of the DCIM method was made by Aksun who proposed a two-level DCIM method in [106]. The advantage of the two-level approach is that it does not require extraction of surface wave poles, which are often difficult to find especially for general multilayered structures. The two-level approach is employed in this chapter for the evaluation of Green's functions.

4.6.2 Two-level DCIM Method

The two-level DCIM method proposed by Aksun in [106] is discussed in this section for the efficient evaluation of the Green's functions due to general electric and magnetic sources.

Sampling Path Used in Two-Level DCIM: The GPOF method [107] requires uniform

sampling along a real variable of a complex function. Although the Sommerfeld integral is a function of k_ρ, the exponential in the Sommerfeld identity (B.8) contains k_{zn}. Therefore, sampling should be made on k_{zn} instead of k_ρ. The sampling path for the Sommerfeld integration using two-level DCIM method [105, 106] is shown in Fig. 4.10, where both the deformed path in the k_ρ plane and its equivalent path in the k_{zn} plane are illustrated.

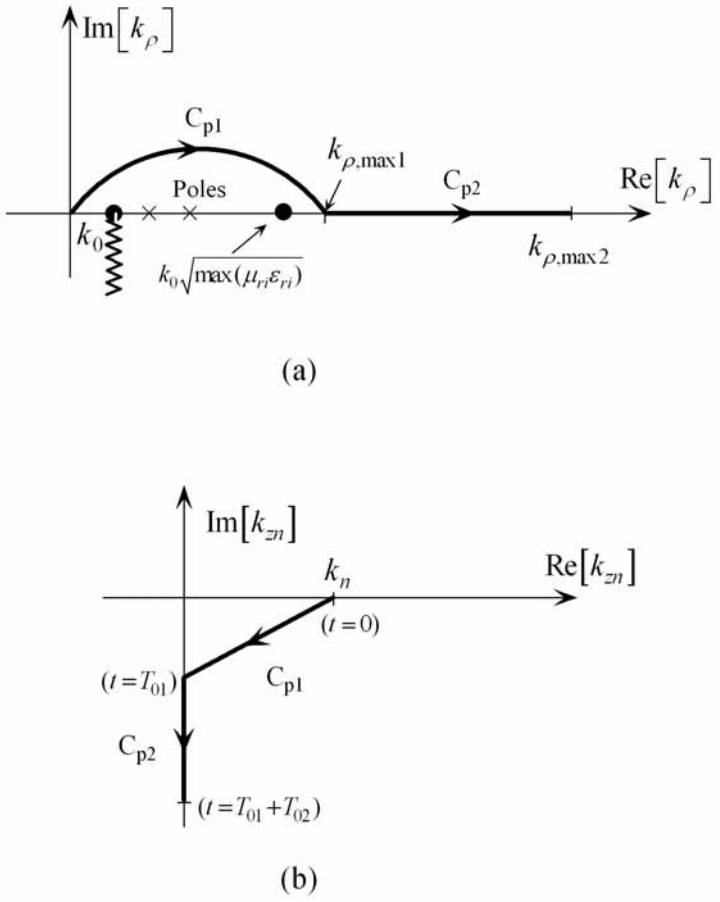

Fig. 4.10 Sampling path used in the two-level DCIM method: (a) the sampling path in the complex k_ρ plane; (b) the corresponding sampling path in the complex k_{zn} plane.

The sampling path C_{p1} and C_{p2} in the k_{zn} plane can be represented by the following parametric equations:

Path I (C_{p1}):

$$k_{zn} = k_n \left[-jt + \left(1 - \frac{t}{T_{01}} \right) \right], \qquad t \in [0, T_{01}], \tag{4.115}$$

Path II (C_{p2}):

$$k_{zn} = -jk_n [T_{01} + t], \qquad t \in [0, T_{02}], \tag{4.116}$$

where t is the running variable sampled uniformly along the corresponding paths.

Determining the Sampling Interval: The first step of the two-level DCIM is to determine T_{01} and T_{02}. The choice of T_{01} must ensure that the branch points and poles are obviated from the sampling path, i.e., to satisfy that

$$k_{\rho,\max 1} = k_n \sqrt{1 + T_{01}^2} > \max(k_n) \;\Rightarrow\; T_{01} > \sqrt{\left[\frac{\max\limits_i (k_i)}{k_n} \right]^2 - 1}\,. \tag{4.117}$$

For non-magnetic material, T_{01} can be chosen as

$$T_{01} = \sqrt{\max(\varepsilon_{rn})} + 1. \tag{4.118}$$

The choice of T_{02} is to ensure that

$$k_{\rho,\max 2} = k_n \sqrt{1 + (T_{01} + T_{02})^2} \tag{4.119}$$

is large enough to account for the contributions from the integral tails. Aksun recommended a value of 200 for T_{02} and 200 for the number of samples [106].

Sampling and Approximating the Green's Functions: Once T_{01} , T_{02} and the number of samples are determined, the second step of the two-level DCIM is to uniformly sample the spectral-domain Green's function $\tilde{f}(k_\rho)$ along C_{p1} and C_{p2} and approximate it by the

GPOF method.

The Green's function is first sampled along C_{p2} and approximated by the GPOF method:

$$\begin{aligned}\tilde{f}^{(2)}(k_\rho) &= \frac{1}{2jk_{zn}}\sum_{i=1}^{m1} R_i^{(2)} e^{s_i^{(2)}t} \\ &= \frac{1}{2jk_{zn}}\sum_{i=1}^{m1} a_i^{(2)} e^{-jk_{zn}b_i^{(2)}}, \qquad k_\rho \in \left[k_{\rho,\max 1},\ k_{\rho,\max 2}\right]\end{aligned} \tag{4.120}$$

where

$$a_i^{(2)} = R_i^{(2)} e^{-s_i^{(2)}T_{01}}, \quad b_i^{(2)} = -\frac{s_i^{(2)}}{k_n}. \tag{4.121}$$

Subsequently, the original spectral-domain Green's function $\tilde{f}(k_\rho)$ is subtracted by $\tilde{f}^{(2)}(k_\rho)$ and approximated along C_{p1}:

$$\begin{aligned}\tilde{f}^{(1)}(k_\rho) = \tilde{f}(k_\rho) - \tilde{f}^{(2)}(k_\rho) &= \frac{1}{2jk_{zn}}\sum_{i=1}^{m2} R_i^{(1)} e^{s_i^{(1)}t} \\ &= \frac{1}{2jk_{zn}}\sum_{i=1}^{m2} a_i^{(1)} e^{-jk_{zn}b_i^{(1)}}, \qquad k_\rho \in \left[0,\ k_{\rho,\max 1}\right]\end{aligned} \tag{4.122}$$

where

$$a_i^{(1)} = R_i^{(1)} e^{s_i^{(1)}T_{01}/(1+jT_{01})}, \quad b_i^{(1)} = \frac{s_i^{(1)}T_{01}}{jk_n(1+jT_{01})}. \tag{4.123}$$

Finally, the closed-form Green's function is given by

$$
\begin{aligned}
f(\rho, z) &= \frac{1}{4\pi} \int_{SIP} \tilde{f}(k_\rho)\, H_0^{(2)}(k_\rho \rho) k_\rho dk_\rho \\
&= \frac{1}{4\pi} \int_{C_{ap2}+C_{ap1}} \left[\tilde{f}^{(2)}(k_\rho) + \tilde{f}^{(1)}(k_\rho) \right] H_0^{(2)}(k_\rho \rho) k_\rho dk_\rho \qquad (4.124) \\
&= \frac{1}{4\pi} \sum_{i=1}^{m2} a_i^{(2)} \frac{e^{-jk_n \sqrt{\rho^2 + \left[b_i^{(2)}\right]^2}}}{\sqrt{\rho^2 + \left[b_i^{(2)}\right]^2}} + \frac{1}{4\pi} \sum_{i=1}^{m1} a_i^{(1)} \frac{e^{-jk_n \sqrt{\rho^2 + \left[b_i^{(1)}\right]^2}}}{\sqrt{\rho^2 + \left[b_i^{(1)}\right]^2}}
\end{aligned}
$$

where it is assumed that only zero-th order Sommerfeld integral is associated with $f(k_\rho)$. If the first-order Sommerfeld integral is involved, the identity in (B.10) can be used to find the closed-formed Green's functions.

DCIM for Strictly Planar Problems: From (4.61) we know that the number of Sommerfeld integrals associated with the Green's functions due to general sources can be reduced to 11 integrals. The GPOF method can be directly applied to their integrands. However, since the spectral domain kernel of the Green's functions depends on three variables k_{zn}, z and z', such an approach requires that the three variables should be fixed before the GPOF method is applied. Obviously this approach is only suitable for strictly planar structures, where only a few number of GPOF operations are needed to handle different combinations of source-field locations (z and z').

DCIM for 3D Problems: If the object to be simulated has an arbitrary shape, the implementation of the DCIM will become quite cumbersome because of the dependency of the spectral domain kernels or equivalently the complex images on k_{zn}, z and z'.

Two situations need to be considered a three-dimensional problem. When the source and the field points are located in the same layer, the spectral domain kernels can always be expressed as [108]

$$\tilde{f}(k_\rho, z, z') = \frac{1}{2jk_{zn}} \sum_i \alpha(k_{zn}) \cdot e^{-jk_{zn}\beta_i(z,z')} \tag{4.125}$$

where $\alpha(k_{zn})$ is independent of z and z', and $\beta_i(z,z')$ represents a simple linear combination of z and z'. The DCIM method can be performed on $\alpha(k_{zn})$, and the resultant complex images are independent of z and z'. Therefore, performing the GPOF method about 5 times – depending on the actual terms in the summation of (4.125) – can lead to an efficient evaluation of the closed-form Green's functions.

Another situation occurs when the source and field points appear in different layers. Then k_{zn} for the source layer in this situation is usually different from k_{zm} for the field layer, which makes it impossible to completely extract the dependency of the spectral domain kernels on k_{zn}, k_{zm}, z and z'. The approach proposed in [109] can alleviate the difficulties encountered in applying the DCIM method to this situation, which is implemented by rewriting the spectral-domain Green's functions in the following form:

$$\tilde{f}(k_\rho, z, z') = \frac{1}{2jk_{zn}} \sum_i \alpha(k_{zm}, z) \cdot e^{-jk_{zn}\beta_i(z')} \tag{4.126}$$

where the dependency on z and z' is grouped with k_{zm}, and k_{zn}, respectively. Therefore, the discrete complex images are dependent on z or z' not both of them, which facilitates creating an interpolation table for Green's functions.

In this chapter if the source and field points are located in the same layer, the remedy for (4.125) is used. If the source and field points are located in different layers, the DCIM method is applied to the original spectral domain kernels in (4.61) and interpolation tables are employed in the MoM matrix filling process. Numerical results will be presented in the following section.

4.6.3 Numerical Results

In this section, two numerical examples are presented to validate the two-level DCIM code developed in this chapter. Some discussions on the DCIM method are also presented.

4.6.3.1 Grounded Three-Layer Structure

The grounded three-layer structure was used in [110] to examine the DCIM method for sources in bounded layers. The geometry of the multilayered structure is shown in Fig. 4.11, which consists of two dielectric layers and one half space.

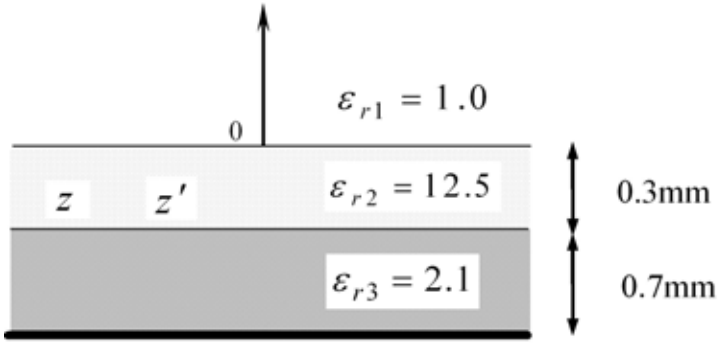

Fig. 4.11 Schematic diagram of a grounded three-layer structure.

In [110] the author claimed that the original DCIM method proposed in [104, 105] failed to obtain accurate results of the Green's function for scalar potentials due to sources in bounded regions because of the artificial branch points introduced by the original DCIM method.

Instead of using the remedy proposed in [110] (referred to as Kipp's modified DCIM method) to correct this problem, accurate results can be produced by using the two-level DCIM method with enough samples for small k_ρ. Similar conclusion is drawn in [111]. Accurate results of G^Φ for the three-layer structure with source and field points located in the second layer are shown in Fig. 4.12. It is to be noted that only the results of G^Φ in the

range of $-2 \le \log_{10}(k_\rho \rho) \le 1$ were given in [110].

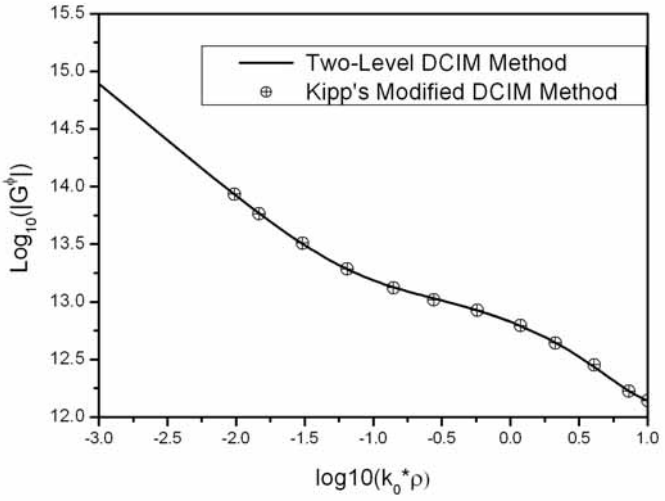

Fig. 4.12 Comparison of the magnitude of Green's function G^{Φ} obtained by different DCIM methods for the grounded three-layer structure.

The results of the Green's functions obtained by the two-level DCIM method are also compared with those by the numerical integration method (cf. Section 4.5), which are shown in Fig. 4.13. Good agreements can be observed. The parameters used in the DCIM method are as follows:

$$\begin{aligned} &f = 30 \text{ GHz}, z = z' = -0.3 \text{ mm}; \\ &T_{01} = 5,\ N_{s1} = 300;\quad T_{02} = 100,\ N_{s2} = 50. \end{aligned} \tag{4.127}$$

where N_{s1} and N_{s2} is the number of samples along C_{p1} and C_{p2}. The CPU time used for computing all the Greens functions by the DCIM method is about 90 seconds, which is only about one-tenth of the time consumed by the numerical integration method. So the two-level DCIM method is accurate and efficient for evaluation of the Green's functions.

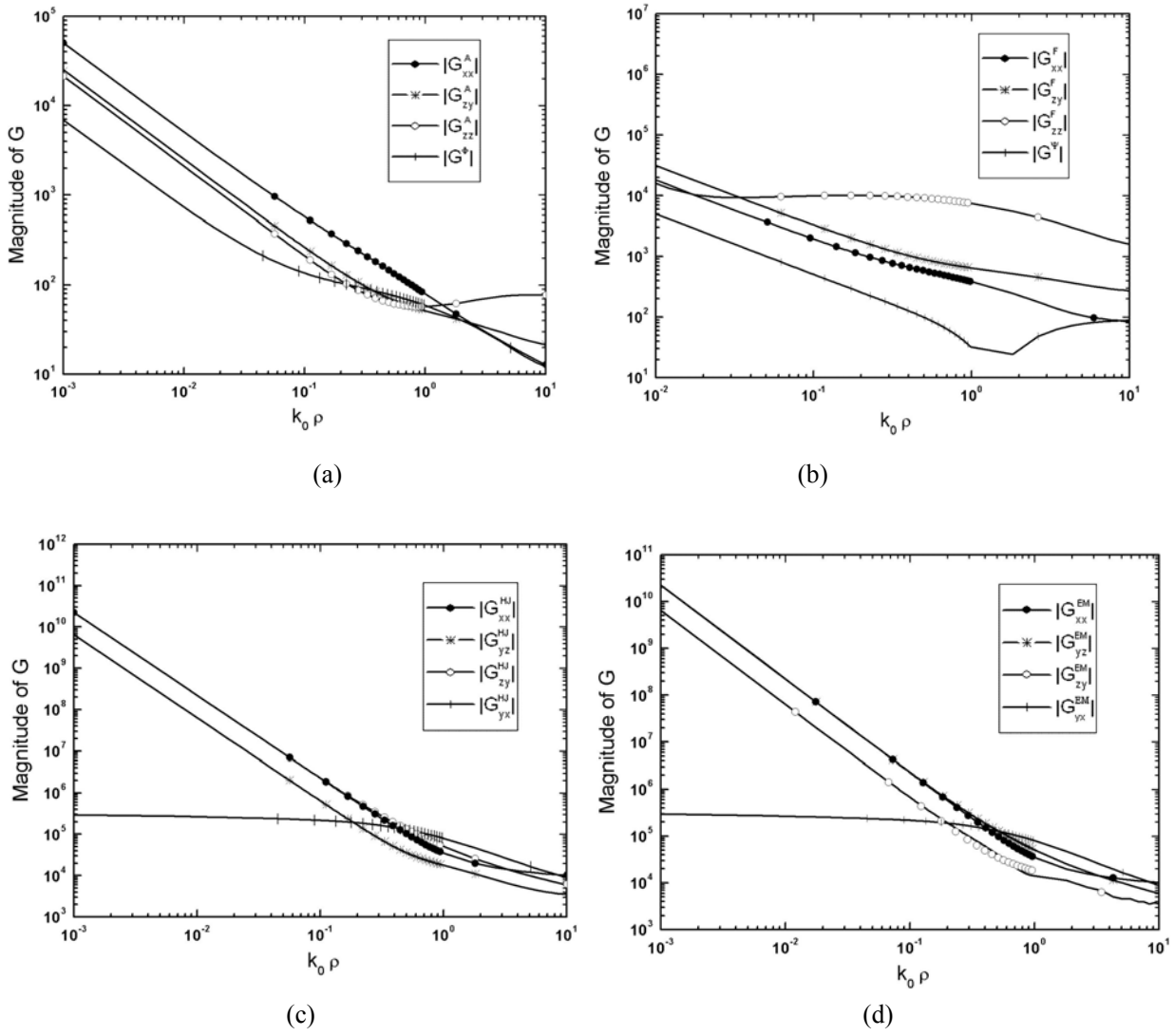

Fig. 4.13 Magnitude of Green's functions for the grounded three-layer structure with $z = z' = -0.3$ mm and $f = 30$ GHz : (a) $G^A_{xx}, G^A_{zy}, G^A_{zz}$ normalized by μ_0 and G^Φ normalized by $1/\varepsilon_0$; (b) $G^F_{xx}, G^F_{zy}, G^F_{zz}$ normalized by ε_0 and G^Ψ normalized by $1/\mu_0$; (c) G^{HJ}_{xx} , G^{HJ}_{yz} , G^{HJ}_{zy} , and G^{HJ}_{yx} ; (d) G^{EM}_{xx} , G^{EM}_{yz} , G^{EM}_{zy} , and G^{EM}_{yx} . Solid lines represent the results obtained by Numerical integration method; Symbols denote the results produced by the DCIM method.

4.6.3.2 PEC backed Five-Layer Media

A PEC backed five-layer structure used in Section 4.5.4 is studied here by the DCIM method. The source and field points are located at $z = -0.4$ mm and $z' = -1.4$ mm , respectively.

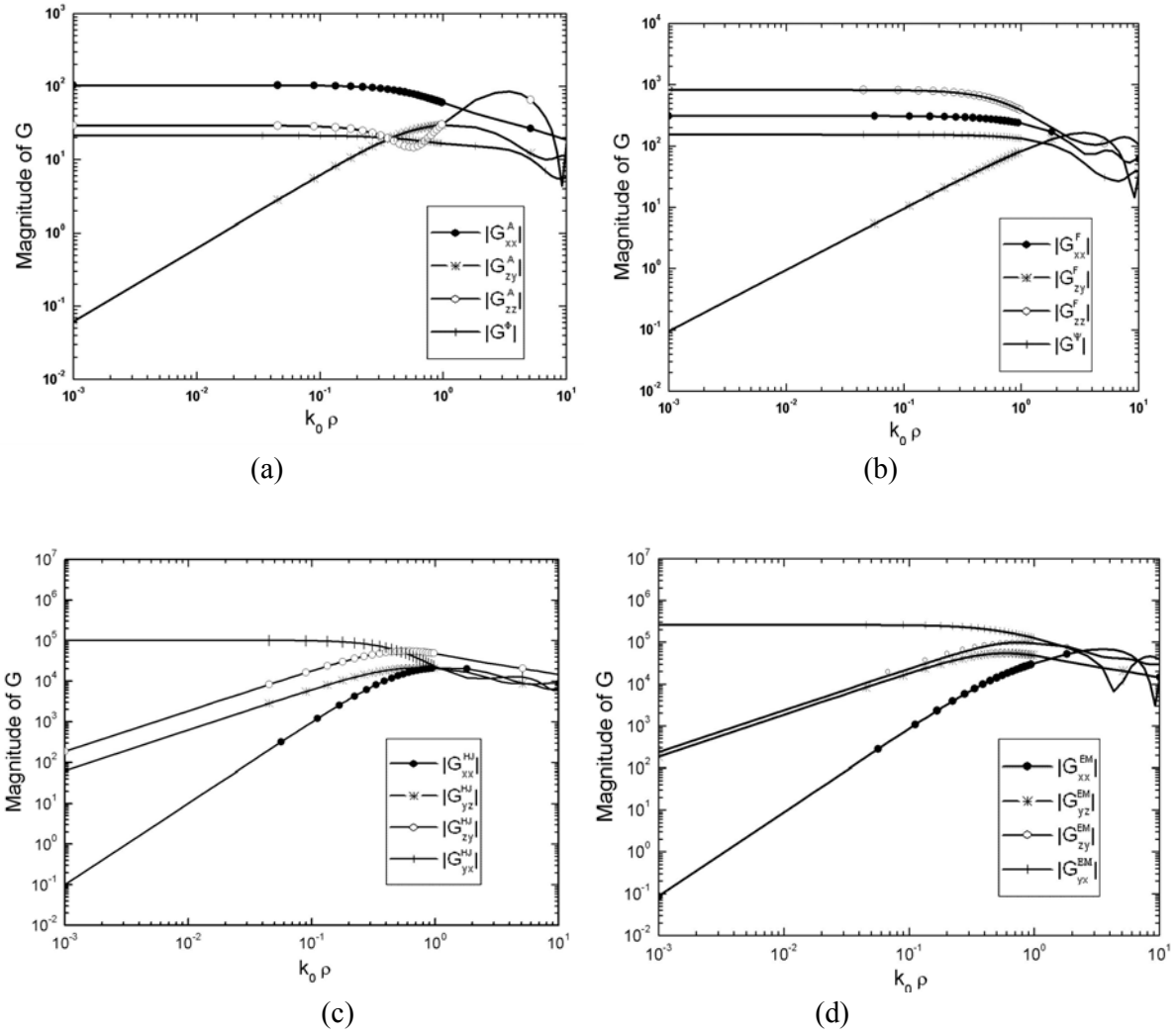

Fig. 4.14 Magnitude of Green's functions for the PEC backed five-layer structure with $z = -0.4$ mm, $z' = -1.4$ mm, and $f = 30$ GHz: (a) $G_{xx}^{A}, G_{zy}^{A}, G_{zz}^{A}$ normalized by μ_0 and G^{Φ} normalized by $1/\varepsilon_0$; (b) G_{xx}^{F}, G_{zy}^{F}, G_{zz}^{F} normalized by ε_0 and G^{Ψ} normalized by $1/\mu_0$; (c) G_{xx}^{HJ}, G_{yz}^{HJ}, G_{zy}^{HJ}, and G_{yx}^{HJ}; (d) G_{xx}^{EM}, G_{yz}^{EM}, G_{zy}^{EM}, and G_{yx}^{EM}. Solid lines --- Numerical integration method; Symbols --- DCIM method.

The Green's functions due to general sources evaluated by the two-level DCIM method are compared with those in Section 4.5.4 by the numerical integration method, where good agreements can be observed Fig. 4.14). The parameters used for the DCIM method are as follows:

$$T_{01} = 6,\ N_{s1} = 300;\quad T_{02} = 100,\ N_{s2} = 50. \tag{4.128}$$

It can be concluded again that the two-level DCIM method is accurate and efficient for evaluation of the Green's functions.

As shown in Fig. 4.15, some results of the Green's functions, e.g., G_{xx}^{EM} are not accurate for very small $k_0\rho$, if not enough samples are used in the DCIM method. However, the results can be greatly improved by using more samples along C_{p1} (300 samples for this example) or extending the sampling interval along C_{p2}.

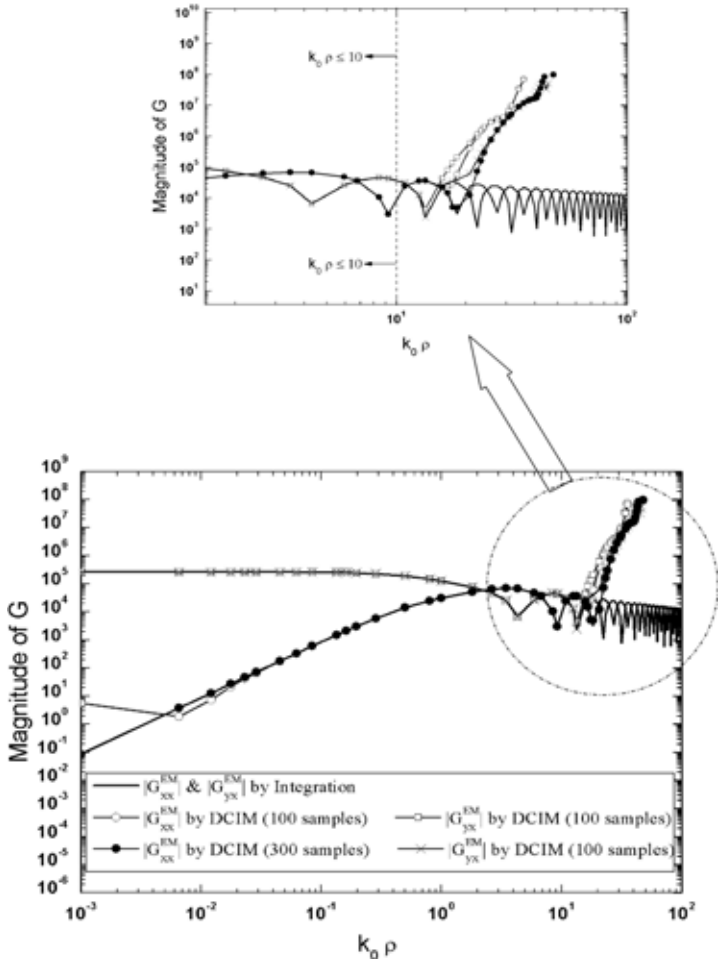

Fig. 4.15 Magnitude of Green's functions G_{xx}^{EM} and G_{yx}^{EM} for the PEC backed five-layer structure with $z = -0.4$ mm, $z' = -1.4$ mm and $f = 30$ GHz. The enlarged area in the dashed circle is to show the disadvantage of the two-level DCIM method without pole extraction.

In addition, the two-level DCIM method without extraction of surface wave poles has one disadvantage, i.e., the method failed to yield accurate results for Green's functions in the far-field region, which can be seen from Fig. 4.15 that the DCIM results may blow up if $k_\rho \rho$ is beyond about 10. The large deviation in the results obtained by the DCIM and numerical integration methods is mainly due to the fact that the surface wave pole contributions will dominate the results in the far-field region.

Remember that the foundation of the DCIM method is the Sommerfeld identity (B.8), whose physical interpretation [91] is that a spherical wave can be expanded as an integral summation of cylindrical waves in the ρ direction, times a plane wave in the z direction over the wave number k_ρ. In the far-field region the spherical waves originating from the complex distances fail to represent the surface waves, which are cylindrical waves. Moreover, the surface wave pole contributions have $1/\sqrt{\rho}$ asymptotic behavior, which is similar to the large argument approximation of the Hankel function. Other disadvantages of the DCIM method [33] include that the DCIM method has no robust built-in convergence criteria and its accuracy may need to be checked against the results obtained by the numerical integration method. Furthermore, the application of this method in multilayered media is still impeded by lack of reliable automated procedures for extraction of the guided wave poles.

Despite of the disadvantages listed above, the two-level DCIM method is efficient for the evaluation of Green's functions for planar multilayered media. The DCIM method without surface-wave pole extractions is still valid for Green's functions in the near-field region, which is usually sufficient for many practical problems.

4.7 Summary

In this chapter we studied the evaluation of Green's functions for planar multilayered media due to general electric and magnetic sources. The formulation-C Green's functions proposed by Michalski are first reviewed and then extended to account for general sources.

Both the numerical integration and DCIM methods are discussed for the efficient evaluation of the Sommerfeld integrals associated with the spatial domain Green's functions. For the first method we perform the large argument approximations of the spectral-domain Green's functions to speed up the numerical evaluation. For the second method we implement a two-level DCIM method without surface-wave pole extractions. Compared to the numerical integration method, the DCIM method is more efficient.

Chapter 5. Numerical Solution of MPIE for Multilayer problems

In the previous chapter the spatial-domain Green's functions for multilayered media have been studied and the mixed-potential integral equation (MPIE) has been obtained. Imposed by appropriate boundary conditions, the integral equation can be solved by the method of moments (MoM). The MPIE-MoM will be discussed in this chapter to lay a foundation for the hybrid method developed in chapter 6.

5.1 Introduction

In this section we will briefly review the procedures of the method of moments (MoM). Consider the following inhomogeneous linear equation:

$$\mathcal{L}(f) = g \tag{5.1}$$

where $\mathcal{L}$ is a linear operator, g is known, and f is to be determined. Approximate solutions to (5.1) can be found by performing the following two-step MoM procedures [112].

The first step of the MoM concerns the unknown f, which is expanded in a series functions:

$$f = \sum_n \alpha_n f_n \tag{5.2}$$

where the coefficients α_n are constants. f_n are called basis functions or expansion functions, which actually form a linear space of the problem. In practice n is a finite number, i.e., the series in (5.2) must be truncated to find an approximate solution to (5.1).

The second step of the MoM is relevant to the observation. Substituting (5.2) into (5.1) and taking the inner product of it with a set of weighting functions or testing functions, $w_1, w_2, \cdots, w_N$ in the range of $\mathcal{L}$, we obtain

$$\sum_{n=1}^{N} a_{mn}\alpha_n = b_n, \qquad m = 1, 2 \cdots N \tag{5.3}$$

where

$$a_{mn} = \langle w_m, \mathcal{L} f_n \rangle, \text{ and } b_n = \langle w_m, g_n \rangle. \tag{5.4}$$

The final matrix form of (5.3) is given by

$$Ax = b. \tag{5.5}$$

The matrix and vectors in (5.5) are defined as

$$A = \left[a_{mn} \right], \quad x = \{\alpha_1 \ \ \alpha_2 \cdots \alpha_N\}^T, \text{ and } b = \{b_1 \ \ b_2 \cdots b_N\}^T \tag{5.6}$$

where T denotes the transpose operation. For electromagnetic problems a_{mn} represents the effect of cell n on cell m, where n is related to the source point and m the observation point.

If m is equal to n, then it stands for a self term.

Some errors may affect the accuracy of the MoM solution [30], such as the modeling error introduced by replacing the actual geometry by perfect electric conductors (PEC's), the truncation errors caused by expansion and weighting functions, and numerical errors in the form of round-off errors in the solution of the MoM matrix equation. A good MoM solution can only be yielded by taking into fair consideration of the above-mentioned factors. In the following sections we will examine some detailed problems related to the implementation of the MoM.

5.2 Implementation of Method of Moments

5.2.1 Basis Functions and Testing Functions

The governing equation for the multilayer problem in the presence of PEC's can be expressed by the following mixed-potential integral equation (MPIE):

$$\hat{n}\times\left[-j\omega\left\langle\overline{\mathbf{G}}^{A}\left(\mathbf{r},\mathbf{r}'\right);\mathbf{J}\left(\mathbf{r}'\right)\right\rangle+\frac{1}{j\omega}\nabla\left\langle G^{\Phi}\left(\mathbf{r},\mathbf{r}'\right);\nabla'\cdot\mathbf{J}\left(\mathbf{r}'\right)\right\rangle\right]=-\hat{n}\times\mathbf{E}^{ext}\left(\mathbf{r}\right) \quad (5.7)$$

where $\hat{n}$ is the unit vector normal to the conducting surfaces; and $\mathbf{E}^{ext}$ is the excitation imposed on the problem.

As mentioned above, the first step to solve the integral equation in (5.7) is to expand the unknown surface current $\mathbf{J}\left(\mathbf{r}'\right)$ by basis functions. In general, there are two categories of basis functions [92, 113]: One is the entire domain basis function and the other is the sub-domain basis function. The advantages of the entire domain basis functions include that they exhibit good convergence property and no meshing of the geometry is needed. However, the

sub-domain basis functions are more flexible in geometry modeling. The sub-domain basis functions can take the form of Dirac delta, pulses and piecewise linear functions.

In this chapter both the RWG [114] and rooftop basis functions [75]. But for brevity, we only use the rooftop basis functions to illustrate the MoM procedures.

The rooftop basis function is the product of a triangular function and a pulse function in two orthogonal directions. Each rooftop basis function is defined over the x- or y-directed current cell. And each current cell comprises two adjacent charge cells sharing a common border perpendicular to either the x-direction or y-direction (see Fig. 5.1). An overlapping of current cells is obtained in such a manner that a charge cells may belong to four different current cells.

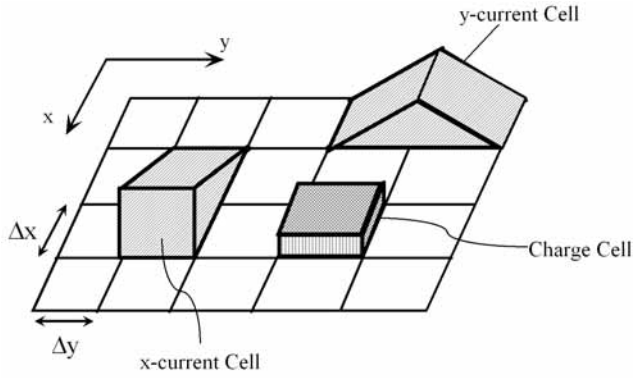

(a)

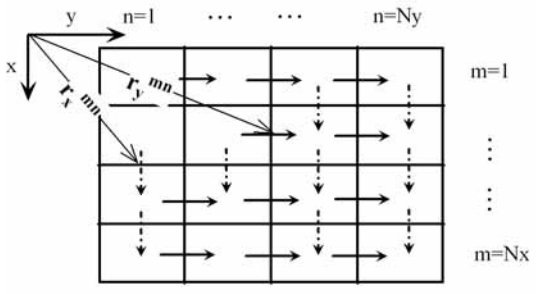

(b)

Fig. 5.1 Roof-top basis functions defined over rectangular patches: (a) Current cells and associated charge cells; (b) Distribution of x-directed and y-directed current cells and their center coordinates.

Assuming that the PEC surface is divided into $N_x \times N_y$ charge cells (see Fig. 5.1b), we can

expand its surface currents in the Cartesian coordinate system as

$$J_x(\mathbf{r}) = \sum_{m=1}^{N_x-1} \sum_{n=1}^{N_y} I_x^{mn} T_x(\mathbf{r} - \mathbf{r}_x^{mn}) \tag{5.8}$$

$$J_y(\mathbf{r}) = \sum_{m=1}^{N_x} \sum_{n=1}^{N_y-1} I_y^{mn} T_y(\mathbf{r} - \mathbf{r}_y^{mn}) \tag{5.9}$$

where $T_x(\mathbf{r})$ and $T_y(\mathbf{r})$ are the rooftop basis functions (Fig. 5.2). They are defined as

$$T_x(\mathbf{r}) = \begin{cases} \dfrac{1-|x|/\Delta x}{\Delta y}, & |\mathrm{x}| < \Delta x \text{ and } |\mathrm{y}| < \Delta y/2 \\ 0, & \text{elsewhere} \end{cases} \tag{5.10}$$

$$T_y(\mathbf{r}) = \begin{cases} \dfrac{1-|y|/\Delta y}{\Delta x}, & |\mathrm{y}| < \Delta y \text{ and } |\mathrm{x}| < \Delta x/2 \\ 0, & \text{elsewhere} \end{cases} \tag{5.11}$$

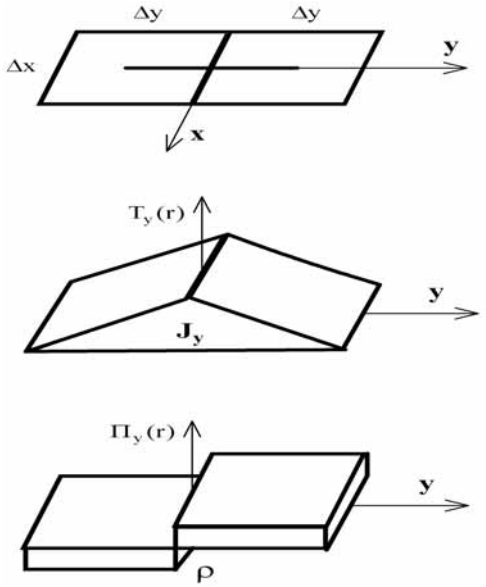

Fig. 5.2 Y-directed current cell, rooftop basis function and associated charge doublets.

and

$$\mathbf{r}_x^{mn} = m\Delta x\hat{x} + (n+\frac{1}{2})\Delta y\hat{y} \tag{5.12}$$

$$\mathbf{r}_y^{mn} = (m+\frac{1}{2})\Delta x\hat{x} + n\Delta y\hat{y}\,. \tag{5.13}$$

Because of the normalization made in (5.10) and (5.11), the unknown expansion coefficients I_x^{mn} and I_y^{mn} have the dimensions of current. Every coefficient represents the total current flowing across the common boundary of two corresponding charge cells [92].

The associated electric surface charge density is obtained from (5.8) and (5.9) by using the charge continuity equation. Specifically, it can be written as

$$\Pi(\mathbf{r}) = -\nabla\cdot\mathbf{T}(\mathbf{r}) \tag{5.14}$$

where $\Pi(\mathbf{r})$ represents a two-dimensional unit pulse function defined over a rectangular patch shown in Fig. 5.2. Finally the charge density can be expressed as

$$\rho_e(\mathbf{r}) = \frac{1}{j\omega}\left[\sum_{m=1}^{N_x-1}\sum_{n=1}^{N_y} I_x^{mn}\Pi_x(\mathbf{r}-\mathbf{r}_x^{mn}) + \sum_{m=1}^{N_x}\sum_{n=1}^{N_y-1} I_y^{mn}\Pi_y(\mathbf{r}-\mathbf{r}_y^{mn})\right] \tag{5.15}$$

where $\Pi(\mathbf{r})$ takes the following form:

$$\Pi_x(\mathbf{r}) = \begin{cases} \dfrac{-1}{\Delta x\Delta y}, & -\Delta x < \mathrm{x} < 0 \text{ and } |\mathrm{y}| < \Delta y/2 \\ \dfrac{1}{\Delta x\Delta y}, & 0 < \mathrm{x} < \Delta x \text{ and } |\mathrm{y}| < \Delta y/2 \\ 0, & \text{elsewhere} \end{cases}, \tag{5.16}$$

$$\Pi_y(\mathbf{r}) = \begin{cases} \dfrac{-1}{\Delta x\Delta y}, & -\Delta y < y < 0 \text{ and } |\mathrm{x}| < \Delta x/2 \\ \dfrac{1}{\Delta x\Delta y}, & 0 < y < \Delta y \text{ and } |\mathrm{x}| < \Delta x/2 \\ 0, & \text{elsewhere} \end{cases}. \tag{5.17}$$

The charge density within every elementary cell remains constant. For the charge cell formed by four overlapping current cells in Fig. 5.1, the electric surface charge density is given by

$$\rho_e(\mathbf{r}) = \frac{1}{j\omega}\left(I_x^{m+1,n} - I_x^{m,n} + I_y^{m,n+1} - I_y^{m,n} \right). \tag{5.18}$$

The electric charge density is discontinuous on the borders between charge cells. However, the scalar potential remains bounded, whereas the electric field becomes singular. Therefore, test function must be selected carefully, avoiding the locations where the electric field is singular [92].

The next step of the MoM is to select suitable testing functions. There are many choices for the testing functions to be used in the MoM, such as the Dirac's delta function, pulse functions and rooftop functions. In this chapter the Galerkin's technique is used for the MoM, i.e., the testing functions are the same as the basis functions in (5.10) and (5.11).

5.2.2 Formulation of MoM Matrix Equation

In order to derive a general formulation for MoM matrix equations using rooftop basis functions and Galerkin's technique, a vector rooftop basis function over two adjacent charge cells is defined and represented by $\mathbf{T}_k$. Then the current and charge density can be expanded as

$$\mathbf{J} = \sum_{k=1}^{N} \alpha_k \mathbf{T}_k \tag{5.19}$$

$$j\omega q = \sum_{k=1}^{N} \alpha_k \Pi_k \tag{5.20}$$

where α_i are unknown coefficients. Π_k is related to $\mathbf{T}_k$ via the continuity equation expressed in (5.14). Substituting (5.19) and (5.20) into (5.7), we can obtain the following MoM matrix equation [92]:

$$\mathbf{Z}\boldsymbol{\alpha} = \mathbf{b} \tag{5.21}$$

where $\boldsymbol{\alpha}$ is the unknown vector and $\boldsymbol{\alpha} = \{\alpha_1, \alpha_1, \cdots \alpha_N\}^T$. The elements of the matrix $\mathbf{Z}$ is

$$z_{ij} = a_{ij} + v_{ij} \tag{5.22}$$

where the contributions from vector and scalar potentials are given by

$$a_{ij} = j\omega \int_{S_i} \mathbf{T}_i(\mathbf{r}) \cdot \int_{S_j} \bar{\mathbf{G}}^A(\mathbf{r}, \mathbf{r}') \cdot \mathbf{T}_j(\mathbf{r}') dS' dS \,, \tag{5.23}$$

$$v_{ij} = j\omega \int_{S_i} \Pi_i(\mathbf{r}) \int_{S_j} G^{\Phi}(\mathbf{r}, \mathbf{r}') \Pi_j(\mathbf{r}') dS' dS \,. \tag{5.24}$$

The element b_i in the right-hand side of (5.21) takes the form of

$$b_i = \int_{S_i} \mathbf{T}_i(\mathbf{r}) \cdot \mathbf{E}^{ext} dS \,. \tag{5.25}$$

It is to be noted that two derivatives appear in the scalar potential term v_{ij} in (5.24). One derivative is passed to the basis functions to produce two offset rectangular charge cells for each rooftop basis function. The other derivative is passed to the testing function. Specifically, derivation of (5.24) has applied the continuity equation (5.14), the edge condition for surface currents, and the following vector identity and Gauss's Theorem [99]:

$$\mathbf{A} \cdot \nabla\Phi = \nabla \cdot (\Phi \mathbf{A}) - \Phi \nabla \cdot \mathbf{A} \tag{5.26}$$

$$\int_S \nabla \cdot \mathbf{A} \, ds = \oint_{l_s} \mathbf{A} \cdot \hat{n} \, dl \,, \tag{5.27}$$

where l_s denotes the line enclosing the surface S; and $\hat{n}$ is the unit normal vector. In particular, if $\mathbf{A}$ has no components perpendicular to the surface boundary, then the integral in (5.27) will be zero.

5.2.3 Excitation and Parameter Extraction

Excitation or equivalently the right-hand side of (5.21) results in the response of an electromagnetic system. And parameter extraction belongs to the post-processing stage of the MoM resolution.

5.2.3.1 Excitation

Excitation is different for different problems. In general, the excitation sources can be classified into two families: plane wave sources and discrete sources.

Plane Wave Sources: Plane wave incident is essentially a distributed source and often used in formulating scattering problems. For multilayer problem the incident field $\mathbf{E}^{ext}$ in (5.7) should be the electric field in the multilayered media in the absence of PEC's. Consider an incident plane wave in layer 1 of a multilayered media:

$$\mathbf{E}^{inc}(\mathbf{r}) = (E_\theta\ \hat{\theta}_1 + E_\phi\ \hat{\phi}_1)e^{j\mathbf{k}_1\cdot\mathbf{r}} \tag{5.28}$$

where the propagation vector $\mathbf{k}_1$ in the Cartesian coordinate system is given by

$$\mathbf{k}_1 = k_1(\sin\theta_1\cos\phi_1\hat{x} + \sin\theta_1\sin\phi_1\hat{y} + \cos\theta_1\hat{z}) \tag{5.29}$$

and (θ_1, ϕ_1) is the incident angle of the plane wave in the spherical coordinate system. Equation (5.28) can be written in the Cartesian coordinate system as

$$\begin{aligned}\mathbf{E}^{inc}(\mathbf{r}) = \Big[& \hat{x}\left(E_\theta \cos\phi_1 \cos\theta_1 - E_\phi \sin\phi_1\right) + \hat{y}\left(E_\theta \sin\phi_1 \cos\theta_1 + E_\phi \cos\phi_1\right)\Big] \\ & + \hat{z} E_\theta \sin\theta_1 \Big]\, e^{jk_1\left[\sin\theta_1\left(\cos\phi_1 x + \sin\phi_1 y\right) + \cos\theta_1 z\right]}\end{aligned} \tag{5.30}$$

Recalling the theory presented in Chapter 4 of this thesis, we can obtain the total "incident" field (including the incident field and the reflected field) in the mth layer due to the plane wave in (5.30) [84]. The incident field in the top layer ($m = 1$) is

$$\begin{aligned}\mathbf{E}_1^{inc}(\mathbf{r}) = \Big\{ & \hat{x}\Big[-E_\phi \sin\phi_1 \left(1 + \bar{\bar{\Gamma}}_1^h e^{-2jk_1 \cos\theta_1 (z - z_1)}\right) \\ & + E_\theta \cos\phi_1 \cos\theta_1 \left(1 + \bar{\bar{\Gamma}}_1^e e^{-2jk_1 \cos\theta_1 (z - z_1)}\right)\Big] \\ & + \hat{y}\Big[E_\phi \cos\phi_1 \left(1 + \bar{\bar{\Gamma}}_1^h e^{-2jk_1 \cos\theta_1 (z - z_1)}\right) \\ & + E_\theta \sin\phi_1 \cos\theta_1 \left(1 + \bar{\bar{\Gamma}}_1^e e^{-2jk_1 \cos\theta_1 (z - z_1)}\right)\Big] \\ & - \hat{z} E_\theta \sin\theta_1 \left(1 - \bar{\bar{\Gamma}}_1^e e^{-2jk_1 \cos\theta_1 (z - z_1)}\right)\Big\}\, e^{jk_1\left[\sin\theta_1\left(\cos\phi_1 x + \sin\phi_1 y\right) + \cos\theta_1 z\right]}\end{aligned} \tag{5.31}$$

and the field in other layers ($m \neq 1$) is shown in the next page.

$$
\begin{aligned}
\mathbf{E}_m^{inc}(\mathbf{r}) = \Bigg\{ & \hat{x}\Bigg[-E_\phi \sin\phi_1 \left(1+\overleftarrow{\Gamma}_1^h\right) \frac{\prod_{k=n+1}^{m-1} \overleftarrow{T}_k^{vh}}{1+\overleftarrow{\Gamma}_m^h t_m} \left[e^{-jk_{zm}(z_m - z)} + \overleftarrow{\Gamma}_m^h e^{-jk_{zm}(d_m + z - z_{m+1})} \right] \\
& + E_\theta \cos\phi_1 \frac{Z_1^e}{\eta_1} \left(1-\overleftarrow{\Gamma}_1^e\right) \frac{\prod_{k=n+1}^{m-1} \overleftarrow{T}_k^{ve}}{1+\overleftarrow{\Gamma}_m^e t_m} \left[e^{-jk_{zm}(z_m - z)} + \overleftarrow{\Gamma}_m^e e^{-jk_{zm}(d_m + z - z_{m+1})} \right] \Bigg] \\
& + \hat{y}\Bigg[E_\phi \cos\phi_1 \left(1+\overleftarrow{\Gamma}_1^h\right) \frac{\prod_{k=n+1}^{m-1} \overleftarrow{T}_k^{vh}}{1+\overleftarrow{\Gamma}_m^h t_m} \left[e^{-jk_{zm}(z_m - z)} + \overleftarrow{\Gamma}_m^h e^{-jk_{zm}(d_m + z - z_{m+1})} \right] \\
& + E_\theta \sin\phi_1 \frac{Z_1^e}{\eta_1} \left(1-\overleftarrow{\Gamma}_1^e\right) \frac{\prod_{k=n+1}^{m-1} \overleftarrow{T}_k^{ve}}{1+\overleftarrow{\Gamma}_m^e t_m} \left[e^{-jk_{zm}(z_m - z)} + \overleftarrow{\Gamma}_m^e e^{-jk_{zm}(d_m + z - z_{m+1})} \right] \Bigg] \\
& - \hat{z} E_\theta \sin\theta_m \frac{\eta_m}{\eta_1} \left(1-\overleftarrow{\Gamma}_1^e\right) \frac{\prod_{k=m+1}^{n-1} \overleftarrow{T}_k^{ie}}{1-\overleftarrow{\Gamma}_m^e t_m} \left[e^{-jk_{zm}(z - z_{m+1})} - \overleftarrow{\Gamma}_m^e e^{-jk_{zm}(d_m + z_m - z)} \right] \Bigg\} \qquad (5.32) \\
& \cdot e^{jk_m[\cos\phi_1 \sin\theta_m x + \sin\phi_1 \sin\theta_m y + \cos\theta_m z]}
\end{aligned}
$$

where z_m, d_m, k_{zm}, Z_1^e, $\overleftarrow{\Gamma}_m^p$, and $\overleftarrow{T}_m$ are the same as those defined in Chapter 4. $\eta_m = \sqrt{\mu_m/\varepsilon_m}$ is the intrinsic impedance for layer m. Furthermore, θ_m can be obtained by the Snell's law:

$$k_1 \sin\theta_1 = k_m \sin\theta_m . \qquad (5.33)$$

Discrete sources: This kind of excitation is usually applied to the circuit problem. Several types of sources can be employed, such as the impressed current source [115-117] and delta gap voltage source [118]. The delta gap voltage source applies delta electric field across an infinitesimal gap of the circuit, which mimic a constant voltage exciting the circuit. Although the delta gap voltage source is an ideal source and may not accurately characterize some practical excitation schemes, it is very simple and good enough for many circuit problems.

After applying the Galerkin's technique to the MoM, the delta gap voltage source produce a non-zero right hand side in the MoM matrix equation: only those entries associated with the delta gap source are non-zero. These non-zero entries may be set to "1", which is actually a normalized value. The voltage delta gap source is used for the circuit problems in this thesis.

5.2.3.2 Parameter Extraction

The MoM resolution yields the current distributions for an electromagnetic problem. The current distributions are used for the subsequent parameter extraction. For the scattering or radiation problems, the concerns are those parameters in the far field, which can be computed by the stationary phase method [91] or simply by the reciprocity theorem [119].

For the circuit problems the scattering parameters are often concerned. Several methods for extraction of scattering parameters have been proposed for this purpose. One methodology, called the matched load simulation (MLS), was presented in [120] for extraction of scattering parameters. At the input port of a circuit, a delta-gap voltage source is placed sufficiently far away from the input reference plane to produce undisturbed current standing wave along the input line as in [121]. The scattering parameters can then be obtained from the standing wave distributions if all the output ports are matched. The matched load is achieved by enforcing a unidirectional current traveling wave propagating along the output line extended from the discontinuities. It is obvious that the MLS is similar to the standing-wave characterization schemes for multiport networks, and it requires pre-determining the propagation constants of the quasi-TEM mode associated with the transmission lines [122].

Another group of methods for scattering parameter extraction works directly on the currents obtained by the MoM resolution and applies numerical techniques to determining the amplitudes and propagation constants of the forward and backward traveling waves on the feed

line [123]. For an N-port network, usually N linearly independent excitations are required. The total current I_k on a microstrip feeding line attached to the k-th port along the z direction can be expanded as forward and backward traveling waves:

$$I_k(z) = A_k\, e^{-j\gamma_k z} - B_k\, e^{j\gamma_k z}, \qquad k = 1, 2, \cdots, N \tag{5.34}$$

where γ_k is the propagation constant of the microstrip line at port k. A_k and B_k are the unknown amplitude of the forward and backward traveling waves, respectively. Since for each port only three unknowns A_k, B_k and γ_k are involved in the expansion equation, it is possible to sample the total current I_k at three distinct locations along z and substitute them into (5.34) to solve for the three unknowns. Such an approach for extraction of scattering parameters is called three-point curve fitting scheme [124]. The assumption made in (5.34) is that only single mode presents on the microstrip feed line, i.e., the incident and reflected traveling waves has propagation constants equal in their amplitudes but opposite in their directions. Care must be taken to avoid samples at null point of a current distribution, where large errors can occur. The reference plane for the current sampling is usually $1/5\,\lambda_g - 1/4\,\lambda_g$ away from the circuit discontinuity [38, 123]. More accurate results can be obtained by the three-point singular value decomposition (SVD) method. The Prony's method or the GPOF method discussed in Chapter 4 has also been successfully applied to extracting the scattering parameters [125].

For the normalized scattering parameters of an N-port network, the normalized incident and reflected waves can be defined as

$$a_k = \frac{A_k}{\sqrt{Z_k^c}}, \quad b_k = \frac{B_k}{\sqrt{Z_k^c}} \qquad k = 1, 2, \cdots, N \tag{5.35}$$

where Z_k^c is the characteristic impedance of the microstrip feed line at port k. The scattering

parameters of an N-port network can be obtained by solving the following equations [126]:

$$b_k = \sum_{l=1}^{N} S_{kl}\, a_l, \qquad l = 1,\ 2, \cdots N\,. \tag{5.36}$$

Equation (5.36) can be simplified if the network of interest is symmetrical, i.e., the number of entries in the scattering matrix to be determined is only $\left[N \times (N+1)\right]/2$.

5.3 Computational Details and Numerical Considerations

5.3.1 Treatment of Self and Overlapped Cell

The MoM code developed in this chapter employs the Gaussian quadrature method [99] for the integrals involved in computing the MoM matrix elements. However, the integration over self or overlapped cells requires special techniques for the treatment of the singularity in the integral kernels in order to obtain more accurate results.

In this chapter we use the popular singularity extraction technique to extract the singularity from the integrand and evaluate it analytically. Then the remaining non-singular part of the integrand can be evaluated by the Gaussian quadrature.

From the previous chapter we know that the singular term extracted from the Green's functions for multilayered media has the form of $\dfrac{e^{-jkR}}{R}$ and $R = \left|\mathbf{r} - \mathbf{r}'\right|$. The singular term can be decomposed into two terms:

$$\frac{e^{-jkR}}{R} = \frac{1}{R} + \frac{e^{-jkR} - 1}{R}. \tag{5.37}$$

The firs term in (5.37) can be computed analytically. The second term contains no singularity,

which can be proved by using the following Taylor series expansion of its exponential term:

$$e^{-jkR} = \sum_{m=0}^{\infty} \frac{(-jkR)^m}{m!}. \tag{5.38}$$

Therefore,

$$\frac{e^{-jkR}-1}{R} = -jk - \frac{k^2 R}{2} + j\frac{k^3 R^2}{6} + \frac{k^4 R^3}{24}\cdots. \tag{5.39}$$

Although using more terms to approximate the left-hand side of (5.39) can lead to more accurate results, in practice two terms is usually enough to produce accurate results.

5.3.2 Solution of MoM Linear Systems of Equations

All the above-mentioned procedures and techniques finally produce a linear system of equations that must be solved to determine the unknown coefficients for the basis functions. Both the direct and iterative methods can be used for solving the MoM matrix equations [30].

The direct methods are straight-forward approaches to solve linear systems of equations. The most commonly used Gaussian elimination method can be found in linear algebra textbooks [30, 99]. Many iterative methods have been applied to solve the linear system of equations, which include the conjugate gradient-fast Fourier transform (CG-FFT) method [127], the biconjugate gradient method [128], the generalized minimal-residual method (GMRES), and the quasi-minimal-residual (QMR) algorithm [129]. Direct methods for the solution of a dense matrix require $O(N^3)$ operations, while iterative methods require $O(PQ)$ with P being the number of iterations and Q the operation count per iteration [30]. More recently, fast algorithms have been intensively studied to achieve $O(N \log N)$ operations. Some of these

fast algorithms include the fast multipole method (FMM), the multilevel fast multipole method (MLFMM), the adaptive integral method (AIM), and the pre-conditioned FFT method [130, 131]. A detailed review of all these algorithms is beyond the scope of this thesis.

In this chapter both the Gaussian elimination algorithm and the biconjugate gradient method are employed to solve the linear system of equations. But only the biconjugate gradient method [132] is briefly presented here. For a general linear equation

$$Ax = b, \tag{5.40}$$

the bi-conjugate gradient (Bi-CG) method generates two CG-like sequences of vectors: one is based on the original matrix A and the other on A^T. Instead of orthogonalizing each sequence they are made mutually orthogonal or bi-orthogonal. The two sequences of residues are updated by

$$r^{(i)} = r^{(i-1)} - \alpha_i A p^{(i)}, \quad \tilde{r}^{(i)} = \tilde{r}^{(i-1)} - \alpha_i A^T \tilde{p}^{(i)} \tag{5.41}$$

and two sequences of search directions are given by

$$p^{(i)} = r^{(i-1)} + \beta_{i-1} p^{(i-1)}, \quad \tilde{p}^{(i)} = \tilde{r}^{(i-1)} + \beta_{i-1} \tilde{p}^{(i-1)}. \tag{5.42}$$

α_i and β_i are chosen as

$$\alpha_i = \frac{\tilde{r}^{(i-1)^T} r^{(i-1)}}{p^{(i)^T} A p^{(i)}}, \quad \beta_i = \frac{\tilde{r}^{(i)^T} r^{(i)}}{\tilde{r}^{(i-1)^T} r^{(i-1)}}, \tag{5.43}$$

which ensure the bi-orthogonality relations

$$\tilde{r}^{(i)^T} r^{(j)} = \tilde{p}^{(i)^T} A p^{(j)} = 0, \qquad \text{if } i \neq j. \tag{5.44}$$

The bi-conjugate gradient (BiCG) method does not minimize a residual, but the generation of the basis vectors is relatively cheap and the memory requirements are modest. It is concluded in [128] that the bi-conjugate gradient algorithm can lead to significant time savings compared to the conjugate gradient method. Sometimes breakdown or near-breakdown situations of the Bi-CG algorithm can be satisfactorily avoided by a restart at the iteration step immediately before the near breakdown step with a perturbed estimate of the solution.

5.4 Numerical Examples

Two multilayered circuits are used to validate the MPIE-MoM code developed in this chapter.

5.4.1 Microstrip-fed Patch Antenna

The physical configuration of an edge-fed microstrip patch antenna [133] is shown in Fig. 5.3a. The spatial-domain MPIE-MoM method is used to simulate the circuit, where rooftop subdomain basis functions are used. The frequency band of interest is 3.9 to 4.5 GHz.

In order to observe the standing wave pattern on the feeding line, the microstrip feeding line used in the MoM simulation is extended to nearly $2\lambda_{g,\min}$ away from its connection point with the patch, where $\lambda_{g,\min}$ is the minimal guided wavelength in the frequency band of interest. The dimensions of the charge cell used in the MoM resolution are $\Delta x = \Delta y = 1.57$ mm, which satisfy the rule of thumb condition, i.e., $\Delta x, \Delta(y) < \lambda_{g,\min}/20$ and accurate results can be expected. The number of charge cells along the feeding line is 35 and the patch is divided into 13 $(\Delta x) \times 15$ (Δy) charge cells (see Fig. 5.3b). The delta gap voltage source is used to excite the circuit.

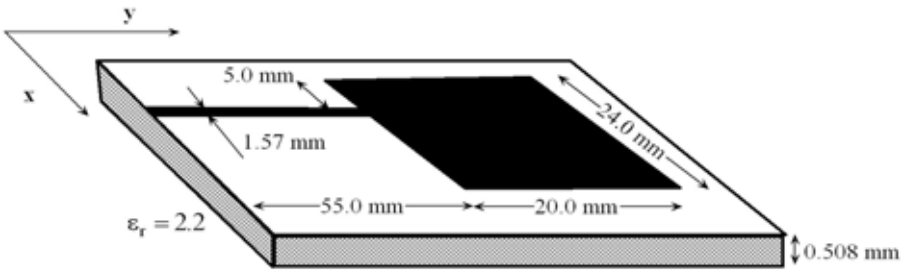

(a)

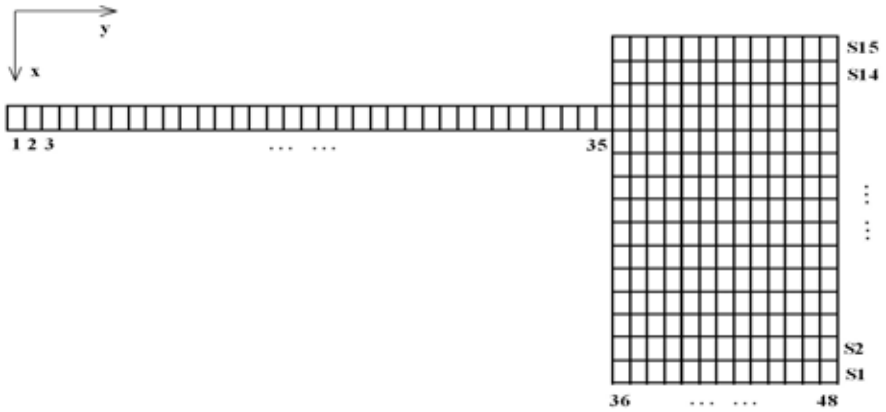

(b)

Fig. 5.3 Microstrip-fed patch antenna: a) Configuration and dimensions; b) Meshing.

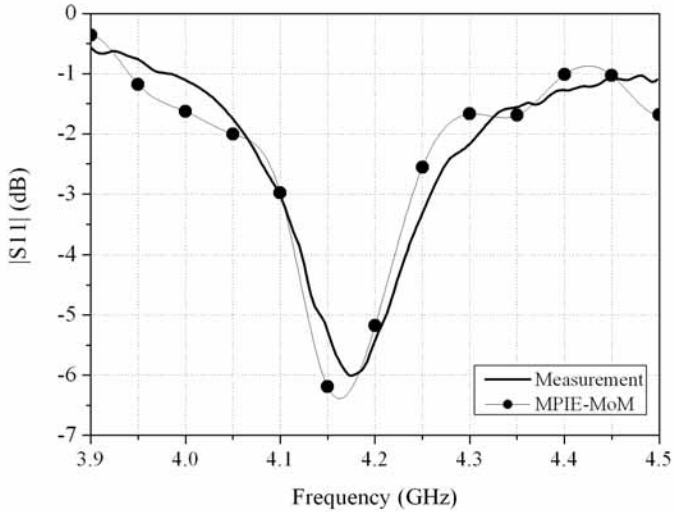

Fig. 5.4 Comparison of the reflection coefficient for the microstrip-fed patch antenna: measurement results vs. MPIE-MoM results.

The reflection coefficient S_{11} is plotted in Fig. 5.4, which is derived from the current distribution on the feeding line using the three-point curve fitting scheme. The MoM results of the reflection coefficient S_{11} are compared with the measurement results reported in [133]. Good agreement can be observed from the comparison shown in Fig. 5.4. The resonant frequency of the patch is accurately captured by the MoM resolution and has less than 1% error with the experimental results. Finally, the current distributions on the microstrip-fed patch, which is excited by the delta gap voltage source, are shown in Fig. 5.5.

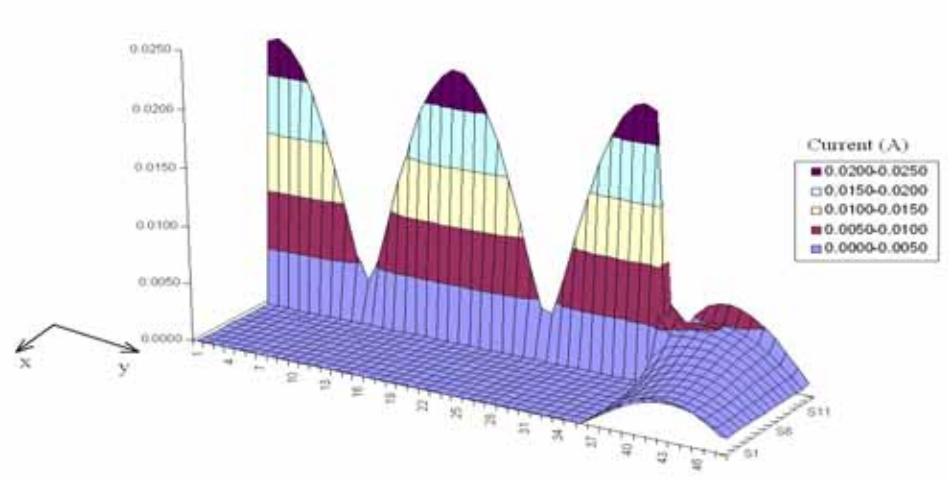

(a)

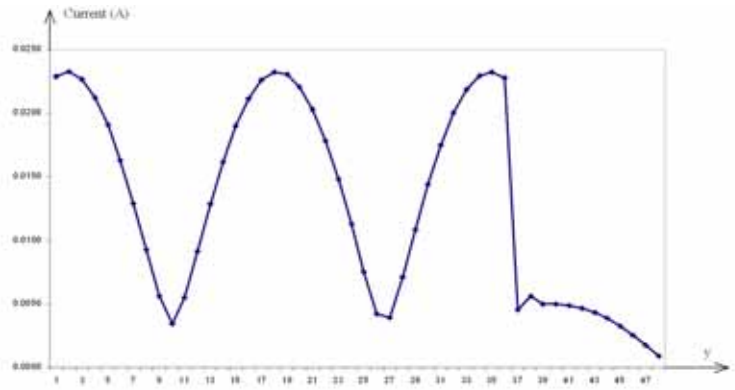

(b)

Fig. 5.5 Current distribution (J_y) from MoM resolution for the microstrip-fed patch antenna: (a) on the surfaces of both the feeding line and the patch; (b) on the surface of the feeding line (across the patch).

5.4.2 Overlap-gap Coupled Microstrip Filter

A five-section overlap-gap-coupled microstrip bandpass filter [38, 134] is show in Fig. 5.6. For the MoM solution of this problem, the RWG basis functions are used. The total number of unknowns are 642. Once again the excitation used for this problem is the delta-gap voltage source.

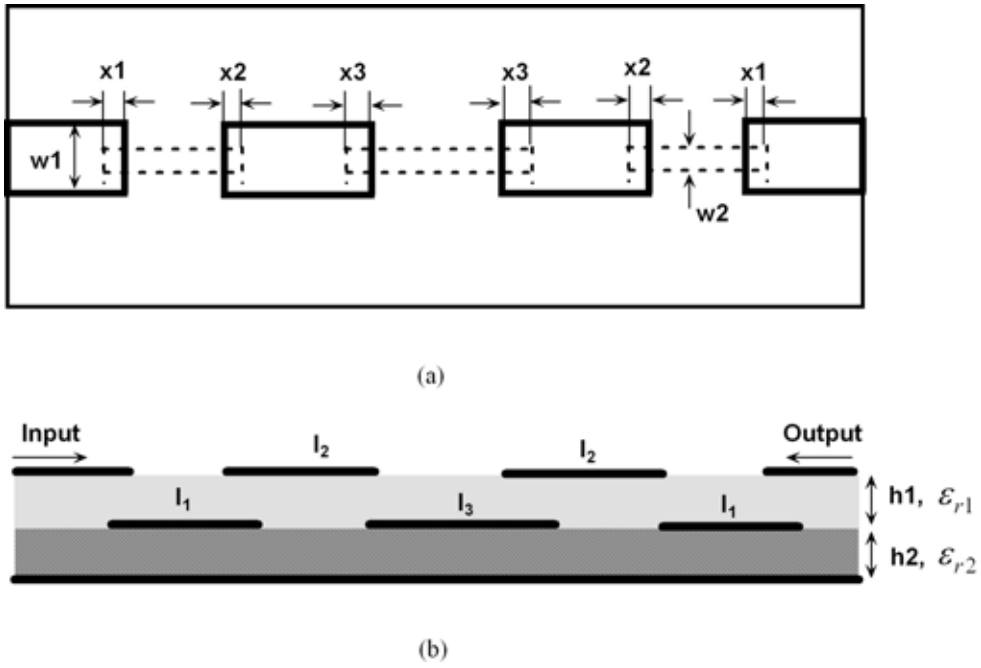

Fig. 5.6 Geometry of a five-section overlap-gap-coupled microstrip filter (unit: mm) --- the overlapped length: $x_1 = 1.311$, $x_2 = 0.386$ and, $x_3 = 0.269$; the width: $w_1 = 0.812$ and $w_2 = 0.458$; the length: $l_1 = 6.99$, $l_2 = 6.457$ and $l_3 = 7.242$; and the thickness: $h_1 = h_2 = 0.254$. The dielectric constants of the substrates are $\varepsilon_1 = 9.8$ and $\varepsilon_2 = 2.2$.

The Bi-CG iterative method is used to solve the MoM matrix equations. The residual error is set to $1e-4$. It takes 105, 76 and 166 iterations for the Bi-CG method to converge at $f = 6.5$ GHz, 10.1 GHz and 14 GHz, respectively (Fig. 5.7).

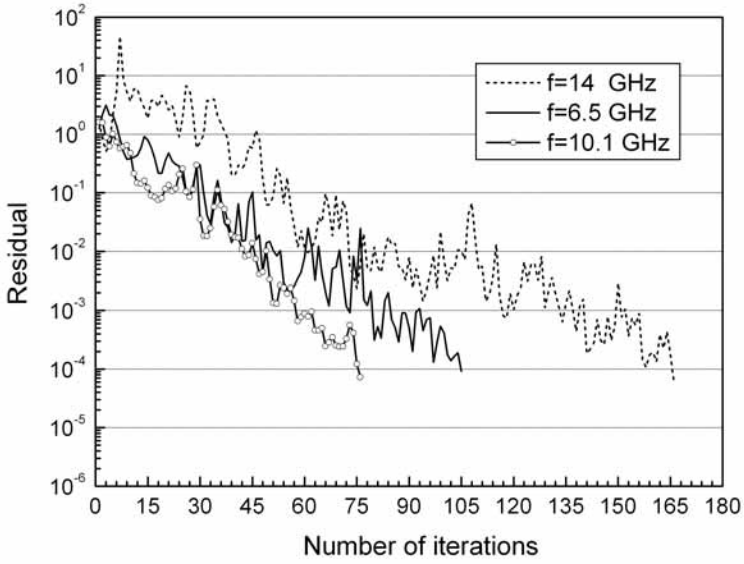

Fig. 5.7 Number of iterations needed for the Bi-CG method to converge to the residue error of 1e-4.

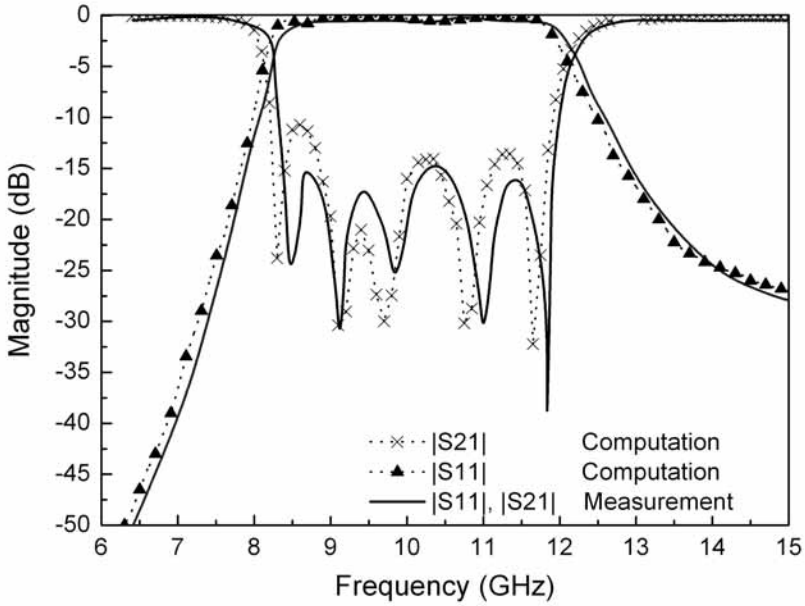

Fig. 5.8 Scattering parameters for the overlap-gap-coupled microstrip filter.

The scattering parameters of the filter are shown in Fig. 5.8. The computational results agree well with the measurement results reported in [38]. The small discrepancy with the measurement data is due to the finite thickness of the metallization and the fabrication tolerance of the substrates, which is discussed in [38]. A total of one hundred sampling frequencies are

used to obtain the scattering parameters in Fig. 5.8. For each frequency the CPU time is about 15 to 32 seconds, which results in a total of 50 minutes' CPU time on a PC.

5.5 Summary

This chapter presents the solution of the MPIE for multilayered structures in the presence of PECs by the methods of moments (MoM). Both the RWG and rooftop basis functions are implemented to approximate the unknown currents and the Galerkin's technique is applied to the MoM solution. Numerical examples validate the MPIE-MoM code developed in this chapter.

Chapter 6. Hybrid FDTD-MPIE Method for Multilayer Circuits with Locally Inhomogeneous Objects

In the previous chapters both the FDTD and the MPIE-MoM methods are employed individually to analyze either single-layer or multilayer passive circuits. In this chapter a new hybrid FDTD-MPIE method is proposed, which is intended to exploit the merits of both methods to analyze multilayer circuits with locally inhomogeneous penetrable objects.

6.1 Introduction

Multilayered planar structures have wide applications such as the multilayer packaging driven by the emerging demands in high frequency applications, and microwave and millimeter wave applications. A specific example of them is the promising multilayer substrate technology using the Low Temperature Co-fired Ceramic (LTCC), which is capable of achieving good design flexibility and optimized integration because the free vertical space of the multilayer substrate can be fully utilized [135]. The three-dimensional nature of the multilayer circuits complicates their modeling and simulation especially in the case of multilayered structures embedded with

locally inhomogeneous penetrable objects.

For such a complex multilayered structure with locally embedded inhomogeneous objects, it is not efficient to perform its modeling by one single computational electromagnetic method, irrespective of the surface integral equation (SIE) techniques, which are solved by the MoM (Method of Moments), or the differential equation techniques such as the FEM (Finite Element Method) and the FDTD (Finite Difference Time Domain) method. The integral equation (IE) techniques solved by the method of moments (MoM) are extensively employed to solve the multilayered planar circuits using spatial-domain Green's functions [33, 38, 78, 105, 106], whereas the differential equation techniques such as the FEM [27] or FDTD method [9, 26] are especially suitable for handling of complex inhomogeneous media.

Based on the idea of taking advantage of individual methods, hybrid techniques are put forward to solve complex problems efficiently. Traditionally the hybrid FEM-IE method is one of the most popular hybrid techniques widely used in electromagnetic modeling because of the versatility of the FEM in geometry and material modeling [27, 28, 36]. Another hybrid technique which couples the powerful yet simple FDTD method with the integral equation method is also attractive, especially when wide band information is needed for some complex geometries.

Either the time-domain or the frequency domain MoM can be combined with the FDTD method to form a hybrid method. In [136-139], a hybrid technique combining the time-domain MoM and FDTD method was presented to analyze scattering problems of a thin wire antenna in the presence of an inhomogeneous dielectric scatterer. But this method may suffer from late-time instability.

In [140], a hybrid frequency domain MoM-FDTD method was successfully applied to

analyzing penetration and coupling problems involving conductors with potentially complex interiors. The hybrid method had the advantage of obviating the needs for computation of Green's functions for the interior problems.

In [141] a hybrid method was introduced, which employed the frequency domain MoM to solve the thin-wire antenna problem and the FDTD method to handle the inhomogeneous dielectric object. This approach employed a combination of Fourier transformation and iterative procedures to coupling the two models. However, the reaction of the back-scattered field and the source was not discussed in detail. Similar methods have been presented in [142] and [143] to compute the Special Absorption Rate (SAR) of a human head in the presence of mobile phones, where the effect of the back-scattered field on the source was neglected in [142], but was thoroughly accounted for in [143] by using the reciprocity theorem.

An interesting hybrid method was proposed in [144], the FDTD method was hybridized with the free-space frequency-domain IE method, where the FDTD method was applied to construct the model of certain bounded regions and then the model is coupled with the IE model describing the remaining bounded and unbounded regions. Similar idea can be traced back to the hybrid FEM-IE method [27].

However, all the above-mentioned hybrid FDTD-MoM methods are formulated in the context of free-space problems. In this chapter a new hybrid method − the hybrid FDTD-MPIE (finite-difference time-domain and mixed-potential integral equation) method is proposed to efficiently analyze the multilayered structure in the presence of locally inhomogeneous penetrable objects.

The hybrid method proposed in this chapter is intended to combine the advantages of the FDTD method for the treatment of inhomogeneous objects and the MPIE method for the

solution of multilayered structures. By using the equivalence principle the original problem can be decomposed into external and internal problems. The FDTD method is employed to model the internal problem consisting of the inhomogeneous objects in the context of the global multilayered planar structure. And the global multilayered structure is solved by the MPIE method using the Formulation-C Green's functions [78] discussed in the previous chapters.

The FDTD and the MPIE models are coupled together by enforcing the continuity of the tangential electric and magnetic fields on the equivalent surfaces. Both the direct and iterative solution approaches are employed to solve the hybrid FDTD-MPIE equations. Furthermore, the DCIM method (discrete complex image method) [105, 106] examined in the previous chapters is applied to build the closed-form expressions of the multilayer Green's functions in spatial domain and improve the overall computational efficiency.

6.2 Methodology Description

6.2.1 Problem Statement

Consider a general planar multilayer problem shown in Fig. 6.1, where the multilayered media consist of N planar layers in the presence of a penetrable object and a PEC. The whole structure is illuminated by incident fields $\mathbf{E}^i$ and $\mathbf{H}^i$. The penetrable object denoted by V_d can be inhomogeneous and characterized by permittivity ε_d and permeability μ_d. The surfaces of the penetrable object and the PEC are represented by S_d and S_c ($S = S_c \bigcup S_d$), respectively.

By applying the equivalence principle [33, 145] we can decompose the original multilayer problem shown in Fig. 6.1 into an external equivalent problem and an internal equivalent problem. For the external equivalent problem the equivalent surface currents $(\mathbf{J}_s, \mathbf{M}_s)$ and the incident fields $(\mathbf{E}^i, \mathbf{H}^i)$ produce the original fields $(\mathbf{E}, \mathbf{H})$ in the region exterior to the penetrable object and null fields inside the penetrable object. In other words, the superposition of the incident $(\mathbf{E}^i, \mathbf{H}^i)$ and scattered fields $(\mathbf{E}^s, \mathbf{H}^s)$ yields the correct fields of the original problems: $(\mathbf{E}, \mathbf{H}) = (\mathbf{E}^i + \mathbf{E}^s, \mathbf{H}^i + \mathbf{H}^s)$. It is to be noted that the incident fields $(\mathbf{E}^i, \mathbf{H}^i)$ here should include the effects of reflected fields in the absence of the penetrable object and the PEC.

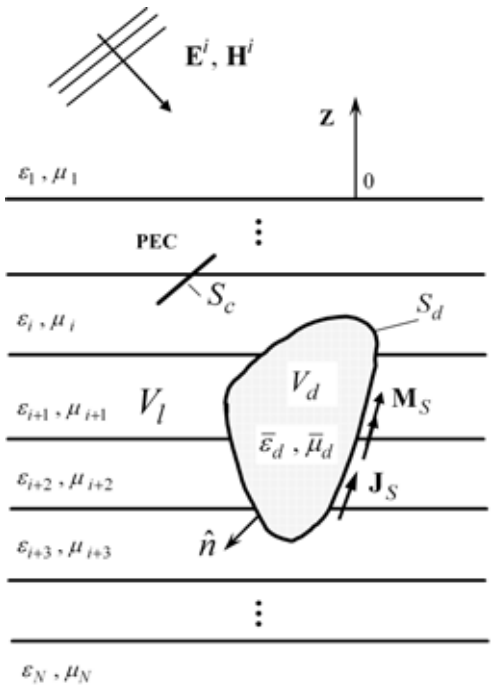

Fig. 6.1 A general multilayered medium in the presence of a penetrable inhomogeneous object and a PEC, which is illuminated by incident fields.

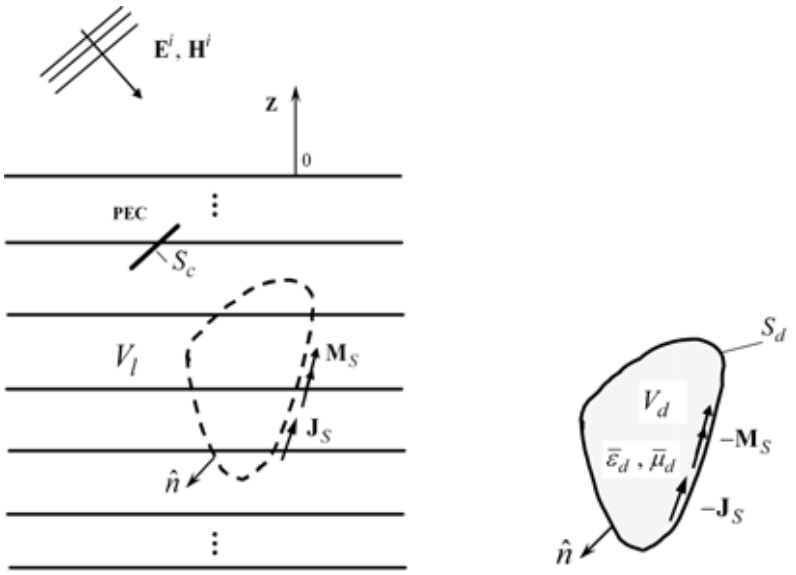

(a) (b)

Fig. 6.2 Equivalent problems: (a) the external problem: the multilayered medium with a PEC illuminated by incident fields; (b) the internal problem: the penetrable inhomogeneous object.

6.2.2 Equivalence Principle and Model Construction

The internal and external equivalent problems are shown in Fig. 6.2. For the internal equivalent problem the electromagnetic fields in the volume of the inhomogeneous object V_d enclosed by the surface S_d are formulated by the FDTD method. Conversely, the fields in the planar multilayered media V_l are formulated by the MPIE method. The perfect electric conductor is also included in the MPIE model.

The FDTD and MPIE models corresponding to the internal and external equivalent problems are coupled together through the boundary conditions on Surfaces S_d and S_c:

$$\begin{aligned} &\hat{n}\times\mathbf{E}_l = \hat{n}\times\mathbf{E}_d \\ &\qquad\qquad \text{on Surface } S_d \\ &\hat{n}\times\mathbf{H}_l = \hat{n}\times\mathbf{H}_d \end{aligned} \tag{6.1}$$

$$\hat{n}\times\mathbf{E}_c = 0 \qquad \text{on Surface } S_c \tag{6.2}$$

where $\mathbf{E}_l$ and $\mathbf{H}_l$ denote the electric and magnetic fields in V_l and $\mathbf{E}_d$ and $\mathbf{H}_d$ in V_d. $\mathbf{E}_c$ is the electric field on the surface of the PEC.

Equations (6.1) and (6.2) are actually the mathematical expressions of the continuity of the tangential fields. In addition the equivalent surface currents $\mathbf{J}_s$ and $\mathbf{M}_s$ can be defined as

$$\mathbf{J}_s = \hat{n}\times\mathbf{H}_l = \hat{n}\times\mathbf{H}_d\,, \tag{6.3}$$

$$\mathbf{M}_s = -\hat{n}\times\mathbf{E}_l = -\hat{n}\times\mathbf{E}_d\,. \tag{6.4}$$

For the external equivalent problem the fields in the planar multilayered structure V_l can be expressed in terms of the equivalent surface current densities $\mathbf{J}_s$ and $\mathbf{M}_s$ by using the Formulation-C mixed potential forms as discussed in the previous chapters:

$$\begin{aligned}\mathbf{E} &= \left\langle \bar{\mathbf{G}}^{EJ};\mathbf{J}_s\right\rangle + \left\langle \bar{\mathbf{G}}^{EM};\mathbf{M}_s\right\rangle \\ &= -j\omega\left\langle \bar{\mathbf{G}}^{A};\mathbf{J}_s\right\rangle + \frac{1}{j\omega}\left\langle G^{\phi},\nabla'\cdot\mathbf{J}_s\right\rangle + \left\langle \bar{\mathbf{G}}^{EM};\mathbf{M}_s\right\rangle\end{aligned} \tag{6.5}$$

$$\begin{aligned}\mathbf{H} &= \left\langle \bar{\mathbf{G}}^{HM};\mathbf{M}_s\right\rangle + \left\langle \bar{\mathbf{G}}^{HJ};\mathbf{J}_s\right\rangle \\ &= -j\omega\left\langle \bar{\mathbf{G}}^{F};\mathbf{M}_s\right\rangle + \frac{1}{j\omega}\left\langle G^{\psi},\nabla'\cdot\mathbf{M}_s\right\rangle + \left\langle \bar{\mathbf{G}}^{HJ};\mathbf{M}_s\right\rangle\end{aligned}. \tag{6.6}$$

Because the cubic cells are used in the FDTD model, the equivalent surface is discretized into small rectangular patches and the fields on the equivalent surface are expanded using rooftop basis functions:

$$\mathbf{E} = \sum_{i=1}^{N} I_i\mathbf{T}_i, \qquad \mathbf{H} = \sum_{i=1}^{N} V_i\mathbf{T}_i, \qquad \text{on surface } S_d \text{ or } S_c \tag{6.7}$$

where the expressions for the rooftop basis $\mathbf{T}_i$ can be found in the previous chapter and is not repeated here. N is the total number of basis functions.

For the internal equivalent problem the inhomogeneous volume V_d is analyzed by the FDTD method. However, the coupling of the FDTD and MPIE models in the hybrid method can not be handled in a straightforward way as that in the frequency-domain hybrid FEM-IE method. In the following sections both the direct and iterative solution approaches used in the hybrid FDTD-MPIE method will be discussed in detail.

6.3 Direct Solution Approach

6.3.1 Coupling of FDTD Model and MPIE Model

The direct solution approach used in the hybrid FDTD-MPIE method employs the FDTD interaction matrix and Galerkin's testing procedure to build an integrated matrix equation for the original problem.

The FDTD interaction matrix approach used in [146] is employed in the direct solution approach. Similar to (6.5) and (6.6) the FDTD interaction matrix describes the relationship between the fields and the equivalent current sources on surface S_d in frequency domain. Since the fields on surface S_d of the MPIE model is expanded using rooftop basis functions, we will impose each of these basis functions as an individual electric or magnetic current source to excite the FDTD model. Corresponding to each source one FDTD simulation can generate a set of data, which fills up one column of the interaction matrix (see Fig. 6.3). In the FDTD simulation the UPML absorbing boundary condition is used to truncate the boundary of the internal equivalent problem. Since for the internal equivalent problem the fields outside the

internal objects are zero, the introduction of ABC in the FDTD simulation does not change the fields inside the objects.

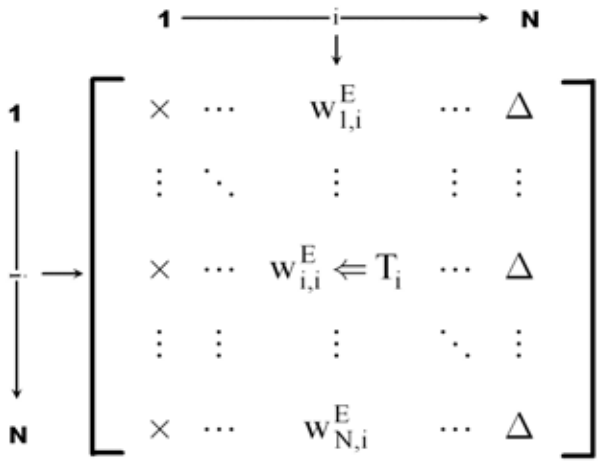

Fig. 6.3 Illustration of constructing the FDTD interaction matrix: Excite the FDTD model by the ith basis function for the electric field to obtain the ith column of the matrix.

Finally the complete interaction matrix can be constructed by performing $2N$ FDTD simulations. All the entries in the interaction matrix are thus pre-computed and stored in a look-up table for the subsequent construction of the integrated coupling equations using Galerkin's procedures for the hybrid problem. The interaction matrix will be used in the process of computing the double integrals to build the final integrated linear systems of equations.

6.3.2 Galerkin's Procedures for Systems of Equations

Hybridization of the FDTD and MPIE models is fulfilled by enforcing the boundary conditions in (6.1) and (6.2). By analogy with the approach used in the hybrid FEM-IE method [27], both boundary conditions are enforced explicitly by using the Galerkin's testing procedure:

$$\iint_{S_d} \overline{T}_j \cdot \hat{n} \times (\mathbf{E}_l - \mathbf{E}_d)\, dS = 0$$
$$\iint_{S_d} \overline{T}_j \cdot \hat{n} \times (\mathbf{H}_l - \mathbf{H}_d)\, dS = 0 \tag{6.8}$$

$$\iint_{S_c} \overline{T}_j \cdot \hat{n} \times \mathbf{E}_c \, dS = 0 \,. \tag{6.9}$$

Equations (6.8) and (6.9) can be eventually converted to linear systems of equations for the original problem in the frequency domain. And the resultant matrix equations can be easily solved to yield the solution for the original multilayer problem with locally inhomogeneous penetrable objects.

6.3.3 Numerical Results

A canonical problem similar to the one used in [36] is analyzed by the proposed hybrid FDTD-MPIE method using the direct solution approach. In this example a four-layer planar structure is normally incident by a plane wave, which is propagating along the z axis with x polarization and an amplitude of 100 V/m. The dimensions and configuration of the problem are shown in Fig. 6.4. A cubic volume is designated as the inhomogeneous object V_d and simulated by the FDTD method. The cubic volume V_d has the same permittivity and permeability as its surrounding layers and the dimension of it is $1\,\text{cm} \times 1\,\text{cm} \times 3\,\text{cm}$ in x, y and z directions, respectively.

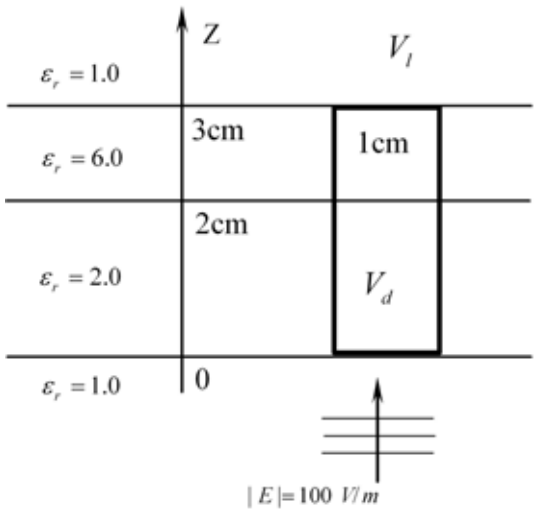

Fig. 6.4 Two dielectric layers normally incident by a plane wave.

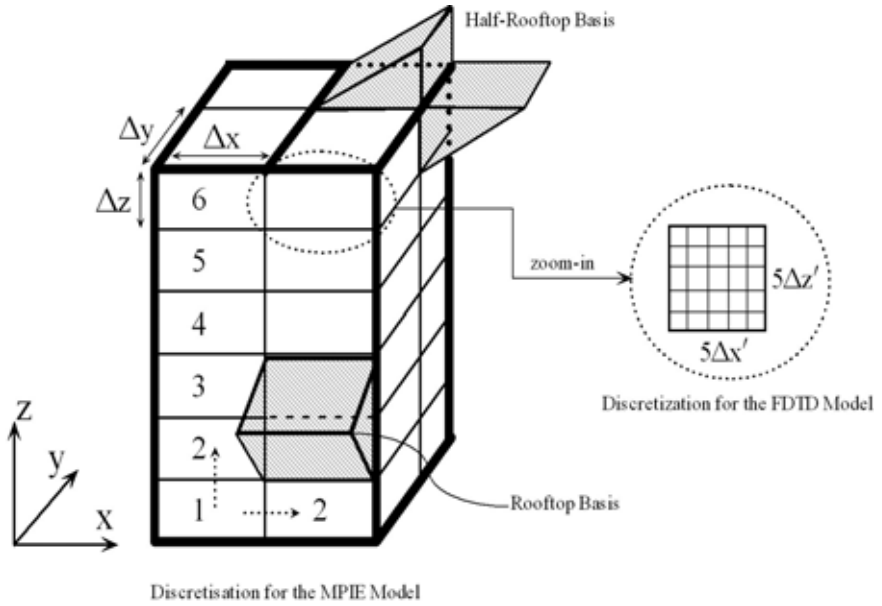

Fig. 6.5 Illustration of the disretization pattern: Disretization used for the MPIE model is shown in the main plot and each charge cell is further divided into 5×5 patches to be used in the FDTD model.

The surface S_d is discretized by two charge cells in the x direction, two charge cells in the y direction and six charge cells in the z direction, i.e., totally $2\Delta x \times 2\Delta y \times 6\Delta z$. And the cell size is $\Delta x = \Delta y = \Delta z = 0.5$ cm. For this specific problem totally 112 rooftops are used. Furthermore, each charge cell is sub-divided into 5×5 patches. Therefore, the number of FDTD cells are $10\Delta x' \times 10\Delta y' \times 30\Delta z'$ and $\Delta x' = \Delta y' = \Delta z' = 0.1$ cm (See Fig. 6.5).

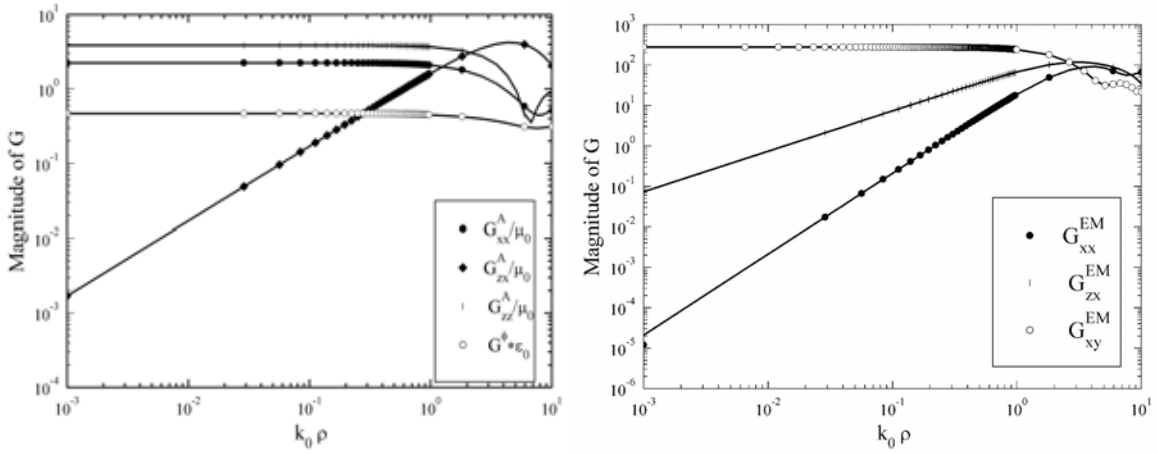

(a) (b)

Fig. 6.6 Magnitude of some typical components of Green's functions at 6 GHz for the four-layer structure ($z = 2.5$ cm and $z' = 0.0$ cm). Both the numerical integration (solid lines) and the DCIM (Symbols) results are shown.

The magnitude of some Green's functions used in the MPIE formulation is shown in Fig. 6.6. The results of Green's functions obtained by DCIM method discussed in the previous chapter agree well with those obtained by the numerical integration method.

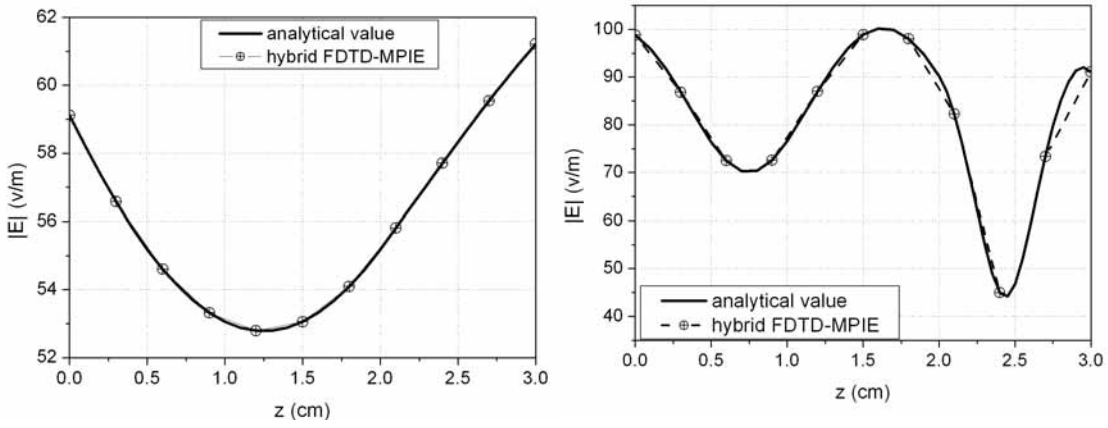

(a) 0.8 GHz (b) 6 GHz

Fig. 6.7 Amplitude of the electric field in V_d along the z axis.

The direct approach is used to solve the problem in this example. The FDTD method is used to build the interaction matrix. The time dependency of the rooftops used as FDTD excitation

sources is in the form of Gaussian pulse. By using the Fourier transform, we can obtain the response of the FDTD model in the frequency range of 0 to $f_{\max}$ in one FDTD run. The results of the electric fields obtained by the hybrid FDTD-MPIE method are shown in Fig. 6.7 and agree well with the analytical solutions.

For solution of problems using the hybrid method, the memory requirement is not a problem for small geometries like V_d in this example. The only concern is the CPU time consumed by creating the FDTD interaction matrix. Since 112 rooftop bases are used, we have to run 112 FDTD simulations. For the discretization shown in Fig. 6.5 it needs about four hours on a PC to construct the FDTD interaction matrix if we run the FDTD simulation one by one. However, the advantage of the hybrid method is that if only the geometry of dielectric V_d remains unchanged, the FDTD interaction matrix can be re-used for a wide frequency range.

To improve the efficiency of the hybrid FDTD-MPIE method, an iterative approach without constructing the FDTD interaction matrix is employed to reduce the solution time.

6.4 Iterative Solution Approach

The iterative approach used in [141, 143] for the solution of the hybrid FDTD-MoM problem offers some advantages over the direct approach discussed in the previous section. Unlike the direct solution approach it obviates the needs to run the FDTD simulation as many times as the number of the basis functions. An accurate solution for the hybrid problem can be achieved usually only after several iterations.

6.4.1 Iterative Procedures

The idea of the iterative solution approach is to formulate the FDTD and the MPIE-MoM

problems independently, and check their solutions at each iteration step against the boundary condition till a steady state solution is obtained.

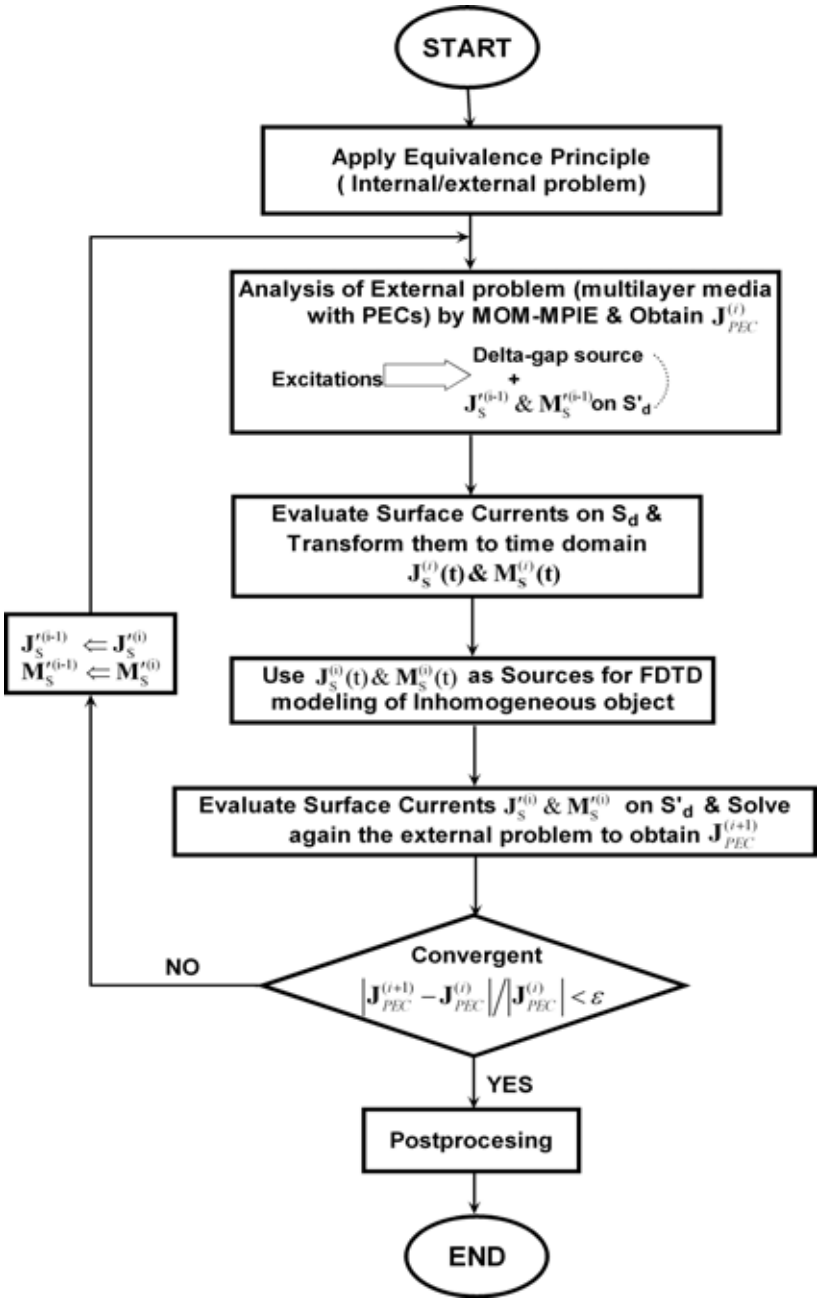

Fig. 6.8 Procedures of the iterative solution approach.

The procedures of the iterative approach are shown in Fig. 6.8. It starts from solving the external problem by the standard MoM technique discussed in Chapter 5 under the assumption that the initial currents on the equivalent surface are zero. After finishing the MOM simulation

the currents on the equivalent surface are considered as the sources for the internal problem, which is solved by the FDTD method. The currents thus obtained from the FDTD simulation for the internal problem are used for the subsequent MoM solution of the external problem. This process is iterated until a steady-state solution is achieved. For weak coupling problems usually three to five iterations are enough to yield accurate results.

6.4.2 Interfaces between FDTD and MoM Model

At each iteration step the fields (cf. (6.5) and (6.6)) obtained from the MoM solution are imposed as the sources for the internal problem solved by the FDTD method. These fields from the MOM solution are used in the FDTD simulation as incident fields implemented by the TF/SF (total field-Scattered field) technique.

The TF/SF technique briefly introduced in Chapter 2 is implemented here for three dimensional problems. As shown in Fig. 6.9c, the TF/SF interface surface (equivalent surface) is denoted by S_d'. The electric field updating equations at the TF/SF interface in the FDTD method are given below [9]:

At $i = i_m$ $(m = 0, 1)$ face:

for j = $j_0 + \frac{1}{2}, \cdots, j_1 - \frac{1}{2}$; $k = k_0, \cdots, k_1$,

$$E_y\Big|_{i_m,j,k}^{n+1} = \left\{E_y\Big|_{i_m,j,k}^{n+1}\right\}_{STD} + (-1)^m \frac{\Delta t}{\varepsilon \Delta x} H_z^{MoM}\Big|_{i_m+\frac{(-1)^{m+1}}{2},j,k}^{n+1/2}, \tag{6.10}$$

and for j = $j_0, \cdots, j_1$; $k = k_0 + \frac{1}{2}, \cdots, k_1 - \frac{1}{2}$,

$$E_z\Big|_{i_m,j,k}^{n+1} = \left\{E_z\Big|_{i_m,j,k}^{n+1}\right\}_{STD} + (-1)^{m+1} \frac{\Delta t}{\varepsilon \Delta x} H_y^{MoM}\Big|_{i_m+\frac{(-1)^{m+1}}{2},j,k}^{n+1/2}. \tag{6.11}$$

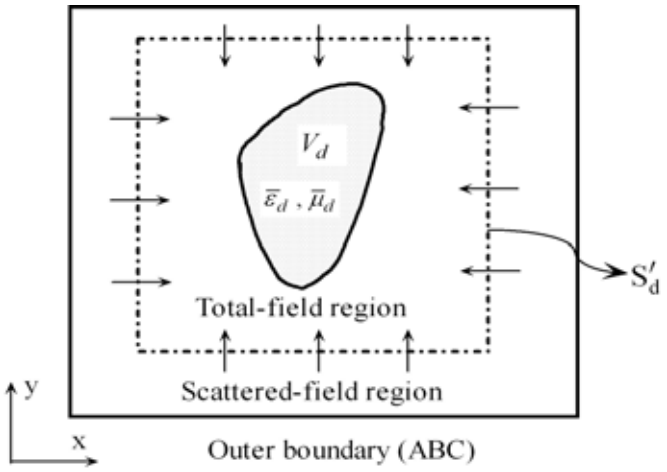

(a)

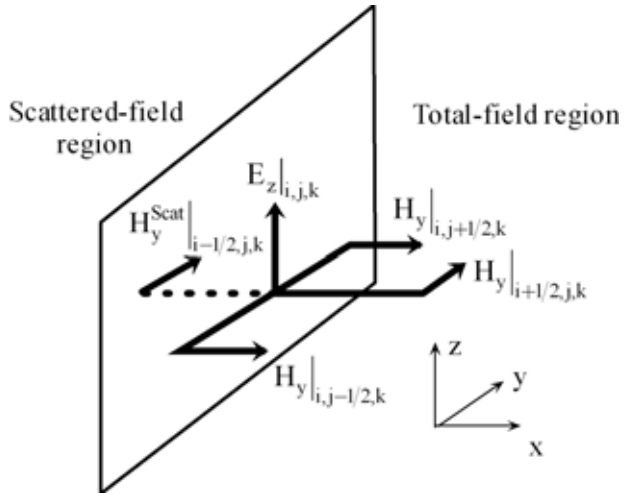

(b)

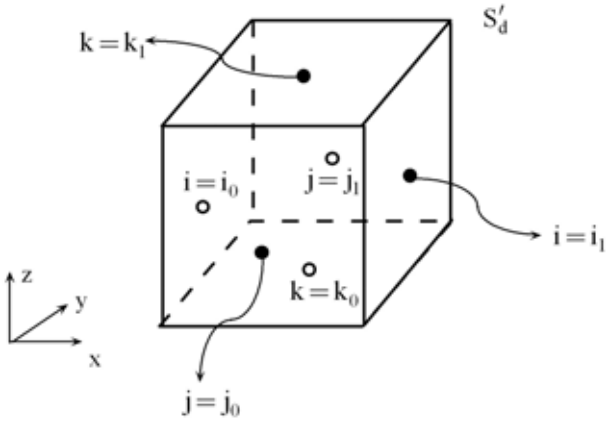

(c)

Fig. 6.9 Equivalent interface S'_d and the TF/SF technique: (a) The cross-section view of the TF/SF interface; (b) Fields at the interface; (c) The six faces comprising S'_d.

At $j = j_m$ $(m = 0, 1)$ face:

for $i = i_0 + \frac{1}{2}, \cdots, i_1 - \frac{1}{2}$; $k = k_0, \cdots, k_1$,

$$E_x\Big|_{i,j_m,k}^{n+1} = \left\{E_x\Big|_{i,j_m,k}^{n+1}\right\}_{STD} + (-1)^{m+1}\frac{\Delta t}{\varepsilon \Delta y} H_z^{MoM}\Big|_{i,j_m+\frac{(-1)^{m+1}}{2},k}^{n+1/2}, \tag{6.12}$$

and for $i = i_0, \cdots, i_1$; $k = k_0 + \frac{1}{2}, \cdots, k_1 - \frac{1}{2}$,

$$E_z\Big|_{i,j_m,k}^{n+1} = \left\{E_z\Big|_{i,j_m,k}^{n+1}\right\}_{STD} + (-1)^{m}\frac{\Delta t}{\varepsilon \Delta y} H_x^{MoM}\Big|_{i,j_m+\frac{(-1)^{m+1}}{2},k}^{n+1/2}. \tag{6.13}$$

At $k = k_m$ $(m = 0, 1)$ face:

for $i = i_0 + \frac{1}{2}, \cdots, i_1 - \frac{1}{2}$; $j = j_0, \cdots, j_1$,

$$E_x\Big|_{i,j,k_m}^{n+1} = \left\{E_x\Big|_{i,j,k_m}^{n+1}\right\}_{STD} + (-1)^{m}\frac{\Delta t}{\varepsilon \Delta z} H_y^{MoM}\Big|_{i,j,k_m+\frac{(-1)^{m+1}}{2}}^{n+1/2}, \tag{6.14}$$

and for $i = i_0, \cdots, i_1$; $k = k_0 + \frac{1}{2}, \cdots, k_1 - \frac{1}{2}$,

$$E_y\Big|_{i,j,k_m}^{n+1} = \left\{E_y\Big|_{i,j,k_m}^{n+1}\right\}_{STD} + (-1)^{m+1}\frac{\Delta t}{\varepsilon \Delta z} H_x^{MoM}\Big|_{i,j,k_m+\frac{(-1)^{m+1}}{2}}^{n+1/2}. \tag{6.15}$$

Similarly, the magnetic field updating equations at the TF/SF interface in the FDTD method are given by [9]

At $i = i_m + (-1)^{m+1}/2$ $(m = 0, 1)$ face:

for j = $j_0, \cdots, j_1$; $k = k_0 + \frac{1}{2}, \cdots, k_1 - \frac{1}{2}$,

$$H_y\Big|_{i_m+\frac{(-1)^{m+1}}{2},j,k}^{n+1/2} = \left\{H_y\Big|_{i_m+\frac{(-1)^{m+1}}{2},j,k}^{n+1/2}\right\}_{STD} + (-1)^{m+1}\frac{\Delta t}{\mu \Delta x} E_z^{MoM}\Big|_{i_m,j,k}^{n}, \tag{6.16}$$

and for j $= j_0 + \frac{1}{2}, \cdots, j_1 - \frac{1}{2}$; $k = k_0, \cdots, k_1$

$$H_z\Big|^{n+1/2}_{i_m+\frac{(-1)^{m+1}}{2},j,k} = \left\{ H_z\Big|^{n+1/2}_{i_m+\frac{(-1)^{m+1}}{2},j,k} \right\}_{STD} + (-1)^m \frac{\Delta t}{\mu \Delta x} E_y^{MoM}\Big|^n_{i_m,j,k}. \qquad (6.17)$$

At $j = j_m + (-1)^{m+1}/2$ $(m = 0, 1)$ face:

for $i = i_0 + \frac{1}{2}, \cdots, i_1 - \frac{1}{2}$; $k = k_0, \cdots, k_1$,

$$H_z\Big|^{n+1/2}_{i,j_m+\frac{(-1)^{m+1}}{2},k} = \left\{ H_z\Big|^{n+1/2}_{i,j_m+\frac{(-1)^{m+1}}{2},k} \right\}_{STD} + (-1)^{m+1} \frac{\Delta t}{\mu \Delta y} E_x^{MoM}\Big|^n_{i,j_m,k}. \qquad (6.18)$$

and for $i = i_0, \cdots, i_1$; $k = k_0 + \frac{1}{2}, \cdots, k_1 - \frac{1}{2}$,

$$H_x\Big|^{n+1/2}_{i,j_m+\frac{(-1)^{m+1}}{2},k} = \left\{ H_x\Big|^{n+1/2}_{i,j_m+\frac{(-1)^{m+1}}{2},k} \right\}_{STD} + (-1)^m \frac{\Delta t}{\mu \Delta y} E_z^{MoM}\Big|^n_{i,j_m,k}. \qquad (6.19)$$

At $k = k_m + (-1)^{m+1}/2$ $(m = 0, 1)$ face:

for $i = i_0 + \frac{1}{2}, \cdots, i_1 - \frac{1}{2}$; $j = j_0, \cdots, j_1$,

$$H_y\Big|^{n+1/2}_{i,j,k_m+\frac{(-1)^{m+1}}{2}} = \left\{ H_y\Big|^{n+1/2}_{i,j,k_m+\frac{(-1)^{m+1}}{2}} \right\}_{STD} + (-1)^m \frac{\Delta t}{\mu \Delta z} E_x^{MoM}\Big|^n_{i,j,k_m}, \qquad (6.20)$$

and for $i = i_0, \cdots, i_1$; $k = k_0 + \frac{1}{2}, \cdots, k_1 - \frac{1}{2}$,

$$H_x\Big|^{n+1/2}_{i,j,k_m+\frac{(-1)^{m+1}}{2}} = \left\{ H_x\Big|^{n+1/2}_{i,j,k_m+\frac{(-1)^{m+1}}{2}} \right\}_{STD} + (-1)^{m+1} \frac{\Delta t}{\mu \Delta z} E_y^{MoM}\Big|^n_{i,j,k_m}. \qquad (6.21)$$

where the $\{\ \}_{STD}$ stands for the corresponding standard updating equations given by (2.10)

and (2.11) in Chapter 2. E^{MoM} and H^{MoM} denote the fields at the interfaces produced by the MoM.

The FDTD simulation yields scattering fields, which are imposed on the external problem as incident fields for the subsequent MOM simulation. The Fourier transform is used to link the frequency-domain MoM and the time-domain FDTD method.

6.4.3 Numerical Results

In this section the hybrid FDTD-MPIE method using the iterative solution approach is validated by several numerical examples.

6.4.3.1 Proximity-fed Rectangular DRAs

In this example a proximity-fed rectangular DRA is analyzed by the hybrid FDTD-MPIE method. The coupling between the microstrip line and the DRA is studied regarding different lateral gaps between them and different stub lengths of the microstrip line.

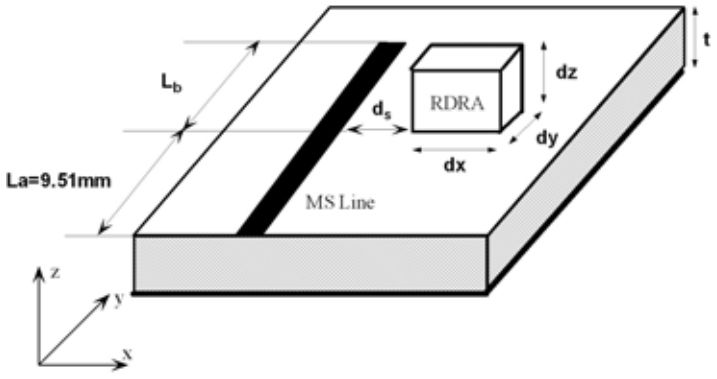

Fig. 6.10 Microstrip fed rectangular DRA.

The configuration of the proximity-fed DRA is shown in Fig. 6.10, where the dimensions of the DRA are dx=dy=9.51 mm and dz=3.18 mm ; six lengths of L_b are studied, which are

denoted as case A ($L_b = 1.59$ mm), case B ($L_b = 6.34$ mm), case C ($L_b = 9.51$ mm), case D ($L_b = 12.68$ mm), case E ($L_b = 15.85$ mm), and case F ($L_b = 20.61$ mm); and the lateral distance between the microstrip line and the rectangular DRA is denoted as $\mathbf{d_s}$. The dielectric constant of the rectangular DRA is $\varepsilon_r = 20.8$. In addition, the thickness of the substrate is $t = 0.635$ mm and the dielectric constant of it is $\varepsilon_r = 2.2$. The microstrip line has a width of 1.9 mm.

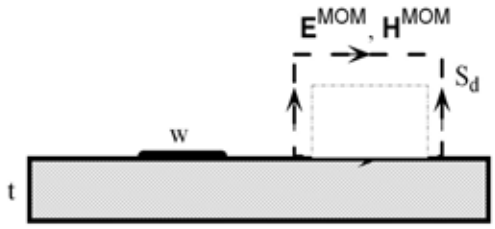

MOM Model

(a)

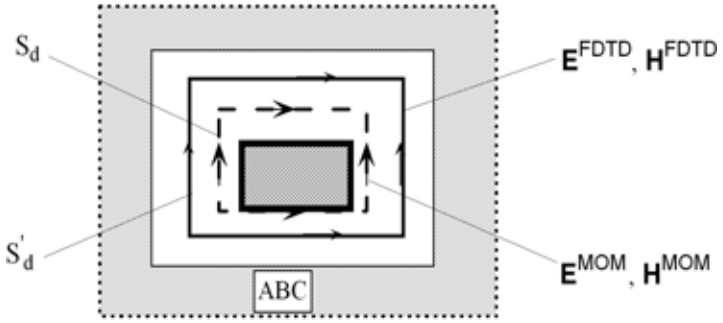

FDTD Model

(b)

Fig. 6.11 Illustration of iterative procedures for the microstrip fed rectangular DRA.

The FDTD model, the MoM model and their coupling during the iterative process are shown in Fig. 6.11. As shown in Fig. 6.11a, the MPIE-MoM is employed in the first iteration to solve the multilayered structure in the presence of the microstrip line but without the

rectangular DRA object. Applying the MoM leads to the solution of the fields on the virtual surface S_d, which are imposed on the subsequent FDTD simulation as external sources. By using the TF/SF technique, we can solve the scattered fields on S_d' due to the presence of the DRA object in the FDTD solution domain. These fields are treated as incident fields for the MoM model in the next iteration. This process is iterated until a steady state solution is achieved. For all the simulations in this example three to five iterations are needed to find an accurate solution.

The Yee cell size in the FDTD model is $\Delta x = \Delta y = 0.23775$ mm and $\Delta z = 0.212$ mm. The FDTD grid size is $56\Delta x \times 56\Delta y \times 31\Delta z$. For the MoM model the charge cell size is $\Delta x' = 0.633$ mm and $\Delta y' = 0.8453$ mm.

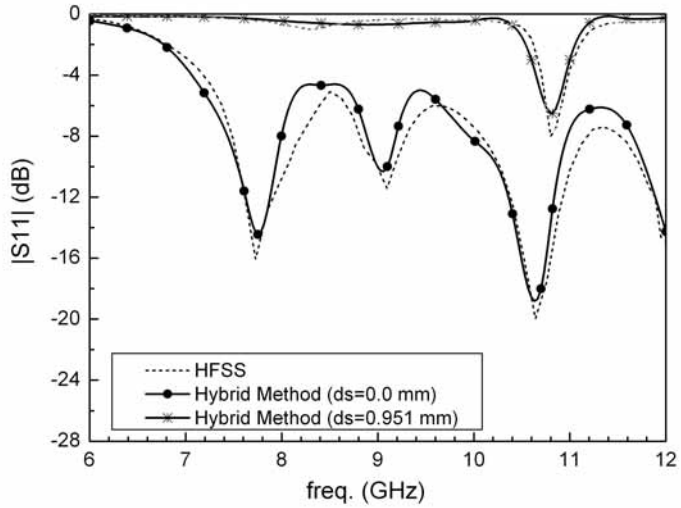

Fig. 6.12 Comparison of the results obtained by the hybrid method with those from the HFSS simulation.

In order to verify the proposed hybrid method, Case E with two different lateral distance ($\mathbf{d_s}$ = 0.0 mm and $\mathbf{d_s}$ = 0.951 mm) is studied in detail. Good agreements can be observed (Fig. 6.12) for the results of the reflection parameters obtained by the hybrid method and the Ansoft HFSS^{TM} commercial software, which verified the accuracy of the proposed hybrid

FDTD-MPIE method proposed in this chapter. Fig. 6.13 shows the convergence of the current at 10.5 GHz on the microstrip line during the iteration process, where three iterations are needed for the hybrid method to converge. For each frequency it takes about 15 to 20 minutes' CPU time on a PC. Compared to the memory usage of 35 MB by the HFSS, the hybrid method only requires less than 5 MB memory. Therefore, the hybrid method is more memory efficient.

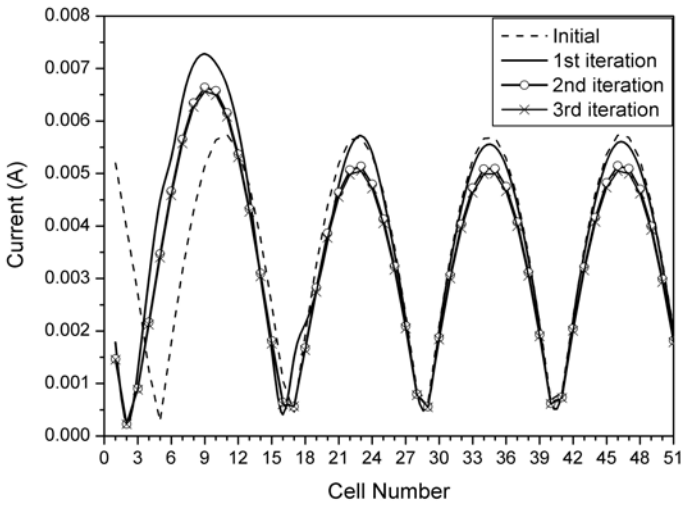

Fig. 6.13 Convergence of the surface current on the microstrip line during the iteration process of the hybrid method ($\mathbf{d_s} = 0.951$ mm).

Now all the six cases with different lengths of the microstrip stubs are analyzed by the hybrid method to study the impact of the stub length on the microstrip coupling effects. Furthermore, three lateral distances: $\mathbf{d_s} = 0.0$ mm , $\mathbf{d_s} = 0.951$ mm and $\mathbf{d_s} = 1.902$ mm are chosen to analyze how the lateral distances affect the magnitude of the coupling. All the results are shown in Fig. 6.14.

It can be seen from Fig. 6.14 that the lateral distance between the microstrip line and the DRA has great influence on their coupling magnitude. In this example, with the lateral distance increasing from 0.0 mm to 1.902 mm, the magnitude of the reflection coefficient is rapidly reduced by more than 80% of its original value. Furthermore, the increase in the lateral distance

shifts the corresponding resonant frequencies to a higher value.

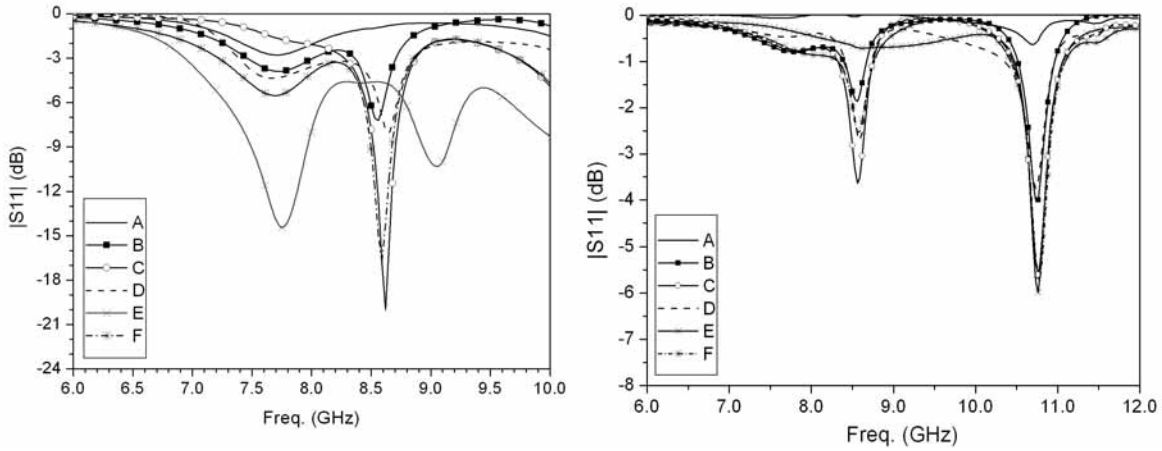

(a) $\mathbf{d_s}$ = 0.0 mm (b) $\mathbf{d_s}$ = 0.951 mm

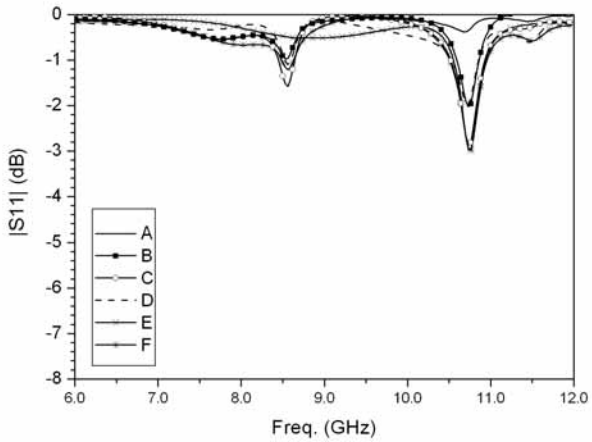

(c) $\mathbf{d_s}$ = 1.902 mm

Fig. 6.14 Reflection coefficients due to different lengths of microstrip stubs and different lateral distance between the microstrip line and the DRA.

Furthermore, we can observe from Fig. 6.14 that the lengths of the stubs of the microstrip feeding line can change the magnitude of the coupling to the DRA. Fig. 6.15 illustrates the reflection coefficients at 8.5 GHz due to different lengths of microstrip stubs in the case of $\mathbf{d_s}$ = 0.0 mm . The comparison shows that maximum coupling can be achieved by changing the length of the stubs. Moreover, the stubs with different lengths may cause some originally

existing maximum coupling disappear (see Fig. 6.14).

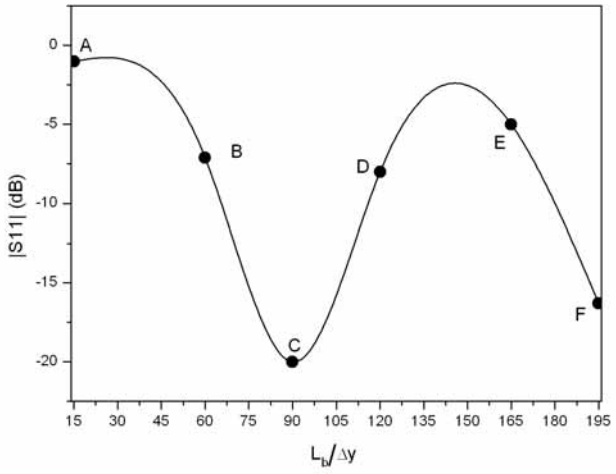

Fig. 6.15 Reflection coefficients at 8.5 GHz due to different lengths of microstrip stubs ($\mathbf{d}_s = 0.0$ mm).

6.4.3.2 Proximity-fed Multi-segment Rectangular DRAs

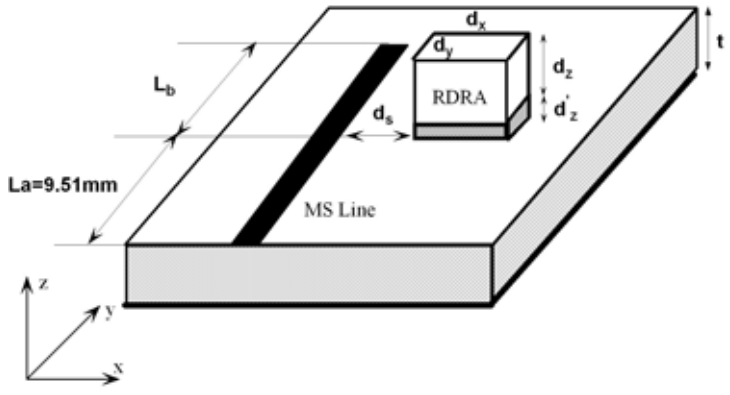

Fig. 6.16 Multi-segment rectangular DRA.

Although the microstrip-fed DRA is compatible with the printed circuits, the coupling between the microstrip line and the DRA is often small compared to other coupling methods. In general, high permittivity materials are needed for the DRA to achieve strong coupling. Conversely, the

DRA must have a low dielectric constant to achieve a wide bandwidth. Therefore, the multi-segment rectangular DRA is devised to resolve the dilemma [147].

In this section a multi-segment rectangular DRA is examined by the hybrid method to study the influence of the thickness and permittivity of the inserted segment on the magnitude of the coupling between the microstrip line and the DRA.

The configuration of the multi-segment rectangular DRA is shown in Fig. 6.16, where the thickness of the inserted segment is denoted as $\mathbf{d}_z'$. The substrate and the dimensions of the DRA are the same as those in the previous example, but a low dielectric constant of the DRA is used, i.e., $\varepsilon_r = 6.5$. In the following simulation the lateral distance $\mathbf{d}_s$ is set to be zero and $L_b = 9.51$ mm (Case C in the previous example).

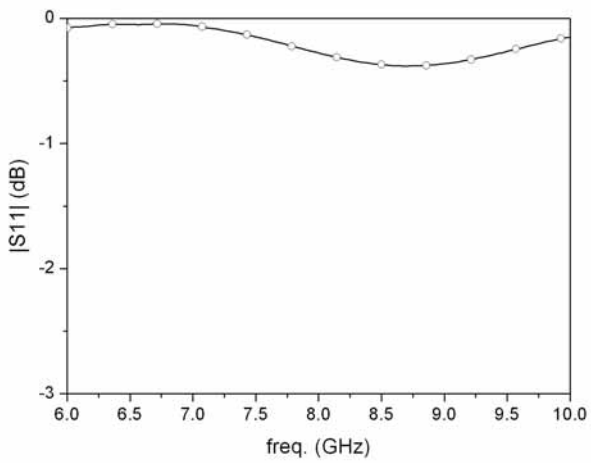

Fig. 6.17 Reflection coefficient of the rectangular DRA without inserted segments.

It can be seen from Fig. 6.17 that for the DRA without inserted segments, the coupling of the microstrip line to the DRA is very small because of the low dielectric constant of the DRA ($\varepsilon_r = 6.5$), which is consistent with the previous discussion. For the studied bandwidth of 6 GHz to 10 GHz, only the DRA with the inserted segment having a length of 1.696 mm can produce a strong coupling and wide bandwidth. Fig. 6.18 illustrates the impact of the

permittivity of the inserts (the thickness of the inserts is fixed as 0.951 mm) on the coupling between the microstrip line and the DRA. The useful strong coupling cannot be excited in this example. However, it can be inferred that by adjusting the thickness and the permittivity of the inserted segments simultaneously, an optimal coupling and wide bandwidth of the rectangular DRA can be achieved. Furthermore, inserting more segments with different permittivity can also achieve the goals of optimal coupling and wide bandwidth [147].

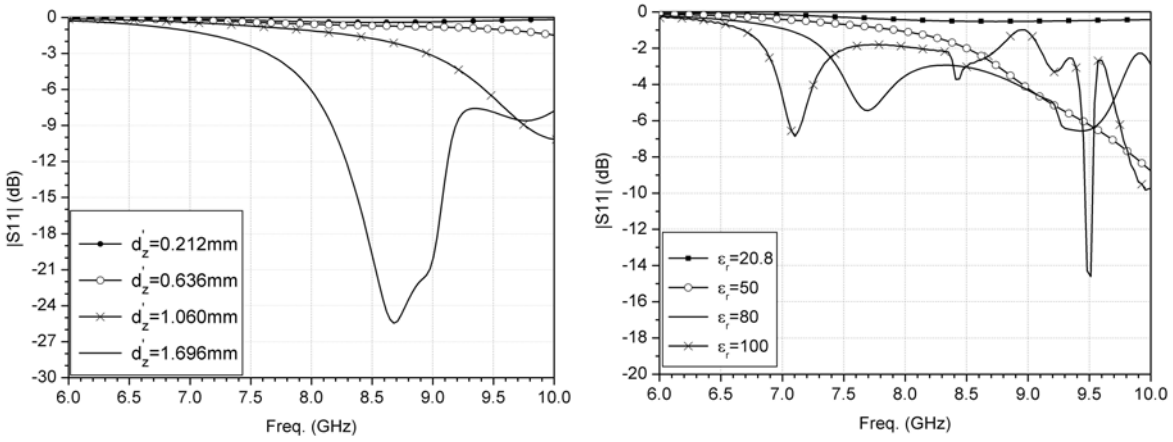

(a) (b)

Fig. 6.18 Reflection coefficient of the rectangular DRA with inserted segments: (a) the relative permittivity of the inserts is 30 but the thickness is different; (b) the thickness of the inserts is 0.633 mm but the permittivity is different.

6.4.3.3 Aperture-fed Rectangular DRA

An aperture-fed rectangular DRA [148] is shown in Fig. 6.19. The aperture is made of a slot cut in the ground plane covering the substrate. The DRA is fed by a microstrip line located at the bottom surface of the substrate. The length of the microstrip stub is 3 mm. The dimensions and other parameters shown in Fig. 6.19 are used for nominal design at 5.5 GHz.

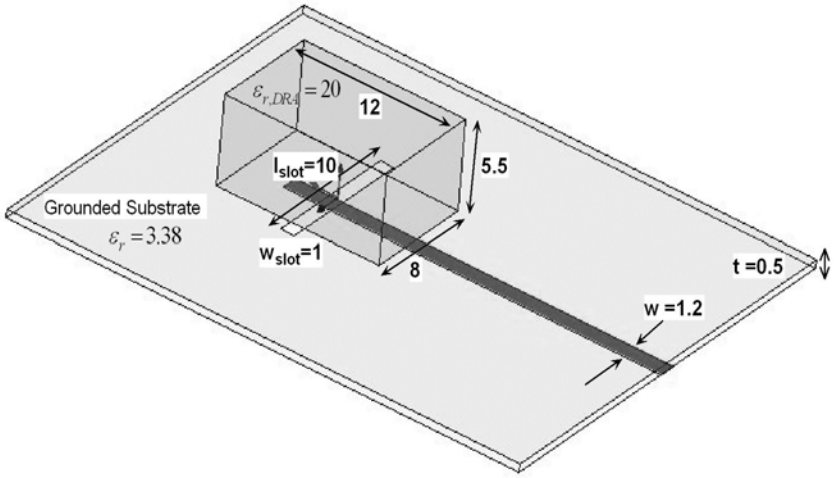

Fig. 6.19 An aperture-fed rectangular DRA (Unit: mm).

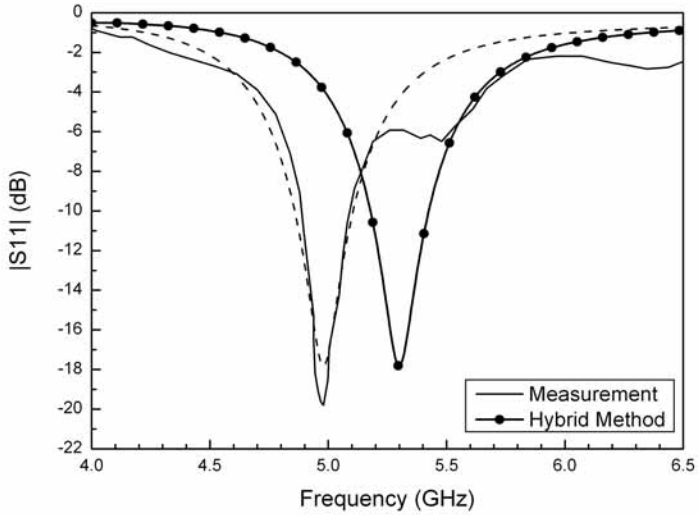

Fig. 6.20 Reflection parameters of an aperture-fed rectangular DRA.

In order to implement the hybrid FDTD-MPIE method, the slot area is designated as the virtual surface to connecting the two models. The FDTD model is used for the internal equivalent problem of the DRA on a ground PEC; and the MPIE model for the external equivalent problem of a microstrip line on a grounded substrate. The reflection parameters computed by the hybrid method are compared with the measurement results reported in [148] (See Fig. 6.20). The dashed line in Fig. 6.20 is the original computational results (represented by a solid line with dots) shifted by 0.3 GHz, which shows that the computational results agree

well with measurement results except for the 0.3 GHz frequency shift. Taking into consideration the nominal design frequency of 5.5 GHz, we can conclude that the computational results are more accurate. The discrepancy between the computational results and the measurement data is probably due to the fabrication tolerance.

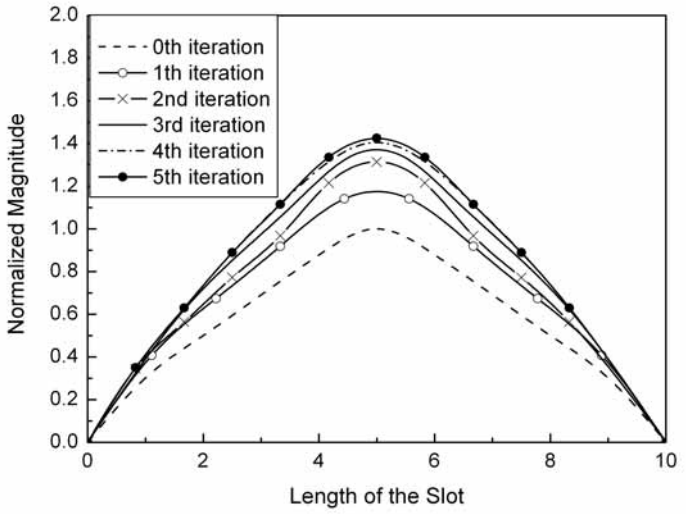

Fig. 6.21 Convergence of the equivalent magnetic currents on the slot surface. The magnitude of the magnetic currents is normalized by the maximum current at the zero-th iteration step.

It takes 3 to 5 iterations for the hybrid method to converge, i.e., the relative error of the currents at two consecutive iteration steps is less than 0.5%. The memory usage is about 10 MB and the CPU time is 25 to 45 minutes for each sampling frequency in Fig. 6.20. We also show in Fig. 6.21 the convergence of the equivalent magnetic currents at 5.3 GHz during the iteration process, where five iterations are needed for the hybrid method to produce an accurate results.

6.4.3.4 Aperture-coupled Rectangular DRA Array

An aperture-coupled rectangular DRA array [149] is shown in Fig. 6.22. It consists four identical aperture-coupled rectangular DRAs and is fed by a corporate feeding network.

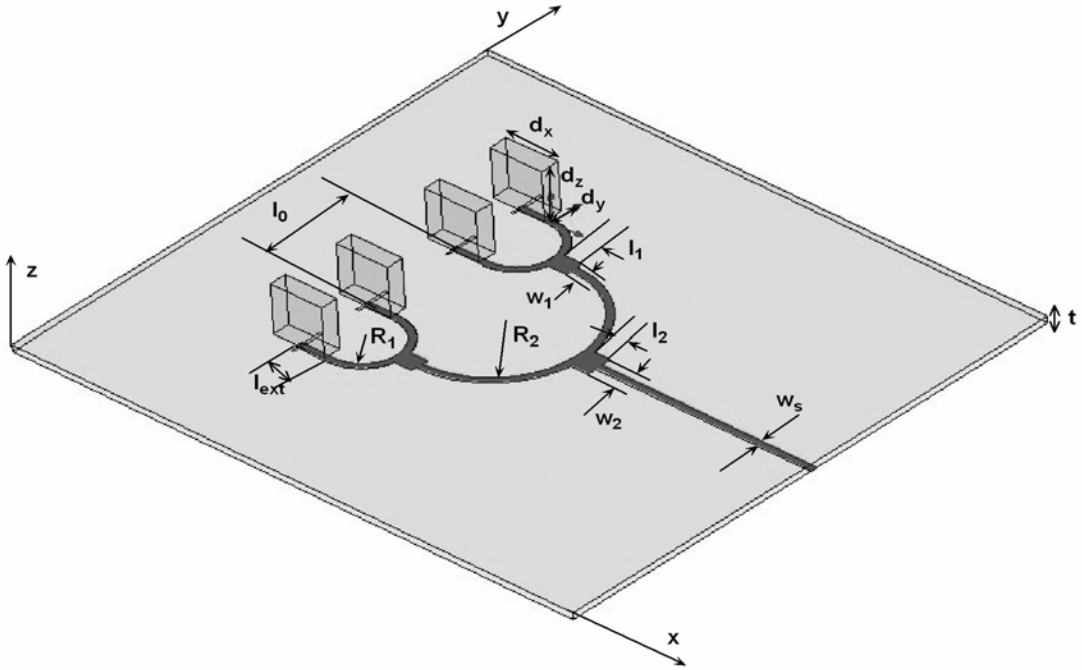

Fig. 6.22 Aperture-coupled rectangular DRA array (Unit: mm). Four identical aperture-coupled DRAs are fed by a corporate feed network. The slot has a width of 0.1 and a length of 1.16. Other parameters are listed as follows --- The DRA: $d_x = dz = 1.91$, $d_z = 0.635$ and $\varepsilon_r = 9.4$; The microstrip: $w_s = 0.25$; The substrate: $t = 0.254$ and $\varepsilon_r = 9.4$; The corporate feed network: $R_1 = 1.32$, $l_1 = 0.647$, $w_1 = 0.67$, $R_2 = 3.05$, $l_2 = 0.67$, $w_2 = 0.932$, $l_{ext} = 1.005$, and $l_0 = 3.57$.

Compared to the previous example, this example is more complex but the hybrid method can be applied in the same way. It takes 3 to 8 iterations for the hybrid method to produce an accurate results. During the course of the iteration, the equivalent magnetic currents on the slot surfaces vary in the same pattern as those shown in Fig. 6.21. The HFSS is also used to modeling the DRA array. The good agreement of the reflection parameters between the computational and the HFSS results shows that the hybrid method is accurate.

Compared to the HFSS simulation which uses about 617 MB memory and 15 minutes' CPU time for each sampling frequency, the hybrid method only requires less than 30 MB memory and the CPU time for each sampling frequency ranges from 20 to 50 minutes. Therefore, we can conclude again that the hybrid method is more memory efficient and fairly fast and efficient.

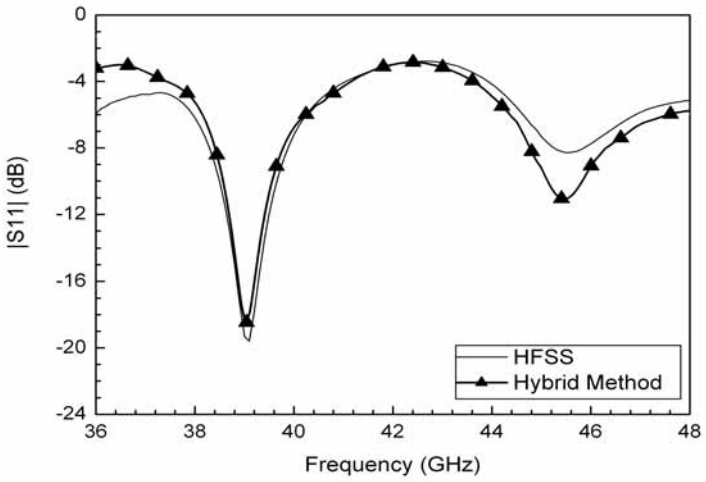

Fig. 6.23 Reflection coefficients for the aperture-coupled Rectangular DRA array.

6.4.3.5 Buried Object in a Three-layer Structure

A cubic object buried in a three-layer structure [150] is shown in Fig. 6.24. A short dipole is placed in the first layer to detect it. The operating frequency of the dipole is 100 MHz.

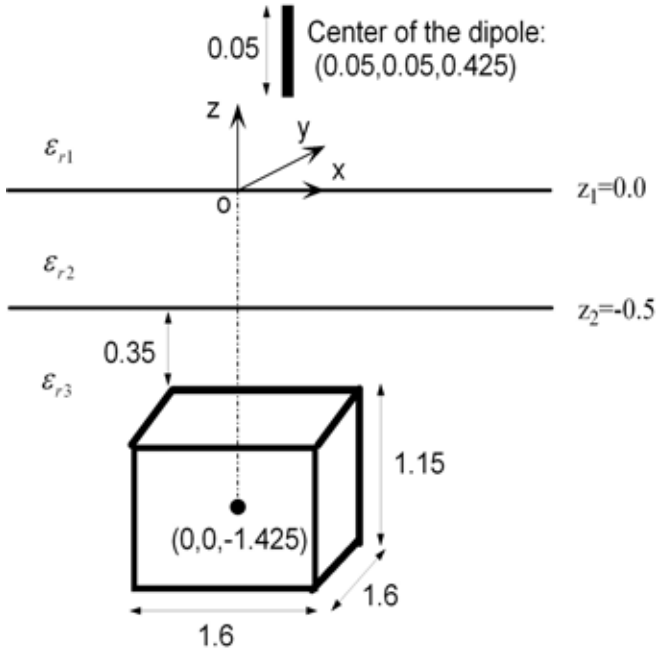

Fig. 6.24. Configuration of a cube ($\varepsilon_r = 9.0$, $\sigma = 0.02$) buried in a three-layer ($\varepsilon_r = 1.0$, 1.21 , and 1.44) structure (Unit of length: m).

In order to use the hybrid method, a virtual surface enclosing the cubic object is placed six FDTD cells away from the surfaces of the object. The FDTD cell size used in the hybrid method is $\Delta x' = \Delta y' = \Delta z' = 0.025$ m and the grid size of the FDTD domain is $74\Delta x \times 74\Delta y \times 74\Delta z$. Three iterations are needed for the hybrid method to converge (Fig. 6.25).

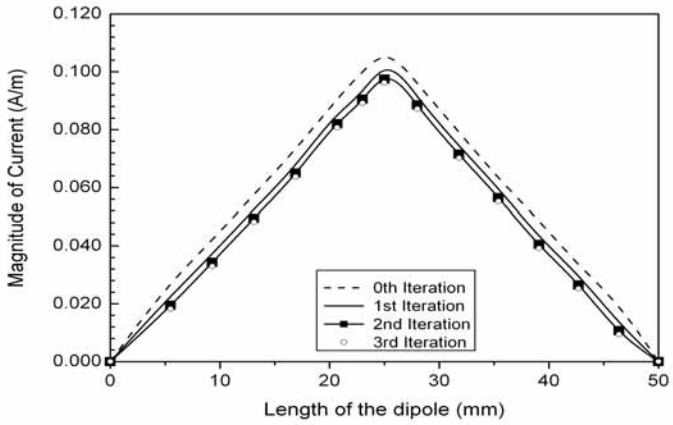

Fig. 6.25. Convergence of the current along the dipole during the iteration process.

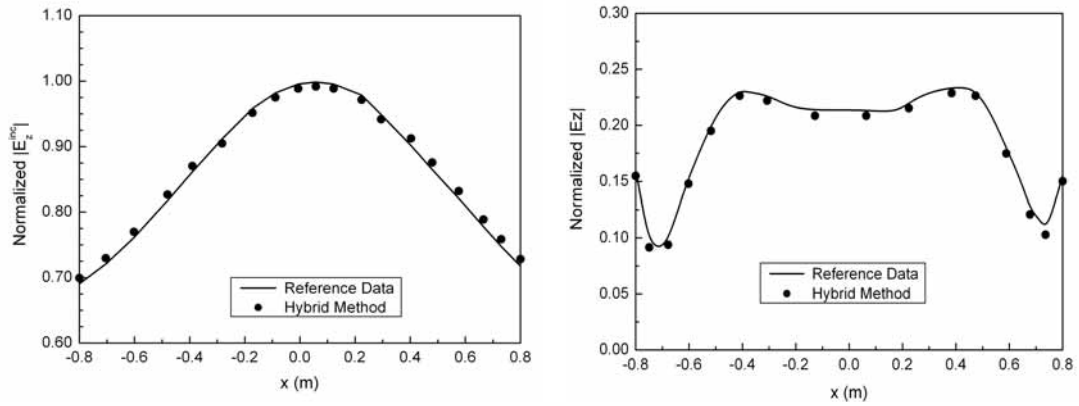

(a) (b)

Fig. 6.26. (a) The incident electric field E_z^{inc} and (b) the total field E_z at $y = -0.15$ m, $z = -1.125$ m and $x \in (-0.8\text{ m}, 0.8\text{ m})$. The reference data is taken from [150].

Fig. 6.26 and Fig. 6.27 show the computational results, where all the electric fields are normalized by the maximum value of E_z^{inc} at $x = 0$ in Fig. 6.26(a). Good agreements can be

observed between the computational results and those presented in [150]. But compared to the FDTD simulation reported in [150] which requires 212 MB memory and more than 6 hours' CPU time, the hybrid method only requires 7.52 MB memory and 32 minutes' CPU time. Therefore, the hybrid method is accurate, fairly fast and more memory efficient.

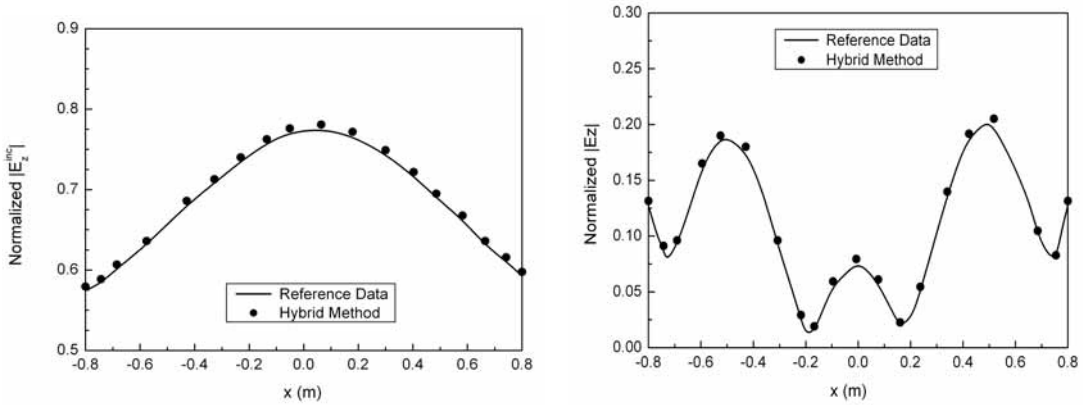

(a) (b)

Fig. 6.27. (a) The incident electric field E_z^{inc} and (b) the total field E_z at $y = 0.05$ m, $z = -1.375$ m and $x \in (-0.8\text{ m}, 0.8\text{ m})$. The reference data is also taken from [150].

6.5 Summary

A new hybrid FDTD-MPIE method is proposed and implemented in this chapter. It can take advantage of the FDTD method for the treatment of inhomogeneous objects and the MPIE method for the solution of multilayered structures. Its implementation and solution by both the direct and iterative approaches are discussed, which shows that the latter approach is more efficient. Numerical experiments also validate that compared to non-hybrid methods and commercial software for the analysis of multilayered structures with locally inhomogeneous penetrable objects, the hybrid method using the iterative solution approach is accurate, fairly fast and more memory efficient.

Chapter 7. Conclusions and Future Work

In this chapter we first conclude this thesis and then discuss the limitations and future work.

7.1 Conclusions

This thesis focuses on developing accurate and efficient numerical methods to analyze high-speed interconnects and multilayer circuits as well as perform mixed electromagnetic (EM) and circuit simulation.

Firstly, the FDTD-macromodeling method was proposed in this thesis for analysis of the mixed EM and circuit problem. Numerical results showed the validity and efficiency of the proposed method.

Two factors contribute to the successful application of the FDTD-macromodeling method for the analysis of the mixed EM and circuit system: 1) The electromagnetic effects of the high-speed interconnects are well accounted for by the full-wave FDTD analysis; 2) The macromodeling approach usually transforms an interconnect subnetwork into low-order equivalent circuits, which overcomes the mixed frequency/time domain problem and facilitates the analysis of the mixed EM and circuit problem by the SPICE simulator.

In summary, the FDTD-macromodeling method, which integrates the FDTD method, the macromodeling approach and the SPICE circuit simulator, is suitable for the analysis of mixed EM and circuit problems to account for the high-speed interconnect effects. Furthermore, the numerical results in this thesis suggest that the FDTD-macromodeling approach may greatly enhance the flexibility of the SPICE simulator for analysis of mixed EM and circuit problems. Such a circuit-oriented approach can greatly reduce the simulation time compared to the totally EM-oriented approach.

Secondly, a hybrid FDTD-MPIE (Finite-difference time-domain and mixed-potential integral equation) method was proposed in this thesis to efficiently analyze multilayered structures with locally inhomogeneous penetrable objects. The Green's functions for multilayer media were extended to account for general electric and magnetic sources. Both the numerical integration method with large argument extractions and the DCIM method were employed to evaluate the Sommerfeld integrals and compute the spatial-domain Green's functions. Both the direct and the iterative approaches were discussed and applied to solving the hybrid FDTD-MPIE model.

Numerical examples demonstrated that the iterative method is more efficient than the direct one, and the new hybrid method can take advantage of the FDTD method for the treatment of inhomogeneous objects and the MPIE method for the solution of multilayered structures. Compared to non-hybrid methods and commercial software for the analysis of multilayered structures with locally inhomogeneous penetrable objects, the hybrid method using the iterative solution approach is accurate, fairly fast and more memory efficient.

7.2 Limitations and Future Work

It should be acknowledged that the numerical approaches presented in this thesis have some limitations.

It is assumed in this thesis that the interconnects and the circuit components in the mixed EM and circuit problem can be physically separated into independent parts. Therefore, the FDTD-macromodeling method may not account well for the strong coupling among tightly packed components in an IC. Nevertheless, the FDTD-macromodeling method proposed in this thesis can still have wide applications in the analysis of off-chip interconnects and packaging problems.

In addition, passivity check of the macromodel is still an ongoing research topic. Because of time constraints, simple approaches for passivity check and passive model construction will be the future research topic of this thesis.

Other interesting topics will also be attempted in the future, which include 1) hybridizing the finite-difference and MoM method both in the time domain; and 2) developing robust and efficient methods for surface-wave pole extraction to further enhance the capability of the DCIM method for the evaluation of multilayer-media Green's functions.

Appendix A Netlist Example

In this appendix we show a netlist used for the SPICE simulation of the example in Section 3.4.1.3 of Chapter 3. The configuration of the circuit is shown in Fig. 3.11. A macromodel based on the scattering parameters, which has two real poles and nine pairs of complex conjugate poles, is created by the vector fitting method. Since the interconnect subnetwork has two ports, totally forty-eight state variables present in the state space equations.

The netlist for the circuit in Fig. 3.11 is given below, which contains both the equivalent circuit of the macromodel and other external lumped circuit elements:

```
*==============================
**********Netlist for transient simulation of the circuit including LPF-type microstrip ************
*==============================

*Transient simulation of the circuit including LPF-type microstrip
*.OPTIONS LIST NODE POST
*Change the integral method from trapezoidal to gear one for smooth results
*.options method=gear
.OP
.nodeset v(700)=0.0 v(800)=0.0
*Transient simulation
.TRAN 0.05ns 12ns
.PRINT TRAN v(702) v(700) V(800)
.PLOT TRAN v(702) v(800)

**********************************
*Circuit Branch #i1
*Input pulse
*vin 702 0 pulse (0 2. 0.1ns 0.1ns 0.1ns 0.5ns 1ns)
vin 702 0 pulse (0 2. 0.1ns 0.1ns 0.1ns 2ns 6ns)
Rp1 700 701 50.0
*Add a dummy independent voltage
vi1 701 703 0.0
Hp1 703 0 vb1 14.142

rin1 702 700 5
*cin1 700 0 80e-12

**********************************
*Circuit Branch #i2
Rp2 800 801 50.0
vi2 801 802 0.0
Hp2 802 0 vb2 14.142

rin2 800 0 50
cin2 800 0 10pf

**********************************
*Circuit branch   #b(a)1
GV101 100 0   1 0        28989690.2888
GV102 100 0   2 0        32605017.4104
GV103 100 0   3 0     57826473909.0225
GV104 100 0   4 0     79936283399.8959
GV105 100 0   5 0         5950453.3978
GV106 100 0   6 0         4183546.0489
GV107 100 0   7 0        23970135.6511
```

```
GV108 100 0   8 0        35649177.9733
GV109 100 0   9 0        -6404357.2008
GV110 100 0 10 0         -9655356.3274
GV111 100 0 11 0          8248047.0061
GV112 100 0 12 0         17707455.4126
GV113 100 0 13 0          -277698.0375
GV114 100 0 14 0          2286955.9474
GV115 100 0 15 0          2130555.7865
GV116 100 0 16 0          5739228.3003
GV117 100 0 17 0       7862815585.4303
GV118 100 0 18 0        329217643.1214
GV119 100 0 19 0       1116131844.7196
GV120 100 0 20 0       6243253389.4539
GV121 100 0 21 0      -5053575237.1981
GV122 100 0 22 0       5023708896.6805
GV123 100 0 23 0      -1160366210.6673
GV124 100 0 24 0       1244198468.0503
GV125 100 0 25 0     138291332657.2460
GV126 100 0 26 0     -13900475879.9272
GV127 100 0 27 0     110714027302.7750
GV128 100 0 28 0      80465979969.7344
GV129 100 0 29 0      -1311480178.1968
GV130 100 0 30 0      -1175489096.5674
GV131 100 0 31 0      11225297045.9511
GV132 100 0 32 0      11320908593.4714
GV133 100 0 33 0    -152311343692.7990
GV134 100 0 34 0     -41184879687.5278
GV135 100 0 35 0     134126783379.0180
GV136 100 0 36 0     -75220467167.2941
GV137 100 0 37 0     -11424597876.1514
GV138 100 0 38 0      10539079874.6883
GV139 100 0 39 0     -22839348075.4080
GV140 100 0 40 0      23639378792.9892
GV141 100 0 41 0       -373378829.7843
GV142 100 0 42 0       -395380816.9644
GV143 100 0 43 0        358109060.0926
GV144 100 0 44 0        411651047.0239
GV145 100 0 45 0       3143334853.7062
GV146 100 0 46 0        840418037.0925
GV147 100 0 47 0     -63921114241.9924
GV148 100 0 48 0       4848268377.8118
*item by d12
GV149 100 0 200 0   -0.0062984
*item by 1/d11
Rd1     100 0 34.698
Ev100 101 102 700 0 0.07071
Hi100 102 0 vi1 3.536
vb1 101 100 0.0

**********************************
*Circuit branch   #b(a)2
GV201 200 0   1 0        32605017.4104
GV202 200 0   2 0        28989690.2888
GV203 200 0   3 0     79936283399.8959
GV204 200 0   4 0     57826473909.0225
GV205 200 0   5 0         4183546.0489
GV206 200 0   6 0         5950453.3978
GV207 200 0   7 0        35649177.9733
GV208 200 0   8 0        23970135.6511
GV209 200 0   9 0        -9655356.3274
GV210 200 0 10 0         -6404357.2008
GV211 200 0 11 0         17707455.4126
GV212 200 0 12 0          8248047.0061
GV213 200 0 13 0          2286955.9474
GV214 200 0 14 0          -277698.0375
GV215 200 0 15 0          5739228.3003
GV216 200 0 16 0          2130555.7865
GV217 200 0 17 0        329217643.1214
GV218 200 0 18 0       7862815585.4303
GV219 200 0 19 0       6243253389.4539
GV220 200 0 20 0       1116131844.7196
GV221 200 0 21 0       5023708896.6805
GV222 200 0 22 0      -5053575237.1981
GV223 200 0 23 0       1244198468.0503
GV224 200 0 24 0      -1160366210.6673
GV225 200 0 25 0     -13900475879.9272
GV226 200 0 26 0     138291332657.2460
GV227 200 0 27 0      80465979969.7344
GV228 200 0 28 0     110714027302.7750
GV229 200 0 29 0      -1175489096.5674
GV230 200 0 30 0      -1311480178.1968
GV231 200 0 31 0      11320908593.4714
GV232 200 0 32 0      11225297045.9511
GV233 200 0 33 0     -41184879687.5278
GV234 200 0 34 0    -152311343692.7990
GV235 200 0 35 0     -75220467167.2941
GV236 200 0 36 0     134126783379.0180
GV237 200 0 37 0      10539079874.6883
```

```
GV238 200 0 38 0     -11424597876.1514
GV239 200 0 39 0      23639378792.9892
GV240 200 0 40 0     -22839348075.4080
GV241 200 0 41 0       -395380816.9644
GV242 200 0 42 0       -373378829.7843
GV243 200 0 43 0        411651047.0239
GV244 200 0 44 0        358109060.0926
GV245 200 0 45 0        840418037.0925
GV246 200 0 46 0       3143334853.7062
GV247 200 0 47 0       4848268377.8118
GV248 200 0 48 0     -63921114241.9924
GV249 200 0 100 0   -0.0062984
Rd2     200 0 34.698
Ev200 201 202 800 0 0.07071
Hi200 202 0 vi2 3.536
vb2 201 200 0.0

**********
*Circuit branch #x1 to x48
Cn1 0 1 1.0e-9
Rn1 0 1     2.1728
GV301 0 1 100 0 1.0e-9
Cn2 0 2 1.0e-9
Rn2 0 2     2.1728
GV302 0 2 200 0 1.0e-9

Cn3 0 3 1.0e-9
Rn3 0 3      .0509
GV303 0 3 100 0 1.0e-9
Cn4 0 4 1.0e-9
Rn4 0 4      .0509
GV304 0 4 200 0 1.0e-9

Cn5 0   5 1.0e-9
Rn5 0   5     1.1205
Gv305 0   5 100 0 2.0e-9
Gv405 0   5   7 0           .25652852E+01
Cn6 0   6 1.0e-9
Rn6 0   6     1.1205
Gv306 0   6 200 0 2.0e-9
Gv406 0   6   8 0           .25652852E+01
Cn7 0   7 1.0e-9
Rn7 0   7     1.1205
Gv307 0   7   5 0          -.25652852E+01
Cn8 0   8 1.0e-9
Rn8 0   8     1.1205
Gv308 0   8   6 0          -.25652852E+01

Cn9 0   9 1.0e-9
Rn9 0   9     1.2337
Gv309 0   9 100 0 2.0e-9
Gv409 0   9 11 0           .51802726E+01
Cn10 0 10 1.0e-9
Rn10 0 10     1.2337
Gv310 0 10 200 0 2.0e-9
Gv410 0 10 12 0           .51802726E+01
Cn11 0 11 1.0e-9
Rn11 0 11     1.2337
Gv311 0 11   9 0          -.51802726E+01
Cn12 0 12 1.0e-9
Rn12 0 12     1.2337
Gv312 0 12 10 0          -.51802726E+01

Cn13 0 13 1.0e-9
Rn13 0 13     2.0517
Gv313 0 13 100 0 2.0e-9
Gv413 0 13 15 0           .86437486E+01
Cn14 0 14 1.0e-9
Rn14 0 14     2.0517
Gv314 0 14 200 0 2.0e-9
Gv414 0 14 16 0           .86437486E+01
Cn15 0 15 1.0e-9
Rn15 0 15     2.0517
Gv315 0 15 13 0          -.86437486E+01
Cn16 0 16 1.0e-9
Rn16 0 16     2.0517
Gv316 0 16 14 0          -.86437486E+01

Cn17 0 17 1.0e-9
Rn17 0 17      .0684
Gv317 0 17 100 0 2.0e-9
Gv417 0 17 19 0           .27809138E+02
Cn18 0 18 1.0e-9
Rn18 0 18      .0684
Gv318 0 18 200 0 2.0e-9
Gv418 0 18 20 0           .27809138E+02
Cn19 0 19 1.0e-9
Rn19 0 19      .0684
```

```
Gv319 0 19 17 0          -.27809138E+02
Cn20 0 20 1.0e-9
Rn20 0 20      .0684
Gv320 0 20 18 0          -.27809138E+02

Cn21 0 21 1.0e-9
Rn21 0 21      .2734
Gv321 0 21 100 0 2.0e-9
Gv421 0 21 23 0          .33463721E+02
Cn22 0 22 1.0e-9
Rn22 0 22      .2734
Gv322 0 22 200 0 2.0e-9
Gv422 0 22 24 0          .33463721E+02
Cn23 0 23 1.0e-9
Rn23 0 23      .2734
Gv323 0 23 21 0          -.33463721E+02
Cn24 0 24 1.0e-9
Rn24 0 24      .2734
Gv324 0 24 22 0          -.33463721E+02

Cn25 0 25 1.0e-9
Rn25 0 25      .0347
Gv325 0 25 100 0 2.0e-9
Gv425 0 25 27 0          .38518510E+02
Cn26 0 26 1.0e-9
Rn26 0 26      .0347
Gv326 0 26 200 0 2.0e-9
Gv426 0 26 28 0          .38518510E+02
Cn27 0 27 1.0e-9
Rn27 0 27      .0347
Gv327 0 27 25 0          -.38518510E+02
Cn28 0 28 1.0e-9
Rn28 0 28      .0347
Gv328 0 28 26 0          -.38518510E+02

Cn29 0 29 1.0e-9
Rn29 0 29      .1582
Gv329 0 29 100 0 2.0e-9
Gv429 0 29 31 0          .63803338E+02
Cn30 0 30 1.0e-9
Rn30 0 30      .1582
Gv330 0 30 200 0 2.0e-9
Gv430 0 30 32 0          .63803338E+02
Cn31 0 31 1.0e-9
Rn31 0 31      .1582
Gv331 0 31 29 0          -.63803338E+02
Cn32 0 32 1.0e-9
Rn32 0 32      .1582
Gv332 0 32 30 0          -.63803338E+02

Cn33 0 33 1.0e-9
Rn33 0 33      .0313
Gv333 0 33 100 0 2.0e-9
Gv433 0 33 35 0          .83562324E+02
Cn34 0 34 1.0e-9
Rn34 0 34      .0313
Gv334 0 34 200 0 2.0e-9
Gv434 0 34 36 0          .83562324E+02
Cn35 0 35 1.0e-9
Rn35 0 35      .0313
Gv335 0 35 33 0          -.83562324E+02
Cn36 0 36 1.0e-9
Rn36 0 36      .0313
Gv336 0 36 34 0          -.83562324E+02

Cn37 0 37 1.0e-9
Rn37 0 37      .0877
Gv337 0 37 100 0 2.0e-9
Gv437 0 37 39 0          .97769064E+02
Cn38 0 38 1.0e-9
Rn38 0 38      .0877
Gv338 0 38 200 0 2.0e-9
Gv438 0 38 40 0          .97769064E+02
Cn39 0 39 1.0e-9
Rn39 0 39      .0877
Gv339 0 39 37 0          -.97769064E+02
Cn40 0 40 1.0e-9
Rn40 0 40      .0877
Gv340 0 40 38 0          -.97769064E+02

Cn41 0 41 1.0e-9
Rn41 0 41      .5754
Gv341 0 41 100 0 2.0e-9
Gv441 0 41 43 0          .12556490E+03
Cn42 0 42 1.0e-9
Rn42 0 42      .5754
Gv342 0 42 200 0 2.0e-9
Gv442 0 42 44 0          .12556490E+03
```

```
Cn43 0 43 1.0e-9
Rn43 0 43      .5754
Gv343 0 43 41 0          -.12556490E+03
Cn44 0 44 1.0e-9
Rn44 0 44      .5754
Gv344 0 44 42 0          -.12556490E+03

Cn45 0 45 1.0e-9
Rn45 0 45      .0449
Gv345 0 45 100 0 2.0e-9
Gv445 0 45 47 0           .12478756E+03
Cn46 0 46 1.0e-9
Rn46 0 46      .0449
Gv346 0 46 200 0 2.0e-9
Gv446 0 46 48 0           .12478756E+03
Cn47 0 47 1.0e-9
Rn47 0 47      .0449
Gv347 0 47 45 0          -.12478756E+03
Cn48 0 48 1.0e-9
Rn48 0 48      .0449
Gv348 0 48 46 0          -.12478756E+03

 .End
```

Appendix B Sommerfeld Integral and Its Properties

B.1 Sommerfeld Integral

Since the spatial-domain MPIE is used in this thesis with the MoM, it is necessary to transform Green's functions from the spectral domain to the spatial domain. It is realized by the two-dimensional inverse Fourier transform:

$$\mathcal{F}^{-1}\left[\tilde{f}(\mathbf{k}_\rho;z)\right]=f(\boldsymbol{\rho};z)=\frac{1}{(2\pi)^2}\int_{-\infty}^{+\infty}\int_{-\infty}^{+\infty}\tilde{f}(\mathbf{k}_\rho;z)e^{j\mathbf{k}_\rho\cdot\boldsymbol{\rho}}dk_x dk_y\,. \tag{B.1}$$

By applying the following equations:

$$\begin{aligned} x&=\rho\cos\phi, & k_x&=k_\rho\cos\xi\\ y&=\rho\sin\phi, & k_y&=k_\rho\sin\xi \end{aligned} \tag{B.2}$$

where ϕ denotes the azimuthal angle and ξ is shown in Fig. 4.2, we can express (B.1) as [98]

$$f(\boldsymbol{\rho};z)=\frac{1}{(2\pi)^2}\int_0^{2\pi}d\xi\int_0^{\infty}\tilde{f}(k_\rho;\xi)e^{jk_\rho\rho\cos(\xi-\phi)}k_\rho\,dk_\rho\,. \tag{B.3}$$

Notice that for the transverse unbounded problem, the following property of rotational symmetry can be applied:

$$\tilde{f}(k_\rho;\xi)=\tilde{f}(k_\rho) \tag{B.4}$$

Moreover, the exponential term in (B.3) can be expanded using the following Jacobi-Anger identity [151]:

$$e^{jk_\rho \rho \cos(\xi-\phi)} = J_0(k_\rho \rho) + 2\sum_{n=1}^{\infty} j^n J_0(k_\rho \rho)\cos\left[n(\xi-\phi)\right], \tag{B.5}$$

which implies that a plane wave can be expanded as a series of cylindrical waves.

Substituting (B.4) and (B.5) into (B.3) and performing the integration w.r.t ξ, we can finally obtain (for $n=0$) the following well-known Sommerfeld integral [90]:

$$f(\boldsymbol{\rho}, z) = S_0[\tilde{f}(k_\rho, z)] = \frac{1}{2\pi}\int_0^{\infty} \tilde{f}(k_\rho, z)\, J_0(k_\rho \rho)\, k_\rho \, dk_\rho \tag{B.6}$$

which can be generalized to the n-th order:

$$S_n[\tilde{f}(k_\rho, z)] = \frac{1}{2\pi}\int_0^{\infty} \tilde{f}(k_\rho, z)\, J_n(k_\rho \rho)\, k_\rho^{n+1}\, dk_\rho . \tag{B.7}$$

B.2 Properties of Sommerfeld Integral

One important property of the zero-th order Sommerfeld integral, which is also the foundation of the DCIM method, is the Sommerfeld identity [90]:

$$\frac{e^{-jkr}}{r} = \int_0^{\infty} \frac{1}{jk_z} \cdot e^{-jk_z|z|} J_0(k_\rho \rho)\, k_\rho dk_\rho \tag{B.8}$$

where $r = \sqrt{\rho^2 + |z|^2}$. The physical interpretation of the Sommerfeld identity is that a spherical wave can be expanded as an integral summation of cylindrical waves in the ρ

direction multiplying a plane wave in the z direction over wave numbers k_ρ [91].

By using the following property of the first kind Bessel function [151]:

$$\frac{\partial J_0(k_\rho \rho)}{k_\rho \partial \rho} = -J_1(k_\rho \rho), \tag{B.9}$$

equation (B.8) can be generalized to its first-order form [97]:

$$(1+jkr)\frac{\rho e^{-jkr}}{r^3} = \int_0^\infty \frac{1}{jk_z} \cdot e^{-jk_z|z|} J_1(k_\rho \rho) k_\rho^2 dk_\rho . \tag{B.10}$$

Another useful identity for the Sommerfeld integral takes the following form [152]:

$$\int_0^\infty e^{-k_\rho \Delta} J_0(k_\rho \rho) k_\rho dk_\rho = \frac{\Delta}{\sqrt{\left(\rho^2 + \Delta^2\right)^3}}. \tag{B.11}$$

Appendix C Transmission Line Green's Functions

Due to the linearity of the transmission line equations in (4.21), the superposition property can be applied to solve V^p and I^p [84, 86]:

$$\begin{aligned} V^p &= < V_v^p, v^p > + < V_i^p, i^p > \\ I^p &= < I_v^p, v^p > + < I_i^p, i^p > \end{aligned} \tag{C.1}$$

where V_v^p, V_i^p, I_v^p and I_i^p are defined as transmission line Green's functions (TLGF's). They are the response of transmission lines excited by unit-strength impulsive sources. Furthermore, $V_v^p(m,z \mid n,z')$ and $I_v^p(m,z \mid n,z')$ denote respectively the voltage and current at point z in layer m due to a 1-V series voltage source at z' in layer n. Similarly, $V_i^p(m,z \mid n,z')$ and $I_i^p(m,z \mid n,z')$ denote respectively the voltage and current at point z in layer m due to a 1-A shunt current source at z' in layer n. A typical segment of the equivalent transmission line network is shown in Fig. C-1.

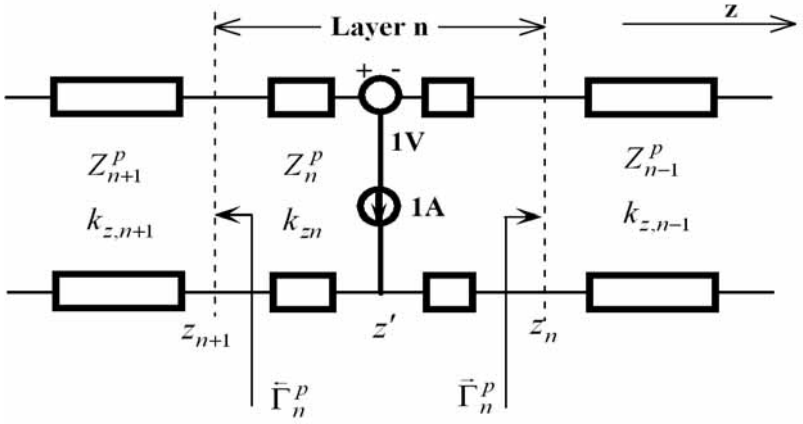

Fig. C-1 Typical transmission line segment and its adjacent segments in the presence of both current and voltage sources.

The TLGF's satisfy the following equations:

$$\begin{aligned} \frac{dV_v^p}{dz} &= -jk_z Z^p I_v^p + \delta(z-z') \\ \frac{dI_v^p}{dz} &= -jk_z Y^p V_v^p \end{aligned} \tag{C.2}$$

$$\begin{aligned} \frac{dV_i^p}{dz} &= -jk_z Z^p I_i^p \\ \frac{dI_i^p}{dz} &= -jk_z Y^p V_i^p + \delta(z-z') \end{aligned} \tag{C.3}$$

where δ is the Dirac delta. In addition, the TLGF's have the following reciprocity property:

$$\begin{aligned} V_i^p(z \mid z') &= V_i^p(z' \mid z), \quad & I_v^p(z \mid z') &= I_v^p(z' \mid z), \\ V_v^p(z \mid z') &= -I_i^p(z' \mid z), \quad & I_i^p(z \mid z') &= -V_v^p(z' \mid z), \end{aligned} \tag{C.4}$$

which will facilitate the derivation of the TLGF's and make the coding in software more concise.

The final solutions of (C.2) and (C.3) are summarized as follows [33, 100]:

Case I − Source and field points located in the same layer ($m = n$):

$$V_i^p(m,z \mid n,z') = \frac{Z_n^p}{2}\left[e^{-jk_{zn}|z-z'|} + \frac{1}{D_n^p}\sum_{s=1}^{4} R_{ns}^p e^{-jk_{zn}\gamma_{ns}} \right] \tag{C.5}$$

$$\begin{aligned} I_i^p(m,z \mid n,z') = \frac{1}{2}\Bigg[& \mathrm{Sign}(z-z') e^{-jk_{zn}|z-z'|} + \frac{1}{D_n^p}\sum_{s=1}^{2} (-1)^s R_{ns}^p\, e^{-jk_{zn}\gamma_{ns}} \\ & + \frac{1}{D_n^p}\sum_{s=1}^{2} (-1)^{s+1} R_{n,s+2}^p\, e^{-jk_{zn}\gamma_{n,s+2}} \Bigg] \end{aligned} \tag{C.6}$$

$$V_v^p(m,z\,|\,n,z') = \frac{1}{2}\left[\mathrm{Sign}(z-z')e^{-jk_{zn}|z-z'|} + \frac{1}{D_n^p}\sum_{s=1}^{4}(-1)^{s+1}R_{ns}^p\, e^{-jk_{zn}\gamma_{ns}} \right] \quad \text{(C.7)}$$

$$I_v^p(m,z\,|\,n,z') = \frac{Y_n^p}{2}\left[e^{-jk_{zn}|z-z'|} - \frac{1}{D_n^p}\sum_{s=1}^{2}R_{ns}^p\, e^{-jk_{zn}\gamma_{ns}} + \frac{1}{D_n^p}\sum_{s=3}^{4}R_{ns}^p\, e^{-jk_{zn}\gamma_{ns}} \right] \quad \text{(C.8)}$$

where

$$p = e \text{ or } h,\ Z_n^e = \frac{k_{zn}}{\omega\varepsilon},\ Z_n^h = \frac{\omega\mu}{k_{zn}},\ k_{zn} = \sqrt{k_n^2 - k_\rho^2}, \quad \text{(C.9)}$$

$$\begin{aligned} \gamma_{n1} &= 2z_n - (z+z'), \quad & \gamma_{n2} &= (z+z') - 2z_{n+1} \\ \gamma_{n3} &= 2d_n + (z-z'), \quad & \gamma_{n4} &= 2d_n - (z-z'), \end{aligned} \quad \text{(C.10)}$$

$$D_n^p = 1 - \vec{\Gamma}_n^p \overleftarrow{\Gamma}_n^p t_n,\ t_n = e^{-2jk_{zn}d_n},\ d_n = z_n - z_{n+1}, \quad \text{(C.11)}$$

$$R_{n1}^p = \vec{\Gamma}_n^p, \quad R_{n2}^p = \overleftarrow{\Gamma}_n^p, \quad R_{n3}^p = R_{n4}^p = \vec{\Gamma}_n^p \overleftarrow{\Gamma}_n^p, \quad \text{(C.12)}$$

$$\vec{\Gamma}_n^p = \frac{\Gamma_{n-1,n}^p + \vec{\Gamma}_{n-1}^p t_{n-1}}{1 + \Gamma_{n-1,n}^p \vec{\Gamma}_{n-1}^p t_{n-1}}, \quad \overleftarrow{\Gamma}_n^p = \frac{\Gamma_{n+1,n}^p + \overleftarrow{\Gamma}_{n+1}^p t_{n+1}}{1 + \Gamma_{n+1,n}^p \overleftarrow{\Gamma}_{n+1}^p t_{n+1}}, \quad \text{(C.13)}$$

$$\Gamma_{ij}^p = \frac{Z_i^p - Z_j^p}{Z_i^p + Z_j^p}, \quad \text{(C.14)}$$

$$\mathrm{Sign}(z-z') = \begin{cases} 1 & \text{if } z > z' \\ -1 & \text{if } z < z' \end{cases}. \quad \text{(C.15)}$$

In the above equations $\vec{\Gamma}_n^p$ and $\overleftarrow{\Gamma}_n^p$ denote the voltage reflection coefficients looking to the directions along the positive and negative z axis, respectively. They are determined by the recursive relations in (C.13). In particular, the voltage reflection coefficients for the outmost layers of a multilayered medium are known:

$\vec{\Gamma}_1^p = 0$ or $\overleftarrow{\Gamma}_1^p = 0$ for the outmost half-space layers; $\vec{\Gamma}_1^p = -1$ or $\overleftarrow{\Gamma}_1^p = -1$ for the outmost PEC layers.

Case II − Source point located below the field point ($m < n$):

$$V_{v,i}^p(m,z \mid n,z') = V_{v,i}^p(n,z_n \mid n,z') \cdot \frac{\prod_{k=m+1}^{n-1} \vec{T}_k^{vp}}{1+\vec{\Gamma}_m^p t_m} \left[e^{-jk_{zm}(z-z_{m+1})} + \vec{\Gamma}_m^p e^{-jk_{zm}(d_m+z_m-z)} \right] \quad \text{(C.16)}$$

$$I_{v,i}^p(m,z \mid n,z') = I_{v,i}^p(n,z_n \mid n,z') \cdot \frac{\prod_{k=m+1}^{n-1} \vec{T}_k^{ip}}{1-\vec{\Gamma}_m^p t_m} \left[e^{-jk_{zm}(z-z_{m+1})} - \vec{\Gamma}_m^p e^{-jk_{zm}(d_m+z_m-z)} \right] \quad \text{(C.17)}$$

where

$$\vec{T}_k^{vp} = \frac{(1+\vec{\Gamma}_k^p) e^{-jk_{zk}d_k}}{1+\vec{\Gamma}_k^p t_k}, \quad \vec{T}_k^{ip} = \frac{(1-\vec{\Gamma}_k^p) e^{-jk_{zk}d_k}}{1-\vec{\Gamma}_k^p t_k}. \quad \text{(C.18)}$$

Case III − Source point located above the field point ($m > n$):

$$V_{v,i}^p(m,z \mid n,z') = V_{v,i}^p(n,z_{n+1} \mid n,z') \cdot \frac{\prod_{k=n+1}^{m-1} \overleftarrow{T}_k^{vp}}{1+\overleftarrow{\Gamma}_m^p t_m} \left[e^{-jk_{zm}(z_m-z)} + \overleftarrow{\Gamma}_m^p e^{-jk_{zm}(d_m+z-z_{m+1})} \right] \quad \text{(C.19)}$$

$$I_{v,i}^p(m,z \mid n,z') = I_{v,i}^p(n,z_{n+1} \mid n,z') \cdot \frac{\prod_{k=n+1}^{m-1} \overleftarrow{T}_k^{ip}}{1-\overleftarrow{\Gamma}_m^p t_m} \left[e^{-jk_{zm}(z_m-z)} - \overleftarrow{\Gamma}_m^p e^{-jk_{zm}(d_m+z-z_{m+1})} \right] \quad \text{(C.20)}$$

where

$$\overleftarrow{T}_k^{vp} = \frac{(1+\overleftarrow{\Gamma}_k^p) e^{-jk_{zk}d_k}}{1+\overleftarrow{\Gamma}_k^p t_k}, \quad \overleftarrow{T}_k^{ip} = \frac{(1-\overleftarrow{\Gamma}_k^p) e^{-jk_{zk}d_k}}{1-\overleftarrow{\Gamma}_k^p t_k}. \quad \text{(C.21)}$$

References

[1] *International Technology Roadmap for Semiconductors (ITRS 2001-2004)*, http://public.itrs.net/.

[2] R. Achar and M. S. Nakhla, "Simulation of High-Speed Interconnects," *Proc. IEEE*, vol. 89, pp. 693-728, May 2001.

[3] A. E. Ruehli and A. C. Cangellaris, "Progress in the Methodologies for the Electrical Modeling of Interconnects and Electronic Packages," *Proc. IEEE*, vol. 89, pp. 740-771, May 2001.

[4] H. B. Bakoglu, *Circuits, interconnections, and packaging for VLSI*. Reading, Massachusetts: Addison-Wesley, 1990.

[5] C.-K. Cheng, J. Lilli, S. Lin, and N. Chang, *Interconnect Analysis and Synthesis*. New York: John Wiley, 1999.

[6] B. Young, *Digital signal integrity: modeling and simulation with interconnects and packages*. Upper Saddle River, NJ: Prentice Hall, 2000.

[7] I. Ierdin, M. Nakhla, and R. Achar, "Circuit Analysis of Electromagnetic Radiations and Field Coupling Effects for Networks with Embedded Full-wave Modules," *IEEE Trans. Electromagn. Compat.*, vol. 42, pp. 449–460, Nov. 2000.

[8] V. A. Thomas, M. E. Jones, M. Piket-May, A. Taflove, and E. Harrigan, "The use of SPICE lumped circuits as sub-grid models for FDTD analysis," *IEEE Microwave Guided Wave Lett.,* vol. 4, pp. 141–143, May 1994.

[9] A. Taflove and S. C. Hagness, C*omputational Electrodynamics: The Finite-Difference Time-Domain Method.* 2nd ed., Boston: Artech House, 2000.

[10] W. Sui, D. A. Christensen, and C. H. Durney, "Extending the Two-Dimensional FDTD Method to Hybrid Electromagnetic Systems with Active and Passive Lumped Elements," I*EEE Trans. Microwave Theory Tech.,* vol. 40, pp. 724-730, Apr. 1992.

[11] C. Yang and V. Jandhyala, "A time domain surface integral technique for mixed electromagnetic and circuit simulation," in E*lectrical Performance of Electronic Packaging,* Monterey: CA, Oct. 2002, pp. 41-44.

[12] R. Sabelka, C. Harlander, and S. Selberherr, "The state of the art in interconnect simulation," in I*nternational Conference on Simulation of Semiconductor Processes and Devices (SISPAD 2000),* Seattle: WA, Sept. 2000, pp. 6-11.

[13] W. H. Kao, C.-Y. Lo, M. Basel, and R. Singh, "Parasitic extraction: current state of the art and future trends," P*roceedings of the IEEE,* vol. 89, pp. 729-739, 2001.

[14] M. Horowitz and R. W. Dutton, "Resistance Extraction from Mask Layout Data," I*EEE Transactions on Computer-Aided Design of Integrated Circuits and Systems,* vol. 2, pp. 145-150, 1983.

[15] R. Singh, "A review of substrate coupling issues and modeling strategies," in P*roc. IEEE*

Custom Integrated Circuits, San Diego: CA, May 1999, pp. 491-499.

[16] K. Nabors and J. White, "FastCap: a multipole accelerated 3-D capacitance extraction program," I*EEE Trans. Computer-Aided Design,* vol. 10, pp. 1447-1459, 1991.

[17] U. Choudhury and A. Sangiovanni-Vincentelli, "Automatic generation of analytical models for interconnect capacitances," I*EEE Trans. Computer-Aided Design,* vol. 14, pp. 470-480, 1995.

[18] N. D. Arora, K. V. Raol, R. Schumann, and L. M. Richardson, "Modeling and extraction of interconnect capacitances for multilayer VLSI circuits," I*EEE Trans. Computer-Aided Design,* vol. 15, pp. 58-67, 1996.

[19] M. W. Beattie and L. T. Pileggi, "Inductance 101: modeling and extraction," in P*roc. Design Automation Conference 2001,* Las Vegas: NV, June 2001, pp. 323-328.

[20] M. Kamon, M. J. Ttsuk, and J. K. White, "FASTHENRY: a multipole-accelerated 3-D inductance extraction program," I*EEE Trans. Microwave Theory Tech.,* vol. 42, pp. 1750-1758, 1994.

[21] H. Hu, D. T. Blaauw, V. Zolotov, K. Gala, M. Zhao, R. Panda, and S. S. Sapatnekar, "Fast on-chip inductance simulation using a precorrected-FFT method," I*EEE Trans. Computer-Aided Design,* vol. 22, pp. 49-66, 2003.

[22] A. E. Ruehli, "Equivalent Circuit Models for Three-Dimensional Multiconductor Systems," I*EEE Trans. Microwave Theory Tech.,* vol. 22, pp. 216-221, 1974.

[23] A. E. Ruehli and P. A. Brennan, "Efficient Capacitance Calculations for Three-Dimensional Multiconductor Systems," I*EEE Trans. Microwave Theory Tech.,* vol. 21, pp. 76-82, 1973.

[24] H. Heeb and A. E. Ruehli, "Three-dimensional interconnect analysis using partial element equivalent circuits," I*EEE Trans. Circuits Syst. I,* vol. 39, pp. 974-982, 1992.

[25] P. J. Restle, A. E. Ruehli, S. G. Walker, and G. Papadopoulos, "Full-wave PEEC time-domain method for the modeling of on-chip interconnects," I*EEE Trans. Computer-Aided Design,* vol. 20, pp. 877-886, 2001.

[26] K. S. Yee, "Numerical solution of initial boundary value problems involving Maxwell's equations in isotropic media," I*EEE Trans. Antennas Propagat.,* vol. 14, pp. 302-307, 1966.

[27] J. L. Volakis, A. Chatterjee, and L. C. Kempel, F*inite element method for electromagnetics: with applications to antennas, microwave circuits, and scattering.* New York: IEEE Press, 1998.

[28] J. Jin, T*he Finite Element Method in Electromagnetics.* 2nd ed., New York: John Wiley & Sons, 2002.

[29] R. F. Harrington, F*ield Computation by Moment Methods.* New York: Macmillan, 1968.

[30] A. F. Peterson, S. L. Ray, and R. Mittra, C*omputational methods for electromagnetics.* New York, IEEE Press, 1998.

[31] W. T. Beyene and J. E. Schutt-Aine, "Efficient transient simulation of high-speed interconnects characterized by sampled data," I*EEE Trans. Comp., Packag., Manufact. Technol. B,* vol. 21, pp. 105-114, Feb. 1998.

[32] M. Elzinga, K. L. Virga, and J. L. Prince, "Improved global rational approximation macromodeling algorithm for networks characterized by frequency-sampled data," I*EEE Trans. Microwave Theory Tech.,* vol. 48, pp. 1461-1468, Sept. 2000.

[33] K. A. Michalski and J. R. Mosig, "Multilayered media Green's functions in integral equation formulations," I*EEE Trans. Antennas Propagat.,* vol. 45, pp. 508-519, Mar. 1997.

[34] T. Watanabe and H. Asai, "Synthesis of time-domain models for interconnects having 3-D structure based on FDTD method," I*EEE Trans. Circuits Syst. II,* vol. 47, pp. 302-305, 2000.

[35] T. Mangold and P. Russer, "Full-wave modeling and automatic equivalent-circuit generation of millimeter-wave planar and multilayer structures," I*EEE Trans. Microwave Theory Tech.,* vol. 47, pp. 851–858, Jun. 1999.

[36] T. F. Eibert and V. Hansen, "3-D FEM/BEM-hybrid approach based on a general formulation of Huygens' principle for planar layered media," IE*EE Trans. Microwave Theory Tech., v*ol. 45, pp. 1105-1112, 1997.

[37] K. A. Michalski, "Mixed-potential integral equation (MPIE) formulation for non-planar microstrip structures of arbitrary shape in multilayered uniaxial media," In*t. J. Microwave Millimeter-Wave Comput.-Aided Eng., v*ol. 3, pp. 420-431, 1993.

[38] M. J. Tsai, F. D. Flaviis, O. Fordham, and N. G. Alexopoulos, "Modeling planar arbitrarily shaped microstrip elements in multilayered media," IE*EE Trans. Microwave Theory Tech., v*ol. 45, pp. 330-337, Mar. 1997.

[39] X. Zhang, J. Fang, K. K. Mei, and Y. Liu, "Calculations of the dispersive characteristics of microstrips by the time-domain finite difference method," IE*EE Trans. Microwave Theory Tech., v*ol. 36, pp. 263-267, Feb. 1988.

[40] D. M. Sheen, S. M. Ali, M. D. Abouzahra, and J. A. Kong, "Application of the three-dimensional finite-difference time-domain method to the analysis of planar microstrip circuits," IE*EE Trans. Microwave Theory Tech., v*ol. 38, pp. 849-857, July 1990.

[41] R. Mittra, W. D. Becker, and P. H. Harms, "A General Purpose Maxwell Solver for the Extraction of Equivalent Circuits of Electronic Package Components for Circuit Simulation," IE*EE Trans. Circuits Syst. I, v*ol. 39, pp. 964-973, Nov. 1992.

[42] P. C. Cherry and M. F. Iskander, "FDTD analysis of high frequency electronic interconnection effects," IE*EE Trans. Microwave Theory Tech., v*ol. 43, pp. 2445-2451, Oct. 1995.

[43] M. Picket-May, A.Taflove, and J. Baron, "FD-TD modeling of digital signal propagation in 3-Dcircuits with passive and active loads," IE*EE Trans. Microwave Theory Tech., v*ol. 42, pp. 1514–1523, Aug. 1994.

[44] P. Ciampolini, P. Mezzanotte, L. Roselli, and R. Sorrentino, "Accurate and efficient circuit simulation with lumped-element FDTD technique," IEE*E Trans. Microwave Theory Tech., vo*l. 44, pp. 2207–2214, Dec. 1996.

[45] X. Zhang and K. K. Mei, "Time-Domain Finite Difference Approach to the Calculation of the Frequency-Dependent Characteristics of Microstrip Discontinuities," IEEE *Trans. Microwave Theory Tech., vol*. 36, pp. 1775-1787, Dec. 1988.

[46] A. Taflove and M. E. Brodwin, "Numerical Solution of Steady-State Electromagnetic Scattering Problems Using the Time-Dependent Maxwell's Equations," IEEE *Trans. Microwave Theory Tech., vol*. 23, pp. 623-630, 1975.

[47] Y. Qian and T. Itoh, "Full wave electromagnetic analysis in the time domain," in Anal*ysis and design of integrated circuit antenna modules, K.* C. Gupta and P. S. Hall, Eds. New York: Wiley, 1999, pp. 84-85.

[48] A. P. Zhao and A. V. Raisanen, "Application of a simple and efficient source excitation technique to the FDTD analysis of waveguide and microstrip circuits," IEEE *Trans. Microwave Theory Tech., vol*. 44, pp. 1535-1539, 1996.

[49] G. Mur, "Absorbing boundary conditions for the finite-difference approximation of the time-domain electromagnetic field equations," IEEE *Trans. Electromagn. Compat., vol*. 23, pp. pp. 377-382, Nov. 1981.

[50] S. D. Gedney, "An anisotropic perfectly matched layer-absorbing medium for the truncation of FDTD lattices," IEEE *Trans. Antennas Propagat., vol*. 44, pp. 1630-1639, 1996.

[51] E. Chiprout and M. Nakhla, Asym*ptotic Waveform Evaluation and Moment Matching for Interconnect Analysis. Bos*ton, MA: Kluwer, 1993.

[52] R. Achar and M. S. Nakhla, "Efficient transient simulation of embedded subnetworks characterized by s-parameters in the presence of nonlinear elements," IEEE *Trans. Microwave Theory Tech., vol*. 46, pp. 2356-2363, Dec. 1998.

[53] L. M. Silveira, I. M. Elfadel, J. K. White, M. Chilukuri, and K. S. Kundert, "Efficient frequency-domain modeling and circuit simulation of transmission lines," IEEE *Trans. Comp. Packag. Manufact. Technol. B, vol*. 17, pp. 505–513, Nov. 1994.

[54] E. C. Chang and S.-M. Kang, "Transient simulation of lossy coupled transmission lines using iterative linear least square fitting and piecewise recursive convolution," IEEE *Trans. Circuits Syst. I, vol.* 43, pp. 923-932, 1996.

[55] R. Neumayer, F. Haslinger, A. Stelzer, and R. Wiegel, "Synthesis of SPICE-compatible broadband electrical models from n-port scattering parameter data," in Proc. *IEEE Symp. Electromagn. Compat., Minn*esota, USA, Aug. 2002, pp. 469-474.

[56] S. Lin and E. S. Kuh, "Transient simulation of lossy interconnects based on the recursive convolution formulation," IEEE *Trans. Circuits Syst. I, vol.* 39, pp. 879-892, Nov.1992 1992.

[57] B. Gustavsen and A. Semlyen, "Rational approximation of frequency domain responses

by vector fitting," IEEE *Trans. Power Delivery, vol.* 14, pp. 1052-1061, July 1999.

[58] W. Pinello, J. Morsey, and A. C. Cangelaris, "Synthesis of SPICE-compatible broadband electrical models for pins and vias," in Proc. *51st electronic. Components and Technology Conf., Orla*ndo, FL, May 2001, pp. 518-522.

[59] J. Vlach and K. Singhal, Compu*ter Methods for Circuit Analysis and Design. New* York: Van Nostrand, 1983.

[60] G. H. Golub and C. F. Van Loan, Matri*x computations. Balt*imore, Md. : Johns Hopkins University Press, 1983.

[61] C. D. Meyer, Matri*x analysis and applied linear algebra. Phil*adelphia: Society for Industrial and Applied Mathematics, 2000.

[62] L. Elsner, "A Remark on Simultaneous Inclusions of the Zeros of a Polynomial by Gershgorin Theorem," Numer. *Math., vol.* 21, pp. 425-427, 1073.

[63] C. T. Chen, Linea*r System Theory and Design. New* York: Oxford University Press, 1998.

[64] T. Palenius and J. Roos, "Comparison of reduced-order interconnect macromodels for time-domain simulation," IEEE *Trans. Microwave Theory Tech., vol.* 52, pp. 2240-2250, 2004.

[65] A. Vladimirescu, The P*Spice Book. New* York: John Wiley & Sons, 1994.

[66] B. Gustavsen and A. Semlyen, "Enforcing passivity for admittance matrices approximated by rational functions," IEEE *Transactions on Power Systems, vol.* 16, pp. 97-104, 2001.

[67] C. P. Coelho, J. Phillips, and L. M. Silveira, "A convex programming approach for generating guaranteed passive approximations to tabulated frequency-data," IEEE *Trans. Computer-Aided Design, vol.* 23, pp. 293-301, 2004.

[68] H. Chen and J. Fang, "Enforcing bounded realness of S parameter through trace parameterization," in Proc. *Electrical Performance of Electronic Packaging, Sant*a Cruz: CA, Oct. 2003, pp. 291-294.

[69] D. Saraswat, R. Achar, and M. S. Nakhla, "A fast algorithm and practical considerations for passive macromodeling of measured/simulated data," IEEE *Transactions on Advanced Packaging, vol.* 27, pp. 57-70, 2004.

[70] D. Saraswat, R. Achar, and M. S. Nakhla, "Global Passivity Enforcement Algorithm for Macromodels of Interconnect Subnetworks Characterized by Tabulated Data," IEEE *Transactions on VLSI Systems, vol.* 13, pp. 819-832, 2005.

[71] S. Grivet-Talocia, "Passivity enforcement via perturbation of Hamiltonian matrices," IEEE *Trans. Circuits Syst. I, vol.* 51, pp. 1755-1769, 2004.

[72] Star-*HSPICE manual. Avan*t Corporation, 1998.

[73] Q. Chu, F. Chang, Y. Lzu, and O. Wing, "Time-domain mode synthesis of microstrip," IEEE *Microwave Guided wave lett., vol.* 7, pp. 9-11, Jan. 1997.

[74] Q.-X. Chu, Y.-P. Lau, and F.-Y. Chang, "Transient analysis of microwave active circuits

based on time-domain characteristic models," IEEE *Trans. Microwave Theory Tech., vol.* 46, pp. 1097-1104, 1998.

[75] A. W. Glisson and D. R. Wilton, "Simple and efficient numerical methods for problems of electromagnetic radiation and scattering from surfaces," IEEE *Trans. Antennas Propagat., vol.* AP-28, pp. 593-603, Sept. 1980.

[76] A. W. Glisson, "Electromagnetic scattering by arbitrarily shaped surfaces with impedance boundary conditions," Radio *Sci., vol.* 27, pp. 935-943, Nov./Dec. 1992.

[77] K. A. Michalski, "On the scalar potential of a point charge associated with a time harmonic dipole in a layered medium," IEEE *Trans. Antennas Propagat., vol.* AP-35, pp. 1299-1301, Nov. 1987.

[78] K. A. Michalski and D. Zheng, "Electromagnetic scattering and radiation by surfaces of arbitrary shape in layered media, Part I: Theory," IEEE *Trans. Antennas Propagat., vol.* 38, pp. 335-344, Mar. 1990.

[79] D. R. Wilton, "Review of current status and trends in the use of integral equations in computational electromagnetics," Elect*romagn., vol.* 12, pp. 287-341, July/Dec. 1992.

[80] J. R. Mosig and F. E. Gardiol, "A dynamical radiation model for microstrip structures," in Advan*ces in Electronics and Electron Physics, vol.* 59, P. W. Hawkes, Ed. New York: Academic, 1982, pp. 139-237.

[81] W. A. Johnson, "Analysis of vertical, tubular cylinder which penetrates an air-dielectric interface and which is excited by an azimuthally symmetric source," Radio *Sci., vol.* 18, pp. 1273-1281, Nov./Dec. 1983.

[82] N. W. Montgomery and D. R. Wilton, "Analysis of arbitrary conducting periodic structures embedded in layered media," in Dig. *IEEE AP-St. Symp., Lond*on, On, Canada, June 1991, pp. 1889-1892.

[83] J. Chen, A. A. Kishk, and A. W. Glisson, "Application of a new MPIE formulation to the analysis of a dielectric resonator embedded in a multilayered medium coupled to a microstrip circuit," IEEE *Trans. Microwave Theory Tech., vol.* 49, pp. 263-279, 2001.

[84] D. L. Zheng, Radiat*ion, scattering, and guidance of electromagnetic fields by conducting objects of arbitrary shape in layered media. PhD.* Thesis, University of Mississippi, 1988.

[85] K. A. Michalski and D. Zheng, "Electromagnetic scattering and radiation by surfaces of arbitrary shape in layered media, Part II: Implementation and results for contiguous half-spaces," IEEE *Trans. Antennas Propagat., vol.* 38, pp. 345-352, Mar. 1990.

[86] L. B. Felsen and N. Marcuvitz, Radiat*ion and Scattering of Waves. Engl*ewood Cliffs, NJ: Prentice Hall, 1973.

[87] W. C. Chew and Q. Liu, "Resonance frequency of a rectangular microstrip patch," IEEE *Trans. Antennas Propagat., vol.* 36, pp. 1045-1056, Aug. 1988.

[88] T.-S. Horng, N. G. Alexopoulos, S.-C. Wu, and H.-Y. Yang, "Full wave spectral analysis for open microstrip discontinuities of arbitrary shape including radiation and surface-wave losses," Int. *J. Microwave Millimeter-Wave Comput.-Aided Eng., vol.* 2, pp.

224-240, 1992.

[89] T. Becks and I. Wolff, "Analysis of 3-D metallization structures by a full-wave spectral domain technique," IEEE *Trans. Microwave Theory Tech., vol.* 40, pp. 2219-2227, Dec. 1992.

[90] A. Sommerfeld, Partia*l Differential Equations in Physics. New* York: Academic, 1949.

[91] W. C. Chew, Waves *and Fields in Inhomogeneous Media. New* York: Van Nostrand Reinhold, 1990.

[92] J. Mosig, "Integral equation technique," in Numeri*cal Techniques for Microwave and Millimeter-Wave Passive Structures, T. I*toh, Ed. New York: Wiley, 1989, pp. 133-213.

[93] G. J. Burke, E. K. Miller, J. N. Brittingham, D. L. Lager, R. J. Lytle, and J. T. Okada, "Computer modeling of antennas near the ground," Elect*romagn., vol.* 1, pp. 29-49, Jan./Mar. 1981.

[94] E. H. Newman and D. Forrai, "Scattering from a microstrip patch," IEEE *Trans. Antennas Propagat., vol.* AP-35, pp. 245-251, Mar. 1987.

[95] A. D. Chave, "Numerical integration of related Hankel transforms by quadrature and continued fraction expansion," Geoph*ys., vol.* 48, pp. 1671-1686, Dec. 1983.

[96] P. Gay-Balmz and J. Mosig, "Three-dimensional planar radiating structures in stratified media," Int. *J. Microwave Millimeter-Wave Computer-Aided Eng., vol.* 7, pp. 330-343, Sept. 1997.

[97] K. A. Michalski, "Extrapolation methods for Sommerfeld integral tails," IEEE *Trans. Antennas Propagat., vol.* 46, pp. 1405-1418, Oct. 1998.

[98] J. A. Kong, Elect*romagnetic wave theory. 2nd* ed., New York: Wiley, 1990.

[99] E. Kreyszig, Advan*ced engineering mathematics. 8th* ed., New York: John Wiley, 1999.

[100] C.-I. G. Hsu, R. F. Harrington, K. A. Michalski, and D. Zheng, "Analysis of a multiconductor transmission lines of arbitrary cross-section in multilayered uniaxial media," IEEE *Trans. Microwave Theory Tech., vol.* 41, pp. 70-78, Jan. 1993.

[101] Y. Liu, MPIE-*MOM analysis of PEC objects in multilayered media. Mast*er Thesis, National University of Singapore, 2000.

[102] F. Ling, J. Liu, and J.-M. Jin, "Efficient electromagnetic modeling of three-dimensional multilayer microstrip antennas and circuits," IEEE *Trans. Microwave Theory Tech., vol.* 50, pp. 1628-1635, 2002.

[103] P. E. Wannamaker, G. W. Hohmann, and W. A. SanFilipo, "Electromagnetic modeling of three-dimensional bodies in layered earths using integral equations," Geoph*ys., vol.* 49, pp. 60-74, Jan. 1984.

[104] D. G. Fang, J. J. Yang, and G. Y. Delisle, "Discrete image theory for horizontal electric dipoles in a multilayered medium," Inst. *Elect. Eng. Proc., vol.* 135, pp. 297-303, Oct. 1988.

[105] Y. L. Chow, J. J. Yang, D. G. Fang, and G. E. Howard, "A closed-form spatial Green's

function for the thick microstrip substrate," IEEE *Trans. Microwave Theory Tech., vol.* 39, pp. 588-592, Mar. 1991.

[106] M. I. Aksun, "A robust approach for the derivation of closed-form Green's functions," IEEE *Trans. Microwave Theory Tech., vol.* 44, pp. 651-658, May 1996.

[107] T. K. Sarkar and O. Pereira, "Using the matrix pencil method to estimate the parameters of a sum of complex exponentials," IEEE *Antennas Propagat. Mag., vol.* 37, pp. 48-55, Feb. 1995.

[108] N. Kinayman and M. I. Aksun, "Efficient use of closed-form Green's functions for the analysis of planar geometries with vertical connections," IEEE *Trans. Microwave Theory Tech., vol.* 45, pp. 593-603, 1997.

[109] Y. Liu, L. W. Li, T. S. Yeo, and M. S. Leong, "Application of DCIM to MPIE-MoM analysis of 3D PEC objects in multilayered media," IEEE *Trans. Microwave Theory Tech., vol.* 50, pp. 157-162, Feb. 2002.

[110] R. A. Kipp and C. H. Chan, "Complex image method for sources in bounded regions of multilayer structures," IEEE *Trans. Microwave Theory Tech., vol.* 42, pp. 860-865, May 1994.

[111] M. Aksun, M. Emre Yavuz, and G. Dural, "Comments on the problems in DCIM," in Anten*nas and Propagation Society International Symposium, 2003. IEEE, Colu*mbus, OH, June 2003, pp. 673-676.

[112] R. F. Harrington, "Matrix methods for field problems," Proc. *IEEE, vol.* 55, pp. 136-149, Feb. 1967.

[113] J. A. Kong, Advan*ced Electromagnetism, Spring 2003, Mass*achusetts Institute of Technology, from MIT OpenCourseWare website, http://ocw.mit.edu.

[114] S. M. Rao, D. R. Wilton, and A. W. Glisson, "Electromagnetic scattering by surfaces of arbitrary shape," IEEE *Trans. Antennas Propagat., vol.* AP-30, pp. 409-418, May 1982.

[115] S.-G. Hsu and R.-B. Wu, "Full wave characterization of a through hole via using the matrix-penciled moment method," IEEE *Trans. Microwave Theory Tech., vol.* 42, pp. 1540-1547, 1994.

[116] S.-G. Hsu and R.-B. Wu, "Full-wave characterization of a through hole via in multi-layered packaging," IEEE *Trans. Microwave Theory Tech., vol.* 43, pp. 1073-1081, 1995.

[117] M. I. Aksun and R. Mittra, "Estimation of spurious radiation from microstrip etches using closed-form Green's functions," IEEE *Trans. Microwave Theory Tech., vol.* 40, pp. 2063-2069, 1992.

[118] A. C. Balanis, Advan*ced engineering electromagnetics. New* York: Wiley, 1989.

[119] F. Ling and J. M. Jin, "Scattering and radiation analysis of microstrip antennas using discrete complex image method and reciprocity theorem," Micro*wave Opt. Tech. Lett., vol.* 16, pp. 212-216, Nov. 1997.

[120] E. K. L. Yeung, J. C. Beal, and Y. M. M. Antar, "Multilayer microstrip structure analysis

with matched load simulation," IEEE *Trans. Microwave Theory Tech., vol.* 43, pp. 143-149, 1995.

[121] P. B. Katehi and N. G. Alexopoulos, "Frequency-Dependent Characteristics of Microstrip Discontinuities in Millimeter-Wave Integrated Circuits," IEEE *Trans. Microwave Theory Tech., vol.* 33, pp. 1029-1035, 1985.

[122] V. I. Okhmatovski, J. Morsey, and A. C. Cangellaris, "On de-embedding of port discontinuities in full-wave CAD models of multiport circuits," IEEE *Trans. Microwave Theory Tech., vol.* 51, pp. 2355-2365, 2003.

[123] R. C. Hall and J. R. Mosig, "The analysis of arbitrarily shaped aperture-coupled patch antennas via a mixed-potential integral equation," IEEE *Trans. Antennas Propagat., vol.* 44, pp. 608, 1996.

[124] D. C. Chang and J. X. Zhang, "Electromagnetic modeling of passive circuit elements in MMIC," IEEE *Trans. Microwave Theory Tech., vol.* 40, pp. 1741-1747, Sept. 1992.

[125] M. Kahrizi, T. K. Sarkar, and Z. A. Maricevic, "Analysis of a wide radiating slot in the ground plane of a microstrip line," IEEE *Trans. Microwave Theory Tech., vol.* 41, pp. 29-37, 1993.

[126] F. Ling, C.-F. Wang, and J.-M. Jin, "An efficient algorithm for analyzing large-scale microstrip structures using adaptive integral method combined with discrete complex-image method," IEEE *Trans. Microwave Theory Tech., vol.* 48, pp. 832-839, 2000.

[127] T. K. Sarkar, Appli*cation of conjugate gradient method to electromagnetics and signal analysis. New* York: Elsevier, 1991.

[128] C. F. Smith, A. F. Peterson, and R. Mittra, "The biconjugate gradient method for electromagnetic scattering," IEEE *Trans. Antennas Propagat., vol.* 38, pp. 938-940, 1990.

[129] Y. Saad, "Iterative methods for sparse linear systems." Boston: PWS Publishing, 1996.

[130] V. Rokhlin, "Rapid solution of integral equations of scattering theory in two dimensions," J. Co*mput. Phys., vol.* 86, pp. 414-439, Feb. 1990.

[131] W. C. Chew, J. M. Jin, E. E. Michielsse, and J. M. Song, Fast *and Efficient Algorithms in Computational Electromagnetic. Bost*on, MA: Artech House, 2001.

[132] R. Barrett, M. Berry, T. F. Chan, J. Demmel, J. Donato, J. Dongarra, V. Eijkhou, R. Pozo, C. Romine, and H. V. d. Vorst, Templ*ates for the Solution of Linear Systems: building blocks for iterative methods. Phil*adelphia, PA: SIAM, 1994.

[133] P. S. Hall, V. F. Fusco, and M. J. Cryan, "Circuit simulator based methods," in Analy*sis and design of integrated circuit antenna modules, K. C.* Gupta and P. S. Hall, Eds. New York: Wiley, 1999, pp. 84-85.

[134] F. Ling, D. Jiao, and J.-M. Jin, "Efficient electromagnetic modeling of microstrip structures in multilayer media," IEEE *Trans. Microwave Theory Tech., vol.* 47, pp. 1810-1818, 1999.

[135] C. Q. Scrantom and J. C. Lawson, "LTCC technology: where we are and where we're

going---II," in Dig. *IEEE MTT-S Int. Symp. Tech. Wireless Appl., Bc.,* Canada, Feb 1999, pp. 193-200.

[136] A. R. Bretones, R. Mittra, and R. G. Martin, "A hybrid technique combining the method of moments in the time domain and FDTD," IEEE *Microwave Guided Wave Lett., vol.* 8, pp. 281-283, 1998.

[137] G. Cerri, P. Russo, A. Schiavoni, G. Tribellini, and P. Bielli, "MoM-FDTD hybrid technique for analysing scattering problems," Elect*ronics Letters, vol.* 34, pp. 438-440, 1998.

[138] G. Cerri, Chiarandini, P. Russo, and A. Schiavoni, "Electromagnetic coupling between arbitrarily bent wires and scatterers analysed by a hybrid MoMTD/FDTD approach," IEEE *Proc. Microwaves, Antennas and Propagation, vol.* 147, pp. 261-266, 2000.

[139] S. Barmada, A. Musolino, and M. Raugi, "Equivalence theorem boundary conditions for FDTD formulations," IEEE *Trans. Magn., vol.* 40, pp. 1049-1052, 2004.

[140] A. Taflove and K. Umashankar, "A hybrid moment method/finite-difference time-domain approach to electromagnetic coupling and aperture penetration into complex geometries," IEEE *Trans. Antennas Propagat., vol.* 30, pp. 617-627, 1982.

[141] Z. Huang, K. R. Demarest, and R. G. Plumb, "An FDTD/MoM hybrid technique for modeling complex antennas in the presence of heterogeneous grounds," IEEE *Trans. Geosci. Remote Sensing, vol.* 37, pp. 2692-2698, 1999.

[142] E. A. Forgy, W. C. Chew, and J. M. Jin, "A hybrid MoM/FDTD technique for studying human head/antenna interactions," in IEEE-*APS Conference on Antennas and Propagation for Wireless Communications, Walt*ham: MA, Nov. 1998, pp. 81-84.

[143] M. A. Mangoud, R. A. Abd-Alhameed, and P. S. Excell, "Simulation of human interaction with mobile telephones using hybrid techniques over coupled domains," IEEE *Trans. Microwave Theory Tech., vol.* 48, pp. 2014-2021, 2000.

[144] H. Rogier, F. Olyslager, and D. De Zutter, "A new hybrid FDTD-BIE approach to model electromagnetic scattering problems," IEEE *Microwave Guided Wave Lett., vol.* 8, pp. 138-140, 1998.

[145] R. F. Harrington, Time-*Harmonic Electromagnetic Field. New* York: McGraw-Hill, 1961.

[146] H. Rogier, D. De Zutter, and F. Olyslager, "Modeling radiation from complex structures using a hybrid FDTD-BIE technique," in IEEE *AP-S Int. Symp., Atla*nta, GA, June 1998, pp. 1808-1811.

[147] A. Petosa, A. Ittipiboon, Y. M. M. Antar, D. Roscoe, and M. Cuhaci, "Recent advances in dielectric-resonator antenna technology," IEEE *Antennas Propagat. Mag., vol.* 40, pp. 35-48, 1998.

[148] K. M. Luk and K. W. Leung, Diele*ctric resonator antennas. Phil*adelphia: Research Studies Press, 2003.

[149] M. G. Keller, M. B. Oliver, D. J. Roscoe, R. K. Mongia, Y. M. M. Antar, and A. Ittipiboon, "EHF dielectric resonator antenna array," Micro*wave Opt. Tech. Lett., vol.* 17, pp.

345-349, 1998.

[150] X. Millard and Q. H. Liu, "Simulation of near-surface detection of objects in layered media by the BCGS-FFT method," IEEE *Trans. Geosci. Remote Sensing, vol.* 42, pp. 327-334, 2004.

[151] G. B. Arfken and H. J. Weber, Mathe*matical methods for physicists. 5th* ed., San Diego: Harcourt/Academic Press, 2001.

[152] A. Badawi and A. Sebak, "Using the complex images method to analyze printed antennas in multilayer dielectric media," J. El*ectromagn. Waves Applicat., vol.* 14, pp. 285-300, Mar. 2000.

Author's Publications

Journal Papers:

[1] Enxiao Liu, Er-ping Li, and Le-wei Li, "Analysis of signal propagation on high-speed planar interconnect systems based on full-wave and macromodeling technique," *Microwave Opt. Technol. Lett.*, vol. 39, pp. 183-187, Nov. 2003.

[2] Er-ping Li, En-xiao Liu, Le-wei Li, and Mook-Seng Leong, "A coupled efficient and systematic full-wave time-domain macromodeling and circuit simulation method for signal integrity analysis of high-speed interconnects," *IEEE Transactions on Advanced Packaging*, vol. 27, No.1, pp. 213-223, Feb. 2004.

[3] En-Xiao Liu, Er-Ping Li, Le-Wei Li, and Zhongxiang Shen, "Finite-Difference Time-Domain macromodel for simulation of electromagnetic interference at high-speed interconnects," *IEEE Transactions on Magnetics,* vol. 41, No. 1, pp. 65-71, Jan. 2005.

[4] En-xiao Liu, Er-ping Li, and Le-wei Li, "Hybrid FDTD-MPIE method for the simulation of locally inhomogeneous multilayer LTCC structure," *IEEE Microwave component and wireless communication letter,* vol. 15, No. 1, pp. 42-44, Jan. 2005

[5] En-xiao Liu, Er-ping Li, and Le-wei Li, "Analysis of Multilayer Planar Circuits by a Hybrid Method," Accepted (Oct. 2005) for publication in *IEEE Microwave component and wireless communication letter*.

Conference publications:

[1] Enxiao Liu, Er-ping Li, Xiao Ying, Le-wei Li, and K. H. Lee. "Transient simulation of high-speed interconnects using coupled model order reduction and FDTD-macromodeling technique," in *International conference on science and engineering computation (IC-SEC 2002)*, Dec. 2002, pp. 283-286.

[2] Er-Ping Li, En-Xiao Liu, Zhongxiang Shen and Le-Wei Li, " FDTD-macromodeling technique for simulation of electromagnetic interference at high-speed interconnects," in *Proceedings of the 14th COMPUMAG Conference on the Computation of Electromagnetic Fields (COMPUMAG 2003)*, Saratoga Springs, NY, USA, Jul. 2003, pp. 156-157.

[3] En-xiao Liu, Er-ping Li, and Le-wei Li, "Hybrid FDTD-MPIE method for the simulation of locally inhomogeneous multilayer LTCC structure," in *Proceedings of the 5th Electronics Packaging Technology Conference (EPTC 2003)*, Dec. 2003, pp. 160-163.

[4] Mark Montrose, En-xiao Liu, Er-ping Li, "Analysis on the effectiveness of PCB edge termination using discrete components instead of implementing the 20-H rule," in *Proc. of IEEE International Symposium on Electromagnetic Compatibility*, Santa Clara, CA, Aug. 2004, pp. 45-50.

[5] En-xiao Liu, Er-ping Li, and Le-wei Li, "Simulation of Locally Inhomogeneous Multilayer Planar Structure by Hybrid Method," in *Proceedings of the 3rd International Conference on Computational Electromagnetics*, Beijing, 2004.

[6] En-xiao Liu, Er-ping Li, and Le-wei Li, "Electrical performance simulation of inhomogeneous multilayer LTCC structure by hybrid method," in *Proceedings of the 6th Electronics Packaging Technology Conference (EPTC 2004)*, Dec. 2004.

[7] Hong-Fang Jin, Er-ping Li, and En-Xiao Liu, "A novel integrated approach for simulation of electromagnetic susceptibility problem," in *Proc. of IEEE International Symposium on Electromagnetic Compatibility*, Chicago, IL, Aug. 2005, pp. 446-450.

[8] Zhi-Hong Liu, Er-ping Li, K. Y See and En-Xiao Liu, "Study on power bus noise isolation using SPICE compatible method," in *Proc. of IEEE International Symposium on Electromagnetic Compatibility, Chicago*, IL, Aug. 2005, pp. 438-441.